Energy Radiation from A Multi-Story Building

Thesis by

Javier Favela

In Partial Fulfillment of the Requirements

for the Degree of

Doctor of Philosophy

California Institute of Technology

Pasadena, California

2004

(Defended April 29, 2004)

© 2004
Javier Favela
All Rights Reserved

Acknowledgements

I would like to thank the faculty, staff, and especially the students of the Seismolab, the GPS Division, and the entire Caltech community for some wonderful years as a graduate student. I shared some good and some not so good times with you, and for being there for both, I thank you. My appreciation goes to my thesis advisor, Tom Heaton, whom I thank for his valuable input and encouragement. Many thanks to Toshiro Tanimoto for believing in me, and for being extra supportive and interested in my work. I would also like to thank Don Anderson for his indispensable advice when he was my academic advisor, and for his invaluable input in our undertaken project. Furthermore, I thank Rob Clayton for being a good academic advisor, and for introducing me to the Geophysics field class. For me, it was a mini-vacation when still doing class-related work, and I had a great time all the times I TA'd it. I thank Luis Rivera, as during his short sabbatical at Caltech, I made a good friend and he helped me to re-focus my attention on my thesis. I also thank him for his continued support and the many readings of one of my manuscript. I thank John Hall for his assurances, valuable comments, and help when I had doubts. I thank Hiroo Kanamori for his insight, input, and all his help. I thank Behnam Hushmand, as his continued support and belief in me was very uplifting. I enjoyed TA'ing your classes and you taught me a lot about experimental work. I thank Brad Aagaard for running his finite element code for some of my experiments and for providing me with invaluable data. I thank Kerry Sieh and Jason Saleeby for putting up with my many questions during the Geology field classes. Thanks to your help, I learned something in the classes and had a good time walking around in the dessert/hot tropics doing field geology. I would also like to thank the Division for the many trips they have, as the

one I went on enriched my life. I also thank Berry Wise, Ph.D. for his help and useful comments.

I would like to thank the GPS Division, Caltech, and the James Irvine foundation for my financial support. I also thank the staff of the Seismolab and the Division, for without their continued commitment, help, and niceness, this place would stop functioning. I will always remember Viola, as her stories always made me smile. The same goes to Michelle Medley, whom I've known the longest, and was always willing to help and offer kind and useful advice. My sincerest gratitude goes to Arnie Acosta and Raul Relles for their technical help, guidance, advice, and countless entertaining stories.

I would like to thank all my office mates (Jascha Polet, Leo Eisner, Xi Song, Martin Griffiths, Brian Savage, Zhimei Yan, Nathan Downey (twice), Qinya Liu, and Rowena Lohman) for their patience, as sharing space is not easy, especially when it's done for such long periods of time. Fortunately for all of you, I always had a crazy nocturnal schedule! I also thank Fidel Santamaria, Douglas Varela, and Brian Savage for sharing a living space with me and generally for being good friends. I also thank my classmates Anupama Venkataraman and Bill Keller, friends and study partners. I also thank (hopefully in order of year they entered Caltech) Hong-Kie Thio, Craig Scrivner, Igor Sidorin, Jane Dmochowski, Deborah Smith, Sidao Ni, John Clinton, Andy Guyader, Carlos Romero, Chen Ji, Elisabeth Nadin, Shengnian Luo, Kaiwen Xia, Georgia Cua, Samuel Case Bradfrod V, Patricia Persaud, Vala Hjorleifsdottir, Ali Ozgun Konca, Min Chen, Alisa Miller, Chris DiCaprio, Xyoli Perez-Campos, Angel Ruiz Angulo, Stephane Litner, and Hannes Helgason for their interaction and friendship. Outside of Caltech (and there are people out there!), I would like to thank my parents (Epifanio and Bernardina), my siblings (Roberto, Pedro, and Vianey), my relatives (to many of you to mention all), Angel Fragoso, Miguel Reyes, Cesar Bocanegra, Daniel Fragoso, Martin Fragoso, Angel Favela, Mario Rebolledo-Vieyra, Javier Corral, Hector Aaron Nevarez, Isaac Saucedo, Sedelia Durand, and Antonio Garcia for their friendship, support, and understanding. I thank the members of Club Latino and the Racquetball club for providing me with many distractions and

fun times. For those of you with whom I took trips with, I truly enjoyed them and I'll have everlasting memories.

Extra special thanks go to Jascha, for being a good friend and providing me with all my TriNet data and help with all kinds of scripts. Thanks a lot for introducing me to Nethack, which probably only took a good 3 months out of my life, for countless coffee breaks, and for being the one person I could always count on not having a scientific discussion with. Thanks for the countless re-reads of this thesis and papers; Leo, for the many interesting adventures, and for being there to cheer me up when I felt a bit down, and for making life at the lab interesting; Douglas, for continued support and generous help in the pursuit of my mathematical endeavors. Your constant push to get me to appreciate art functioned somewhat. Thanks for all the good times and all the horrible times teaching in the summer!; John and Gerogia, for being there and for stressing out with me towards the end; Vala, the silver bullet, for being a good friend, workout partner, and for introducing me to the Icelandic bunch at Caltech. We had many good times, but somehow I don't recall them all. It's a good thing you like to take pictures! I always enjoyed hanging out with you and Oliver; Ernesto Mercado, for without him I don't know what I would have done for lunch all these years. I ate at your catering service for my entire graduate career (give or take a few days), and I enjoyed every meal, the conversation, and the advice. You are a pearl to many people at Caltech. When in Philadelphia, I searched for an equal to your Philly steak sandwich, and out of 14 tries in 10 days, I could not find your equal. Thank you!

A cheers up to Leo, Martin, Douglas, John, Brian, Angel, and Angel, my drinking buddies! Special thanks to Brian, who showed me how to make my own beer. Lastly, I also want to thank Dave, the owner of Lucky Baldwins. I've handed over a fortune to you, and I enjoyed every drop of it. Thanks for introducing me to many of my favorite beers.

To my parents, siblings, nephews and nieces, family, friends, anyone who influenced my life in a positive way, and anyone who influenced it in a negative but fun/exciting manner. Without knowing you, I wouldn't be who I am. Without your support and help, I could not have done this. For you, a toast for every hair I've lost. Thank you!

Abstract

Damping limits the resonance of vibrating systems and thus higher anelastic damping is generally favored for engineered structures subjected to earthquake motions. However, there are elastic processes that can mimic the effects of anelastic damping. In particular, buildings lose kinetic energy when their motions generate elastic waves in the Earth; this is referred to as radiation damping. Unlike anelastic damping, strong radiation damping may not always be desirable, as reciprocity can be used to show that buildings may be strongly excited by elastic waves of similar characteristics to those generated by the building's forced vibrations. As a result, it is important to understand the radiation damping of structures to be able to improve their design.

Several experiments, using Caltech's nine-story Millikan Library as a controlled source, were performed to investigate the radiation damping of the structure. The building was forced to resonate at its North-South and East-West fundamental modes, and seismometers were deployed around the structure in order to measure the waves generated by the library's excitation. From this "local" data set, we determine the elastic properties of the soils surrounding the structure and estimate what percentage of the total damping of the structure is due to energy radiation. Using Fourier transforms, we were also able to detect these waves at distances up to 400 km from the source using the broadband stations of the Southern California Seismic Network. This "regional" data set is used in an attempt to identify arrival times and to constrain the type of waves being observed at regional distances.

Table of Contents

Acknowledgements **iii**

Abstract **vii**

Notation **xxi**

1 Introduction **1**

2 Instrumentation and Data Reduction Procedures **10**

2.1 Force Generating System 10

2.2 Building Accelerometers 13

2.3 Seismometers for Local Tests 15

2.4 Seismometers for Regional Tests 16

2.5 Data Reduction Procedures 17

3 Theoretical Solution to Energy Radiation Problem **19**

3.1 Solution of the Elastic Wave Equations 24

3.2 Body Waves from a Shearing Motion 28

3.3 Body Waves from a Rocking Motion 34

3.4 Rayleigh Waves from a Shearing Motion 40

3.5 Rayleigh Waves from a Rocking Motion 44

3.6 Building Results 47

3.7 Kinetic Energy in a Half-Space and Energy Radiation Estimate . . . 53

4 Surface Wave Modelling **63**

4.1 Displacement Data from Millikan II Experiments 65
4.2 Phase Data from Millikan II Experiments 78
4.3 Conclusions 87

5 Finite Element Model Results **88**
5.1 Velocity Models 92
5.2 Point Force Validation 96
5.3 Velocity Model Results and Comparisons 102

6 Regional Observations **120**
6.1 Displacements 121
6.1.1 Method 121
6.1.2 Observations 124
6.2 Signal Velocities 139
6.2.1 Method and Results 139
6.3 Conclusions 142

A Millikan's Natural Frequencies below 9.5 Hz and Accelerometer Data **144**

B Millikan Roof Calibration **183**

C More Power Radiation Estimates **208**
C.1 Direct Method from Millikan Library Acceleration Data 208
C.2 FEM Central Node Estimate 209
C.3 Impedance Function Estimates 212
C.3.1 Impedance Functions from *Wong and Luco* (1978) 213
C.3.2 Impedance Functions from *Mita and Luco* (1989) 214

D Steepest Descent Method **216**
D.0.3 Integral Involving Cylindrical Bessel Function J_0 217
D.0.4 Integral Involving Cylindrical Bessel Function J_1 222
D.0.4.1 Solution Utilizing the Derivative of the Bessel Function 222

D.0.4.2 Independent Derivation of Solution 224

E Mathematica Codes **229**

E.1 Detailed Explanation of the Codes 231

E.1.1 Detailed Explanation of J_0 Codes 231

E.1.2 Detailed Explanation of J_1 Codes 233

E.2 Derivation of Displacement Field for Shearing Motion 236

E.3 Derivation of Displacement Field for Rocking Motion 253

E.4 Integration of Total Displacement Field 265

List of Figures

1.1 Picture of Millikan Library facing North-West. 4
1.2 Millikan Library floor plans and cross sections. 5

2.1 Shaker picture with full buckets. 11
2.2 Approximate location of shaker on the roof of Millikan Library. 13

3.1 Flowchart for Chapter 3. 23
3.2 Coordinate system used 28
3.3 Displacement field for U_R, shearing motion 33
3.4 Displacement field for U_θ, shearing motion 33
3.5 Displacement field for U_ϕ, shearing motion 34
3.6 Displacement field for U_R, rocking motion 39
3.7 Displacement field for U_θ, rocking motion 40
3.8 EW mode shape 50
3.9 NS mode shape 50
3.10 Velocity field wave-fronts for the radiated waves 54
3.11 Integral partitions over the half-space for Equation 3.77 55

4.1 L4C-3D seismometer locations for the Millikan II experiments. 64
4.2 Amplitude decay curves for the North-line setup, East-West shaking, experiment A. 67
4.3 Overlayed amplitude decay curve for the North-line setup, East-West shaking, radial direction experiments A - D. 75
4.4 Polar plot of the NE and SW quarter circle displacements for all 3 components for a NS shake 77

4.5 Polar plot of the NE and SW quarter circle displacements for all 3 components for an EW shake. 77

4.6 Phase velocity minimization curves for an East-West shake recorded along the east line. The phase data shown are for the first shake (A). Shown are the radial, transverse, and vertical components. Sub-figures A and C show worst case scenarios for the linear fits, as there are outliers in the data. 86

5.1 Displacement replication for 4 different experiments. 89

5.2 FEC model geometry 90

5.3 Experiment locations from Luco et al. for a similar experiment. 90

5.4 Normalized displacement plots for the Luco et al. experiments 91

5.5 FEC distributed nodes for source. 97

5.6 Displacement comparisons for point forces vs. distributed forces. 100

5.7 Displacement comparisons for point forces vs. distributed forces 2. . . 101

5.8 EW shake, East line, rad. comp. normalized amplitudes and phases . . 109

5.9 EW shake, East line, vert. comp. normalized amplitudes and phases . 109

5.10 EW shake, North line, trans. comp. normalized amplitudes and phases 110

5.11 NS shake, North line, rad. comp. normalized amplitudes and phases . 110

5.12 NS shake, North line, vert. comp. normalized amplitudes and phases . 111

5.13 NS shake, East line, trans. comp. normalized amplitudes and phases . 111

5.14 EW shake, FEM smooth model simulation, time 1.4 seconds, surface . 112

5.15 EW shake, FEM smooth model simulation, time 1.9 seconds, surface . 112

5.16 EW shake, FEM smooth model simulation, time 2.5 seconds, surface . 113

5.17 EW shake, FEM smooth model simulation, time 5.4 seconds, surface . 113

5.18 EW shake, FEM smooth model simulation, time 1.4 seconds, EW slice 114

5.19 EW shake, FEM smooth model simulation, time 1.9 seconds, EW slice 114

5.20 EW shake, FEM smooth model simulation, time 2.5 seconds, EW slice 115

5.21 EW shake, FEM smooth model simulation, time 5.4 seconds, EW slice 115

5.22 EW shake, FEM smooth model simulation, time 1.3 seconds, surface . 116

5.23 NS shake, FEM smooth model simulation, time 1.8 seconds, surface . . 116
5.24 NS shake, FEM smooth model simulation, time 2.3 seconds, surface . . 117
5.25 NS shake, FEM smooth model simulation, time 5.3 seconds, surface . . 117
5.26 NS shake, FEM smooth model simulation, time 1.3 seconds, NS slice . 118
5.27 NS shake, FEM smooth model simulation, time 1.8 seconds, NS slice . 118
5.28 NS shake, FEM smooth model simulation, time 2.3 seconds, NS slice . 119
5.29 NS shake, FEM smooth model simulation, time 5.3 seconds, NS slice . 119

6.1 Spectral amplitudes at TriNet stations MIK, PAS, and GSC. 123
6.2 Topographic map of Southern California for the combined NS shakes. . 131
6.3 Topographic map of Southern California for the combined EW shakes. 132
6.4 Individual shake maps of Southern California for the NS shakes. 133
6.5 Individual shake maps of Southern California for the EW shakes. . . . 134
6.6 Azimuthal dependence of the displacements corrected for distance decay rates for the combined NS and EW shakes. 135
6.7 Displacement distance decay curves for the combined NS and EW shakes 136
6.8 Normalized displacement distance decay curves for the combined NS and EW shakes 137
6.9 Normalized displacement distance decay curves for the individual NS and EW shakes 138
6.10 RFFTs for four stations near Millikan Library. 141
6.11 Signal velocities for TriNet stations 142

A.1 Picture of Millikan Library 150
A.2 Millikan Library diagrams 151
A.3 Graphical depiction of Table A.2 153
A.4 Kinemetrics VG-1 synchronized vibration generator (Shaker) 155
A.5 Lin-Log normalized peak displacement curves for the frequency sweep performed on July 10, 2002 159
A.6 Resonance curves and mode shapes for the EW fundamental mode under two loading conditions 164

A.7 Resonance curves and mode shapes for the NS fundamental mode under two loading conditions 165
A.8 Resonance curves and mode shapes for the torsional fundamental mode 167
A.9 Resonance curves and mode shapes for second and third EW modes . . 168
A.10 Resonance curves and mode shapes for the second NS mode 170
A.11 Resonance curves and mode shapes for the second torsional mode . . . 172
A.12 Least squares curve fitting for EW modes. Tilt and translation removed. 174
A.13 Least squares curve fitting for NS modes. Tilt and translation removed. 175
A.14 Theoretical mode shapes for a cantilevered bending beam 177
A.15 Theoretical mode shapes for a cantilevered shear beam 178

B.1 Seismometer set up for calibration experiments conducted on the roof of Millikan Library. 184
B.2 North component particle velocities for the L4C-3D seismometers used in the roof calibration after removing the nominal instrument response. Excitation in the NS direction. 185
B.3 North component particle velocities for the L4C-3D seismometers used in the roof calibration after removing the individual SCEC determined instrument responses. Excitation in the NS direction. 185
B.4 SCEC calculated velocity responses for the north component of the L4C-3D seismometers used for the Millikan experiments. 186
B.5 SCEC calculated velocity responses for the east component of the L4C-3D seismometers used for the Millikan experiments. 186
B.6 SCEC calculated velocity responses for the vertical component of the L4C-3D seismometers used for the Millikan experiments. 187
B.7 SCEC calculated phase responses for the north component of the L4C-3D seismometers used for the Millikan experiments. 187
B.8 SCEC calculated phase responses for the east component of the L4C-3D seismometers used for the Millikan experiments. 188

B.9 SCEC calculated phase responses for the vertical component of the L4C-3D seismometers used for the Millikan experiments. 188

List of Tables

1.1 Summary of modal frequency and damping values for Millikan Library since 1966 7

2.1 Shaker shear force variable "MR" for all combination of masses 12
2.2 Maximum frequency (Hz) tolerated by the shaker for each mass combination 12

3.1 Surficial soil properties from refraction experiment 21
3.2 Estimated half-space model from Chapter 5 22
3.3 Floor mass estimates for Millikan Library 49
3.4 EW shake force and kinetic energy calculations 51
3.5 NS shake force and kinetic energy calculations 52

4.1 EW shake, radial comp., decay values 68
4.2 EW shake, transverse comp., decay values 68
4.3 EW shake, vertical comp., decay values 68
4.4 NS shake, radial comp., decay values 69
4.5 NS shake, transverse comp., decay values 69
4.6 NS shake, vertical comp., decay values 69
4.7 Torsional shake, radial comp., decay values 70
4.8 Torsional shake, transverse comp., decay values 70
4.9 Torsional shake, vertical comp., decay values 70
4.10 EW shake, radial comp., decay values, minus the close in stations . . . 71
4.11 EW shake, transverse comp., decay values, minus the close in stations . 71
4.12 EW shake, vertical comp., decay values, minus the close in stations . . 71

4.13 NS shake, radial comp., decay values, minus the close in stations . . . 72
4.14 NS shake, transverse comp., decay values, minus the close in stations . 72
4.15 NS shake, vertical comp., decay values, minus the close in stations . . . 72
4.16 Torsional shake, radial comp., decay values, minus the close in stations 73
4.17 Torsional shake, transverse comp., decay values, minus the close in stations 73
4.18 Torsional shake, vertical comp., decay values, minus the close in stations 73
4.19 Phase velocities, EW shake, radial component. 80
4.20 Phase velocities, EW shake, transverse component. 80
4.21 Phase velocities, EW shake, vertical component. 80
4.22 Phase velocities, NS shake, radial component. 81
4.23 Phase velocities, NS shake, transverse component. 81
4.24 Phase velocities, NS shake, vertical component. 81
4.25 Phase velocities, Torsional shake, radial component. 82
4.26 Phase velocities, Torsional shake, transverse component. 82
4.27 Phase velocities, Torsional shake, vertical component. 82
4.28 Phase velocities, EW shake, radial component, minus the close in stations. 83
4.29 Phase velocities, EW shake, transverse component, minus the close in stations. 83
4.30 Phase velocities, EW shake, vertical component, minus the close in stations. 83
4.31 Phase velocities, NS shake, radial component, minus the close in stations. 84
4.32 Phase velocities, NS shake, transverse component, minus the close in stations. 84
4.33 Phase velocities, NS shake, vertical component, minus the close in stations. 84
4.34 Phase velocities, Torsional shake, radial component, minus the close in stations. 85
4.35 Phase velocities, Torsional shake, transverse component, minus the close in stations. 85
4.36 Phase velocities, Torsional shake, vertical component, minus the close in stations. 85

5.1 Literature search soil properties for Millikan Library 93
5.2 Soil properties for linearly interpolated velocity model, "Smooth" . . . 93
5.3 Model 2LayerA from Neighbourhood algorithm 96
5.4 Model 2LayerB from Neighbourhood algorithm 96
5.5 Applied model forces 102
5.6 Velocity model misfits 103
5.7 Observed, theoretical, and FEC model energy radiation estimates . . . 105
5.8 Viscous damping estimates for all the models presented 106
5.9 2LayerA model component misfits 107
5.10 2LayerB model component misfits 108
5.11 Smooth model component misfits 108

6.1 Estimated energy flux from Millikan Library from the shaker. 126
6.2 Distance decay rates and transition distances (R_T) for the NS shakes. . 127
6.3 Distance decay rates and transition distances (R_T) for the EW shakes. 127

A.1 Accelerometer locations for Millikan Library 145
A.2 History of Millikan Library strong motion behavior - fundamental modes. 152
A.3 Shaker constant, A_i (N·sec^2), and limiting frequencies [Hz] for different configurations of lead weights in the shaker. 155
A.4 Summary of results for modeshape testing of August 28, 2002 160
A.5 Ratio of frequencies for bending beam behavior, shear beam behavior, and the observed behavior of Millikan Library. 173
A.6 Summary of Millikan Library modal frequency and damping analysis experiments 1967-1994. 180
A.7 Summary of Millikan Library modal frequency and damping analysis experiments 1987-2003. 181
A.8 References which correspond to footnote numbers in Tables A:6 and A:7. 182

B.1 Instrument responses (positive pulses) for the L4C-3D seismometers used 192
B.2 Instrument responses (negative pulses) for the L4C-3D seismometers used 193

B.3 Roof calibration 1, East component, f=1.105 194
B.4 Roof calibration 1, North component, f=1.105 194
B.5 Roof calibration 1, vertical component, f=1.105 194
B.6 Roof calibration 2, East component, f=1.117 195
B.7 Roof calibration 2, North component, f=1.117 195
B.8 Roof calibration 2, vertical component, f=1.117 195
B.9 Roof calibration 1, East component, f=1.120 196
B.10 Roof calibration 1, North component, f=1.120 196
B.11 Roof calibration 1, vertical component, f=1.120 196
B.12 Roof calibration 1, East component, f=1.126 197
B.13 Roof calibration 1, North component, f=1.126 197
B.14 Roof calibration 1, vertical component, f=1.126 197
B.15 Roof calibration 1, East component, f=1.627 198
B.16 Roof calibration 1, North component, f=1.627 198
B.17 Roof calibration 1, vertical component, f=1.627 198
B.18 Roof calibration 2, East component, f=1.627 199
B.19 Roof calibration 2, North component, f=1.627 199
B.20 Roof calibration 2, vertical component, f=1.627 199
B.21 Roof calibration 1, East component, f=1.651 200
B.22 Roof calibration 1, North component, f=1.651 200
B.23 Roof calibration 1, vertical component, f=1.651 200
B.24 Roof calibration 2, East component, f=1.651 201
B.25 Roof calibration 2, North component, f=1.651 201
B.26 Roof calibration 2, vertical component, f=1.651 201
B.27 Roof calibration 1, East component, f=1.672 202
B.28 Roof calibration 1, North component, f=1.672 202
B.29 Roof calibration 1, vertical component, f=1.672 202
B.30 Roof calibration 2, East component, f=1.672 203
B.31 Roof calibration 2, North component, f=1.672 203
B.32 Roof calibration 2, vertical component, f=1.672 203

B.33 Roof calibration 2, East component, f=1.700 204
B.34 Roof calibration 2, North component, f=1.700 204
B.35 Roof calibration 2, vertical component, f=1.700 204
B.36 Roof calibration 1, East component, f=2.249 205
B.37 Roof calibration 1, North component, f=2.249 205
B.38 Roof calibration 1, vertical component, f=2.249 205
B.39 Roof calibration 2, East component, f=2.252 206
B.40 Roof calibration 2, North component, f=2.252 206
B.41 Roof calibration 2, vertical component, f=2.252 206
B.42 Roof calibration 2, East component, f=2.356 207
B.43 Roof calibration 2, North component, f=2.356 207
B.44 Roof calibration 2, vertical component, f=2.356 207

C.1 EW shake displacement and phase data 210
C.2 NS shake displacement and phase data 210
C.3 FEM central node displacement and phase data 211

Notation

P	Maximum horizontal shear force on the disk
M	Maximum moment on the rocking disk
t	Time
T	Period
f	Frequency in Hertz
$\omega = 2\pi f$	Angular frequency
ω_D	Resonant frequency
ω_0	Undamped natural frequency
$V_P = \sqrt{\frac{\lambda_o+2\mu}{\rho}}$	Compressional (P) wave velocity
$V_S = \sqrt{\frac{\mu}{\rho}}$	Shear (S) wave velocity
V_R	Rayleigh wave velocity
$h = \frac{\omega}{V_P}$	P wavenumber
$k = \frac{\omega}{V_S}$	S wavenumber
$k_R = \frac{\omega}{V_R}$	Rayleigh wavenumber
λ	Wavelength
ϕ	Azimuth with respect to the direction of the horizontal force or with respect to the line perpendicular to the axis of rotation of the rocking disk
θ	Angle with the free surface
$F(\zeta)$	Rayleigh's frequency equation
$F'(\zeta)$	$\frac{dF(\zeta)}{d\zeta}$
r_0	Building's radius (or equivalent radius, if not circular)
r	Radial distance along the surface (in cylindrical coordinates)

z	Depth (in cylindrical coordinates)
R	Radial distance (in spherical coordinates)
$\alpha = \sqrt{\zeta^2 - h^2}$	When in exponent, corresponding term is associated with P waves
$\beta = \sqrt{\zeta^2 - k^2}$	When in exponent, corresponding term is associated with S waves
ζ	Separation variable
$\Lambda = \frac{k}{h} = \frac{V_P}{V_S}$	P to S wave velocity ratio
$\Lambda_{RP} = \frac{V_R}{V_P}$	Rayleigh to P wave velocity ratio
$\Lambda_{RS} = \frac{V_R}{V_S}$	Rayleigh to S wave velocity ratio
μ	Shear modulus, Lame constant
$\lambda_o = K - \frac{2}{3}\mu$	Lame's second constant
ρ	Soil density
K	Bulk modulus
ϵ_{ij}	Strain components
σ_{ij}	Stress components
e	Kinetic energy density
E_{Rad}	Total radiated energy
E_{Kin}	Building's kinetic energy
E_{Avg}	Average kinetic energy for N cycles
U_R	Radial displacement field in spherical coordinates
V_R	Radial velocity field in spherical coordinates
U_θ	θ (depth angle) displacement field in spherical coordinates
V_θ	θ (depth angle) velocity field in spherical coordinates
U_ϕ	Azimuthal displacement field in spherical and cylindrical coordinates (Tangential)
V_ϕ	Azimuthal velocity field in spherical and cylindrical coordinates (Tangential)
U_r	Radial displacement field in cylindrical coordinates
U_z	Vertical displacement field in cylindrical coordinates

$\xi \approx \frac{\delta_m}{2\pi m}$	Viscous damping ratio
$\delta_m = \ln\left(\frac{x_n}{x_{n+m}}\right)$	Logarithmic decrement; for small damping, it is approximately equal to the fractional decrease in amplitude over one cycle of the vibration
$J_0(\zeta r)$	Cylindrical Bessel functions of the zeroth kind
$J_1(\zeta r)$	Cylindrical Bessel function of the first kind
h_i	Inter-story height
E_A	Mean displacement error
E_P	Mean phase error
E_T	Mean model error
N_F	Mean normalizing factor
A_R	Radiated signal amplitudes for regional experiments
A_T	Total signal amplitude for regional experiments
N	Noise level for radiated spectra for regional experiements
σ	Mean standard deviation for regional experiments
P_{avg}	Mechanical power estimate from shaker

Chapter 1

Introduction

Damping limits the resonance of vibrating systems and thus higher anelastic damping is generally favored for engineered structures subjected to earthquake motions. However, there are elastic processes that can mimic the effects of anelastic damping. In particular, buildings lose kinetic energy when their motion generates elastic waves in the Earth, which is referred to as radiation damping. Unlike anelastic damping, strong radiation damping may not always be desirable. Reciprocity can be used to show that buildings may be strongly excited by elastic waves of similar characteristics to those generated by vibrations of the building. For example, buildings with a resonance frequency close to that of the soil column beneath them will have large radiation damping. While this might be a preferred condition to damp motions of the structure caused by sources such as wind, it may also prove to be disastrous when earthquake induced motions are involved. This will be especially true if the soil column underneath the buildings resonates harmonically at a frequency close to or slightly higher than the natural frequency of the structures it is supporting. For example, during the 1985 Michoacán, México earthquake large engineered structures in México City, more than 300 km from the earthquake's epicenter, were subjected to long harmonic ground motions that caused significant structural damage to buildings with frequencies slightly higher than the soil resonant frequency (*Beck and Hall*, 1986). México City is partly located on an old lake bed (*Hall and Beck*, 1986; *Campillo et al.*, 1989; *Lomnitz et al.*, 1999), and it has been shown that the lake bed deposits amplify ground motions with frequencies between 0.5 and 0.25 Hz (*Sanchez-Sesma et al.*, 1988; *Singh*

et al., 1988a,b; *Kanamori et al.*, 1993). These motions damaged approximately 20% of the engineered structures between 5 and 12 stories tall (eigen-frequencies between 2 and 0.8 Hz) (*Beck and Hall*, 1986). Similar soft soil conditions to México City exist in several cities with large downtown regions, such as: San Francisco, California; Tokyo, Japan; and to a lesser extent, Seattle, Washington; and Los Angeles, California. In these cities, the large structures are located closer to known earthquake faults than in México City, and a large earthquake could prove disastrous. Therefore, it is imperative that engineers can estimate the radiation damping of a designed building prior to construction, as this will aid in designing safer structures. To this end, this thesis proposes a method of estimating the radiation damping for a structure.

The work presented here estimates what percentage of the total damping of a structure, Robert A. Millikan Memorial Library (Millikan Library), is due to energy radiation. I also study the waves radiated by the building to determine the elastic properties of the soils surrounding the structure, and to investigate amplification factors at regional distances. Furthermore, displacement data recorded at TriNet stations is used in an attempt to identify signal velocities and to constrain the type of waves being observed at regional distances. From the data analysis presented here, it will become clear that a thorough knowledge of the supporting soil column is needed to fully understand the building's energy radiation damping. The properties of the upper few hundred meters of soil near the building need to be known, and can be estimated by either: drilling and analyzing deep boreholes (currently not common practice even for tall buildings); by performing an inversion of the data from seismometers located around a pre-existing building generated by vibration tests; or by collecting and processing reflection profiles at proposed sites of large structures. I conducted several tests using Millikan Library as a controlled source. The building was forced to resonate at its three fundamental modes (North-South (NS), East-West (EW), and Torsional (Tor)), and seismometers were deployed around Pasadena and Caltech in order to measure the waves generated by the library's excitation for various experiments. Waves excited by the forced vibration of the library were observed at distances as far away as 400 km on stations of the TriNet seismographic network,

with station Mammoth Lakes (MLAC) being the most distant station to record the signal.

Millikan Library is a nine-story reinforced concrete building located on the Caltech campus in Pasadena, California. As Figures 1.1 and 1.2 show, it has prominent shear walls on the East and West facades (to resist NS motions), as well as NS facing shear walls in the elevator core and a moment resisting frame on the North and South facades (to resist EW motions). The building dimensions are given in Figure 1.2, and it can be seen in the NS foundation cross section that the foundation allows more rocking in the NS direction than in the EW direction

The foundation allows more rocking in the NS direction than in the EW direction, due to the stepped design acting somewhat like a rocking chair (*Foutch*, 1976), shown in Figure 1.2c. All of the library's shear walls have a continuous uniform thickness of 0.3 meters (12 inches). However, due to an increase in reinforcing steel towards the bottom of the structural members, their lower portions have moments of inertia approximately 6% higher (due to a density increase) than their upper portions (*Teledyne-Geotech*, 1971). For a detailed description of the library and its characteristics, please refer to *Kuroiwa* (1969), *Foutch* (1976), as well as *Bradford et al.* (2004) which is included in Appendix A.

The first published report that Millikan Library was an efficient energy radiator was by *Jennings* (1970) who reported observing the signal from the library at the Mount Wilson Observatory, at a distance of 12 km. This signal was generated during a forced excitation of Millikan Library to investigate the building's structural characteristics, similar to the experiments performed for this investigation. Though many studies have been conducted on the building, questions still abound about some of its properties. This thesis addresses some of these outstanding issues and expands the previous knowledge of the structure and its soil-structure interaction.

For his Ph.D. thesis, *Kuroiwa* (1969) performed multiple full scale shaking experiments during the construction of Millikan Library as it was being built. Most of his experiments took place after the finishing work on the building had begun, with the building's exterior completed, but the building not fully functional. He estimated the

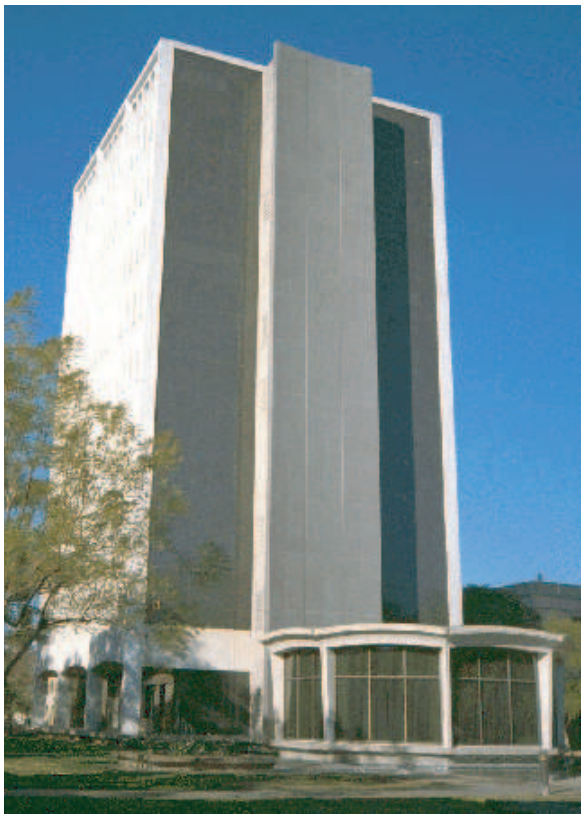

Figure 1.1 Picture of Millikan Library facing North-West. The eastern shear wall and the southern moment resisting frame are clearly visible, as well as the attached conference room in the eastern part of the building. Figure courtesy of the Caltech Archives.

masses (in 10^3 Kg) of each floor to be, from top to bottom: $M_{Roof} = 1179$, M_9 to $M_3 = 885$, $M_2 = 1104$, and $M_1 = 1034$. However, these masses seem to be for an occupied building including books, as these masses are very similar to those calculated in Table 3.3. In his thesis, *Kuroiwa* (1969) describes an extensive list of properties and characteristics for the building, which are summarized here.

- Because the library's total damping is small (less than 2 % of critical damping), the resonant frequency (n_d) found from a displacement response curve (a plot of the peak displacement for a particular frequency versus the corresponding frequency) is within 1 % of the resonant frequency (n_a) from the corresponding acceleration response curve. These two frequencies are related by the equation

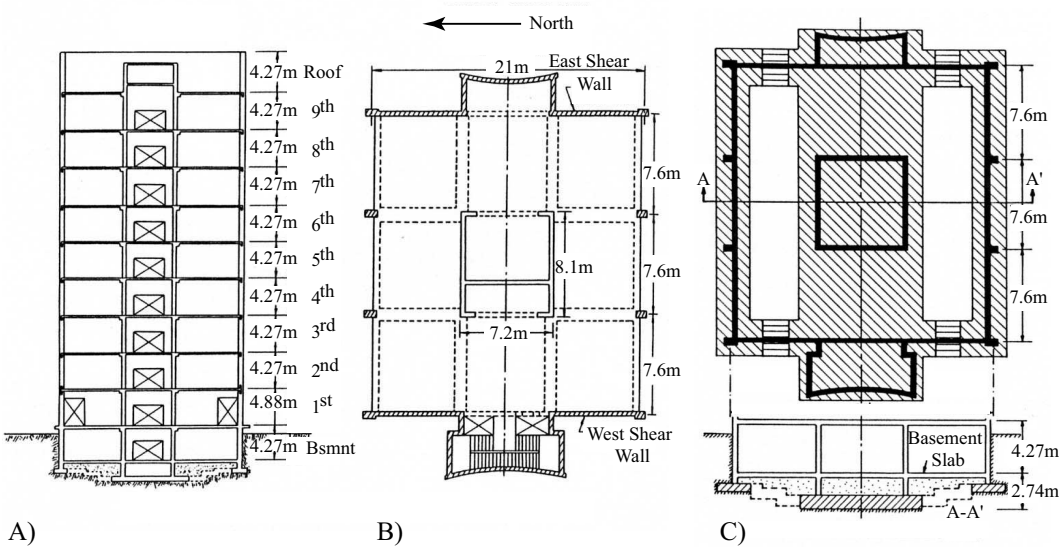

Figure 1.2 A) A North-South cross section of Millikan Library, B) a sketch of a typical floor plan, and C) a sketch of the plan view and the cross section of the foundation of Millikan Library. This figure is modified from a figure in *Luco et al.* (1986), and since all of the original measurements are in feet, the measurements given here are rounded off at the second decimal place.

$n_d = n_a(1 - 2\xi^2)$, where ξ is the fraction of critical viscous damping for the structure. In this thesis, natural frequencies estimated from acceleration, velocity, and displacement measurements will be used interchangeably since they are so close to each other. A velocity response curve is used when performing the experiments for this thesis.

- Due to the small motions involved during the forced shaking, the building is assumed to be approximately linear elastic. The floor slabs are very stiff for in-plane shear deformations and it is assumed that they deform approximately as rigid bodies (for horizontal motions). Therefore, measuring horizontal displacements or accelerations anywhere on the floor will yield similar results in the absence of torsional motions. The estimation of vertical displacements in the basement is more complex due to the interaction of the foundation and the shear walls with the basement slab (the same holds true for all floor slabs).

- The building's center of torsion is located approximately 0.75 meters west of the building's geometric center (in plan view).

- The natural frequencies of the building decrease slightly as the force levels are increased (also shown in *Clinton et al.* (2004)), a characteristic of a system with a nonlinear softening spring.

- It can be assumed that the building is fixed at the foundation, and that the back fill surrounding the building has no effect on the building's motion.

- The building's damping increases with increasing levels of excitation force.

In a technical report to Caltech, *Teledyne-Geotech* (1971) measured the natural frequencies of Millikan Library using ambient vibrations. The report compares the post San Fernando earthquake natural frequencies with those measured previously. The table presented in the report is incorporated in an exhaustive natural frequency and structural damping summary table for Millikan Library compiled and expanded by *Clinton* (2004), which covers the time period from the first reported measurements for Millikan Library until the present. An abridged table is provided here in Table 1.1.

Between August and December 1974, *Foutch* (1976) performed forced vibration tests on Millikan Library to determine the building's behavior and modelled the structure, including soil-structure interaction effects, to investigate the interdependence of the horizontal and vertical load carrying systems. I summarize his findings for Millikan Library as follows:

- He uses the same floor masses for the analysis as in *Kuroiwa* (1969). Furthermore, he modelled the foundation using an elastic half-space with a shear wave velocity (V_S) of 500 m/s, a density (ρ) of 1760 Kg/m^3, and an equivalent circular foundation radius (r_0) of 12.5 m for Millikan Library.

- The North-South (NS) motions of the structure are dominated by the behavior of the shear wall at the East and West ends of the building.

Test	East - West		North - South		Torsional		Remark
	$f_0[\xi_0]$	$f_1[\xi_1]$	$f_0[\xi_0]$	$f_1[\xi_1]$	$f_0[\xi_0]$	$f_1[\xi_1]$	
1966-1967	1.46-1.51	6.2	1.89-1.98	-	2.84-2.90	-	A,F,M
	[0.7-1.7]		[1.2-1.8]		[0.9-1.6]		
Mar 1967	1.49 [1.5]	6.1	1.91 [1.6]	-	2.88	-	A
Apr 1968	1.45	6.1	1.89	9.18	2.87	9.62	A
M6.7 February 9 1971 San Fernando eqk. at a distance of 44 km							
Feb 9 1971	1.02 [0.06]	4.93 [0.05]	1.61 [0.06]	7.82 [0.05]	-	-	E
Feb 1971	1.27 [2.5]	5.35 [0.9]	1.8 [3]	9.02 [0.2]	2.65 [2]	9.65 [0.5]	A
Jul 1975	1.21 [1.8]	-	1.79 [1.8]	-	-	-	F
May 1976	1.27	-	1.85	-	2.65	-	A
M6.1 October 1 1987 Whittier Narrows eqk. at a distance of 19 km							
Oct 1 1987	0.932 [0.04]	4.17 [0.08]	1.30 [0.06]	6.64 [0.18]	-	-	E
May 1988	1.18	-	1.70	-	-	-	F
M5.8 June 28 1991 Sierra Madre eqk. at a distance of 18 km							
June 28 1991	0.92	-	1.39	-	-	-	E
May 1993	1.17	-	1.69	-	2.44	-	F
M6.7 January 17 1994 Northridge eqk. at a distance of 34 km							
Jan 17 1994	0.94	-	1.33	-	-	-	E
Jan 20 1994	1.13	4.40-4.90	1.65	8.22-8.24	2.39	-	A
	[1.2-2.1]	[1.0]	[0.7-1.5]	[0.2-0.3]	[0.3-0.5]		F
Dec 2001	1.12 [1.63]	-	1.63 [1.65]	-	2.34	-	F
Aug 2002	1.14 [2.28]	4.93	1.67 [2.39]	7.22	2.38 [1.43]	6.57	F

Table 1.1 Summary of modal frequencies and damping values for Millikan Library between 1966 and August 2002. f_0 and f_1 are the natural frequencies for the fundamental mode and the first overtone, in Hz. ξ_0 and ξ_1 are the corresponding critical damping ratios in %. For the Remark column, the following codes are used to specify which method excited the library for the estimation of the properties given: A=Ambient, F=Forced Vibration, E=Earthquake Motions, M=Manned Excitation of the Library. Distances are given from the earthquake epicenter to Millikan Library. Adapted from *Clinton et al.* (2004).

- In the NS direction, rocking of the structure accounts for 25% of the roof displacement, while rigid body translation contributes 4% (see Figures 3.8 and 3.9). Therefore, nearly 30% of the roof motion is due to rigid body motions of the structure in the NS direction. These numbers agree with the values calculated in Table 3.5 as well as those given by *Bradford et al.* (2004).

- For East-West (EW) shaking, there is little vertical motion of the slab around the perimeter of the building, but there is a significant amount at the East and West ends of the central core wall.

- In the EW direction, the basement translation accounts for 2% of the total roof displacement, however, due to the basement slab deformations, it is difficult to compute the rigid rotation of the base.

- The effect of soil-structure interaction is more significant in the stiffer NS direction.

- A drop of 11% of the NS fundamental frequency of the structure occurs between the time of the experiments performed by *Kuroiwa* (1969) and that of those performed by *Foutch* (1976). This drop is attributed to the occurrence of the 1971 San Fernando earthquake, which is believed to have fractured brittle connections that connect Millikan Library with adjacent structures through a system of underground utility tunnels.

- A lumped mass model (where floor masses are considered to be point masses, inter-floor stiffnesses given by a single spring element, and inter-story damping is represented by a single viscous damper) allowing for shear and bending deformations best fits the mode shapes of both *Kuroiwa* (1969) and *Foutch* (1976). However, this result might be specific to Millikan Library, due to its high rigidity.

Jennings and Kuroiwa (1968) and *Luco et al.* (1975) carried out experiments to measure the amplitude of surface waves excited by Millikan Library, as was done

for this thesis. However, due to the limited technology in the recording instruments of the time, and their experimental setup, precise time information (such as GPS time stamps) was not available. This limitation prevented the investigators from performing a phase analysis of the type carried out here in order to constrain the velocity structure under Millikan Library and to eventually compute the radiated energy of the building. The results of *Jennings and Kuroiwa* (1968) and *Luco et al.* (1975) will be presented in the chapters for which the data is relevant.

The thesis chapters that ensue, follow the order in which the collected waveforms were processed as well as how the problem was approached, and not the order in which the data was collected. Due to difficulties in data processing after the first experiment, which at the time were attributed to instrument location error, and a continuous GPS data campaign to try and resolve the perceived problem (see Chapter 4), a second and simplified experiment was conducted to better understand the problem.

Chapter 2

Instrumentation and Data Reduction Procedures

This chapter describes the instrumentation and the data reduction procedures used for the performed experiments. These descriptions include the instruments used inside as well as outside the building, and the force generating system.

2.1 Force Generating System

A model VG-1 synchronized vibration generator system was used to carry out the forced vibration tests performed on Millikan Library. This generator is permanently attached to the building's roof for the civil engineering class experiments performed on the library at Caltech. It was manufactured by *Kinemetrics* (1975) and it is currently powered by an electric 5-horsepower motor (Raul Relles, Engineering technician at Caltech, Personal Communication, 2001). The previous version of the shaker was powered by a 1-horsepower motor, however, both the frequency controller and the motor were upgraded a few years before the start of the tests presented here, to obtain better frequency control (Raul Relles, Personal Communication, 2001). The force generating mechanism consists of two counter-rotating baskets, subdivided into three sectors (two large sectors at the outside of the bucket, and one small one located at the center), which may be loaded with a variable number of lead masses of two distinct sizes (see Figure 2.1). The result of the controlled spinning of the two counter-rotating baskets is a linearly polarized horizontal sinusoidal force applied to the building's roof.

This force in turn causes the building to oscillate between two extreme positions, and as the oscillations take place, the floor slabs in the building undergo translational and rotational in-plane motions, while various points on the floor slab also move vertically due to bending deformations in the slab (*Foutch*, 1976) and in the building.

Figure 2.1 Picture of the force generating mechanism used to shake Millikan Library. The shaker is pictured here with full buckets (exerts maximum force).

The maximum amplitude of the sinusoidal force (in Newtons) generated by the shaker is obtained from Equation 2.1.

$$Force = \omega^2 MR = 4\pi^2 f^2 MR \tag{2.1}$$

where M is the mass of the two counter-rotating baskets plus any extra mass in the buckets, ω is the rotational frequency in radians per second, and R is the distance from the rotation axis to the center of mass of either bucket (since both buckets are identically loaded). Once the forcing frequency and loading condition are established, the sinusoidal motion generated by the shaker is known, as long as waveforms of the floor's motions are accurately recorded. However, it should be kept in mind that

the frequency control is done through a feedback mechanism, and therefore minor oscillations in frequency should be expected.

Table 2.1 lists the values of MR for various combinations of masses and Table 2.2 provides the maximum allowable operational frequencies for these mass combinations. The tables are modified from the *Kinemetrics* (1975) operations manual to be in SI units, and are given for completeness.

	0	$S1$	$S2$	$S3$	$S4$
0	6	11	16	21	26
$L1$	22	27	32	37	42
$L2$	39	44	49	54	59
$L3$	55	60	65	70	75
$L4$	71	76	81	86	91

Table 2.1 "MR" $(Kg * m)$ for each combination of masses. S = small mass (center section), and L = large mass (side sections). The number (1, 2, 3, 4) following an "S" or "L" indicates the number of masses of that size placed in each section of the corresponding size in each bucket.

	0	$S1$	$S2$	$S3$	$S4$
0	9.7	7.2	6.0	5.2	4.7
$L1$	5.0	4.6	4.2	3.9	3.7
$L2$	3.8	3.6	3.4	3.3	3.1
$L3$	3.2	3.1	3.0	2.8	2.8
$L4$	2.8	2.7	2.6	2.6	2.5

Table 2.2 Maximum frequency (Hz) for each mass combination. S = small mass (center section), and L = large mass (side sections). The number (1, 2, 3, 4) following an "S" or "L" indicates the number of masses of that size placed in each section of the corresponding size in each bucket.

It should be noted that the shaker is located south of the building's East-West centerline (see Figure 2.2), which allows for the excitation of torsional modes when the appropriate frequencies are excited (otherwise, torsional effects would be negligible).

However, the shaker is located close to the North-South line crossing the building's center of mass. The axis of rotation for the shaker weights is located approximately 10.7 m West of the inside of the East shear wall and approximately 5.2 m North of the inside of the southern wall, as shown in a map view sketch of the library's roof in Figure 2.2.

As is visible in Figure 2.1, the baskets are connected to the motor by chains. The shaker's design provides a very simple mechanism for re-orienting the baskets to change the excitation direction, but the directional adjustments are limited by the number of discrete chain links to steps of $3\frac{1}{3}$ degrees. This implies that the force orientation may deviate slightly from the desired shaking direction, up to $\pm 1\frac{2}{3}$ degrees.

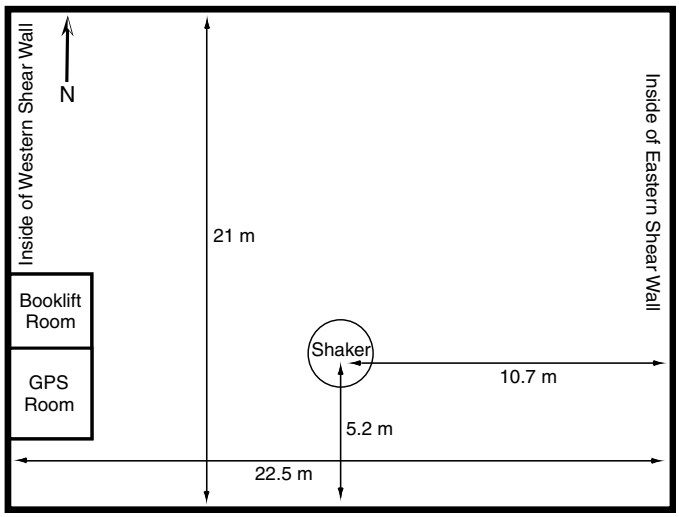

Figure 2.2 Approximate location of shaker on the roof of Millikan Library. Measurements are to the shaker's center of rotation.

2.2 Building Accelerometers

In 1996, Millikan Library was equipped with 36 accelerometers connected to two 18-channel, 19-bit digital Mt. Whitney recorder systems built by Kinemetrics, operated by the United States Geological Survey (USGS), and jointly owned by the USGS and

Caltech. Due to requirements by both the City of Pasadena and the USGS at the time of the experiments, it was only possible to acquire data in the context of this thesis from the Mt. Whitney system on three occasions, namely the night of June 15, 1998, the morning of May 19, 2001, and the morning of August 28, 2002. Data was collected for the building's three fundamental natural frequencies for the first two experiments, while for the third experiment data was additionally collected for a number of frequencies to investigate interesting building behaviors. The recording time for each frequency was approximately 15 minutes for the first two experiments, while for the third experiment data was collected in approximately one minute intervals, allowing for time to change the frequency and to let the building response settle to the forcing frequency. The waveforms collected from the Mt. Whitney system were recorded at 200 samples per second (sps).

For the first and second set of local experiments (those in the Pasadena and Caltech area), data was also collected from Millikan Library using an L4C-3D short period seismometer (described in Section 2.3) located on the roof of Millikan; this provides a means to calibrate individual experiments with respect to the data collected on June 15, 1998. It was found that amplitude differences at different observation points between shakes are small for slightly different excitation frequencies for the same loading configuration, and as a result the base station seismometer is only used to normalize the phase data. All data from the L4C-3D seismometers was recorded at 50 sps.

In May 2001, the continuously telemetered TriNet station MIK was installed on the East end of the ninth floor of Millikan Library. This station uses a 24-bit Quanterra datalogger to record a 3-component Kinemetrics Episensor accelerometer at 80 sps and lower. For the regional experiments (presented in Chapter 6), data for the base station was collected from TriNet station MIK. Before the first regional experiment was carried out, an experiment was performed on May 19, 2001, to verify the floor data (accelerations from the Mt. Whitney system) collected in 1998, and additionally calibrated MIK with the L4C-3D seismometer located on the building's roof to insure that the waveforms from station MIK could be used interchangeably with

those of the short period instrument. The location and orientation of the L4C-3D roof seismometer were kept constant for all the experiments so that the calibration would remain valid. Appendix A provides a list of the type of accelerometer on each floor, and an approximate location, as well as floor maps with more detailed locations for the accelerometers. Station MIK is used as a base station for all of the regional experiments performed for this thesis.

2.3 Seismometers for Local Tests

For the experiments in 1998, 17 Mark Products L4C-3D (short-period) seismometers were used, while for the experiments performed in 2000 only 14 L4C-3D seismometers were utilized. These instruments were supplied by the Southern California Earthquake Center's (SCEC) office in Santa Barbara. L4C-3D seismometers have a 1 second natural period and SCEC's Portable Broadband Instrument Center (PBIC), located at the University of California at Santa Barbara, has studied their responses over time and provides the responses for each individual seismometer. The instruments were calibrated with respect to each other on the roof of Millikan Library when it was being excited at its maximum amplitude, as described in Appendix B, and these waveforms suggest that the seismometers' nominal response best describes its actual response.

All of the data collected from the portable L4C-3D seismometers was recorded at 50 sps. Most of the instruments for the first portable experiment were oriented to magnetic North, whereas for the second experiment, all of the seismometers were oriented to geographic North. For the Pasadena area, the magnetic declination is 13.5^{o}E (*Peddie* (1993), and http://www.ngdc.noaa.gov/seg/pltfld/declination.shtml). The walls of Millikan Library are oriented with respect to geographic North.

2.4 Seismometers for Regional Tests

For the regional set of experiments, data was collected from the Southern California TriNet network (*Hauksson et al.*, 2001). This set of experiments consists of four long (four to six hours) continuous shakes, for which data was collected at 20 sps. For the first two experiments, the waveform data from sites with instruments of different types were compared to investigate the response of the TriNet short-period seismometers versus the broadband ones, which have better known responses. It was found that the amplitude response of the short-period seismometers varied by as much as a factor of 3 with respect to the corresponding broadband sensors at the frequencies of interest. Since the main purpose of the experiments was to measure displacements due to waves emanating from the library excitation, it was decided that only the broadband sensors should be used for the study so as to reduce the data collection effort and processing time. Furthermore, no accelerometer data was collected for the first two experiments. In the third shake, accelerometers were used and they showed a consistent amplitude response when compared to the corresponding broadband sensors (Toshiro Tanimoto, personal communication, 2002). However, since many of the accelerometer sites are co-located with the broadband sites, it was also decided to forego collecting the accelerometer data for any test other than the third test.

Therefore, only broadband channels were analyzed (BHE/N/Z) for all TriNet stations, as well as for Berkeley Digital Seismic Network (BDSN) stations (*Uhrhammer et al.*, 1996). The broadband channels used in this study are all recorded at 20 sps, and a large portion of them are stored continuously at the Souther California Earthquake Data Center (SCEDC) for the TriNet channels and at the Northern California Earthquake Center (NCEDC) for the BDSN stations.

At the completion of this thesis, TriNet and the data archives could be accessed through the following "URLs":

- TriNet: http://www.trinet.org
- SCEDC: http://www.scecdc.scec.org
- NCEDC: http://quake.geo.berkeley.edu/ncedc

The pertinent information on the individual stations used (all stations available at the time of the experiments were processed) can be found at either the TriNet or NCEDC internet addresses.

2.5 Data Reduction Procedures

Almost identical data reduction procedures were followed for all of the collected data, with the exception of the first few steps which could vary slightly. All data processing was done utilizing either the Seismic Analysis Code (SAC, http://www.llnl.gov/sac) or Matlab (The Matworks Co.). If the original data format was not in SAC format, the data was first converted into SAC format.

In SAC, all waveforms were lined up with the same origin time (for each experiment), the mean amplitude and a linear trend were removed from the record, and the ends of the record were sharply tapered to zero. Subsequently, the instrument responses were removed (to displacement), and all data files were cut to the same length. The cut windows were determined from the experiment length, and by using the recording from the library itself. The beginning cut time was chosen to be after the library's displacement settled (usually a few minutes after the initial excitation), and the end cut time was chosen to be just before the shaking stopped, with both values determined from the library's record. If the files needed to be rotated, they were rotated to geographic North at this stage of the processing. The processed data files were then cut into different file segments corresponding to the different experiments performed.

If the displacements were estimated by integrating the energy of the waveforms using a Fourier Transform, this calculation was also completed in SAC. However, if the signal was of high enough amplitude in the time domain for all of the instruments

used in the experiment, then Matlab was used to compute the signal amplitude and phase by minimizing the error between the data and a sinusoid of variable amplitude, frequency, and phase. A fairly accurate forcing frequency was known for each experiment from the shaker's frequency controller digital output, and as a result, this parameter was narrowed down significantly, minimizing the computation time. An exception to estimating the phase from the time domain (using Matlab) occurred for the short-period instrument calibrations which were performed on the roof of Millikan Library. At the time of the calibration experiment, I did not have a fast and reliable code which estimated the best fitting sinusoid to the data, and instead, trigonometric identities were used to reliably estimate the signal's relative phase by taking advantage of the fact that the waveforms have similar amplitudes and phases. The details of this method are given in Appendix B.

Chapter 3

Theoretical Solution to Energy Radiation Problem

The calculation of the radiated energy from a building was undertaken with the objective of deriving a simple equation that could estimate the building's damping due to energy radiation, with only the prior knowledge of basic site specific soil parameters and estimated forces from a building or building model. It was the hope that once the site specific soil properties were known, it would be possible to use a simple half-space to estimate a minimum damping coefficient for any building, once the forces exerted on the soil are determined. However, after performing several experiments, it was quickly realized that the half-space model is too simplistic; it predicts monotonically decaying seismic amplitudes with distance away from the source, whereas more complex patterns are typically observed. As the data in later chapters will show, deviations from a monotonically decaying radiated displacement field are extremely repeatable, and thus tell us something about the soil properties and the soil column under the building and its interaction with the superstructure. However, I believe that even though the half-space model lacks the complexity necessary to compute the radiated energy for this experiment, it provides insight into solving a more general problem that involves either a layered soil model or continuous soil property changes with depth.

Perhaps the simplest radiation model is to consider the problem of a rigid disk on the surface of a half-space; this disk is subjected to forces and force couples.

Since I am concerned with radiated energy, only the far-field ($r \longrightarrow \infty$) solution for the displacement field is investigated. *Cherry* (1962) solved for the displacement field for such a source for a harmonic load applied horizontally to the surface of a semi-infinite space, and *Bycroft* (1956) derived, in integral form, the solution for the displacement field for a rigid disk under a rocking motion on the surface of a semi-infinite space. I use the displacement fields derived by *Bycroft* (1956) and *Cherry* (1962) to calculate the body wave energy radiated into a half-space by a rigid disk, and by following the analysis of *Miller and Pursey* (1954), I also compute the radiated energy from Rayleigh waves for both a harmonic horizontal load and a harmonic rocking motion. Even though the body waves and the surface waves are related to the same displacement field, the analysis for each one is presented separately to simplify the presentation, grouping the analysis of body waves (Sections 3.2 and 3.3) and surface waves (Sections 3.4 and 3.5). This is done because the procedure to solve for each displacement field is similar. *Johnson* (1974) solves a very similar problem for the body wave solutions utilizing the Green's Function approach, however the method used here is more intuitive and provides a direct physical approach.

In the following analysis, the wave energy is calculated for the entire volume, and it will be assumed that the waves have travelled long distances. By normalizing the average energy for the volume by the number of building cycles used to compute the energy, an average energy per individual oscillation cycle can be computed. The excited waves travel at different velocities, and as a result, the energy integral is subdivided into various integrals as a function of distance from the source. One of these integrals involves the entire displacement field from the source up to the distance that the Rayleigh wavefront has travelled, the next from the Rayleigh wavefront to the shear wavefront, and the last from the shear wavefront to the compressional wavefront. However, SV head waves are generated by the free surface interface (a P to SV conversion), and these will be ignored in the calculation of the radiated energy, as these SV head waves are transformed compressional waves required to keep the free surface traction free and are small compared to other terms.

To estimate the radiated energy using this model, we must know some basic prop-

erties of Millikan Library and the soil surrounding it. Due to the intermixing of theoretical analysis with the experimental data collected and analyzed for Millikan Library, Figure 3.1 provides a flowchart which hopefully aids in understanding the organization of this chapter as well as simplifying the problem set-up and the undertaken solution. The values given in Table 3.1 represent the top 3 meters of soil, and were calculated from a local refraction experiment. According to Dr. Ronald F. Scott (personal communication, 1998), and to Dr. Behnam Hushmand (personal communication, 2001), these values are representative velocities for the top soil around Caltech and Millikan Library. Furthermore, *Luco et al.* (1975) report that Millikan Library has an equivalent circular foundation radius, r_0, of approximately $13m$. This number is used as the rigid disk's radius to estimate second-order effects ($\frac{r_0^2}{R}$, $\frac{1}{R^2}$) in Appendix E, but these are not presented in the main text to simplify the presentation, as the leading order terms ($\frac{1}{R}$) dominate the displacement fields. However, the second-order effects are presented in the appendix to verify that the magnitudes of these contributions are indeed smaller than those of the leading order terms in the Far-field approximation.

V_P	$597\ m/s$
V_S	$316\ m/s$
ρ	$1850\ Kg/m^3$
Λ	1.89

Table 3.1 Surficial soil properties for the area surrounding Millikan Library from a refraction experiment near Millikan Library. V_P is the compressional (P) wave velocity, V_S is the shear (S) wave velocity, ρ is the soil density, and $\Lambda = \frac{V_P}{V_S}$.

Furthermore, apart from this surficial model, I will also use a "best estimate" velocity model which is determined and explored in Chapter 5. The properties of this model are those of the top layer for the velocity model given in Table 5.3. It is presented here as both these models will be used at the end of the chapter to estimate the energy radiation from the half-space model, which are then compared to observed building results. Furthermore, the derivation of the displacement fields in Sections 3.2

to 3.5 will assume that the applied force and moment are in the EW direction, as in an EW shake. For a NS shake, the radiation patterns should be rotated by 90^o.

V_P	710 m/s
V_S	376 m/s
ρ	1910 Kg/m^3
Λ	1.89

Table 3.2 Estimated half-space soil properties for the area surrounding Millikan Library. V_P is the compressional (P) wave velocity, V_S is the shear (S) wave velocity, ρ is the soil density, and $\Lambda = \frac{V_P}{V_S}$.

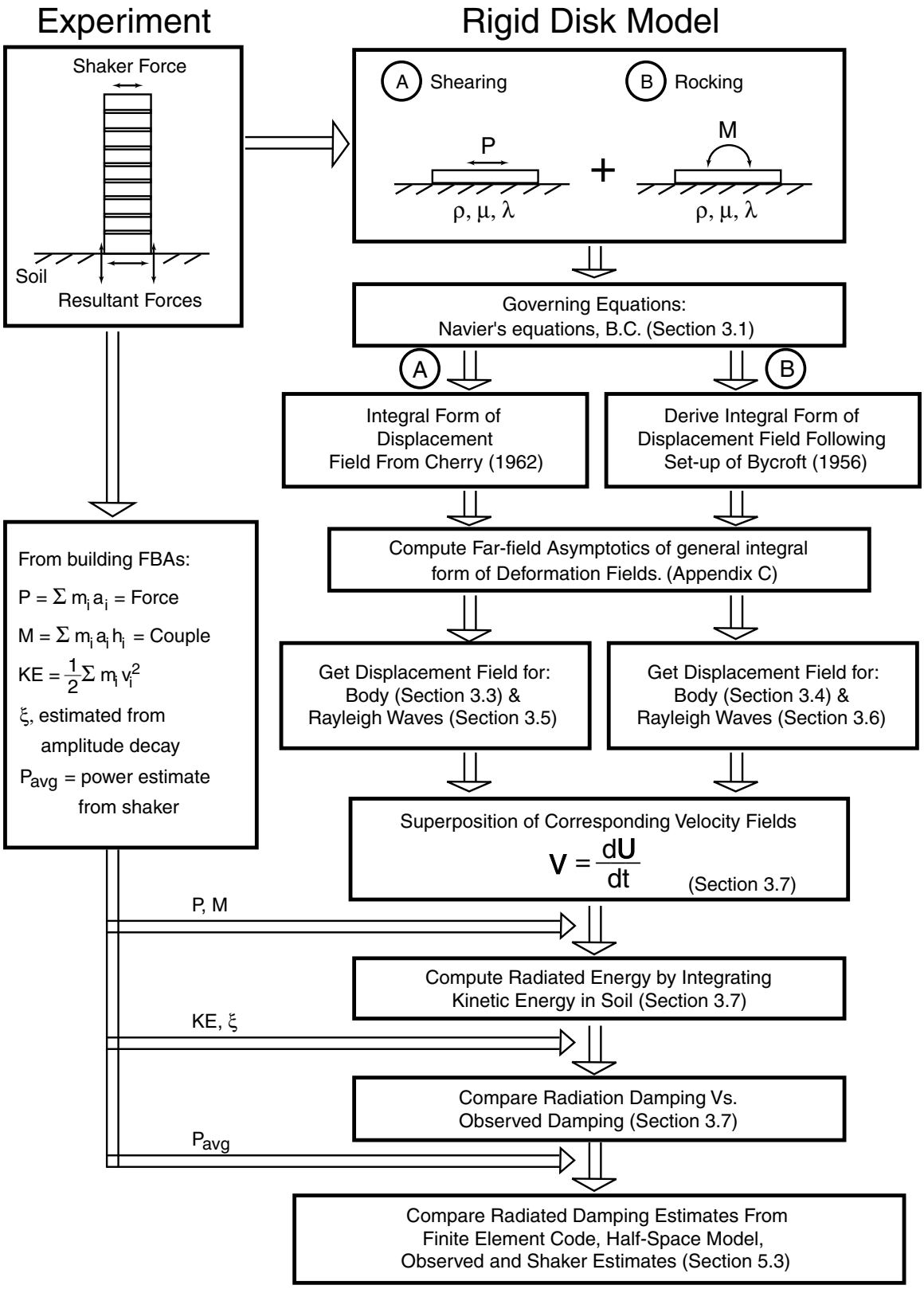

Figure 3.1 Flowchart to explain procedure and presentation order of theoretical model in Chapter 3.

3.1 Solution of the Elastic Wave Equations

In the absence of body forces, the dynamics of a homogeneous isotropic elastic solid are governed by the Navier equations. The vector displacement equations of motion can be written as

$$\rho \frac{\partial^2 \mathbf{U}}{\partial t^2} = (\lambda_o + 2\mu)\nabla(\nabla \cdot \mathbf{U}) - \mu \nabla \times \nabla \times \mathbf{U} \tag{3.1}$$

where ρ is the material density, μ (the shear modulus) and λ_o are the Lam*é* constants for an isotropic medium. To solve the elastodynamic problem, the Helmholtz decomposition of a vector field is introduced. Thus

$$\mathbf{U} = \nabla\varphi + \nabla \times \boldsymbol{\psi}, \qquad \nabla \cdot \boldsymbol{\psi} = 0 \tag{3.2}$$

where φ is a scalar potential and $\boldsymbol{\psi}$ is a vector potential. Substitution of this displacement field yields the following decoupled set of wave equations

$$\frac{\partial^2 \varphi}{\partial t^2} = V_P^2 \nabla^2 \varphi \tag{3.3}$$

$$\frac{\partial^2 \boldsymbol{\psi}}{\partial t^2} = V_S^2 \nabla^2 \boldsymbol{\psi}, \qquad \nabla \cdot \boldsymbol{\psi} = 0 \tag{3.4}$$

where the wave speeds are given by $V_P = \sqrt{\frac{\lambda_o + 2\mu}{\rho}}$ for compressional waves, and by $V_S = \sqrt{\frac{\mu}{\rho}}$ for shear waves. Note that the wave equation for $\boldsymbol{\psi}$ is a vector equation, and therefore it describes a total of three equations (given in Equation 3.7). The proceeding summary of equations in cylindrical coordinates follows the presentation of *Achenbach* (1993). Denoting the displacement components in cylindrical coordinates in the r, ϕ, and z directions by U_r, U_ϕ, and U_z, respectively, the relation between the displacement components and the potentials follow from Equation 3.2.

$$U_r = \frac{\partial \varphi}{\partial r} + \frac{1}{r}\frac{\partial \psi_z}{\partial \phi} - \frac{\partial \psi_\phi}{\partial z}$$

$$
\begin{aligned}
U_\phi &= \frac{1}{r}\frac{\partial \varphi}{\partial \phi} + \frac{\partial \psi_r}{\partial z} - \frac{\partial \psi_z}{\partial r} \\
U_z &= \frac{\partial \varphi}{\partial z} + \frac{1}{r}\frac{r\partial \psi_\phi}{\partial r} - \frac{1}{r}\frac{\partial \psi_r}{\partial \phi}
\end{aligned}
\tag{3.5}
$$

where φ satisfies Equation 3.3, and the Laplacian in cylindrical coordinates is defined as

$$
\nabla^2 = \frac{\partial}{\partial r^2} + \frac{1}{r}\frac{\partial}{\partial r} + \frac{1}{r^2}\frac{\partial^2}{\partial \phi^2} + \frac{\partial^2}{\partial z^2} \tag{3.6}
$$

The components of the vector potential $\boldsymbol{\psi}$ satisfy the equations

$$
\begin{aligned}
\frac{1}{V_S^2}\frac{\partial \psi_r^2}{\partial t^2} &= \nabla^2 \psi_r - \frac{\psi_r}{r^2} - \frac{2}{r^2}\frac{\partial \psi_\phi}{\partial \phi} \\
\frac{1}{V_S^2}\frac{\partial \psi_\phi^2}{\partial t^2} &= \nabla^2 \psi_\phi - \frac{\psi_\phi}{r^2} - \frac{2}{r^2}\frac{\partial \psi_r}{\partial \phi} \\
\frac{1}{V_S^2}\frac{\partial \psi_z^2}{\partial t^2} &= \nabla^2 \psi_z
\end{aligned}
\tag{3.7}
$$

In cylindrical coordinates, the strain-displacement relations are given by

$$
\begin{aligned}
\epsilon_{rr} = \frac{\partial U_r}{\partial r} \qquad \epsilon_{\phi\phi} &= \frac{U_r}{r} + \frac{1}{r}\frac{\partial U_\phi}{\partial \phi} \qquad \epsilon_{zz} = \frac{\partial U_z}{\partial z} \\
2\epsilon_{r\phi} &= 2\epsilon_{\phi r} = \frac{\partial U_\phi}{\partial r} - \frac{U_\phi}{r} + \frac{1}{r}\frac{\partial U_r}{\partial \phi} \\
2\epsilon_{\phi z} &= 2\epsilon_{z\phi} = \frac{1}{r}\frac{\partial U_z}{\partial \phi} + \frac{\partial U_\phi}{\partial z} \\
2\epsilon_{zr} &= 2\epsilon_{rz} = \frac{\partial U_r}{\partial z} + \frac{\partial U_z}{\partial r}
\end{aligned}
\tag{3.8}
$$

and the stress-strain relations in cylindrical coordinates are of the forms

$$\begin{aligned}
\sigma_{rr} &= \lambda_o\left(\frac{\partial U_r}{\partial r}+\frac{U_r}{r}+\frac{1}{r}\frac{\partial U_\phi}{\partial \phi}+\frac{\partial U_z}{\partial z}\right)+2\mu\frac{\partial U_r}{\partial r}\\
\sigma_{\phi\phi} &= \lambda_o\left(\frac{\partial U_r}{\partial r}+\frac{U_r}{r}+\frac{1}{r}\frac{\partial U_\phi}{\partial \phi}+\frac{\partial U_z}{\partial z}\right)+2\mu\left(\frac{U_r}{r}+\frac{1}{r}\frac{\partial U_\phi}{\partial \phi}\right)\\
\sigma_{zz} &= \lambda_o\left(\frac{\partial U_r}{\partial r}+\frac{U_r}{r}+\frac{1}{r}\frac{\partial U_\phi}{\partial \phi}+\frac{\partial U_z}{\partial z}\right)+2\mu\frac{\partial U_z}{\partial z}\\
\sigma_{r\phi} &= \mu\left(\frac{\partial U_\phi}{\partial r}-\frac{U_\phi}{r}+\frac{1}{r}\frac{\partial U_r}{\partial \phi}\right)\\
\sigma_{\phi z} &= \mu\left(\frac{1}{r}\frac{\partial U_z}{\partial \phi}+\frac{\partial U_\phi}{\partial z}\right)\\
\sigma_{zr} &= \mu\left(\frac{\partial U_r}{\partial z}+\frac{\partial U_z}{\partial r}\right)
\end{aligned} \tag{3.9}$$

And the constitutive relation for a homogeneous isotropic solid is given by

$$\sigma_{ij} = \lambda_o\epsilon_{kk}\delta_{ij}+2\mu\epsilon_{ij} \tag{3.10}$$

In this chapter, the temporal response in the solutions of the wave equation will be sinusoidal due to the periodic nature of the forcing. Therefore the potentials can be assumed to have a separable structure, such that φ and $\boldsymbol{\psi}$ are given by

$$\begin{aligned}
\varphi(\mathbf{x},t) &= \varphi(\mathbf{x})e^{-i\omega t}\\
\boldsymbol{\psi}(\mathbf{x},t) &= \boldsymbol{\psi}(\mathbf{x})e^{-i\omega t}
\end{aligned} \tag{3.11}$$

where ω is the forcing frequency, which in the case presented in this thesis is one of the resonant frequencies of Millikan Library. The wave equations reduce to the

Helmholtz equations for the spatial components of the potentials. These are given by

$$\nabla^2\varphi + h^2\varphi = 0 \qquad \nabla^2\boldsymbol{\psi} + k^2\boldsymbol{\psi} = 0, \qquad \nabla\cdot\boldsymbol{\psi} = \mathbf{0}$$

where the wave numbers h and k are given by

$$h = \frac{\omega}{V_P} \qquad k = \frac{\omega}{V_S} \tag{3.12}$$

The structure of the general separable solution to the Helmholtz equation, in cylindrical coordinates, that remains bounded is of the form

$$A_n(\zeta)J_n(\zeta r)e^{-\sqrt{\zeta^2-h^2}z+in\phi}$$

where ζ and n are separation constants, and $A_n(\zeta)$ is an amplitude term that is determined based on the boundary conditions. The problems to be solved in Sections 3.2 and 3.3 are the shearing and rocking of a rigid disk on the surface of a semi-infinite medium, respectively. The boundary conditions for problems of this type include the specification of both displacement and stress at a free surface, as well as bounded stresses at infinity. The general boundary conditions are given by

- at z = 0,

$$\begin{aligned} \boldsymbol{\sigma}\mathbf{n} &= \mathbf{S}(r,\phi), & r &\le r_0 \\ \mathbf{U} &= \mathbf{U}(r,\phi), & r &\le r_0 \\ \boldsymbol{\sigma} &= \mathbf{0}, & r &> 0 \end{aligned}$$

- $\mathbf{U} \to \mathbf{0}$ as z and $r \to \infty$

where $\mathbf{S}$ and $\mathbf{U}$ are a prescribed stress vector and displacement field, respectively, under the disk.

In these particular problems, no initial conditions are required since we are interested in the steady-state harmonic response of the medium, such that all transient response has decayed.

3.2 Body Waves from a Shearing Motion

This section presents the calculation of energy in the form of compressional (P) and shearing (S) body waves radiated away from a circular foundation (rigid disk) undergoing horizontal (shearing) harmonic motion. I use the displacement field derived in Equations 17 through 19 in *Cherry* (1962) as the displacement field to integrate using the method presented in the previous section. Furthermore, since *Cherry* (1962) solves for the displacement field using an asymptotic solution, this section also serves to verify that the method developed here gives the same leading order term solution as that achieved by Cherry. In the analysis that follows, we utilize the initial stress field used by *Bycroft* (1956), as *Cherry* (1962) removes some constants from his stress field for convenience. This change eliminates the dependence of Cherry's solution on the foundation's radius, which should not appear in the far-field solution to the problem (it only depends on the applied shear force). However, since only constants are involved, the solution maintains the same form. Figure 3.2 shows the coordinate system used throughout the rest of this chapter.

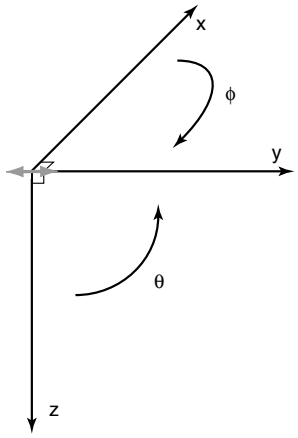

Figure 3.2 Coordinate system for the equations used in this chapter. The plane created by x and y defines the free surface, while z is the depth coordinate.

From the following boundary conditions at the free surface, ($z = 0$), in polar

coordinates,

$$\begin{aligned} U_r(t) &= d(t)\sin\phi \qquad (r \le r_0) \\ U_\phi(t) &= d(t)\cos\phi \qquad (r \le r_0) \\ \sigma_{rz} &= \sigma_{z\phi} = 0 \qquad (r \ge r_0) \end{aligned} \tag{3.13}$$

where $d(t)$ is the horizontal displacement of the rigid plate, r_0 is the radius of the disk, and U_r, U_ϕ, and U_z are the displacements of a point at r, ϕ, z in these coordinate directions (radial, tangential, and depth). Assuming a particular solution similar to that given in Equations 3.28 through 3.33, in conjunction with the boundary conditions given by Equation 3.13, and forcing the disk to remain horizontal when a force is applied, one can solve for $A(\zeta)$ and $C(\zeta)$. The procedure is used in the next section. Using this method, *Bycroft* (1956) and *Cherry* (1962) find the stress field under the plate to be

$$\sigma_{rz} = \frac{P\sin\phi}{2\pi r_0\sqrt{r_0^2 - r^2}} \qquad (r \le r_0)$$

$$\sigma_{z\phi} = \frac{P\cos\phi}{2\pi r_0\sqrt{r_0^2 - r^2}} \qquad (r \le r_0)$$

where P is the maximum applied shear force. The sinusoidal nature of the excitation force ($\sin(\omega t)$) has been neglected for convenience, and will be brought in once the displacement field is calculated. The displacement field calculated by *Cherry* (1962) is provided in Equations 3.22 through 3.24 in the proceeding analysis. The displacement field is given in cylindrical coordinates, where r and ϕ give the coordinates of a point on the free surface ($z = 0$) of the half-space. After the solution is achieved, it is transformed to spherical coordinates to simplify the integration of the displacement fields. The following integrals have been expanded and re-arranged to match the integral format presented in Appendix D in order to easily visualize the required

integrations. By utilizing the Bessel function identity

$$\frac{\partial}{\partial r}J_1(\zeta r) = \zeta J_0(\zeta r) - \frac{J_1(\zeta r)}{r} \tag{3.14}$$

to expand the integral form of the displacement field given by *Cherry* (1962) in Equations 17 to 19 to integrals of the form solved in Appendix D, the displacement field is as follows,

$$\begin{aligned}
U_r &= \frac{P\sin\phi}{2\pi\mu r_0}\Bigg[-\int_0^\infty \frac{2\zeta\sqrt{\zeta^2-k^2}}{F(\zeta)}\sin(\zeta r_0)\zeta J_0(\zeta r)\, e^{-\alpha z}\, d\zeta + \\
&\quad \int_0^\infty \frac{2\sqrt{\zeta^2-k^2}}{\zeta r F(\zeta)}\sin(\zeta r_0)\zeta^2 J_1(\zeta r)\, e^{-\alpha z}\, d\zeta + \\
&\quad \int_0^\infty \frac{\sin(\zeta r_0)}{r\zeta^3\sqrt{\zeta^2-k^2}}\zeta J_1(\zeta r)\, e^{-\beta z}\, d\zeta + \\
&\quad \int_0^\infty \frac{(2\zeta^2-k^2)\sqrt{\zeta^2-k^2}}{\zeta F(\zeta)}\sin(\zeta r_0)\zeta J_0(\zeta r)\, e^{-\beta z}\, d\zeta + \\
&\quad -\int_0^\infty \frac{(2\zeta^2-k^2)\sqrt{\zeta^2-k^2}}{\zeta^3 r F(\zeta)}\sin(\zeta r_0)\zeta^2 J_1(\zeta r)\, e^{-\beta z}\, d\zeta\Bigg]
\end{aligned} \tag{3.15}$$

$$\begin{aligned}
U_\phi &= \frac{P\cos\phi}{2\pi\mu r_0}\Bigg[-\int_0^\infty \frac{2\sqrt{\zeta^2-k^2}}{\zeta r F(\zeta)}\sin(\zeta r_0)\zeta^2 J_1(\zeta r)\, e^{-\alpha z}\, d\zeta + \\
&\quad \int_0^\infty \frac{\sin(\zeta r_0)}{\zeta\sqrt{\zeta^2-k^2}}\zeta J_0(\zeta r)\, e^{-\beta z}\, d\zeta + \\
&\quad -\int_0^\infty \frac{\sin(\zeta r_0)}{\zeta^3 r\sqrt{\zeta^2-k^2}}\zeta^2 J_1(\zeta r)\, e^{-\beta z}\, d\zeta + \\
&\quad \int_0^\infty \frac{(2\zeta^2-k^2)\sqrt{\zeta^2-k^2}}{\zeta^3 r F(\zeta)}\sin(\zeta r_0)\zeta^2 J_1(\zeta r)\, e^{-\beta z}\, d\zeta\Bigg]
\end{aligned} \tag{3.16}$$

$$U_z = \frac{P\sin\phi}{2\pi\mu r_0}\Bigg[\int_0^\infty \frac{2\sqrt{\zeta^2-h^2}\,\sqrt{\zeta^2-k^2}}{\zeta F(\zeta)}\sin(\zeta r_0)\zeta^2 J_1(\zeta r)\, e^{-\alpha z}\, d\zeta +$$

$$- \int_0^\infty \frac{(2\zeta^2 - k^2)}{\zeta F(\zeta)} \sin(\zeta r_0) \zeta^2 J_1(\zeta r)\, e^{-\beta z}\, d\zeta \Bigg] \tag{3.17}$$

where,

$$\alpha = \sqrt{\zeta^2 - h^2} \quad \text{and} \quad \beta = \sqrt{\zeta^2 - k^2}$$

the symbols commonly used for the P and S wave velocities, α and β, are here only used in the exponentials to distinguish which integrals are associated with compressional waves (α) and shear waves (β). Instead, the symbols V_P and V_S specify the wave velocities. Also,

$$h = \frac{\omega}{V_p} \quad \text{and} \quad k = \frac{\omega}{V_s} \quad \text{and} \quad \Lambda = \frac{k}{h} = \frac{V_P}{V_S}$$

where h and k are wavenumbers, and $F(\zeta)$ is the Rayleigh frequency equation (*Bycroft*, 1956) given by,

$$\begin{aligned} F(\zeta) &= (k^2 - 2\zeta^2)^2 - 4\sqrt{\zeta^2 - h^2}\sqrt{\zeta^2 - k^2}\zeta^2 \\ &= (k^2 - 2\zeta^2)^2 - 4\alpha\beta\zeta^2 \end{aligned} \tag{3.18}$$

where $\zeta = -m \sin\theta$ (the saddle point) and m can take on the values of either h or k, depending on the type of waves, P or S, being studied, respectively. Expanding $F(\zeta)$ for both saddle points, it is found that the Rayleigh frequency equation becomes either

$$F(-h\sin\theta) = h^4 \Big[(\Lambda^2 - 2\sin^2\theta)^2 - 4\sin^2\theta\cos\theta\sqrt{\Lambda^2 - \sin^2\theta} \Big] \tag{3.19}$$

or

$$F(-k\sin\theta) = k^4 \left[(1 - 2\sin^2\theta)^2 - 4\sin^2\theta\cos\theta\sqrt{\frac{1}{\Lambda^2} - \sin^2\theta}\, \right] \tag{3.20}$$

After performing the necessary integrations and transforming the resulting displacement fields to obtain a spherical coordinate set by utilizing the following transformation,

$$U_R = U_r \sin\theta + U_z \cos\theta \qquad\qquad U_\theta = U_r \cos\theta - U_z \sin\theta \tag{3.21}$$

As illustrated in Appendix E.2, the first-order terms ($\frac{1}{R}$) of the displacement field are as follows

$$U_R = \frac{P}{2\pi R\mu}\left[\frac{h^4\sqrt{\Lambda^2-\sin^2\theta}}{F(-h\sin\theta)}\,\sin 2\theta\sin\phi\right]\,\sin(\omega t - hR) \tag{3.22}$$

$$U_\theta = \frac{P}{2\pi R\mu}\left[\frac{k^4(1-2\sin^2\theta)}{F(-k\sin\theta)}\,\cos\theta\sin\phi\right]\,\sin(\omega t - kR) \tag{3.23}$$

$$U_\phi = \frac{P}{2\pi R\mu}\,[\cos\phi]\,\sin(\omega t - kR) \tag{3.24}$$

where the sinusoidal time variant has been incorporated into the solution, and equal signs are used for the displacement field as only the first-order terms will be used in a later section to estimate the radiated energy of the model. This field is in agreement with the asymptotic field computed by *Cherry* (1962). The higher order terms are omitted for brevity, as for most of the integrals, they include several dozen terms and would be too cumbersome to read. If the reader wishes to obtain these terms, he/she can use the method given in Appendix E to compute them for the integrals presented here or ones with similar structure. Figures 3.3 through 3.5 provide plots of the displacement fields given by Equations 3.22 through 3.24, minus the sinusoidal time term. It should be noted here that the reason that Figure 3.4a has the large peak associated with it is that the square root term in Equation 3.20 becomes imaginary when $\sin\theta = \frac{1}{\Lambda}$, and the behavior of the amplitude of U_θ changes dramatically at this point. This is not the case for Equation 3.19, and therefore terms containing it do not show this behavior.

Taking the time derivative of the displacement field to obtain the velocity field to

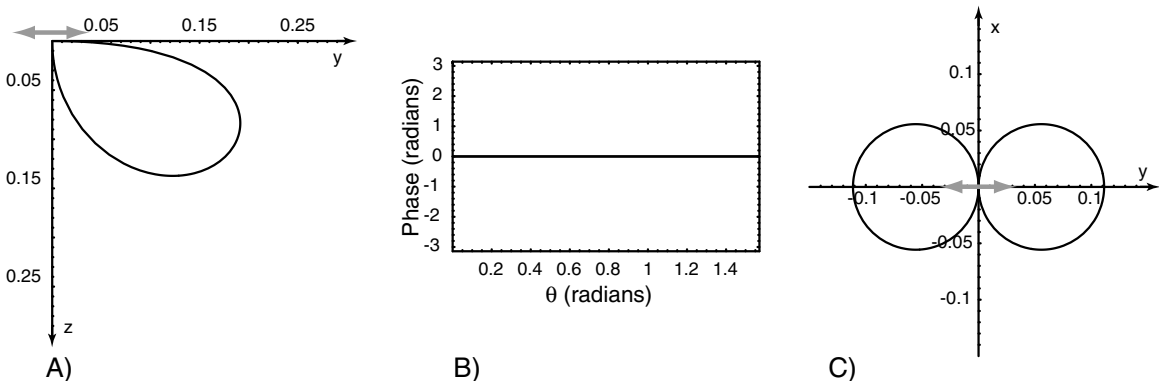

Figure 3.3 Displacement field for U_R. The gray arrows through the origin show the excitation direction for a horizontal force. All three figures correspond to the first term of the expansion ($1/R$ term). Figure A shows a vertical polar cross section ($\phi = \pi/2$), figure B the corresponding phase argument, and figure C the corresponding polar map views of the radiation patterns ($\theta = \pi/8$, $z = 0$). The harmonic source for the left and right plots is located at the plot's origin, and it oscillates along the x axis.

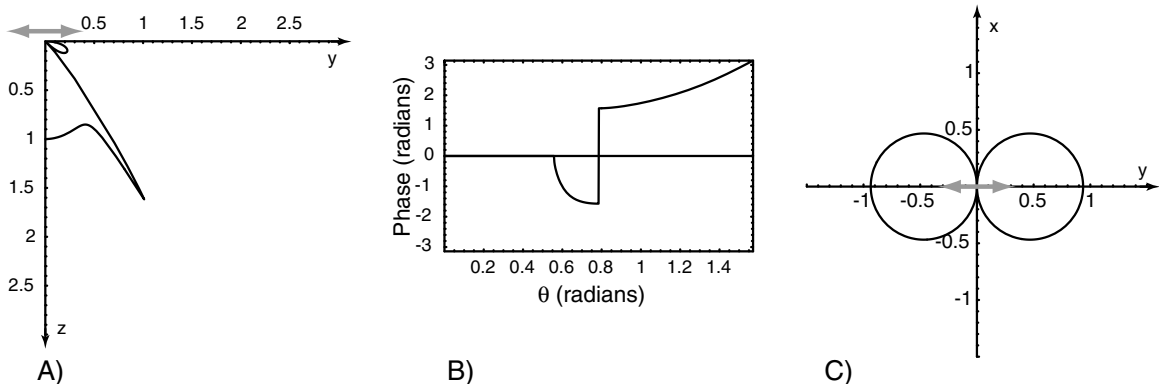

Figure 3.4 Displacement field for U_θ. The gray arrows through the origin show the excitation direction for a horizontal force. All three figures correspond to the first term of the expansion ($1/R$ term). Figure A shows a vertical polar cross section ($\phi = \pi/2$), figure B the corresponding phase argument, and figure C the corresponding polar map views of the radiation patterns ($\theta = \pi/8$, $z = 0$). The large peak present at approximately 35^o from the vertical axis is due to the asymptotic expansion. The harmonic source for the left and right plots is located at the plot's origin, and it oscillates along the x axis.

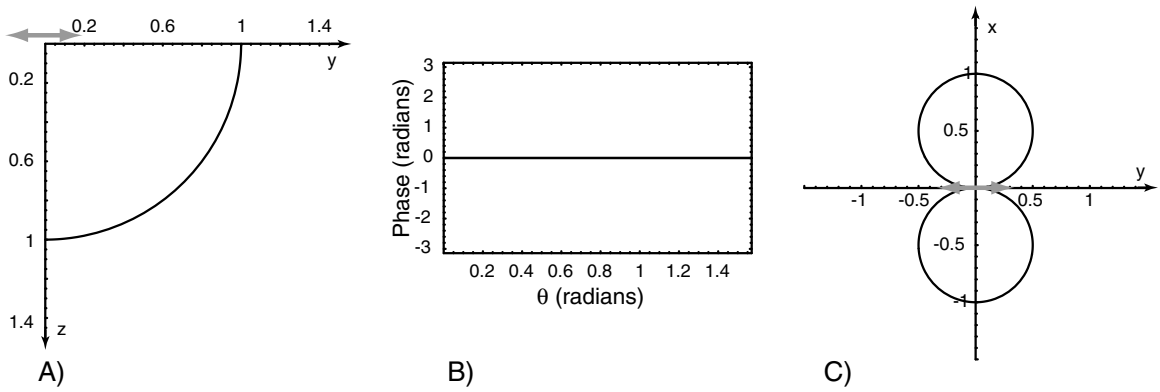

Figure 3.5 Displacement field for U_ϕ. The gray arrows through the origin show the excitation direction for a horizontal force. All three figures correspond to the first term of the expansion ($1/R$ term). Figure A shows a vertical polar cross section ($\phi = \pi/2$), figure B the corresponding phase argument, and figure C the corresponding polar map views of the radiation patterns ($\theta = \pi/8$, $z = 0$). The harmonic source for the left and right plots is located at the plot's origin, and it oscillates along the x axis.

be integrated at a later section,

$$V_R = \frac{P\omega}{2\pi R\mu}\left[\frac{h^4\sqrt{\Lambda^2-\sin^2\theta}}{F(-h\sin\theta)}\,\sin 2\theta\sin\phi\right]\cos(\omega t - hR) \tag{3.25}$$

$$V_\theta = \frac{P\omega}{2\pi R\mu}\left[\frac{k^4(1-2\sin^2\theta)}{F(-k\sin\theta)}\,\cos\theta\sin\phi\right]\cos(\omega t - kR) \tag{3.26}$$

$$V_\phi = \frac{P\omega}{2\pi R\mu}\left[\cos\phi\right]\cos(\omega t - kR) \tag{3.27}$$

the final result is achieved.

3.3 Body Waves from a Rocking Motion

This section provides the procedure for calculating the body wave energy radiated into a half-space from a circular foundation undergoing rocking motion. I follow the method of *Bycroft* (1956) and use his general displacement and stress conditions (in

cylindrical coordinates) provided in Equations 180-185 in *Bycroft* (1956)(labelled here as 3.28 through 3.30). Assume a solution of the form.

$$U_r(\zeta) = -\left[\frac{A(\zeta)e^{-\alpha z}}{h^2} - \frac{C(\zeta)\beta e^{-\beta z}}{k^2}\right]\frac{\partial J_1(\zeta r)}{\partial r}\sin\phi\, e^{i\omega t} \tag{3.28}$$

$$U_\phi(\zeta) = -\left[\frac{A(\zeta)e^{-\alpha z}}{h^2} - \frac{C(\zeta)e^{-\beta z}}{k^2}\right]\frac{J_1(\zeta r)}{r}\cos\phi\, e^{i\omega t} \tag{3.29}$$

$$U_z(\zeta) = \left[\frac{A(\zeta)\alpha e^{-\alpha z}}{h^2} - \frac{C(\zeta)\zeta^2\beta e^{-\beta z}}{k^2}\right]J_1(\zeta r)\sin\phi\, e^{i\omega t} \tag{3.30}$$

$$\sigma_{zz}(\zeta) = \mu\left[A(\zeta)\Big(\frac{\lambda_o}{\mu} - \frac{2\alpha^2}{h^2}\Big)e^{-\alpha z} + \frac{2C(\zeta)\beta\zeta^2}{k^2}e^{-\beta z}\right]J_1(\zeta r)\sin\phi\, e^{i\omega t} \tag{3.31}$$

$$\sigma_{zr}(\zeta) = \mu\left[\frac{2A(\zeta)\alpha}{h^2}e^{-\alpha z} - C(\zeta)\Big(\frac{\beta^2}{k^2} + \frac{\zeta^2}{k^2}\Big)e^{-\beta z}\right]\frac{\partial J_1(\zeta r)}{\partial r}\sin\phi\, e^{i\omega t} \tag{3.32}$$

$$\sigma_{r\phi}(\zeta) = \mu\left[\frac{2A(\zeta)\alpha}{h^2}e^{-\alpha z} - C(\zeta)\Big(\frac{\beta^2}{k^2} + \frac{\zeta^2}{k^2}\Big)e^{-\beta z}\right]\frac{J_1(\zeta r)}{r}\cos\phi\, e^{i\omega t} \tag{3.33}$$

where ζ is an arbitrary parameter. From the following boundary conditions, in polar coordinates, at the surface, $z = 0$,

$$U_z = \Theta_0\, r\sin\phi\sin(\omega t) \qquad (r \le r_0)$$

$$\sigma_{zz} = 0 \qquad (r > r_0)$$

$$\sigma_{rz} = \sigma_{z\phi} = 0 \qquad (r \ge 0)$$

where Θ_0 is the angle of rotation of the circular rigid plate about a horizontal axis, ϕ is the angle in the horizontal plane measured from the horizontal axis of rotation, and U_z is the displacement field under the disk. By setting the shear stress equal to zero at the free surface, $\sigma_{zr}(\zeta) = \sigma_{z\phi}(\zeta) = 0$, we can solve for $C(\zeta)$

$$C(\zeta) = \frac{2A(\zeta)\alpha k^2}{h^2}\frac{1}{(\beta^2 + \zeta^2)} \tag{3.34}$$

and by substituting into Equation 3.31, we find that the normal stress is

$$\sigma_{zz}(\zeta) = \frac{A(\zeta)\mu}{h^2}\left[\Big(\frac{\Lambda h^2}{\mu} - 2\alpha^2\Big)e^{-\alpha z} + \frac{4\alpha\beta\zeta^2}{\beta^2 + \zeta^2}e^{-\beta z}\right]J_1(\zeta r)\sin\phi\, e^{i\omega t} \tag{3.35}$$

At $z = 0$, Equation 3.35 becomes

$$\sigma_{zz}(\zeta) = \frac{A(\zeta)\mu}{h^2}\left[\frac{\Lambda h^2}{\mu} - 2(\zeta^2 - h^2) + \frac{4\alpha\beta\zeta^2}{\beta^2 + \zeta^2}\right] J_1(\zeta r)\sin\phi\, e^{i\omega t}$$

After some simplification and by using Rayleigh's frequency equation (3.18), the normal stress is given by

$$\sigma_{zz}(\zeta) = \frac{\mu A(\zeta)F(\zeta)}{h^2(k^2 - 2\zeta^2)} J_1(\zeta r)\sin\phi\, e^{i\omega t}$$

For convenience, I will stop writing the exponential time term, and it will be reintroduced towards the end of the analysis. Since the above equations are valid only for individual ζ, but the boundary conditions used to this point must also be true for any sum of ζ, the solution for the stress field can now be generalized by integrating from 0 to ∞ with respect to ζ, which gives

$$\sigma_{zz} = \int_0^\infty \frac{\mu A(\zeta)F(\zeta)}{h^2(k^2 - 2\zeta^2)} J_1(\zeta r)\sin\phi\, d\zeta \tag{3.36}$$

From *Bycroft* (1956), equation 187, we know that

$$\sigma_{zz} = \int_0^\infty K\sin\phi\, J_1(\zeta r)\zeta I(\zeta)\, d\zeta \tag{3.37}$$

where

$$I(\zeta) = \frac{r_0}{\zeta}\left[\frac{\sin(\zeta r_0)}{\zeta r_0} - \cos(\zeta r_0)\right]$$

and,

$$K = \frac{-3M}{2\pi r_0^3}$$

and the moment, M, necessary to rotate the rigid plate through an angle Θ_0 about

the horizontal axis, is found to be

$$M = \frac{16\mu r_0^3\,\Theta_0\,(1-\Lambda^{-2})}{3} \tag{3.38}$$

by (*Bycroft*, 1956). By equating Equations 3.36 and 3.37, we get that

$$A(\zeta) = \frac{-3Mh^2\zeta(k^2-2\zeta^2)}{2\pi r_0^3\mu F(\zeta)}\left[\frac{r_0}{\zeta}\Big(\frac{\sin(\zeta r_0)}{\zeta r_0} - \cos(\zeta r_0)\Big)\right] \tag{3.39}$$

Now use Equation 3.39 to solve for the displacement field in cylindrical coordinates (Equations 3.28 through 3.30).

$$U_z(\zeta) = \frac{-3M\alpha}{2\pi r_0^2\mu F(\zeta)}\Big[\frac{\sin(\zeta r_0)}{\zeta r_0} - \cos(\zeta r_0)\Big]\Big[(k^2-2\zeta^2)e^{-\alpha z} + 2\zeta^2 e^{-\beta z}\Big]J_1(\zeta r)\sin\phi$$

Generalize the displacement field by integrating from 0 to ∞ with respect to ζ, and then rewrite in a form similar to that of Equations D.4 and D.44, which gives

$$\begin{aligned} U_z &= \frac{-3M\sin\phi}{2\pi r_0^2\mu}\Big[\int_0^\infty E_1(\zeta)\zeta^2 J_1(\zeta r)e^{-\alpha z}\,d\zeta\; + \\ &\qquad \int_0^\infty E_2(\zeta)\zeta^2 J_1(\zeta r)e^{-\beta z}\,d\zeta\Big] \end{aligned} \tag{3.40}$$

where E_1 and E_2 are defined by the following functions

$$E_1(\zeta) = \frac{(k^2-2\zeta^2)\sqrt{\zeta^2-h^2}\,[\sin(\zeta r_0) - \zeta r_0\cos(\zeta r_0)]}{\zeta^3 r_0 F(\zeta)} \tag{3.41}$$

$$E_2(\zeta) = \frac{2\sqrt{\zeta^2-h^2}\,[\sin(\zeta r_0) - \zeta r_0\cos(\zeta r_0)]}{\zeta r_0 F(\zeta)} \tag{3.42}$$

Similarly to U_z,

$$U_\phi(\zeta) = -\left[\frac{A(\zeta)e^{-\alpha z}}{h^2} - \frac{2A(\zeta)\alpha\beta e^{-\beta z}}{h^2(\beta^2+\zeta^2)}\right]\frac{J_1(\zeta r)}{r}\cos\phi$$

which after a similar analysis yields,

$$U_\phi = \frac{3M\cos\phi}{2\pi r_0^2\mu}\Bigg[\int_0^\infty E_3(\zeta)\zeta^2 J_1(\zeta r)e^{-\alpha z}\,d\zeta + \int_0^\infty E_4(\zeta)\zeta^2 J_1(\zeta r)e^{-\beta z}\,d\zeta\Bigg] \tag{3.43}$$

where E_3 and E_4 are defined as

$$E_3(\zeta) = \frac{(k^2-2\zeta^2)\,[\sin(\zeta r_0)-\zeta r_0\cos(\zeta r_0)]}{r\,\zeta^3\,r_0F(\zeta)} \tag{3.44}$$

$$E_4(\zeta) = \frac{2\alpha\beta\,[\sin(\zeta r_0)-\zeta r_0\cos(\zeta r_0)]}{r\,\zeta^3\,r_0F(\zeta)} \tag{3.45}$$

And for U_r,

$$U_r(\zeta) = \left[\frac{-A(\zeta)e^{-\alpha z}}{h^2}+\frac{C(\zeta)\beta e^{-\beta z}}{k^2}\right]\frac{\partial J_1(\zeta r)}{\partial r}\sin\phi$$

after substituting for $A(\zeta)$, $C(\zeta)$, the derivative of the Bessel Function by using Equation 3.14, and performing the previous analysis, this gives

$$\begin{aligned} U_r = \frac{3M\sin\phi}{2\pi r_0^2\mu}\Bigg[&-\int_0^\infty \frac{(k^2-2\zeta^2)\,[\sin(\zeta r_0)-\zeta r_0\cos(\zeta r_0)]}{r\,\zeta^3\,r_0F(\zeta)}\,\zeta^2\,J_1(\zeta r)\,e^{-\alpha z} - \\ &\int_0^\infty \frac{2\alpha\beta\,[\sin(\zeta r_0)-\zeta r_0\cos(\zeta r_0)]}{r\,\zeta^3\,r_0F(\zeta)}\,\zeta^2\,J_1(\zeta r)\,e^{-\beta z} + \\ &\int_0^\infty \frac{(k^2-2\zeta^2)\,[\sin(\zeta r_0)-\zeta r_0\cos(\zeta r_0)]}{\zeta\,r_0F(\zeta)}\,\zeta\,J_0(\zeta r)\,e^{-\alpha z} + \\ &\int_0^\infty \frac{2\alpha\beta\,[\sin(\zeta r_0)-\zeta r_0\cos(\zeta r_0)]}{\zeta\,r_0F(\zeta)}\,\zeta\,J_0(\zeta r)\,e^{-\beta z}\Bigg] \end{aligned} \tag{3.46}$$

After performing the necessary integrations and transforming the resulting displacement fields to obtain a spherical coordinate set as illustrated in Appendix E.3, the

first term of the displacement field is found to be

$$U_R = \frac{M}{2\pi R\mu}\left[\frac{ih^5 \sin 2\theta(\Lambda^2 - 2\sin^2\theta)}{2F(-h\sin\theta)}\sin\phi\right]\sin(\omega t - hR) \quad (3.47)$$

$$U_\theta = \frac{-M}{2\pi R\mu}\left[\frac{2k^5\cos\theta\sin^2\theta\sqrt{\Lambda^2\sin^2\theta - 1}}{F(-k\sin\theta)}\sin\phi\right]\sin(\omega t - kR) \quad (3.48)$$

$$U_\phi = 0 \quad (3.49)$$

where the sinusoidal time variant has been incorporated to the solution. Only the first-order terms ($\frac{1}{R}$) are given once again, as only these will be used to estimate the radiated energy. Figures 3.6 and 3.7 provide plots of the displacement fields given by Equations 3.47 through 3.49, minus the sinusoidal time term.

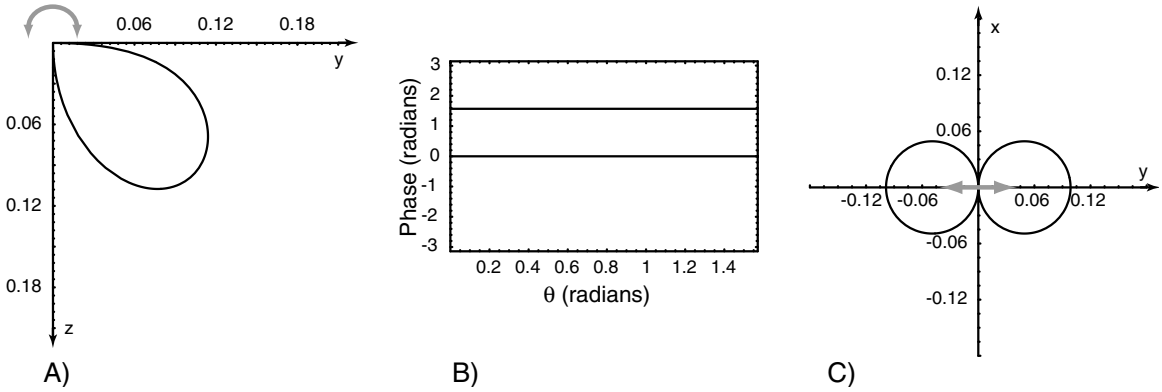

Figure 3.6 Displacement field for U_R. The gray arrows through the origin show the excitation direction for a single couple. All three figures correspond to the first term of the expansion ($1/R$ term). Figure A shows a vertical polar cross section ($\phi = \pi/2$), figure B the corresponding phase argument, and figure C the corresponding polar map views of the radiation patterns ($\theta = \pi/8$, $z = 0$). The harmonic source for the left and right plots is located at the plot's origin, and it oscillates along the x axis.

Taking the time derivative of the displacement field to obtain the velocity field to be integrated in a subsequent section,

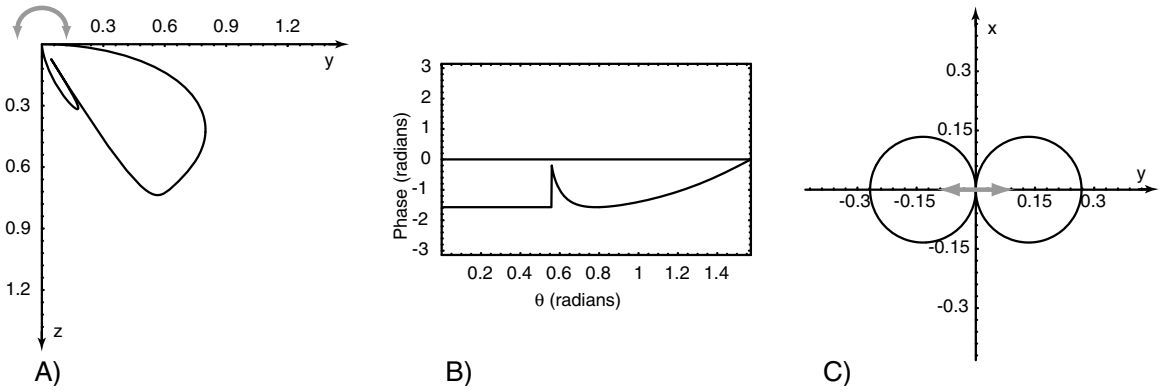

Figure 3.7 Displacement field for U_θ. The gray arrows through the origin show the excitation direction for a single couple. All three figures correspond to the first term of the expansion ($1/R$ term). Figure A shows a vertical polar cross section ($\phi = \pi/2$), figure B the corresponding phase argument, and figure C the corresponding polar map views of the radiation patterns ($\theta = \pi/8$, $z = 0$). The harmonic source for the left and right plots is located at the plot's origin, and it oscillates along the x axis.

$$V_R = \frac{M\omega}{2\pi R\mu}\left[\frac{ih^5 \sin 2\theta(\Lambda^2 - 2\sin^2\theta)}{2F(-h\sin\theta)}\ \sin\phi\right]\cos(\omega t - hR) \tag{3.50}$$

$$V_\theta = \frac{-M\omega}{2\pi R\mu}\left[\frac{2k^5 \cos\theta \sin^2\theta\sqrt{\Lambda^2\sin^2\theta - 1}}{F(-k\sin\theta)}\ \sin\phi\right]\cos(\omega t - kR) \tag{3.51}$$

$$V_\phi = 0 \tag{3.52}$$

the final result is achieved.

3.4 Rayleigh Waves from a Shearing Motion

This section provides the calculation of energy radiated away from a circular foundation undergoing shearing motion in the form of Rayleigh waves, following the method of *Miller and Pursey* (1954) which expands the method used by *Bycroft* (1956). It has been shown by *Miller and Pursey* (1954) that the poles of the integrand occur

on the real axis at points $\zeta_0 = \pm k_R$, where $k_R > k$. If $\theta > \arcsin(\Lambda^{-1})$, the deformation of the contour mentioned in Section D will cause it to move across the pole at $\zeta_0 = -k_R$ and this will give rise to a residue term which must be added to the integrals presented in the previous two sections. This term corresponds to the Rayleigh wave. Since, however, this term contains a factor $e^{-Rf(\zeta)}$ and $\zeta > k$, the contribution from the pole will be asymptotically negligible except when $\theta = \frac{\pi}{2}$.

The following analysis is in cylindrical coordinates, where r and ϕ give the coordinates of a point on the free surface ($z = 0$) of the half-space. From Equation 3.16 through 3.18, we know that the displacement field is

$$
\begin{aligned}
U_r &= \frac{P\sin\phi}{2\pi\mu r_0}\Bigg[-\int_0^\infty \frac{2\zeta\sqrt{\zeta^2-k^2}}{F(\zeta)}\sin(\zeta r_0)\zeta J_0(\zeta r)\, e^{-\alpha z}\, d\zeta + \\
&\quad \int_0^\infty \frac{2\sqrt{\zeta^2-k^2}}{\zeta r F(\zeta)}\sin(\zeta r_0)\zeta^2 J_1(\zeta r)\, e^{-\alpha z}\, d\zeta + \\
&\quad \int_0^\infty \frac{\sin(\zeta r_0)}{r\zeta^3\sqrt{\zeta^2-k^2}}\zeta J_1(\zeta r)\, e^{-\beta z}\, d\zeta + \\
&\quad \int_0^\infty \frac{(2\zeta^2-k^2)\sqrt{\zeta^2-k^2}}{\zeta F(\zeta)}\sin(\zeta r_0)\zeta J_0(\zeta r)\, e^{-\beta z}\, d\zeta + \\
&\quad -\int_0^\infty \frac{(2\zeta^2-k^2)\sqrt{\zeta^2-k^2}}{\zeta^3 r F(\zeta)}\sin(\zeta r_0)\zeta^2 J_1(\zeta r)\, e^{-\beta z}\, d\zeta\Bigg] \\
U_\phi &= \frac{P\cos\phi}{2\pi\mu}\Bigg[-\int_0^\infty \frac{2\sqrt{\zeta^2-k^2}}{\zeta r F(\zeta)}\sin(\zeta r_0)\zeta^2 J_1(\zeta r)\, e^{-\alpha z}\, d\zeta + \\
&\quad \int_0^\infty \frac{\sin(\zeta r_0)}{\zeta\sqrt{\zeta^2-k^2}}\zeta J_0(\zeta r)\, e^{-\beta z}\, d\zeta + \\
&\quad -\int_0^\infty \frac{\sin(\zeta r_0)}{\zeta^3 r\sqrt{\zeta^2-k^2}}\zeta^2 J_1(\zeta r)\, e^{-\beta z}\, d\zeta + \\
&\quad \int_0^\infty \frac{(2\zeta^2-k^2)\sqrt{\zeta^2-k^2}}{\zeta^3 r F(\zeta)}\sin(\zeta r_0)\zeta^2 J_1(\zeta r)\, e^{-\beta z}\, d\zeta\Bigg]
\end{aligned}
$$

$$U_z = \frac{P\sin\phi}{2\pi\mu}\left[\int_0^\infty \frac{2\sqrt{\zeta^2-h^2}\,\sqrt{\zeta^2-k^2}}{\zeta F(\zeta)}\sin(\zeta r_0)\zeta^2 J_1(\zeta r)\,e^{-\alpha z}\,d\zeta + \right.$$

$$\left. -\int_0^\infty \frac{(2\zeta^2-k^2)}{\zeta F(\zeta)}\sin(\zeta r_0)\zeta^2 J_1(\zeta r)\,e^{-\beta z}\,d\zeta\right]$$

From the method of residues, the contribution from the residue for an integral of the type $I_C = \oint_C e^{Rf(\zeta)}\frac{\chi(\zeta)}{F(\zeta)}d\zeta$ is (*Miller and Pursey*, 1954)

$$I_C = \frac{2\pi i\chi(\zeta_0)\,e^{Rf(\zeta_0)}}{F'(\zeta_0)} \tag{3.53}$$

as $F(\zeta)$ has a simple pole at ζ_0, where $F'(\zeta_0)$ is the derivative of the Rayleigh frequency equation evaluated at ζ_0, and ζ_0 is a zero of $F(\zeta)$. The contribution to the displacement field for each integral of the form of Equation D.16 for terms involving J_0 and of Equation D.55 for terms involving J_1, is as follows (showing only terms of order $r^{-\frac{1}{2}}$).

$$U_r = \frac{iP\sin\phi e^{-\frac{i\pi}{4}-ir\zeta_0}}{\mu r_0\sqrt{2\pi r}F'(\zeta_0)}\left[-2\zeta_0^{\frac{3}{2}}\sqrt{\zeta_0^2-k^2}\sin(\zeta_0 r_0)\,e^{-\alpha_1 z}\ + \right.$$

$$\left.\zeta^{-\frac{1}{2}}(2\zeta_0^2-k^2)\sqrt{\zeta_0^2-k^2}\sin(\zeta_0 r_0)e^{-\beta_1 z}\right] \tag{3.54}$$

$$U_\phi \approx 0 \tag{3.55}$$

$$U_z = \frac{P\sin\phi e^{-\frac{i\pi}{4}-ir\zeta_0}}{\mu r_0\sqrt{2\pi r}F'(\zeta_0)}\left[-2\zeta_0^{\frac{1}{2}}\sqrt{\zeta_0^2-k^2}\sqrt{\zeta_0^2-h^2}\sin(\zeta_0 r_0)\,e^{-\alpha_1 z} + \right.$$

$$\left.\zeta_0^{\frac{1}{2}}\left(2\zeta_0^2-k^2\right)\sin(\zeta_0 r_0)\,e^{-\beta_1 z}\right] \tag{3.56}$$

where $\alpha_1 = \frac{\omega}{V_R}\sqrt{1-(\frac{V_R}{V_P})^2}$, $\beta_1 = \frac{\omega}{V_R}\sqrt{1-(\frac{V_R}{V_S})^2}$, $F'(k_R) = -4k_R^3 N$,

and

$$N = 2\Big(\Lambda_{RS}^2 - 2 + \sqrt{1-\Lambda_{RP}^2}\sqrt{1-\Lambda_{RS}^2}\Big) + \frac{\sqrt{1-\Lambda_{RP}^2}}{\sqrt{1-\Lambda_{RS}^2}} + \frac{\sqrt{1-\Lambda_{RS}^2}}{\sqrt{1-\Lambda_{RP}^2}}$$

substituting $h = \frac{\omega}{V_P}$, $k = \frac{\omega}{V_S}$, $k_R = \frac{\omega}{V_R}$, $\Lambda_{RS} = \frac{V_R}{V_S}$, and $\Lambda_{RP} = \frac{V_R}{V_P}$, Taylor expanding for $\sin(\zeta_0 r_0)$, and introducing the sinusoidal time dependence of the source as in Section 3.2, simplifies Equations 3.54 through 3.56, which yields

$$\begin{aligned} U_r = \frac{P\omega^{\frac{7}{2}}}{\mu\sqrt{2\pi r}V_R^{\frac{7}{2}}F'(\zeta_0)} \Big[&- 2\sqrt{1-\Lambda_{RS}^2}\, e^{-\alpha_1 z} + \\ &(2-\Lambda_{RS}^2)\sqrt{1-\Lambda_{RS}^2}\, e^{-\beta_1 z}\Big] \cos\left(\omega t - r\zeta_0 + \frac{\pi}{4}\right)\sin\phi \end{aligned} \tag{3.57}$$

$$U_\phi \approx 0 \tag{3.58}$$

$$\begin{aligned} U_z = \frac{P\omega^{\frac{7}{2}}}{\mu\sqrt{2\pi r}V_R^{\frac{7}{2}}F'(\zeta_0)} \Big[&- 2\sqrt{1-\Lambda_{RS}^2}\sqrt{1-\Lambda_{RP}^2}\, e^{-\alpha_1 z} + \\ &(2-\Lambda_{RS}^2)\, e^{-\beta_1 z}\Big] \cos\left(\omega t - r\zeta_0 - \frac{\pi}{4}\right)\sin\phi \end{aligned} \tag{3.59}$$

where the expected phase shift between the radial and vertical component in a Rayleigh wave is evident in the sinusoidal time term, and the vertical component is 90^0 behind the radial term.

Now transform the displacement field to spherical coordinates as in the previous two sections, which gives

$$
\begin{aligned}
U_R \;=\; & \frac{P\omega^{\frac{7}{2}}}{\mu\sqrt{2\pi R}\,V_R^{\frac{7}{2}}F'(\zeta_0)}\Bigg[-2\sqrt{1-\Lambda_{RS}^2}\,\Bigg(\sqrt{\sin\theta}\,\cos(\omega t-R\zeta_0\sin\theta+\frac{\pi}{4})\;+\\
& \sqrt{1-\Lambda_{RP}^2}\frac{\cos\theta}{\sqrt{\sin\theta}}\,\cos(\omega t-R\zeta_0\sin\theta-\frac{\pi}{4})\Bigg)\,e^{-\alpha_1 z}\;+\\
& (2-\Lambda_{RS}^2)\Big(\sqrt{1-\Lambda_{RS}^2}\sqrt{\sin\theta}\,\cos(\omega t-R\zeta_0\sin\theta+\frac{\pi}{4})\;+\\
& \frac{\cos\theta}{\sqrt{\sin\theta}}\,\cos(\omega t-R\zeta_0\sin\theta-\frac{\pi}{4})\Big)\,e^{-\beta_1 z}\Bigg]\,\sin\phi
\end{aligned}
\tag{3.60}
$$

$$
U_\phi \;\approx\; 0 \tag{3.61}
$$

$$
\begin{aligned}
U_\theta \;=\; & \frac{P\omega^{\frac{7}{2}}}{\mu\sqrt{2\pi R}\,V_R^{\frac{7}{2}}F'(\zeta_0)}\Bigg[-2\sqrt{1-\Lambda_{RS}^2}\Big(\frac{\cos\theta}{\sqrt{\sin\theta}}\,\cos(\omega t-R\zeta_0\sin\theta+\frac{\pi}{4})\;-\\
& \sqrt{1-\Lambda_{RP}^2}\sqrt{\sin\theta}\,\cos(\omega t-R\zeta_0\sin\theta-\frac{\pi}{4})\Big)\,e^{-\alpha_1 z}\;+\\
& (2-\Lambda_{RS}^2)\Big(\sqrt{1-\Lambda_{RS}^2}\frac{\cos\theta}{\sqrt{\sin\theta}}\,\cos(\omega t-R\zeta_0\sin\theta+\frac{\pi}{4})\;-\\
& \sqrt{\sin\theta}\,\cos(\omega t-R\zeta_0\sin\theta-\frac{\pi}{4})\Big)\,e^{-\beta_1 z}\Bigg]\,\sin\phi
\end{aligned}
\tag{3.62}
$$

The velocity field is not shown here, as it is quite lengthy and fairly simple to derive from the shown displacement field.

3.5 Rayleigh Waves from a Rocking Motion

This section provides the calculation of energy radiated away from a circular foundation undergoing rocking motion in the form of Rayleigh waves. From the calculation of body wave energy for a foundation undergoing rocking motion in Section 3.3, we

have that

$$
\begin{aligned}
U_r &= \frac{3M\sin\phi}{2\pi r_0^2\mu}\Bigg[-\int_0^\infty \frac{(k^2-2\zeta^2)\,[\sin(\zeta r_0)-\zeta r_0\cos(\zeta r_0)]}{r\,\zeta^3\,r_0F(\zeta)}\,\zeta^2\,J_1(\zeta r)\,e^{-\alpha z}\;+\\
&\quad -\int_0^\infty \frac{2\alpha\beta\,[\sin(\zeta r_0)-\zeta r_0\cos(\zeta r_0)]}{r\,\zeta^3\,r_0F(\zeta)}\,\zeta^2\,J_1(\zeta r)\,e^{-\beta z}\;+\\
&\quad \int_0^\infty \frac{(k^2-2\zeta^2)\,[\sin(\zeta r_0)-\zeta r_0\cos(\zeta r_0)]}{\zeta\,r_0F(\zeta)}\,\zeta\,J_0(\zeta r)\,e^{-\alpha z}\;+\\
&\quad \int_0^\infty \frac{2\alpha\beta\,[\sin(\zeta r_0)-\zeta r_0\cos(\zeta r_0)]}{\zeta\,r_0F(\zeta)}\,\zeta\,J_0(\zeta r)\,e^{-\beta z}\Bigg]\\
U_\phi &= \frac{3M\cos\phi}{2\pi r_0^2\mu}\Bigg[\int_0^\infty \frac{(k^2-2\zeta^2)\,[\sin(\zeta r_0)-\zeta r_0\cos(\zeta r_0)]}{r\,\zeta^3\,r_0F(\zeta)}\zeta^2J_1(\zeta r)\,e^{-\alpha z}\,d\zeta\;+\\
&\quad \int_0^\infty \frac{2\alpha\beta\,[\sin(\zeta r_0)-\zeta r_0\cos(\zeta r_0)]}{r\,\zeta^3\,r_0F(\zeta)}\zeta^2J_1(\zeta r)\,e^{-\beta z}\,d\zeta\Bigg]\\
U_z &= \frac{-3M\sin\phi}{2\pi r_0^2\mu}\Bigg[\int_0^\infty \frac{\alpha(k^2-2\zeta^2)[\sin(\zeta r_0)-\zeta r_0\cos(\zeta r_0)]}{\zeta^3r_0F(\zeta)}\zeta^2J_1(\zeta r)e^{-\alpha z}d\zeta\;+\\
&\quad \int_0^\infty \frac{2\alpha\,[\sin(\zeta r_0)-\zeta r_0\cos(\zeta r_0)]}{\zeta r_0F(\zeta)}\zeta^2J_1(\zeta r)\,e^{-\beta z}\,d\zeta\Bigg]
\end{aligned}
$$

Applying the same method as in the previous section, the contribution to the displacement field for each integral of the form of Equation D.16 for terms involving J_0 and of Equation D.55 for terms involving J_1, is as follows (showing only terms of order $r^{-\frac{1}{2}}$).

$$U_r = \frac{3iM\sin\phi e^{-\frac{i\pi}{4}-ir\zeta_0}}{r_0^3\mu\sqrt{2\pi r}F'(\zeta_0)}\Big[\zeta^{-\frac{1}{2}}\,(k^2-2\zeta^2)\,[\sin(\zeta r_0)-\zeta r_0\cos(\zeta r_0)]\,e^{-\alpha_1 z}\;+ \\ 2\zeta^{-\frac{1}{2}}\,\alpha\beta\,[\sin(\zeta r_0)-\zeta r_0\cos(\zeta r_0)]\,e^{-\beta_1 z}\Big] \tag{3.63}$$

$$U_\phi \approx 0 \tag{3.64}$$

$$U_z = \frac{3M\sin\phi e^{-\frac{i\pi}{4}-ir\zeta_0}}{r_0^3\mu\sqrt{2\pi r}F'(\zeta_0)}\Big[\zeta^{-\frac{3}{2}}\,\alpha(k^2-2\zeta^2)\,[\sin(\zeta r_0)-\zeta r_0\cos(\zeta^3 r_0)]\,e^{-\alpha_1 z}\;+ \\ 2\zeta^{\frac{1}{2}}\,\alpha\,[\sin(\zeta r_0)-\zeta r_0\cos(\zeta r_0)]\,e^{-\beta_1 z}\Big] \tag{3.65}$$

substituting $h=\frac{\omega}{V_P}$, $k=\frac{\omega}{V_S}$, $k_R=\frac{\omega}{V_R}$, $\Lambda_{RS}=\frac{V_R}{V_S}$, and $\Lambda_{RP}=\frac{V_R}{V_P}$, Taylor expanding for $\sin(\zeta_0 r_0)$ and $cos(\zeta r_0)$, and introducing the sinusoidal time dependence of the source as in Section 3.2, simplifies Equations 3.63 through 3.65, which yields

$$U_r = \frac{M\omega^{\frac{9}{2}}}{\mu\sqrt{2\pi r}V_R^{\frac{9}{2}}F'(\zeta_0)}\Big[(\Lambda_{RS}^2-2)\,e^{-\alpha_1 z}\;+ \\ 2\sqrt{1-\Lambda_{RP}^2}\sqrt{1-\Lambda_{RS}^2}\,e^{-\beta_1 z}\Big]\cos\left(\omega t-r\zeta_0+\frac{\pi}{4}\right)\sin\phi \tag{3.66}$$

$$U_\phi \approx 0 \tag{3.67}$$

$$U_z = \frac{M\omega^{\frac{9}{2}}}{\mu\sqrt{2\pi r}V_R^{\frac{9}{2}}F'(\zeta_0)}\Big[\sqrt{1-\Lambda_{RP}^2}(\Lambda_{RS}^2-2)\,e^{-\alpha_1 z}\;+ \\ 2\sqrt{1-\Lambda_{RP}^2}\,e^{-\beta_1 z}\Big]\cos\left(\omega t-r\zeta_0-\frac{\pi}{4}\right)\sin\phi \tag{3.68}$$

Again transform the displacement field to spherical coordinates, which gives

$$\begin{aligned} U_R &= \frac{M\omega^{\frac{9}{2}}}{\mu\sqrt{2\pi R}\,V_R^{\frac{9}{2}}F'(\zeta_0)}\Bigg[(\Lambda_{RS}^2-2)\left(\sqrt{\sin\theta}\,\cos\left(\omega t - R\zeta_0\sin\theta+\frac{\pi}{4}\right)\,+\right.\\ &\left.\sqrt{1-\Lambda_{RP}^2}\frac{\cos\theta}{\sqrt{\sin\theta}}\,\cos\left(\omega t - R\zeta_0\sin\theta-\frac{\pi}{4}\right)\right)e^{-\alpha_1 z}\,+\\ &2\sqrt{1-\Lambda_{RP}^2}\Big(\sqrt{1-\Lambda_{RS}^2}\sqrt{\sin\theta}\,\cos\left(\omega t - R\zeta_0\sin\theta+\frac{\pi}{4}\right)\,+\\ &\left.\frac{\cos\theta}{\sqrt{\sin\theta}}\,\cos\left(\omega t - R\zeta_0\sin\theta-\frac{\pi}{4}\right)\right)e^{-\beta_1 z}\Bigg]\,\sin\phi \end{aligned} \tag{3.69}$$

$$U_\phi \approx 0 \tag{3.70}$$

$$\begin{aligned} U_\theta &= \frac{M\omega^{\frac{9}{2}}}{\mu\sqrt{2\pi R}\,V_R^{\frac{9}{2}}F'(\zeta_0)}\Bigg[(\Lambda_{RS}^2-2)\Big(\frac{\cos\theta}{\sqrt{\sin\theta}}\,\cos\left(\omega t - R\zeta_0\sin\theta+\frac{\pi}{4}\right)\,-\\ &\left.\sqrt{1-\Lambda_{RP}^2}\sqrt{\sin\theta}\,\cos\left(\omega t - R\zeta_0\sin\theta-\frac{\pi}{4}\right)\right)e^{-\alpha_1 z}\,+\\ &2\sqrt{1-\Lambda_{RP}^2}\Big(\sqrt{1-\Lambda_{RS}^2}\frac{\cos\theta}{\sqrt{\sin\theta}}\,\cos\left(\omega t - R\zeta_0\sin\theta+\frac{\pi}{4}\right)\,-\\ &\left.\sqrt{\sin\theta}\,\cos\left(\omega t - R\zeta_0\sin\theta-\frac{\pi}{4}\right)\right)e^{-\beta_1 z}\Bigg]\,\sin\phi \end{aligned} \tag{3.71}$$

Once again, the velocity field is omitted for conciseness.

3.6 Building Results

The building's floor displacements and rotations are calculated using the accelerometers located throughout Millikan Library. There are at least three horizontal accelerometers per floor, as well as three vertical accelerometers in the basement. For simplicity, it will be assumed that all the displacements for the NS and EW modes

take place in a vertical plane in either the NS or EW direction, respectively, and that the floor slabs are rigid, as was shown by *Foutch* (1976) for forced vibrations of the library. The rigidity of the floor slabs implies that accelerometer measurements for each floor are valid throughout the floor, as long as floor rotations about a vertical rotation axis are accounted for. With these assumptions, the maximum kinetic energy of the building (E_{Kin}), the applied shear force (P), and the applied moment (M) on the ground can be computed by

$$E_{Kin} = \sum_{i=Basement}^{Roof} \frac{1}{2} m_i v_{i0}^2 = \sum_{i=Basement}^{Roof} \frac{1}{2} m_i \omega^2 x_{i0}^2 \tag{3.72}$$

$$P = \sum_{i=Basement}^{Roof} m_i a_{i0} = \sum_{i=Basement}^{Roof} m_i x_{i0} \omega^2 \tag{3.73}$$

$$M = \sum_{i=Basement}^{Roof} m_i a_{i0} h_i = \sum_{i=Basement}^{Roof} m_i x_{i0} h_i \omega^2 \tag{3.74}$$

where x_{i0}, v_{i0}, and a_{i0} represent the maximum displacement, velocity, and acceleration at the i^{th} floor, h represents the story height measuring from the basement floor, and m represents the lumped mass for each floor as given in the structural calculations of Millikan Library, but modified to correct for the live loads (mostly books) added since the building's construction. The correction of the the masses is presented in Table 3.3, and it is assumed that the entire live loads are present in the individual floors. The live loads are estimated from the building's design plans (except for the 6th floor which changed use since the building's construction) and they correspond to the floor uses at the time of the September, 2001 shake. A lumped mass model is one where the mass of the structure is assumed to be concentrated at discrete points. In our case, the mass is assumed to be concentrated at the floor slabs, which implies that the mass from the inter-story columns is lumped along with the weight of the floor slab. We also assume that the center of rotation for the building is located

at the basement floor level, although is is probably located under (but close to) the basement floor [Jennings, 2000, personal communication]. Figures 3.8 and 3.9 show the mode shapes obtained from the EW and the NS shakes, as well as the proportion that rigid body rotation and translation contribute to the total floor displacements. It is clear from the two figures that the NS mode undergoes significantly more rigid body rotation than the EW mode.

	Mass (10^3 *Kg*)	*Floor Area* (ft^2)	*Live Load* (Kg/ft^2)	*Max. Live Load Mass* (10^3 *Kg*)	*Total Mass* (10^3 *Kg*)
*Floor*1	826	2749	15	41	867
*Floor*2	826	4249	15	64	890
*Floor*3	681	2825*	68*	192	873
*Floor*4	681	2825*	68*	192	873
*Floor*5	681	2825*	68*	192	873
*Floor*6	681	4249	15	64	745
*Floor*7	681	2825*	68*	192	873
*Floor*8	681	2825*	68*	192	873
*Floor*9	681	2825*	68*	192	873
Roof	979	4249	0	0	979
Total	7398			1321	8719

Table 3.3 This table presents the total floor masses for each floor for the lumped mass model. The values for the superstructure for floors 1−roof are from the Millikan structural calculations (minus the live load percentage that are assumed there). The floor areas denoted with an asterisk, are for book storage only, as all the other live loads in that floor are small in comparison. The other floor areas are for library operations, and represent space used in the library similarly to office space. The live loads denoted with an asterisk are from the Millikan structural calculations, and the other live loads are 65% of the *UBC* (1997)'s uniform loads for office space. A percentage of the uniform loads are used as no correction for walls or partitions is used, there is not much furniture in the floors, and approximately 25% of the floor area is utilized as hallways. No live load is used in the roof, as the structural plans account for the mechanical equipment under the dead load calculation. Note that the areas are given in ft^2.

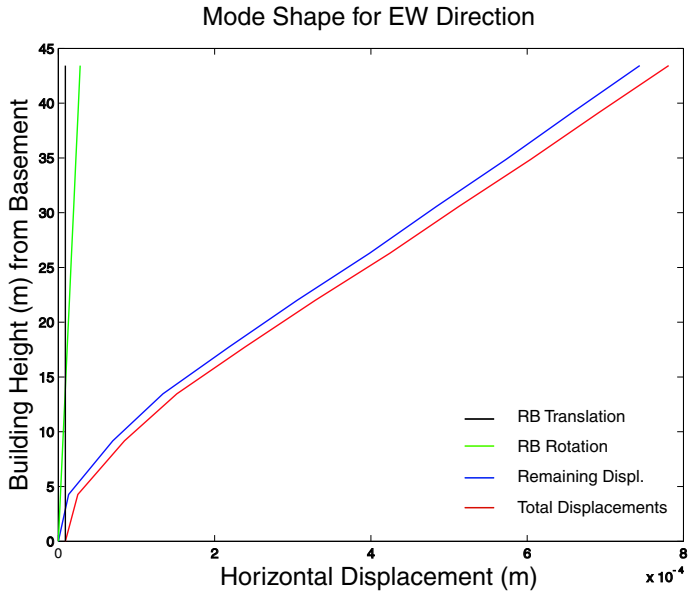

Figure 3.8 Mode shape decomposition for EW shaking. In the legend, RB is an acronym for rigid body. Note that most of the displacements in the EW mode shape are due to internal building deformations and not to rigid body motions.

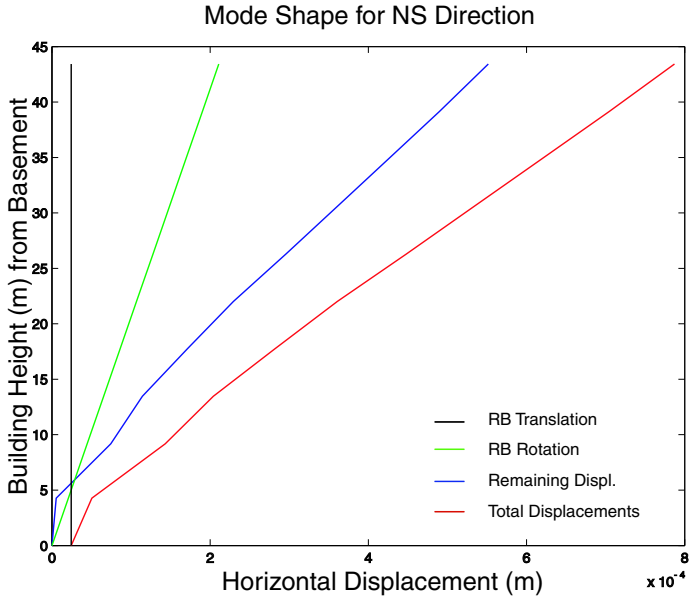

Figure 3.9 Mode shape decomposition for NS shaking. In the legend, RB is an acronym for rigid body. Note that approximately 30% of the displacements are due to rigid body rotations.

Tables 3.4 and 3.5 show the detailed calculations for the maximum applied force, the maximum applied moment, and the total energy per cycle (maximum kinetic energy) for the EW and NS modes.

	Total Displ. (m)	*Mass (10^3 Kg)*	*Height (m)*	*Shear Force, P (10^3 N)*	*Moment, M (10^3 Nm)*	*Kinetic Energy (J)*
*Floor*1	$2.499 * 10^{-5}$	867	4.28	1.1	4.5	0.01
*Floor*2	$8.468 * 10^{-5}$	890	9.17	3.7	33.8	0.16
*Floor*3	$1.516 * 10^{-4}$	873	13.46	6.5	87.2	0.49
*Floor*4	$2.389 * 10^{-4}$	873	17.74	10.2	181.0	1.22
*Floor*5	$3.291 * 10^{-4}$	873	22.02	14.1	309.6	2.31
*Floor*6	$4.242 * 10^{-4}$	745	26.30	15.5	406.7	3.28
*Floor*7	$5.128 * 10^{-4}$	873	30.58	21.9	669.9	5.62
*Floor*8	$6.044 * 10^{-4}$	873	34.86	25.8	900.1	7.80
*Floor*9	$6.918 * 10^{-4}$	873	39.14	29.6	1156.6	10.22
Roof	$7.811 * 10^{-4}$	979	43.43	37.4	1625.1	14.61
Total				165.8	5374.5	45.73

Table 3.4 This table shows the building's kinetic energy (E_{Kin}), as well as the applied force (P) and the applied moment(M) for an East-West experiment. All values other than mass and height are given for the peak values, as they are sinusoidal in nature. The displacement data are acquired from the Mt. Whitney system in Millikan Library. For this experiment, the frequency of excitation is f=1.1133 Hz.

As can be seen from these tables,

$$E_{Kin(EW)} = 45.7\ J \qquad E_{Kin(NS)} = 106.1\ J$$
$$P_{EW} = 1.66E5\ N \qquad P_{NS} = 3.84E5\ N$$
$$M_{EW} = 5.37E6\ Nm \qquad M_{NS} = 1.21E7\ Nm$$

where the subscripts represent the shaking direction at the respective resonant frequency. For the complete details of the accelerometer data, please refer to Appendix A.

	Total Displ. (m)	*Mass (10^3 Kg)*	*Height (m)*	*Shear Force, P (10^3 N)*	*Moment, M (10^3 Nm)*	*Kinetic Energy (J)*
$Floor1$	$5.059 * 10^{-5}$	867	4.28	4.6	19.9	0.12
$Floor2$	$1.433 * 10^{-4}$	890	9.17	13.5	123.8	0.97
$Floor3$	$2.041 * 10^{-4}$	873	13.46	18.9	254.0	1.93
$Floor4$	$2.817 * 10^{-4}$	873	17.74	26.0	462.1	3.67
$Floor5$	$3.608 * 10^{-4}$	873	22.02	33.4	734.7	6.02
$Floor6$	$4.481 * 10^{-4}$	745	26.30	35.4	929.9	7.92
$Floor7$	$5.239 * 10^{-4}$	873	30.58	48.4	1481.5	12.69
$Floor8$	$6.191 * 10^{-4}$	873	34.86	57.2	1995.6	17.72
$Floor9$	$7.044 * 10^{-4}$	873	39.14	65.1	2549.3	22.94
$Roof$	$7.870 * 10^{-4}$	979	43.43	81.6	3544.5	32.12
$Total$				384.1	12095.3	106.14

Table 3.5 This table shows the building's kinetic energy (E_{Kin}), as well as the applied force (P) and the applied moment(M) for a North-South experiment. All values other than mass and height are given for the peak values, as they are sinusoidal in nature. The displacement data are acquired from the Mt. Whitney system in Millikan Library. For this experiment, the frequency of excitation is f=1.6380 Hz.

3.7 Kinetic Energy in a Half-Space and Energy Radiation Estimate

To calculate the average kinetic energy density of the generated wavefield over N periods of oscillation at a particular point in space, the following equation can be employed (*Lay and Wallace*, 1995),

$$e = \frac{\rho}{2NT} \int_0^{NT} \mathbf{V}^2 dt \tag{3.75}$$

where T is the period of one oscillation, and $\mathbf{V}^2$ is the square of the velocity field and is defined by

$$\mathbf{V}^2 = V_R^2 + V_\theta^2 + V_\phi^2 \tag{3.76}$$

To calculate the average kinetic energy density in a volume, Equation 3.75 must be integrated over the half-space volume where the displacement field is not zero. Due to the nature of the displacement field, most of the integrals done here will be in spherical coordinates. However, integrals involving only Rayleigh waves will be carried out in cylindrical coordinates to simplify the math.

The contributions to the velocity field from the different types of generated waves (P, S, Rayleigh) vary with distance from the source due to the different wave velocities, as shown by the leading wavefronts depicted in Figure 3.10. It should again be mentioned that I am only integrating first-order terms, as they represent most of the energy in the generated displacement field. As the integrals are to be performed over $\mathbf{V}^2$ and over a volume, and all the components in the displacement field are independent of each other, the integrals can have different limits from those depicted in Figure 3.10. For example, for V_ϕ^2, the Rayleigh waves and the P waves have no displacements in the ϕ component, and therefore the limits for the distance integral are from $R = 0 \rightarrow V_S NT$. For the purpose of performing the integrals, I will take N to be very large, as the solution derived in the previous sections is valid in the far-field. It will be assumed that the contribution of the near-field terms is small compared to that of the far-field for the large distances and the large number of cycles involved in

the integral ($N \gg 1$). Furthermore, in order to simplify the integration, the integral over the volume where only Rayleigh waves exist, will be performed in cylindrical coordinates to simplify the integral forms involved.

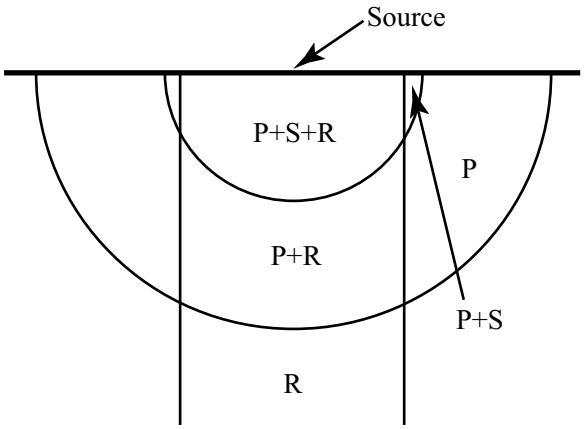

Figure 3.10 Leading displacement field wavefronts for the different radiated waves; Compressional (P), Shear (S), and Rayleigh (R) waves.

Therefore, the energy integral can be separated into multiple integrals over the different components. In the following formulation, the first subscript after the velocity component represents the component being integrated, the subscripts in parentheses indicate which waves are contributing to the integral for the integrated region, and the number subscript corresponds to a region shown in Figure 3.11.

$$
\begin{aligned}
E_{Avg} \;=\; \frac{\rho}{2NT}\Bigg[& \int_{T=0}^{NT}\int_{\phi=0}^{2\pi}\int_{R=0}^{V_P NT}\int_{\theta=0}^{\theta_P} V^2_{R(P+R)(1)}\; R^2\sin\theta\, d\theta\, dR\, d\phi\, dt \;+ \\
& \int_{T=0}^{NT}\int_{\phi=0}^{2\pi}\int_{R=0}^{\frac{V_R NT}{\sin\theta}}\int_{\theta=\theta_P}^{\frac{\pi}{2}} V^2_{R(P+R)(2)}\; R^2\sin\theta\, d\theta\, dR\, d\phi\, dt \;+ \\
& \int_{T=0}^{NT}\int_{\phi=0}^{2\pi}\int_{R=0}^{V_P NT}\int_{\theta=\theta_P}^{\frac{\pi}{2}} V^2_{R(P)(2+3)}\; R^2\sin\theta\, d\theta\, dR\, d\phi\, dt \;- \\
& \int_{T=0}^{NT}\int_{\phi=0}^{2\pi}\int_{R=0}^{\frac{V_R NT}{\sin\theta}}\int_{\theta=\theta_P}^{\frac{\pi}{2}} V^2_{R(P)(2)}\; R^2\sin\theta\, d\theta\, dR\, d\phi\, dt \;+
\end{aligned}
$$

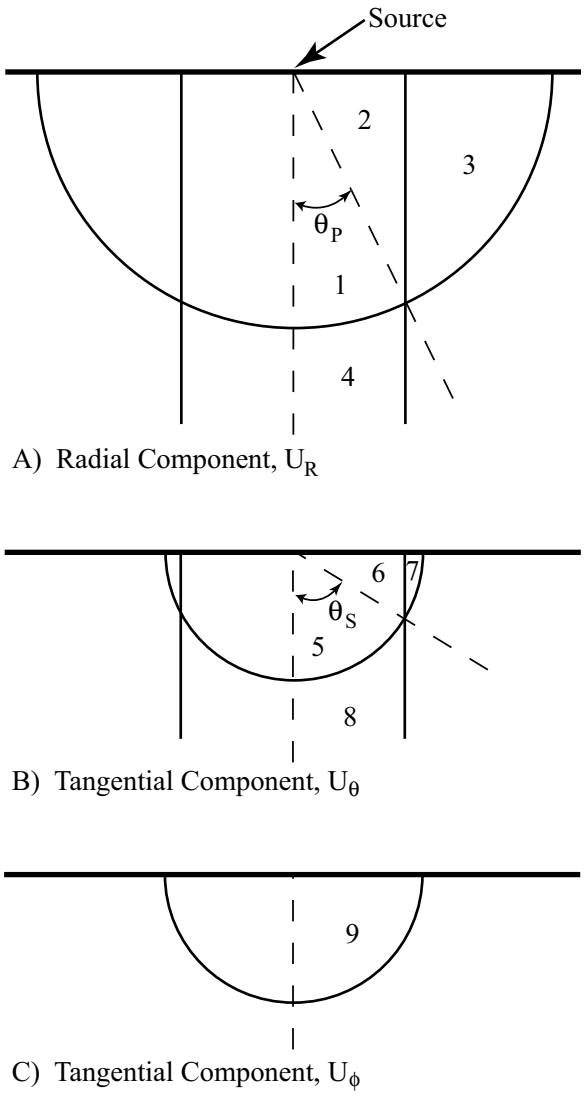

Figure 3.11 Integral partitions over the half-space for the individual displacement components. The numbers in the different regions shown are used to identify which integral in Equation 3.77 corresponds to a particular region of integration for the different displacement field components. A) Radial Component (U_R), B) Tangential Component (U_θ), and C) Tangential Component (U_ϕ).

$$\int_{T=0}^{NT}\int_{\phi=0}^{2\pi}\int_{z=\sqrt{(V_PNT)^2-r^2}}^{\infty}\int_{r=0}^{V_RNT}(V_{r_\alpha}+V_{z_\alpha})^2_{(R)(4)}\;r\,dr\,dz\,d\phi\,dt\;+$$

$$\int_{T=0}^{NT}\int_{\phi=0}^{2\pi}\int_{R=0}^{V_SNT}\int_{\theta=0}^{\theta_S}V^2_{\theta(S+R)(5)}\;R^2\sin\theta\,d\theta\,dR\,d\phi\,dt\;+ \tag{3.77}$$

$$\int_{T=0}^{NT}\int_{\phi=0}^{2\pi}\int_{R=0}^{\frac{V_RNT}{\sin\theta}}\int_{\theta=\theta_S}^{\frac{\pi}{2}}V^2_{\theta(S+R)(6)}\;R^2\sin\theta\,d\theta\,dR\,d\phi\,dt\;+$$

$$\int_{T=0}^{NT}\int_{\phi=0}^{2\pi}\int_{R=0}^{V_SNT}\int_{\theta=\theta_S}^{\frac{\pi}{2}}V^2_{\theta(S)(6+7)}\;R^2\sin\theta\,d\theta\,dR\,d\phi\,dt\;-$$

$$\int_{T=0}^{NT}\int_{\phi=0}^{2\pi}\int_{R=0}^{\frac{V_RNT}{\sin\theta}}\int_{\theta=\theta_S}^{\frac{\pi}{2}}V^2_{\theta(S)(6)}\;R^2\sin\theta\,d\theta\,dR\,d\phi\,dt\;+$$

$$\int_{T=0}^{NT}\int_{\phi=0}^{2\pi}\int_{z=\sqrt{(V_SNT)^2-r^2}}^{\infty}\int_{r=0}^{V_RNT}(V_{r_\beta}+V_{z_\beta})^2_{(R)(8)}\;r\,dr\,dz\,d\phi\,dt\;+$$

$$\int_{T=0}^{NT}\int_{\phi=0}^{2\pi}\int_{R=0}^{V_SNT}\int_{\theta=0}^{\frac{\pi}{2}}V^2_{\phi(S)(9)}\;R^2\sin\theta\,d\theta\,dR\,d\phi\,dt\Bigg]$$

where

$$\theta_P = sin^{-1}\Big(\frac{V_R}{V_P}\Big)\qquad \theta_S = sin^{-1}\Big(\frac{V_R}{V_S}\Big) \tag{3.78}$$

For the time integrals (over N oscillation cycles), the integrals involved are of the following form,

$$\int_0^{NT}\sin^2(\omega t-\alpha)dt=\int_0^{NT}\cos^2(\omega t-\alpha)dt=\frac{NT}{2} \tag{3.79}$$

$$\int_0^{NT}\sin(\omega t-\alpha+\frac{\pi}{4})\sin(\omega t-\alpha-\frac{\pi}{4})dt=\frac{NT}{2} \tag{3.80}$$

$$\int_0^{NT}\sin(\omega t)\cos(\omega t)dt=0 \tag{3.81}$$

and can be performed first to simplify the results. Similarly, the integrals with respect to azimuth (ϕ, the angle along the surface) can be subsequently performed by

$$\int_0^{2\pi} \sin^2\phi \, d\phi = \int_0^{2\pi} \cos^2\phi \, d\phi = \pi \tag{3.82}$$

Substitution of the results from Equations 3.79 and 3.82 into Equation 3.77 yields

$$\begin{aligned}
E_{Avg} \;=\; & \frac{\rho\pi}{4}\Bigg[\int_{R=0}^{V_P NT} \int_{\theta=0}^{\theta_P} V^2_{R(P+R)(1)} \; R^2 \sin\theta \, d\theta \, dR \; + \\
& \int_{R=0}^{\frac{V_R NT}{\sin\theta}} \int_{\theta=\theta_P}^{\frac{\pi}{2}} V^2_{R(P+R)(2)} \; R^2 \sin\theta \, d\theta \, dR \; + \\
& \int_{R=0}^{V_P NT} \int_{\theta=\theta_P}^{\frac{\pi}{2}} V^2_{R(P)(2+3)} \; R^2 \sin\theta \, d\theta \, dR \; - \\
& \int_{R=0}^{\frac{V_R NT}{\sin\theta}} \int_{\theta=\theta_P}^{\frac{\pi}{2}} V^2_{R(P)(2)} \; R^2 \sin\theta \, d\theta \, dR \; + \\
& \int_{z=\sqrt{(V_P NT)^2 - r^2}}^{\infty} \int_{r=0}^{V_R NT} (V_{r_\alpha} + V_{z_\alpha})^2_{(R)(4)} \; r \, dr \, dz \; + \\
& \int_{R=0}^{V_S NT} \int_{\theta=0}^{\theta_S} V^2_{\theta(S+R)(5)} \; R^2 \sin\theta \, d\theta \, dR \; + \\
& \int_{R=0}^{\frac{V_R NT}{\sin\theta}} \int_{\theta=\theta_S}^{\frac{\pi}{2}} V^2_{\theta(S+R)(6)} \; R^2 \sin\theta \, d\theta \, dR \; + \\
& \int_{R=0}^{V_S NT} \int_{\theta=\theta_S}^{\frac{\pi}{2}} V^2_{\theta(S)(6+7)} \; R^2 \sin\theta \, d\theta \, dR \; - \\
& \int_{R=0}^{\frac{V_R NT}{\sin\theta}} \int_{\theta=\theta_S}^{\frac{\pi}{2}} V^2_{\theta(S)(6)} \; R^2 \sin\theta \, d\theta \, dR \; + \\
& \int_{z=\sqrt{(V_S NT)^2 - r^2}}^{\infty} \int_{r=0}^{V_R NT} (V_{r_\beta} + V_{z_\beta})^2_{(R)(8)} \; r \, dr \, dz \; +
\end{aligned} \tag{3.83}$$

$$\int_{R=0}^{V_S NT} \int_{\theta=0}^{\frac{\pi}{2}} V^2_{\phi(S)(9)}\, R^2 \sin\theta \, d\theta \, dR \Bigg]$$

Due to the significant number of integrals involved and the large number of terms to be integrated, instead of presenting all of the integrals, I will only show the types of distance integrals involved. The integrals over θ will not be shown, as they need to be computed numerically (Appendix E) and the integrands are long and complicated. The integrals dependent only on body waves ($V^2_{R(P)}$, $V^2_{\theta(S)}$, $V^2_{\phi(S)}$) involve integrals of the form

$$\int_a^b \frac{1}{R^2} R^2 dR \;=\; R|_a^b \tag{3.84}$$

Integrals involving only Rayleigh waves ($V^2_{R(R)}$, $V^2_{\theta(R)}$) include integrals of the form

$$\int_a^b \frac{1}{r} r dr \;=\; r|_a^b \tag{3.85}$$

$$\int_a^b e^{-2\alpha z} dz \;=\; -\frac{e^{-2\alpha z}}{2\alpha}|_a^b \tag{3.86}$$

The more complicated of the forms includes a mix of a body wave (P or S) and a Rayleigh wave. These integrals include 3 types of integrals, namely

$$\int_a^b \frac{1}{R^2} R^2 dR = R|_a^b \tag{3.87}$$

$$\int_a^b \frac{e^{-2\alpha R\cos\theta}}{R} R^2 dR = -\frac{e^{-2\alpha_1 R\cos\theta}}{4\alpha_1^2 \cos^2\theta}(2\alpha_1 R\cos\theta + 1) \tag{3.88}$$

$$\int_a^b \frac{e^{-\alpha R\cos\theta}\cos(hR - Rk_0\sin\theta)}{R^{\frac{3}{2}}} R^2 dR \tag{3.89}$$

Integrals 3.88 and 3.89 behave like near-field terms, as the integrands decay exponentially with distance. As a result, they are only important near the source, as the integral's contribution with distance quickly diminishes to zero, causing the integral to reach a constant value. The same is true for 3.86, except that the limit closer

to the source is at the P wavefront, and therefore this integrand never takes on any large values. I will ignore these terms, as they can be neglected in the far-field (large N) and due to their constant values, when dividing the total average kinetic energy (E_{Avg}) by the number of cycles of oscillation, the contribution from the integral is negligible.

I calculate the moment, M, the building induces on the soil and the shearing force, P, on the soil's surface for each of the building's natural frequencies in section 3.6 as

$$P_{EW} \approx 1.66E5\ N \qquad P_{NS} \approx 3.84E5\ N$$
$$M_{EW} \approx 5.37E6\ Nm \qquad M_{NS} \approx 1.21E7\ Nm$$

After finding the zeros of $F(\zeta)$ for the soil properties ($\Lambda \approx 1.89$) given in Tables 3.1 (model 1) and 3.2 (model 2), we can achieve an estimate of the building's damping. From the zeros of $F(\zeta)$, it is found that

$$V_R \;=\; 0.9282 V_S$$

Therefore, the integrals in Equation 3.83 can be solved as shown in Appendix E.4, where the appropriate values for a half-space have been used. However, the appendix only calculates the kinetic energy, and therefore the values given there must be multiplied by two to include the potential energy (*Achenbach*, 1993). For model 1 the integrals give that the energy radiated per cycle is

$$E_{EW1} = 0.366\ J \qquad E_{NS1} = 3.984\ J$$

and for model 2

$$E_{EW2} = 0.204\ J \qquad E_{NS2} = 2.224\ J$$

As can be seen from the detailed results presented in Appendix E.4, the generated shear body waves are the largest contributor to the radiated kinetic energy, and the

Rayleigh waves have a negligible contribution. From the radiated energy per cycle, the radiated power is estimated to be

$$\begin{aligned} E_{Rad(EW1)} &= 0.408\,Watts \qquad E_{Rad(NS1)} = 6.526\,Watts \\ E_{Rad(EW2)} &= 0.228\,Watts \qquad E_{Rad(NS2)} = 3.642\,Watts \end{aligned} \tag{3.90}$$

From Section 3.6, we know that the building's kinetic energy per cycle is

$$E_{Kin(EW)} = 45.7\,J \qquad E_{Kin(NS)} = 106.1\,J \tag{3.91}$$

In order to compute the damping due to energy being radiated away from the building, we have to compare the radiated energy with the building's kinetic energy. Using Equation 3.72 in section 3.6 and following the derivation of the logarithmic decrement of damping derived in *Housner and Hudson* (1980), the building's damping can be calculated using the kinetic energy of two successive cycles in free vibration. For the first cycle, the maximum kinetic energy is given by

$$E_{Kin_1} = \frac{1}{2} m\omega^2 x^2 \tag{3.92}$$

and for the second cycle,

$$E_{Kin_2} = \frac{1}{2} m\omega^2 (x - \Delta x)^2 \tag{3.93}$$

where x is the maximum displacement of the first cycle and Δx is the change in maximum displacement between the two cycles. If we calculate the change in kinetic energy (ΔE_{Kin}) and divide it by the total initial kinetic energy (E_{Kin} from Equation 3.91), and furthermore assume that Δx is small with respect to x, we get

$$\frac{\Delta E_{Kin}}{E_{Kin}} \approx 2\frac{\Delta x}{x} \approx 2\delta \tag{3.94}$$

where δ is commonly referred to as the logarithmic decrement of damping. Furthermore, δ can be related to the viscous damping ratio(ξ) by

$$\xi \approx \frac{\delta}{2\pi} \approx \frac{\Delta E_{Kin}}{4\pi E_{Kin}} \tag{3.95}$$

In order to calculate the percentage of damping attributed to the radiated energy per cycle, substitute the computed radiated kinetic energy per cycle for ΔE_{kin}.

$$\begin{aligned} \Delta E_{Kin(EW1)} &= 0.366\ J \qquad \Delta E_{Kin(NS1)} = 3.984\ J \\ \Delta E_{Kin(EW2)} &= 0.204\ J \qquad \Delta E_{Kin(NS2)} = 2.224\ J \end{aligned}$$

Using the values in Equation 3.91, the radiated kinetic energy damping ratios are estimated to be

$$\begin{aligned} \xi_{EW1} &= 0.06\% \qquad \xi_{NS1} = 0.29\% \\ \xi_{EW2} &= 0.04\% \qquad \xi_{NS2} = 0.17\% \end{aligned} \tag{3.96}$$

The observed damping ratios for Millikan Library are computed by fitting a decaying exponential to the peaks of the free amplitude decay of the building displacements, which yields the following damping values

$$\xi_{EW} = 1.63\% \qquad \xi_{NS} = 1.65\% \tag{3.97}$$

As can be seen, the observed damping ratios for Millikan Library are much larger than the estimated radiated kinetic energy values computed here, and are also in general agreement with the other experimental values given in table A:7 (*Bradford et al.* (2004)). Therefore, it may be concluded that the half-space model applied here is not a proper mathematical model, or that processes within the structure are dissipating most of the energy input into the building. The half-space model fails to account for resonances in the soil layers, and therefore an alternative should

be explored. Multi-layer cases will be examined in Chapter 5 by utilizing a Finite Element Model, and it will be shown that the damping values estimated here for the half-space model are in general agreement with those of the Finite Element Models.

Chapter 4

Surface Wave Modelling

For the experiments performed in 1998, the field GPS units provided by SCEC were utilized to obtain precise locations of the portable seismometers. Seismometer sites were chosen throughout Pasadena at locations volunteered by members of the Caltech community, who kindly offered a place in their residence to install a temporary seismometer. As a result, a fairly random distribution of sites was achieved, however, with a concentration in the NW part of Caltech. At the time, it was believed that wavelengths in the order of 600 to 700 meters would be observed, and that errors in the GPS measurements (in the order of few meters) would not have a large influence on the data analysis. After collecting and processing the data, it was found that the observed wavelengths were most likely between 500 and 600 meters, which made the errors from the portable GPS units slightly more important. Furthermore, the measurements did not show the anticipated surface wave like behavior.

It was determined that the possibility existed that significant errors were introduced by inaccuracies in the instrument locations, and as a result, a continuous GPS campaign was performed to confirm and/or correct the seismometer positions. This campaign was carried out in 1999 with the assistance of Mr. Jeff Behr at the USGS who helped determine, through an experimental process, that the necessary accuracy of tens of centimeters could be achieved by continuously recording GPS data for as little as 30 minutes, and furthermore showed me how to process the collected data. However, after repeating the data analysis with the improved seismometer locations, the same inconsistencies in the data remained. As a result, a second set of experi-

ments (which will be referred to as Millikan II) was designed and carried out in the year 2000. The seismometer locations for this test are shown in Figure 4.1. These experiments were designed to explore both the radial and azimuthal radiation patterns close to the building, and all the seismometers were located within the confines of the Caltech campus. The experiments conducted prior to the Millikan II experiments will not be mentioned in the remainder of this thesis and their data will be analyzed at a later date, utilizing the tools and knowledge developed in this thesis.

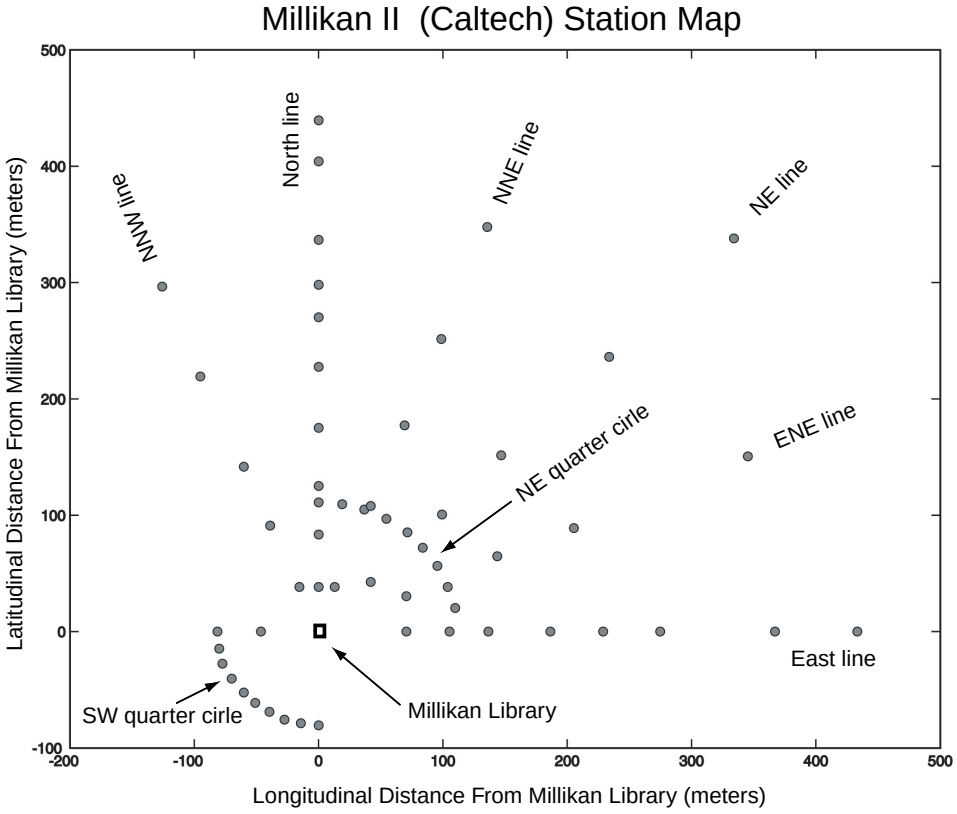

Figure 4.1 Seismometer locations for the Millikan II experiments. The seismometers were set out in different lines and semi-circles to collect data during 6 different set-ups, while the same experiments were replicated for the different seismometer set-ups. Millikan is shown as a square at the origin, while the seismometers that functioned properly during the experiments are depicted as circles.

This chapter describes the procedure and results from performing a linear fit to both the phase and amplitude data collected during the Millikan II experiments.

The linear fit performed in this chapter supposes that the building excites dominant seismic wave phases, as it was expected that the surface waves would dominate the generated wave field.

4.1 Displacement Data from Millikan II Experiments

The waveforms collected from the Millikan II experiments were analyzed in order to determine their maximum amplitude decay with distance for the area surrounding Millikan Library to an extent of approximately 500 m from the source. The experiments were organized such that the seismometers were located in radial lines or in quarter circles originating at the Library's center, and the same experiment was repeated 4 times without modifying the instrument set-up for the duration of the experiment (the difference between experiments being slightly different excitation frequencies and labelled experiment A, B, C, and D) such that the experiment repeatability could be assessed. The obtained decay rates will provide a constraint on the type of waves being observed. Due to the building's location very close to the Earths' surface, it is expected that the Library is in a prime location to excite fundamental mode surface waves. Due to the anticipated generation of surface waves and their smaller geometric spreading rates with distance, they are expected to dominate the waveforms, and a linear regression on the signal's amplitude should suffice to find the amplitude decays.

The following procedure was used to compute the particle velocity decay for the seismometer locations in the Millikan II experiments, and was carried out using Matlab:

For each experiment, i.e., shaking direction and excitation frequency

For each seismometer line

For each component

1) The particle velocities are sorted by distance.

2) The logarithm of the velocities and the logarithm of the distance from the source are fit using a linear regression of the form $ax + b$.

3) If it is assumed that the amplitude decay comes from geometric spreading, the a term provides the amplitude decay.
For the small distances being considered, this is a good assumption. as the waves have undergone less than 3 cycles in the crust.

End

End

End

If fundamental mode Rayleigh and Love waves are being recorded, the expected amplitude decays should be close to $R^{-0.5}$. The Rayleigh waves will be observed on the radial and the vertical components, while the Love waves will be measured on the transverse component. However, as can be seen from the theoretical radiation patterns derived in chapter 3, there are some source-receiver geometries where it is expected that the waveforms on certain components will be very small, as the instruments are nodal to certain waves. Figure 4.2 is a visual example of the procedure described above for the calculation of the particle velocity decays. Tables 4.1 through 4.3 list all the decay values calculated for each of the experiments performed in radial lines and for each component for an East-West shake, while Tables 4.4 through 4.6 list the decay values for a North-South shake, and lastly, Tables 4.7 through 4.9 for a Torsional shake. It should be noted that the torsional motion present in the EW shake are minimal, as the EW natural frequency is well separated from that of the torsional natural frequency, even though the shaker is set-up to excite torsional modes when shaking in the EW direction. For those receiver lines theoretically located on

nodes for surface waves, an asterisk(*) has been inserted in the cells that are expected to show nodal amplitudes.

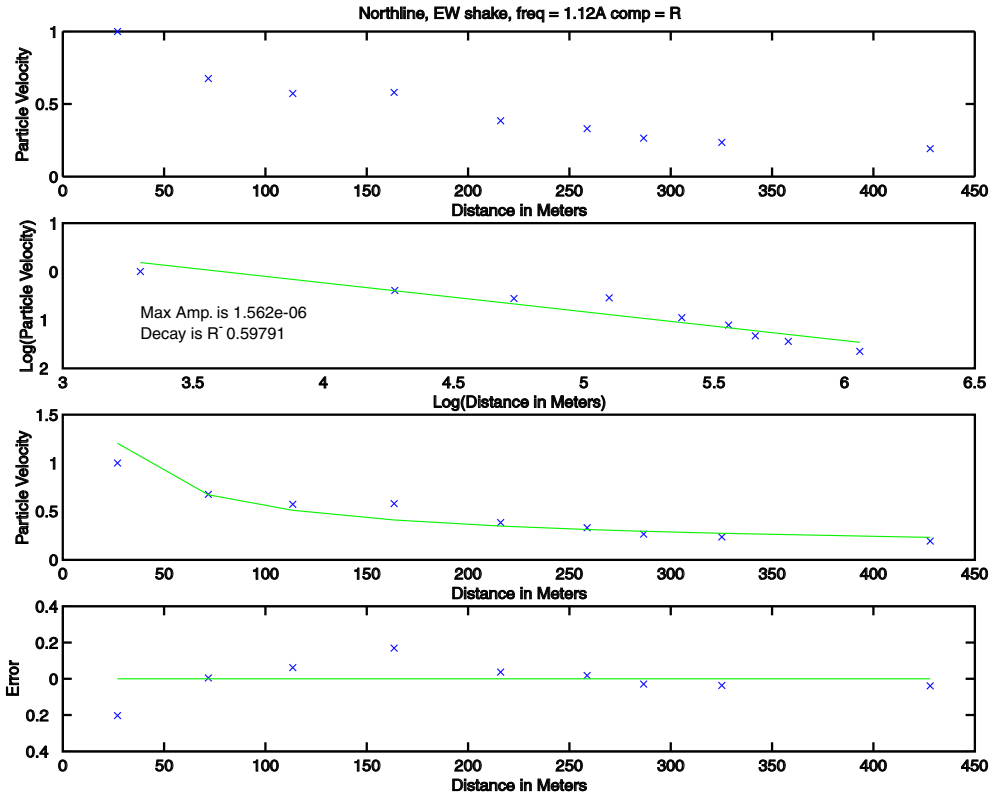

Figure 4.2 Amplitude decay curve for the North-line setup, East-West shaking, in the radial direction, for experiment A. The top plot shows the normalized particle velocity (to the highest velocity measurement for the experiment, 1.562E-6 m/s for the case shown) data plotted versus distance. The second plot from the top shows the logarithmic values for both the normalized particle velocity and distance for the same data as in the top plot, and the solid line is the best fitting RMS line to the data. The resulting particle velocity decay curve is proportional to $R^{-0.598}$. The third plot shows the data from the top plot, together with the best fitting amplitude decay curve. Finally, the bottom plot shows the difference between the best fitting curve and the data.

Tables 4.1 through 4.9 show that there appear to be no consistent particle decay values for the different seismometer lines, nor any correlation between values for the radial and vertical components. However,from these tables and from Figure 4.3

	Experiment A	*Experiment B*	*Experiment C*	*Experiment D*
East line	−1.1804	−1.1683	−1.1729	−1.1434
ENE line	−0.5073	−0.5222	−0.5443	−0.5458
North line	−0.5979*	−0.6040*	−0.6188*	−0.6110*
NE line	−0.9082	−0.9030	−0.8851	−0.8831
NNE line	−1.0427	−1.0360	−1.0420	−1.0715
NNW line	−0.6405	−0.6276	−0.6273	−0.6227

Table 4.1 Particle velocity decay values for the radial component for an East-West Shake, in the form of R^n, where n is given in the table. A * is inserted for cells that are expected to show nodal amplitudes.

	Experiment A	*Experiment B*	*Experiment C*	*Experiment D*
East line	−0.5011*	−0.3480*	−0.5218*	−0.2505*
ENE line	−0.8056	−0.8144	−0.8255	−0.8256
North line	−0.9085	−0.9075	−0.9021	−0.9198
NE line	−0.9490	−0.9513	−0.9553	−0.9565
NNE line	−0.8645	−0.8598	−0.8679	−0.9017
NNW line	−0.9015	−0.9138	−0.9199	−0.9234

Table 4.2 Particle velocity decay values for the transverse component for an East-West Shake, in the form of R^n, where n is given in the table. A * is inserted for cells that are expected to show nodal amplitudes.

	Experiment A	*Experiment B*	*Experiment C*	*Experiment D*
East line	−0.5832	−0.5851	−0.5778	−0.5787
ENE line	−0.2653	−0.2585	−0.2456	−0.2483
North line	−0.0201*	−0.0241*	−0.0348*	−0.0210*
NE line	−0.4966	−0.4970	−0.4934	−0.4945
NNE line	−0.4421	−0.4489	−0.4586	−0.4800
NNW line	−0.6517	−0.6405	−0.6293	−0.6091

Table 4.3 Particle velocity decay values for the vertical component for an East-West Shake, in the form of R^n, where n is given in the table. A * is inserted for cells that are expected to show nodal amplitudes.

	Experiment A	*Experiment B*	*Experiment C*	*Experiment D*
East line	-0.5949^*	-0.6021^*	-0.5944^*	-0.5844^*
ENE line	-0.9457	-0.9374	-0.9192	-0.9141
North line	-0.8358	-0.8591	-0.8541	-0.8555
NE line	-0.6785	-0.6748	-0.6588	-0.6550
NNE line	$+0.5466$	$+0.5402$	$+0.4080$	$+0.4007$
NNW line	-0.9001	-0.8992	-0.8979	-0.8970

Table 4.4 Particle velocity decay values for the radial component for a North-South Shake, in the form of R^n, where n is given in the table. A * is inserted for cells that are expected to show nodal amplitudes.

	Experiment A	*Experiment B*	*Experiment C*	*Experiment D*
East line	-0.7570	-0.7426	-0.7582	-0.7645
ENE line	-0.5125	-0.5174	-0.5198	-0.5199
North line	-0.3446^*	-0.3652^*	-0.3458^*	-0.3547^*
NE line	-0.6589	-0.6619	-0.6687	-0.6706
NNE line	-0.8576	-0.8600	-0.8474	-0.8454
NNW line	-1.1173	-1.1132	-1.1074	-1.1049

Table 4.5 Particle velocity decay values for the transverse component for a North-South Shake, in the form of R^n, where n is given in the table. A * is inserted for cells that are expected to show nodal amplitudes.

	Experiment A	*Experiment B*	*Experiment C*	*Experiment D*
East line	-0.5297^*	-0.5098^*	-0.5351^*	-0.5466^*
ENE line	-0.4937	-0.5018	-0.5061	-0.5078
North line	-0.6357	-0.6560	-0.6552	-0.6563
NE line	-0.5369	-0.5348	-0.5352	-0.5353
NNE line	-0.8119	-0.8176	-0.8262	-0.8284
NNW line	-0.8205	-0.8189	-0.8245	-0.8253

Table 4.6 Particle velocity decay values for the vertical component for a North-South Shake, in the form of R^n, where n is given in the table. A * is inserted for cells that are expected to show nodal amplitudes.

	Experiment A	*Experiment B*	*Experiment C*	*Experiment D*
East line	−0.3218	−0.3422	−0.3729	−0.3800
ENE line	−0.8051	−0.8038	−0.8044	−0.7979
North line	−0.9854	−0.9802	−0.9851	−0.9529
NE line	−0.3638	−0.3240	−0.3074	−0.2425
NNE line	−0.4160	−0.4264	−0.4286	−0.4349
NNW line	−1.3076	−1.2809	−1.2826	−1.2623

Table 4.7 Particle velocity decay values for the radial component for a Torsional Shake, in the form of R^n, where n is given in the table.

	Experiment A	*Experiment B*	*Experiment C*	*Experiment D*
East line	−0.8039	−0.8034	−0.8025	−0.8033
ENE line	−0.4619	−0.4791	−0.4792	−0.4938
North line	−0.2932	−0.2876	−0.3001	−0.2772
NE line	−0.7005	−0.7056	−0.7038	−0.7074
NNE line	−0.4103	−0.4174	−0.4138	−0.4236
NNW line	−0.6053	−0.6163	−0.6153	−0.6249

Table 4.8 Particle velocity decay values for the transverse component for a Torsional Shake, in the form of R^n, where n is given in the table.

	Experiment A	*Experiment B*	*Experiment C*	*Experiment D*
East line	−0.4368	−0.4463	−0.4430	−0.4449
ENE line	−0.9810	−0.9780	−0.9650	−0.9564
North line	−0.3855	−0.3777	−0.3952	−0.3635
NE line	−0.7628	−0.7689	−0.7630	−0.7697
NNE line	−1.3826	−1.4056	−1.3982	−1.4205
NNW line	−1.1216	−1.1200	−1.1192	−1.1149

Table 4.9 Particle velocity decay values for the vertical component for a Torsional Shake, in the form of R^n, where n is given in the table.

	Experiment A	*Experiment B*	*Experiment C*	*Experiment D*
East line	−0.6354	−0.6432	−0.6193	−0.6057
ENE line	−0.3797	−0.4232	−0.4770	−0.4765
North line	−1.1713*	−1.1880*	−1.1722*	−1.3000*
NE line	−1.0158	−0.9978	−0.9493	−0.9455
NNE line	−1.4385	−1.4092	−1.4257	−1.4999
NNW line	−0.8070	−0.7779	−0.7725	−0.7490

Table 4.10 Particle velocity decay values for the radial component for an East-West Shake with the data close to the building removed, in the form of R^n, where n is given in the table. A * is inserted for cells that are expected to show nodal amplitudes.

	Experiment A	*Experiment B*	*Experiment C*	*Experiment D*
East line	−1.0265*	−0.7564*	−0.9055*	−0.3807*
ENE line	−0.6770	−0.7050	−0.7383	−0.7388
North line	−0.8664	−0.8619	−0.8536	−0.8538
NE line	−1.0088	−1.0130	−1.0275	−1.0309
NNE line	−1.0484	−1.0449	−1.0757	−1.1869
NNW line	−0.8751	−0.9018	−0.9096	−0.8978

Table 4.11 Particle velocity decay values for the transverse component for an East-West Shake with the data close to the building removed, in the form of R^n, where n is given in the table. A * is inserted for cells that are expected to show nodal amplitudes.

	Experiment A	*Experiment B*	*Experiment C*	*Experiment D*
East line	−0.4831	−0.4953	−0.4655	−0.4762
ENE line	−0.1792	−0.4232	−0.4770	−0.1499
North line	+0.2772*	+0.2645*	+0.3091*	+0.1699*
NE line	−0.3119	−0.3101	−0.3035	−0.3066
NNE line	−0.0759	−0.0681	−0.0982	−0.1547
NNW line	+0.0277	+0.0342	+0.0445	+0.0538

Table 4.12 Particle velocity decay values for the vertical component for an East-West Shake with the data close to the building removed, in the form of R^n, where n is given in the table. A * is inserted for cells that are expected to show nodal amplitudes.

	Experiment A	*Experiment B*	*Experiment C*	*Experiment D*
East line	-0.5730^*	-0.5124^*	-0.5738^*	-0.5959^*
ENE line	-0.9948	-0.9900	-0.9700	-0.9648
North line	-0.7311	-0.8293	-0.8469	-0.8367
NE line	-0.5776	-0.5653	-0.5415	-0.5375
NNE line	-0.0521	-0.0841	-0.0102	-0.0008
NNW line	-0.9166	-0.9169	-0.9079	-0.8970

Table 4.13 Particle velocity decay values for the radial component for a North-South Shake with the data close to the building removed, in the form of R^n, where n is given in the table. A * is inserted for cells that are expected to show nodal amplitudes.

	Experiment A	*Experiment B*	*Experiment C*	*Experiment D*
East line	-0.3998	-0.4207	-0.4015	-0.4005
ENE line	-0.6085	-0.5853	-0.5542	-0.5493
North line	$+0.0650^*$	$+0.0627^*$	$+0.0610^*$	$+0.0674^*$
NE line	-0.3629	-0.3641	-0.3736	-0.3801
NNE line	-1.0339	-1.0412	-1.0103	-1.0075
NNW line	-0.3937	-0.4293	-0.3088	-0.2943

Table 4.14 Particle velocity decay values for the transverse component for a North-South Shake with the data close to the building removed, in the form of R^n, where n is given in the table. A * is inserted for cells that are expected to show nodal amplitudes.

	Experiment A	*Experiment B*	*Experiment C*	*Experiment D*
East line	-0.2713^*	-0.4953^*	-0.2794^*	-0.2449^*
ENE line	-0.9948	-0.0236	-0.9700	-0.9141
North line	-0.1657	$+0.0627$	-0.1624	-0.1503
NE line	-0.2212	-0.2175	-0.2168	-0.2130
NNE line	-0.2221	-0.2190	-0.2304	-0.2329
NNW line	-0.1787	-0.1739	-0.1796	-0.1792

Table 4.15 Particle velocity decay values for the vertical component for a North-South Shake with the data close to the building removed, in the form of R^n, where n is given in the table. A * is inserted for cells that are expected to show nodal amplitudes.

	Experiment A	*Experiment B*	*Experiment C*	*Experiment D*
East line	+0.0051	+0.0135	+0.0279	+0.0258
ENE line	−0.7566	−0.8038	−0.7536	−0.7424
North line	+0.0769	+0.0663	+0.0925	+0.1029
NE line	+0.9356	+0.9119	+1.0303	+1.1430
NNE line	−0.3847	−0.3923	−0.3895	−0.3940
NNW line	−1.1553	−1.1160	−1.1228	−1.0946

Table 4.16 Particle velocity decay values for the radial component for a Torsional Shake with the data close to the building removed, in the form of R^n, where n is given in the table.

	Experiment A	*Experiment B*	*Experiment C*	*Experiment D*
East line	−0.6546	−0.6476	−0.6395	−0.6378
ENE line	−0.2583	−0.2786	−0.2802	−0.3000
North line	−0.0094	−0.0198	−0.0062	−0.0375
NE line	−0.5637	−0.5695	−0.5651	−0.5721
NNE line	−0.5613	−0.5761	−0.5820	−0.6027
NNW line	−0.3503	−0.3661	−0.3644	−0.3772

Table 4.17 Particle velocity decay values for the transverse component for a Torsional Shake with the data close to the building removed, in the form of R^n, where n is given in the table.

	Experiment A	*Experiment B*	*Experiment C*	*Experiment D*
East line	−1.0992	−1.1340	−1.1259	−1.1108
ENE line	−0.4613	−0.3608	−0.3542	−0.2499
North line	−0.7399	−0.7576	−0.6997	−0.8002
NE line	−0.3843	−0.3857	−0.3621	−0.3442
NNE line	−0.6546	−0.6561	−0.6437	−0.6269
NNW line	−0.4721	−0.4755	−0.4743	−0.4712

Table 4.18 Particle velocity decay values for the vertical component for a Torsional Shake with the data close to the building removed, in the form of R^n, where n is given in the table.

which shows the results for the 4 similar experiments (A through D) for the same instrument line, it can be seen that the values between experiments for each individual seismometer line are very consistent. Figure 4.3 also shows that there are only small differences in the measured displacements, which can be attributed to slightly different excitation frequencies; small variations in background noise levels; and inherent errors in the displacement measuring technique. The differences in the displacements may be due to the slightly different excitation frequencies, but if this were the case and standing modes are being observed instead of the direct radiated waves, the resulting displacement field from a standing mode could be different for similar frequencies, depending on the complexity and the spatial distribution of the wave reflectors causing the standing mode. Furthermore, different frequencies will also generate similar patterns with distance for radiated waves, which should have a consistent decay trend not observed in the data, and therefore this is probably not the most likely source of the observed error differences. Small variations in noise levels interact with the amplitude estimation technique, and these two error sources cannot be separated from each other. However, it is expected that the background noise levels only experience small variations due to the experiment times (after midnight) and the small time span between the individual experiments. Therefore, since the generated displacement patterns are consistent for similar experiments, this suggests that the difference in the displacements most likely can be attributed to the background noise levels and/or errors in estimating the displacements.

The displacement measurements are repeatable for similar experiments, but it's interesting to note that they are inconsistent for the different instrument configurations (as the decay rates are not always similar for the different experiments). Possibly, two different effects are being measured and compared, namely near and far-field terms. In order to investigate the dependence on distance and remove the largest part of the near-field term, it will be assumed that instruments closer to the building's geometric center will contain a greater near-field signal. This will be shown to be a fair assumption in Chapter 5. Therefore, removing the data from the instruments closest to the building, also removes the heaviest contribution to the measured particle velocities in

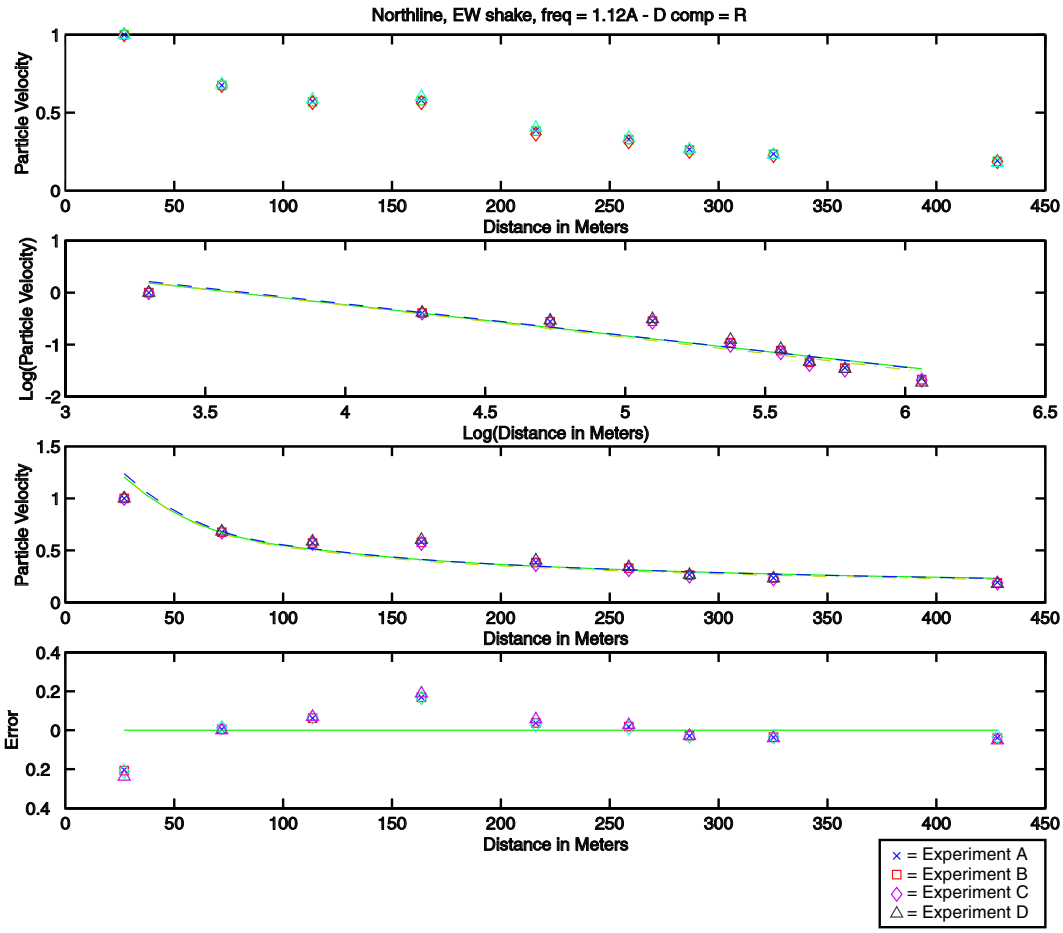

Figure 4.3 Overlayed amplitude decay curve for the North-line setup, East-West shaking, radial direction, experiments A - D. The top plot is the normalized measured particle velocity data plotted versus distance. The second plot from the top is the logarithm (for both the particle velocity and distance) of the top plot, and the four lines are the best fitting lines to the data. The resulting amplitude decays are given in table 4.1. The third plot shows the same data as the top plot, but the best fitting amplitude decay curves are also shown. The bottom plot shows the difference between the best fitting curves and the data.

the near-field. For the purpose of studying the near-field dependence, the waveforms collected from distances closer than 150 meters (100 meters if the seismometer line only includes 4 instruments, in order to keep 3 data points) from the building were discarded, and the analysis performed for Tables 4.1 and 4.9 was repeated. If there is an interaction between the near and far-field terms, the decay rates should differ

from the previously calculated ones. Similar patterns are observed from Tables 4.10 through 4.18, as were seen from the original data-set, although there is some variation between the values and sometimes the variation is quite large. There is a repeatability for similar experiments with the same seismometer configuration, but no correlation is observed for different source and receiver arrangements. For example, for both the EW and NS shakes, it is expected that the NNE and NNW seismometer lines should show a very similar displacement decay, but it is clear from the tables that the results do not exhibit the symmetry expected from the theoretical displacement fields in Chapter 3.

Another possible explanation is that there are dipping structures in the area, but this seems unlikely, as it is expected that dipping layers originate from the mountains to the North, and that the layers dip to the South. However, the expected slopes in the 600 m over which the experiment takes place should be negligible as they should be quite gentle due to their alluvial fan origins.

The layers would also be fairly stable in the East-West direction, and therefore the amplitude values for the NNE and NNW lines should be similar and theoretically indistinguishable, independent of the direction of shaking. Furthermore, the radiation patterns present for the quarter-circles covered by the two seismometer set-ups used is very clear, and the displacements are presented in polar plots in Figures 4.4 and 4.5. Note that the displacements are not corrected for distance, and as a result, those of the SW quadrant are larger, as the instruments are closer to the building than those of the NE quadrant. This leaves 3-D effects from a heterogeneous medium as an alternative, and because of the repeatability of the various data points along a particular seismometer line, this option should be explored to explain the variations in displacement at the different seismometer locations. However, due to the frequencies involved (natural frequencies of Millikan), 3-D effects cannot be explored at this point, as there are no current velocity models that possess the appropriate frequency resolution. As an alternative, in Chapter 5, a 1-D layered velocity model will be tested to see how well the synthetic data fits the measured displacements.

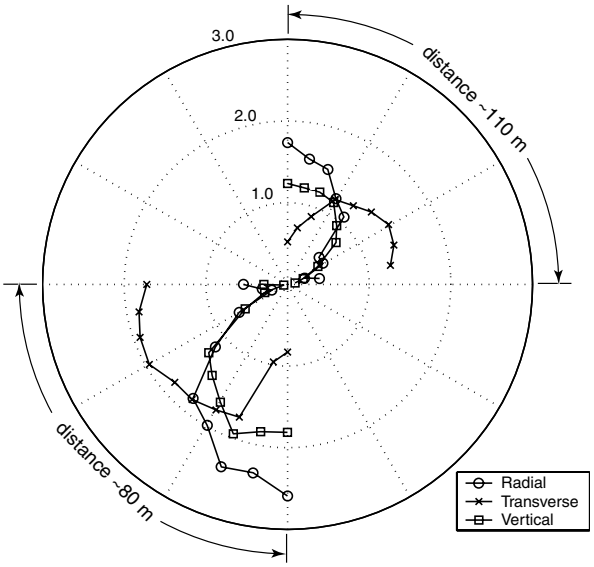

Figure 4.4 Polar plot of the NE and SW quarter circle displacements for all 3 components for an NS shake. The radial component displacements are shown in circles, the transverse component in x's, and the vertical component in squares. Displacements are in microns and not normalized for distance. The displacement scale is in the NW quadrant. The NE quadrant stations are 110 meters from Millikan Library's center, while the SW quadrant stations are 80 meters away. Note that there is a radiation pattern present for all components.

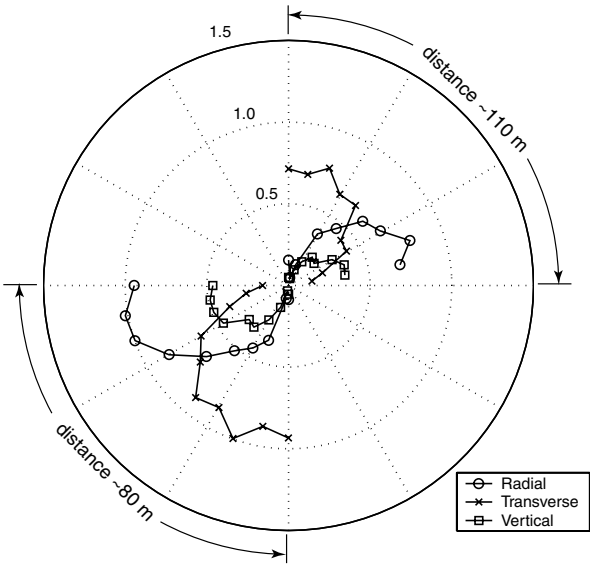

Figure 4.5 Same as Figure 4.4, except for an EW shake.

4.2 Phase Data from Millikan II Experiments

The same data used in Section 4.1 was also analyzed to determine phase velocities for the area surrounding Millikan Library. Similarly to the previous section, an assumption is made that the surface waves will dominate the generated wave field. As a result, a linear regression on the relative waveform phases should produce the phase velocity for the collected data.

The following loop utilizing this procedure was used to accomplish the linear regressions:

For each experiment

For each seismometer line

For each component (Radial, Transverse, and Vertical)

1) The data are sorted by distance, and the initial phase values are restricted to be within $-\pi$ and π.

2) An initial and lower bound wavelength for the waves being investigated is assumed.

3) Phase velocities are computed for the data points in space using this wavelength, with the building's center as the zero phase value.

4) The data phase values are unwrapped by taking into account the distance from the building's center and the assumed wavelength.

5) The theoretical and the unwrapped phase values are individually subtracted. If the difference between the two values is greater than $\pm\pi$, the difference is corrected to be within $\pm\pi$ by either adding or subtracting a factor of 2π.

6) The Root Mean Square (RMS) error is computed for all the points in a particular line.

7) The procedure is repeated for a slightly longer wavelength.

End

After the loop is completed, the wavelength with the least error is the best fitting wavelength, and by multiplying the wavelength by

the frequency of excitation, the phase velocity is computed.

End

End

As can be seen from Tables 4.19 to 4.36, the phase velocity values obtained are stable for similar experiments for a particular seismometer line. Furthermore, the difference for experiments with large variations in the values comes from competing local minima, similar to the ones shown in Figure 4.6. It should be noted that most of the plots have clear global minima, and that the case shown in Figure 4.6 is a worst-case scenario. Furthermore, for the particular case shown in this figure, the transverse component is located on a node for the EW shake, and the phase data could be unreliable. However, the scatter shown for the transverse component is consistent for similar experiments, and this further demonstrates the repeatability of the collected waveforms, as the data is also repeatable for instruments located on nodal lines. Therefore, it can be assumed that the observed waveforms are not dominated by noise, and that they are reliable (as are the measurements made from them).

The measured relative waveform phases lead to the supposition that there may be superimposed surface wave modes, or that 3-D effects are important for the problem being studied. The presence of multiple modes might also explain the large error between the measured and the best-fitting linear phases, as a constant phase velocity should not be expected to fit the data in this case. Furthermore, this could explain why the calculated phase velocities differ for different seismometer setups, as both the seismometer spacing and the distance between measurements have an influence on the linear fit.

Similarly to the previous section, the waveforms collected for stations at distances less than 150 meters from the building were removed (100 meters for instrument lines containing only 4 instruments), to minimize the near-field effects. The results of these linear fits are provided in Tables 4.28 through 4.36. The phase velocity values

	Experiment A	*Experiment B*	*Experiment C*	*Experiment D*
East line	1026	591	533	967
ENE line	824	836	836	832
North line	989	995	952	1069
NE line	691	683	683	683
NNE line	747	724	730	707
NNW line	622	626	630	633

Table 4.19 Phase velocities in meters/second computed for the radial component for an East-West Shake

	Experiment A	*Experiment B*	*Experiment C*	*Experiment D*
East line	1211	581	1704	1123
ENE line	725	723	731	731
North line	545	546	547	544
NE line	530	529	531	832
NNE line	548	547	553	555
NNW line	501	501	500	498

Table 4.20 Phase velocities in meters/second computed for the transverse component for an East-West Shake

	Experiment A	*Experiment B*	*Experiment C*	*Experiment D*
East line	1708	767	688	1549
ENE line	1128	1143	1171	1170
North line	1102	1114	1057	1240
NE line	1029	1039	1067	1069
NNE line	1186	1232	1312	1485
NNW line	910	940	967	1034

Table 4.21 Phase velocities in meters/second computed for the vertical component for an East-West Shake

	Experiment A	*Experiment B*	*Experiment C*	*Experiment D*
East line	567	513	560	493
ENE line	570	567	564	567
North line	565	566	565	565
NE line	794	309	308	310
NNE line	605	604	608	611
NNW line	477	476	480	482

Table 4.22 Phase velocities in meters/second computed for the radial component for a North-South Shake

	Experiment A	*Experiment B*	*Experiment C*	*Experiment D*
East line	510	474	505	448
ENE line	537	534	534	536
North line	512	512	512	511
NE line	578	269	271	270
NNE line	478	481	482	483
NNW line	492	497	492	493

Table 4.23 Phase velocities in meters/second computed for the transverse component for a North-South Shake

	Experiment A	*Experiment B*	*Experiment C*	*Experiment D*
East line	544	509	539	474
ENE line	719	716	716	718
North line	642	638	638	638
NE line	314	315	315	316
NNE line	648	647	648	651
NNW line	520	519	523	524

Table 4.24 Phase velocities in meters/second computed for the vertical component for a North-South Shake

	Experiment A	*Experiment B*	*Experiment C*	*Experiment D*
East line	540	458	535	572
ENE line	571	572	572	571
North line	490	516	482	517
NE line	286	290	250	289
NNE line	318	935	919	949
NNW line	566	575	573	572

Table 4.25 Phase velocities in meters/second computed for the radial component for a Torsional Shake

	Experiment A	*Experiment B*	*Experiment C*	*Experiment D*
East line	540	587	535	569
ENE line	527	526	528	527
North line	456	456	457	457
NE line	460	461	464	463
NNE line	460	466	466	465
NNW line	449	457	455	456

Table 4.26 Phase velocities in meters/second computed for the transverse component for a Torsional Shake

	Experiment A	*Experiment B*	*Experiment C*	*Experiment D*
East line	528	451	528	565
ENE line	755	765	767	779
North line	602	603	601	609
NE line	578	584	582	587
NNE line	596	605	606	611
NNW line	546	561	557	562

Table 4.27 Phase velocities in meters/second computed for the vertical component for a Torsional Shake

	Experiment A	*Experiment B*	*Experiment C*	*Experiment D*
East line	1567	523	466	1257
ENE line	809	817	809	806
North line	1066	1069	985	1103
NE line	694	681	678	684
NNE line	848	795	789	740
NNW line	661	660	665	671

Table 4.28 Phase velocities in meters/second computed for the radial component for an East-West Shake with the data close to the building removed.

	Experiment A	*Experiment B*	*Experiment C*	*Experiment D*
East line	1503	512	432	1725
ENE line	695	687	699	700
North line	434	434	434	423
NE line	507	508	508	511
NNE line	515	517	524	521
NNW line	502	494	490	484

Table 4.29 Phase velocities in meters/second computed for the transverse component for an East-West Shake with the data close to the building removed.

	Experiment A	*Experiment B*	*Experiment C*	*Experiment D*
East line	1708	633	560	1725
ENE line	1414	1426	1480	1474
North line	1664	1664	1667	1658
NE line	1057	1069	1054	1058
NNE line	1437	1617	1670	1663
NNW line	1102	1142	1197	1313

Table 4.30 Phase velocities in meters/second computed for the vertical component for an East-West Shake with the data close to the building removed.

	Experiment A	*Experiment B*	*Experiment C*	*Experiment D*
East line	552	478	542	444
ENE line	580	567	551	551
North line	601	490	494	491
NE line	794	258	257	257
NNE line	587	588	598	600
NNW line	503	504	508	510

Table 4.31 Phase velocities in meters/second computed for the radial component for a North-South Shake with the data close to the building removed.

	Experiment A	*Experiment B*	*Experiment C*	*Experiment D*
East line	534	471	524	427
ENE line	545	534	544	546
North line	527	523	524	523
NE line	578	238	238	239
NNE line	503	502	513	515
NNW line	528	525	546	549

Table 4.32 Phase velocities in meters/second computed for the transverse component for a North-South Shake with the data close to the building removed.

	Experiment A	*Experiment B*	*Experiment C*	*Experiment D*
East line	699	601	681	521
ENE line	787	716	771	770
North line	689	676	669	669
NE line	314	271	272	272
NNE line	699	700	710	710
NNW line	549	548	554	557

Table 4.33 Phase velocities in meters/second computed for the vertical component for a North-South Shake with the data close to the building removed.

	Experiment A	*Experiment B*	*Experiment C*	*Experiment D*
East line	540	413	526	588
ENE line	558	559	561	560
North line	243	399	240	397
NE line∗	267	271	264	273
NNE line	361	714	710	741
NNW line	543	550	552	555

Table 4.34 Phase velocities in meters/second computed for the radial component for a Torsional Shake with the data close to the building removed.

	Experiment A	*Experiment B*	*Experiment C*	*Experiment D*
East line	556	599	544	606
ENE line	527	528	528	530
North line	428	426	427	423
NE line	295	294	297	298
NNE line	481	489	490	488
NNW line	483	487	487	491

Table 4.35 Phase velocities in meters/second computed for the transverse component for a Torsional Shake with the data close to the building removed.

	Experiment A	*Experiment B*	*Experiment C*	*Experiment D*
East line	558	425	542	613
ENE line	839	858	855	865
North line	529	532	521	524
NE line	335	579	579	580
NNE line	580	585	585	583
NNW line	529	536	536	539

Table 4.36 Phase velocities in meters/second computed for the vertical component for a Torsional Shake with the data close to the building removed.

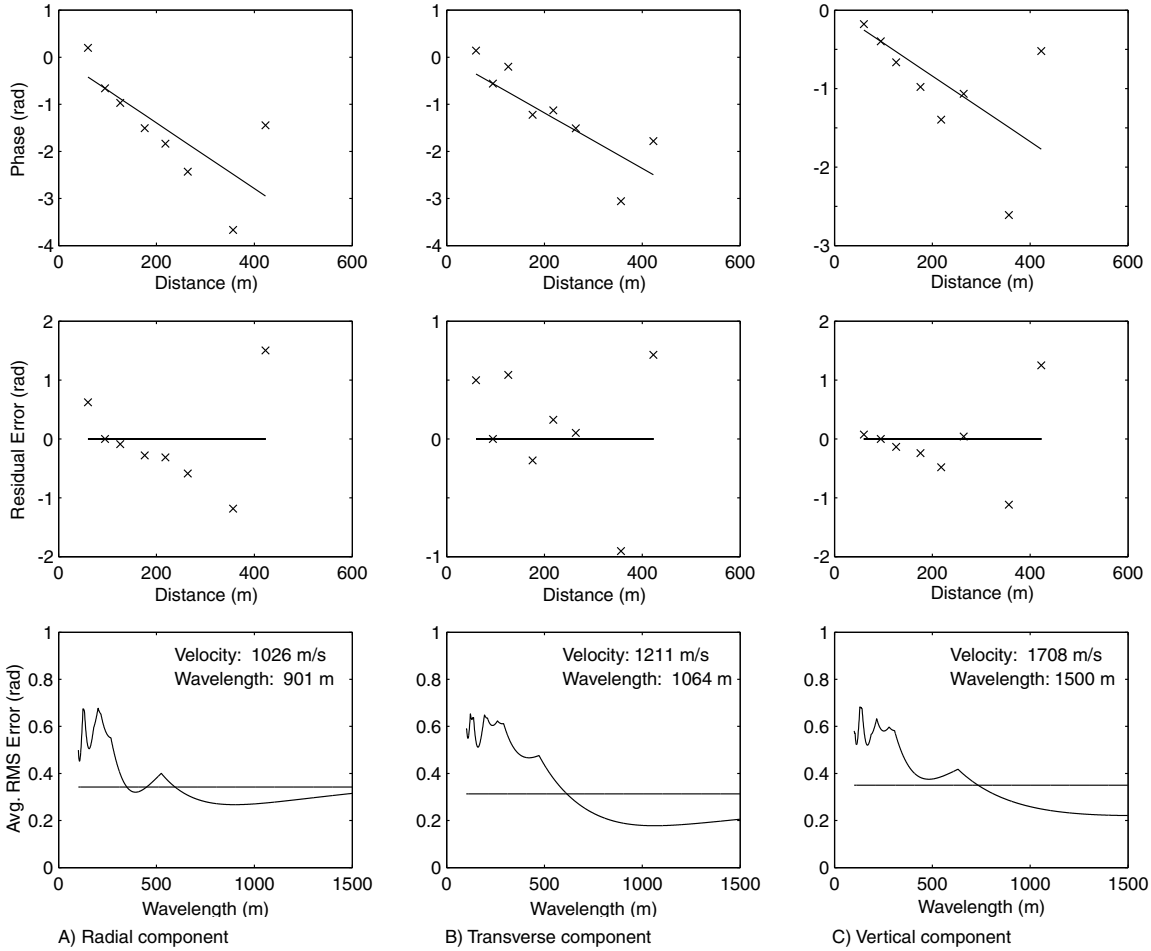

Figure 4.6 Phase velocity minimization curves for an East-West shake recorded along the east line. The phase data shown are for the first shake (A). Shown are the radial, transverse, and vertical components. Sub-figures A and C show worst case scenarios for the linear fits, as there are outliers in the data.

calculated from the data of all of the seismometers and those obtained after removing the data for the closest instruments are very similar, which is incompatible with the observed displacements being due to the interference of multiple surface wave modes. The good agreement between these results also supports that there is no interaction between near and far-field waves, as otherwise the measured phase velocities would be different for the two cases.

4.3 Conclusions

The observed similarity between the waveform data for experiments with the same seismometer set-ups and shaking directions, shows that the observations are real. Therefore a suitable explanation should be provided for the data. The phase velocities measured for the different seismometer set-ups are consistent with a lack of interaction between near and far-field waves. From these same calculations, it can also be seen that the predominant phase velocities are between 500 and 600 m/s. The linear phase assumption and monotonically decaying amplitudes with distance from the source do not fit the observations well, as the fundamental surface wave model used is too simplistic and cannot explain the variations in displacements from site to site, including the increase in amplitude as the distance from the station to the source increases (Figures 4.2, 4.3, and 5.1).

Various hypotheses for the origin of the amplitude variations are presented in this chapter, however, all but 3-D structure effects can be discarded as being too simplistic. Furthermore, due to the lack of appropriate velocity models for the frequencies in question, computer modelling of these effects is not a realistic approach to solving the problem at this time. Instead, in Chapter 5, a Finite Element Code (FEM) will be used to compute synthetics and to estimate the energy radiation from Millikan Library. To accomplish this, a 1-D velocity model derived in Section 5.1 is used as input for the FEM code. While this approach will not resolve all of the major inconsistencies of the observed waveforms with the generated synthetics, it will provide insight into the problem while providing a good estimate of the building's energy radiation.

Chapter 5

Finite Element Model Results

The waveforms collected from the experiments performed on the Caltech campus, shown as "Millikan II" in Figure 4.1, contain certain characteristics, such as amplitude increases with distance, which cannot be explained by a half-space model. Figures 4.2 and 5.1 show some of these amplitude variations for EW and NS shakes, as described in Chapter 4, along a line of instruments directly North or East of the library. These figures also show that the generated displacements can be reproduced extremely well for each of the four different experiments. As the bottom plot in Figure 5.1 shows, this is true even for theoretically nodal seismometer locations and components.

Luco et al. (1975) performed similar experiments to those carried out for this thesis. Their instrument configuration is shown in Figure 5.3, and the corresponding displacements (normalized by the theoretical surface wave decay rate) for three lines (denoted by the letters a, b, and c in both figures) are presented in Figure 5.4. As in Figure 5.1, Figure 5.4 shows the amplitude variations with distance for different instrument lines, but here the station locations are sparsely spaced and thus undersample the variations more clearly observed in the experimental set-up on the Caltech campus.

In order to model these spatial amplitude variations close to the structure and to estimate the radiation damping of the building, the Finite Element Code (FEC) of *Aagaard* (1999) is used. The FEC utilizes absorbing boundary conditions to simulate an infinite layered medium. Sinusoidal point forces on nodes are used to simulate the forces that the building exerts on the ground. The validity of the modelling

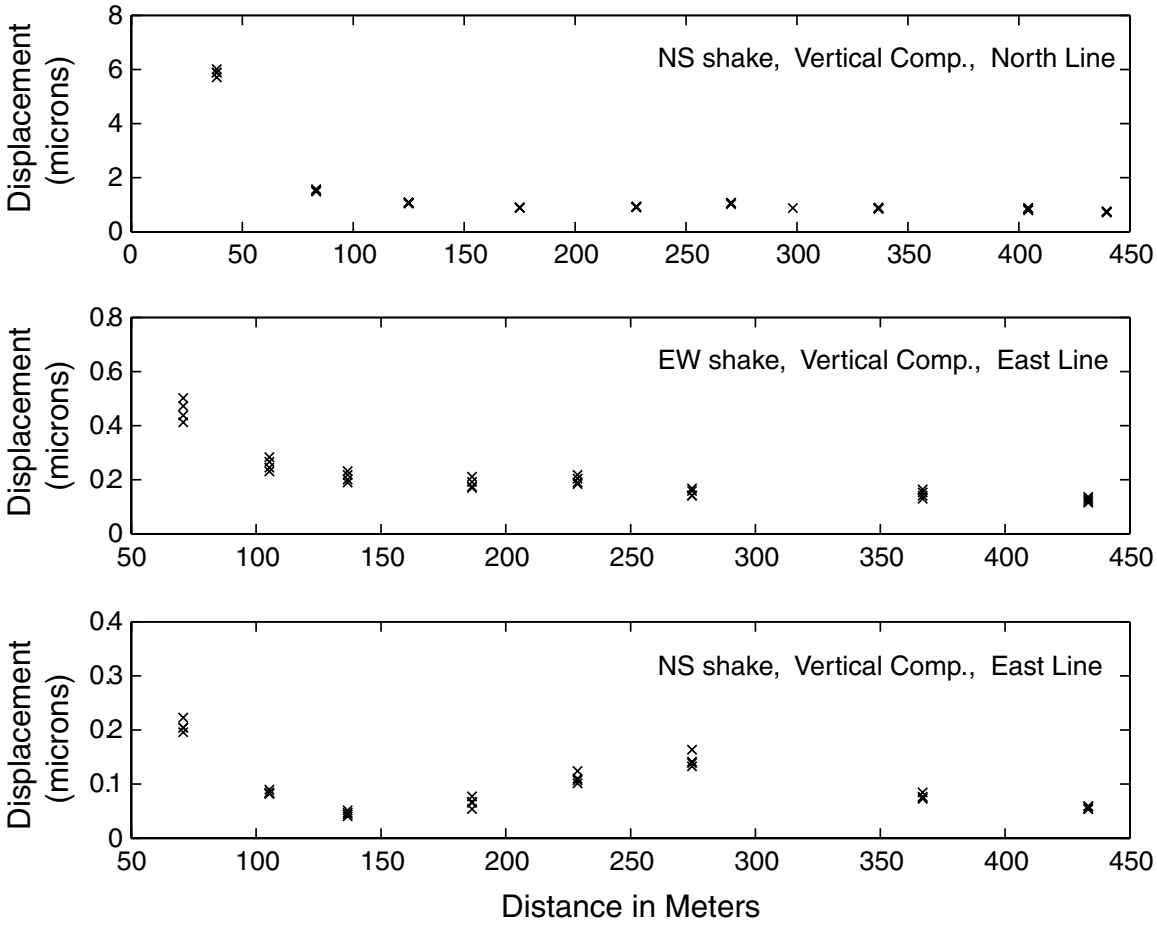

Figure 5.1 All the panels show the maximum displacements for the vertical component for the four experiments performed for each shake. The top panel shows displacements for a NS shake along a NS line of instruments, the middle panel for an EW shake along an EW line of instruments, and the bottom panel for a NS shake for an EW line of instruments. Note our ability to replicate the data and the amplitude increases with increasing distance from the library.

of the forces that the building exerts on the ground with point forces is explored in Section 5.2. By tracking the energy dissipated by the absorbing boundaries, the radiated energy from the applied forces can be estimated. Furthermore, tetrahedral elements are used to model the soil, and to speed up the computation, the element size increases with depth in steps depending on layer velocity. The domain used in the FEC encompasses a region 3 km long, 3 km wide, and 1.5 km deep, as shown

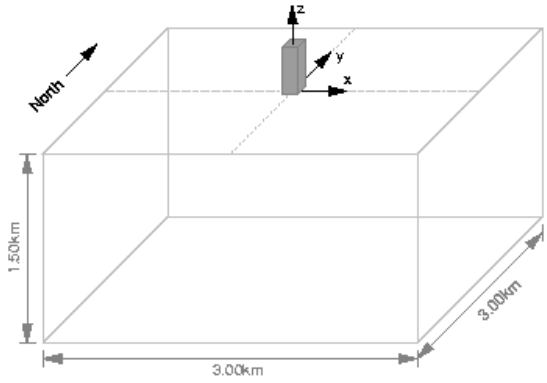

Figure 5.2 Geometry used for the Finite Element Code. The gray rectangular box shown depicts the location of Millikan Library on the model, and point forces are substituted at the bottom of it when the model is run.

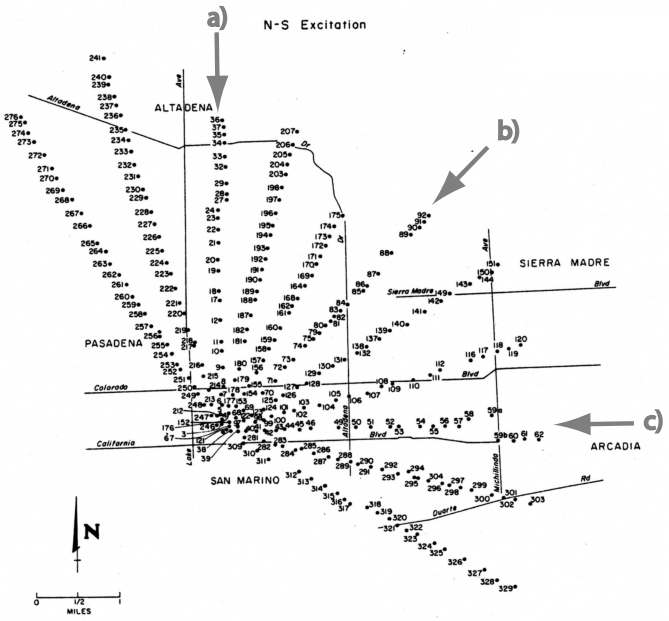

Figure 5.3 Locations of measurements for experiments performed by *Luco et al.* (1975). The letters a, b, and c refer to the lines for which results are presented in Figure 5.4. Millikan Library is located just North of California Blvd. where lines a and c intersect. Figure from *Luco et al.* (1975).

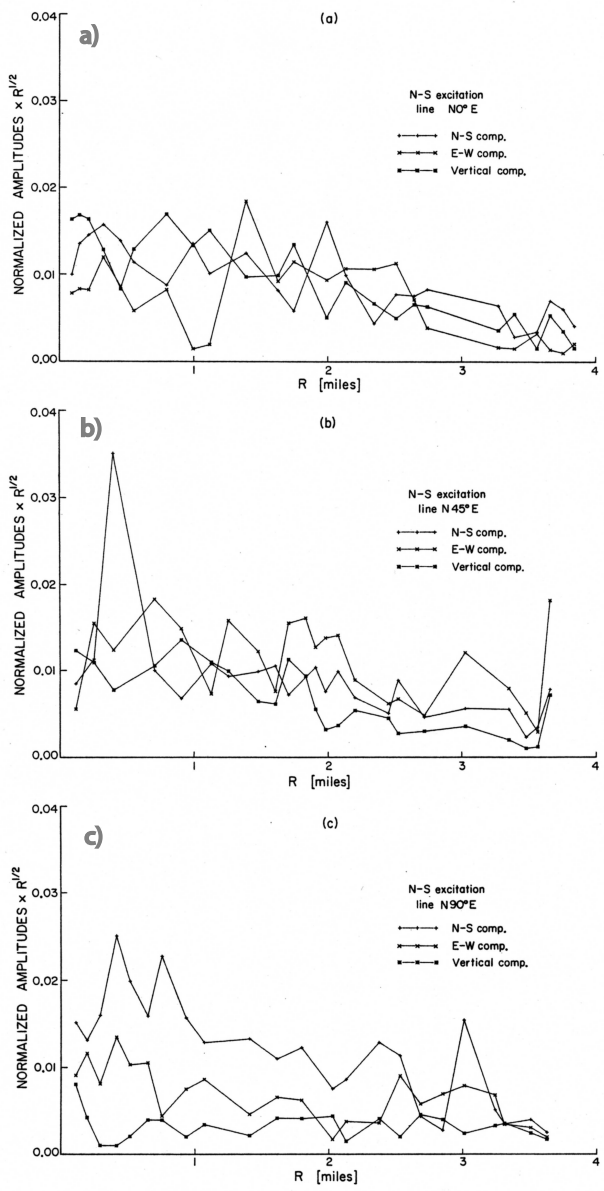

Figure 5.4 Displacements along lines a) $N0^oE$, b) $N45^oE$, and c) $N90^oE$ for a NS shake (see Figure 5.3). The displacements shown have been normalized by a surface wave decay rate of $R^{-0.5}$. Note that the data decays at a rate faster than that assumed, and that the displacements oscillate (not monotonically decreasing) in a manner similar to that of the data presented in Figure 5.1. Figure from *Luco et al.* (1975).

in Figure 5.2. The forces are applied at the model's center on the surface nodes as described in the Section 5.2. For a detailed description of the code, refer to *Aagaard* (1999).

5.1 Velocity Models

To obtain an accurate velocity model for the Pasadena area, a literature search was carried out, which produced relevant technical reports by *Shannon & Wilson and Associates* (1966a,b,c), and *Duke and Leeds* (1962) that focus on sites in the Los Angeles region and incorporate borehole measurements from various locations in and around Pasadena to estimate soil densities and velocities. *Shannon & Wilson and Associates* (1966a,b) include data from a 130 m deep borehole located approximately 60 meters SW of Millikan Library (located South of Arms Laboratory and East of Robinson Laboratory). *Duke and Leeds* (1962) include a velocity model for a site on the Caltech campus near the Athenaeum building, located East of the library. Data from much shallower boreholes around Caltech was also obtained from Caltech's Architectural and Engineering Services Department courtesy of Architect Elvin L. Nixon, for various buildings located around Millikan Library. Furthermore, the results of a refraction survey routinely performed for a class at Caltech (CE 180), which takes place approximately 100 meters NE of Millikan Library, are incorporated in the soil properties for the surficial 3 meters. However, this layer is too thin to be incorporated into a Finite element model as it would require very small elements, increasing the computation time significantly, and is only included for completeness. *Shannon & Wilson and Associates* (1966b) also report that the water level under Millikan Library is estimated to be at a depth of approximately 73 meters. The material properties from these sources are summarized and compiled into a single velocity model shown in Table 5.1.

Table 5.1 is very detailed, and due to computational constraints, the velocity model has to be simplified. It is not feasible to run a FEC with a very small node spacing, as the computation times involved would be very large due to the small time

$Depth(m)$	$Density(Kg/m^3)$	$V_p(m/s)$	$V_s(m/s)$
$0-3$	1748	306	220
$3-7$	1907	673	310
$7-31$	1907	673	322
$31-97$	1957	1421	502
$97-113$	2065	1794	666
$113-413$	2065	1894	680
$half-space$	2500	5505	2258

Table 5.1 Material properties for soil under Millikan Library from literature search.

steps required. Instead, the velocity model was modified to the linearly interpolated material properties shown in Table 5.2.

$Depth(m)$	$Density(Kg/m^3)$	$V_p(m/s)$	$V_s(m/s)$
0	1907	673	322
112	2065	1894	680
321	2065	1894	680
577	2500	5505	2258
1500	2500	5505	2258

Table 5.2 Material properties used for the first test of the Finite Element Code (FEC). There is a linear interpolation between the given data points, and this model will be referred to as the "Smooth" model.

Furthermore, velocity models were also obtained using the Neighbourhood Algorithm of *Sambridge* (1999a,b) and forward modelling with the Green's function method of *Hisada* (1994, 1995). *Gueguen et al.* (2000) have successfully modelled the pull-out tests (an experiment where the top of a structure is displaced from its resting position and released instantaneously) of a model structure at the Volvi test site located near Thessaloniki, Greece, for distances closer than 50 meters from the source using the Green's function method of *Hisada* (1994, 1995). In this work, the Green's function code was able to match the shape of the generated displacements

very well, however, the predicted amplitudes varied by up to 50% from the measured ones. These amplitude differences may be due to inaccurate force estimates (from the model structure used) or soil velocity differences between the real Earth and their velocity model. The latter is more probable, as the force estimates are easier to constrain than the small 3-D velocity structure variations that can affect the observed amplitudes.

Due to the possibility that the estimated forces can be inaccurate, to emphasize the fitting of the shape of the measured displacements over their absolute amplitudes, an error function for normalized displacements is used in this study. At this stage, it should be clarified that since the observation points and the FEC nodes are usually not located at the same distance from the source, a polynomial is used to fit the synthetics and to interpolate both the phase and amplitude at the locations of the observations. For the displacement plots shown at the end of the chapter, the node amplitude values are also provided by simple dots, to qualitatively show the reader the adequacy of the polynomials used. From now on in this chapter, the interpolated data points will be referred to as either the predicted or synthetic data points or waveforms, where as the results from the experiments will be referred to as the observed data points or waveforms. The displacement errors between the predicted and the observed waveforms are calculated for the six non-nodal components of the EW and the NS radial lines shown in Figure 4.1 for both shaking directions. The mean displacement error, E_A, is computed by averaging the six Root Mean Squared (RMS) errors for each normalized component line. The waveform and synthetic with the largest amplitudes for each line are normalized to 1, and the remainder of the data points are normalized accordingly. The ratio of the maximum data amplitude to the maximum synthetic amplitude is called the normalizing factor. Subsequently, the synthetics for each line are re-normalized to obtain the lowest RMS error. These normalizations generate a normalizing factor for each component in each line, and a mean normalizing factor (N_F) is computed from the average of the individual factors.

The phase velocities of the radiated signal are independent of force magnitude and only depend on velocity structure. Therefore, the synthetics' phase difference with

those of the measured waveforms at each station, is a real measure of the differences in velocity between the soil and the model. To eliminate some errors due to the finite size of the building and the point forces used in the model, the phase error between the data and synthetics is calculated relative to the first instrument in any one of the instrument lines. Subsequently, the mean phase error, E_P, is computed from the average of the six relative RMS errors for the non-nodal components of the radial lines. The mean model error, E_T, is then computed for a velocity model by:

$$E_T = E_P + 2\pi E_A$$

where the normalized total amplitude error is multiplied by a factor of 2π to make the phase and amplitude errors similar in amplitude. Then, the Neighbourhood Algorithm, in conjunction with the *Hisada* (1994, 1995) code to forward model synthetics, were used to find the best-fitting velocity models utilizing only the previously mentioned normalized total displacement error and the total phase error. Various runs were performed for each set-of parameters by implementing different model error schemes (eg. phase error only, amplitude error only, and the above mentioned combination), where the initial velocity model parameters were set according to plausible and realistic properties. Since only relatively few waveforms are available, it was found that only a limited number of variables can be resolved. If more than 6 variables are specified, the model does not converge on any solution. As a result, the various layer densities were fixed to be those of Table 5.1, and the density for layer 2 was chosen to be either 1957 or 2065 Kg/m^3 for the different runs. Moreover, the half-space properties were chosen from the same table, with the exception of the shear wave speed, which was modified to be that of the equivalent Poisson solid ($\nu = 0.25$, $\lambda = \mu$, $V_P = \sqrt{3}V_S$). This was done, as the half-space velocity was first determined by approximating it from other sources, but it was later found that *Duke and Leeds* (1962) also provides an estimate for it which is close to the Poisson solid value, but never mentions the source of the data. This estimate, together with the results from the Neighbourhood Algorithm for the top layers led to the modification of the half-

space to the value of a Poisson solid. The following are variables to be determined by the Neighbourhood Algorithm: Layer 1 thickness, V_P, V_S; Layer 2 thickness, V_P, V_S. For the second layer, the obtained ratio for V_P and V_S is very close to that of a Poisson solid, and for simplicity it is assumed that the second layer is a Poisson solid. Tables 5.3 and 5.4 summarize the two solutions obtained for the optimal 2 layer velocity models.

$Depth(m)$	$Density(Kg/m^3)$	$V_p(m/s)$	$V_s(m/s)$
45	1907	710	376
375	1957	1410	814
1500	2500	5505	3178

Table 5.3 Material properties obtained from the use of the Neighbourhood algorithm for the first of the two converging solutions. There is no linear interpolation between the given data points, as this model is a layered model. This model will be referred to as model Layer2A.

$Depth(m)$	$Density(Kg/m^3)$	$V_p(m/s)$	$V_s(m/s)$
45	1907	830	440
375	1957	1590	843
1500	2500	5505	3178

Table 5.4 Material properties obtained from the use of the Neighbourhood algorithm for the second of the two converging solutions. There is no linear interpolation between the given data points, as this model is a layered model. This model will be referred to as model Layer2B.

5.2 Point Force Validation

To verify that the point forces used provide accurate displacements and energy estimates, a test is performed were the forces are distributed among 9 nodes (distributed force scenario) instead of the 1 node for the horizontal force and the 2 nodes for the

couple (point force scenario, even though point couple requires two forces at two different nodes). When the 9 node distributed force scenario is used, there is a complete symmetry for the model. This is not the case when the point force scenario is used, as 2 nodes are required for the applied couple. Due to the need for two nodes, the first is chosen to be at the model's geometric center and the second node is either to the East or North of the first node for an EW or a NS shake, respectively. For the distributed force scenario, extra nodes are added at the center of the model (as shown in Figure 5.5) such that the nodes where the forces are applied are 25 m apart, while the rest of the surface elements remain in a very similar configuration to the mesh used in the point force scenario. This node positioning in turn creates an equivalent building area 4 times larger than the actual floor area of Millikan Library. The shear force (P) and overturning moment (M) were distributed amongst the 9 nodes in a manner proportional to the tributary area of the node (total element area connected to the node), as shown in Figure 5.5. Moreover, as this is only a test, it will only be performed for an EW shake, as the results should be similar for the NS shake.

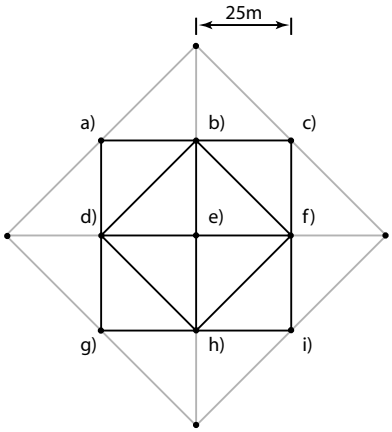

Figure 5.5 Distributed node locations for source. Dark lines delineate the larger building floor plan, whereas the actual floor plan is $\frac{1}{4}$ of the size. Node spacing for source are 25 m.

Assuming uniform shear stress, τ_{xx}, from the horizontal displacements for the area covered by the new building "floor plan", and utilizing the node distance, l, as a

length scale, the total shear force is

$$P = 4\tau_{xx} l^2$$

The shear force at each node is then equal to the sum over its elements of the product of the shear stress and the tributary area for the node, resulting in the following horizontal node forces

$$P_x^{a,c,g,i} = \frac{1}{24} P$$

$$P_x^{b,d,e,f,h} = \frac{1}{6} P$$

For the calculation of the vertical forces to apply to the nodes, it is assumed that the vertical stress, σ_{zz}, varies linearly with distance from the centerline and the moment arm is $2l$. The total moment associated with the vertical stress is

$$M = \frac{4}{3} \sigma_{zz,m} l^3$$

where $\sigma_{zz,m}$ is the maximum stress at the EW edges for an EW shake. For an EW shake, due to symmetry, it is known that the total vertical force at nodes b,e, and h is zero. The vertical force at each of the remaining nodes is then equal to the sum over its elements of the product of the vertical stress and the tributary area for the node, which results in the following forces for the nodes

$$F_z^{b,e,h} = 0$$

$$F_z^{a,c,g,i} = \frac{3M}{32l}$$

$$F_z^{d,f} = \frac{5M}{16l}$$

The total forces for an EW shake were applied to the model as either a horizontal point force and a vertical force couple or the distributed force case described above. This was done for the various force scenarios described in the list below, utilizing the velocity model given in Table 5.3. In the following list, as mentioned before, "point moment" refers to two vertical point forces applied at two adjacent nodes, and the force is a horizontal shear force. The amplitudes of the applied force and moment are computed using the method shown in Section 3.6, and to compute the vertical forces applied at the nodes, divide the moment by the node spacing.

- Point Force and Point Moment together
- Point Force only
- Distributed Force only
- Point Moment only
- Distributed Moment only

The resulting displacements along EW and NS lines in the model are presented in Figures 5.6 and 5.7. As can be clearly seen, the point forces generate very similar displacements to those of the distributed forces. Furthermore, the displacements from the shear force are significantly larger than those of the overturning moment, and generate the overall pattern in the observed displacement field, as is shown in Figure 5.7. This is true for both the EW and NS shaking directions, as the ratio of moment to shear force is approximately 30 for both cases. Moreover, these figures also show the extent for which the point forces directly influence the nodes at which the forces are applied and those directly adjacent to them (the very near-field). It is found that nodes closer than 150 meters to the model's geometric center are directly influenced by the applied point forces. As a result, any data points within 150 meters of the source are discarded. It is unfortunate that this distance is so large, as it forces us to discard a significant portion of our data points, and limits 4 out of 6 lines to 2 seismometers per line. Since the East and North instrument lines used the most

instruments and are the longest, these are the only two lines that are used to compute the errors described in the previous and following section.

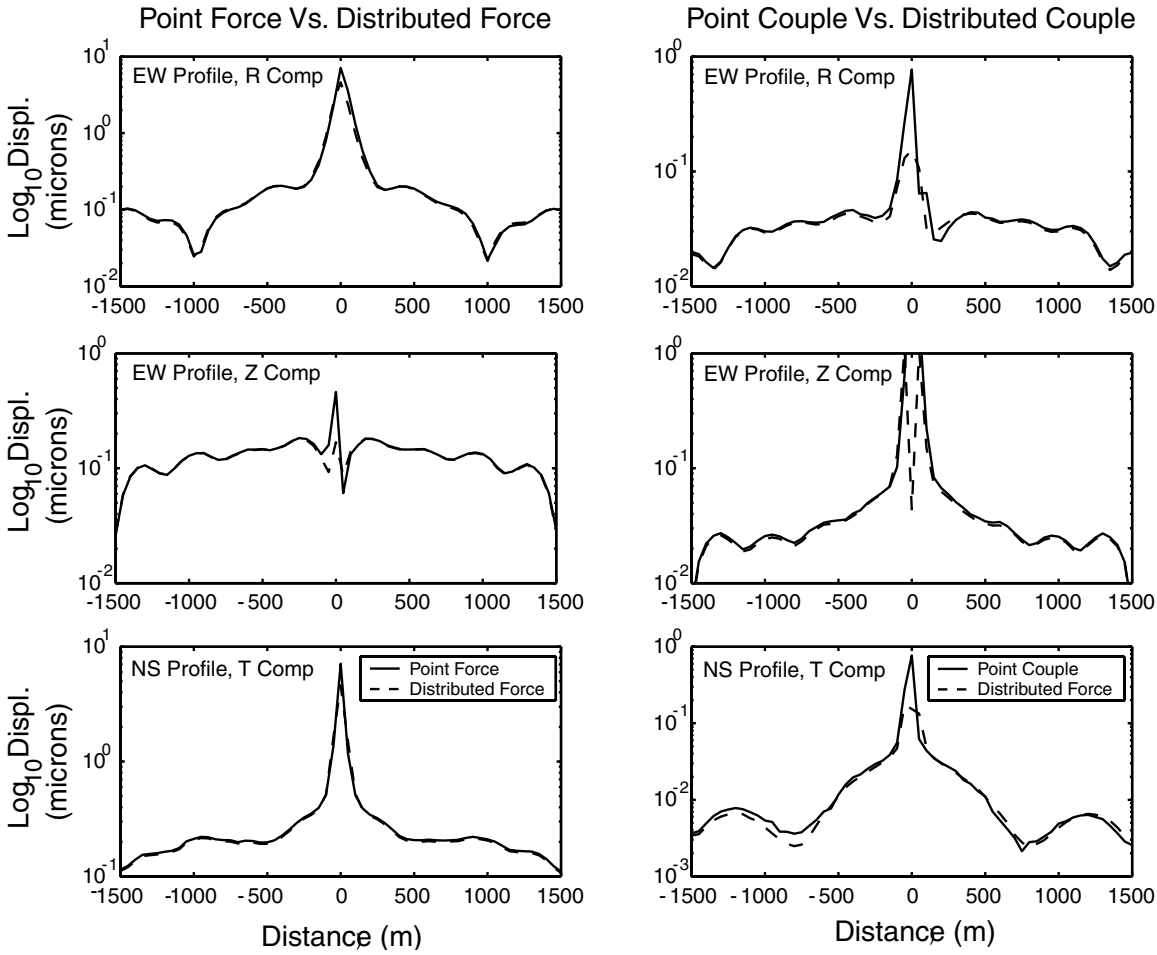

Figure 5.6 Displacement comparisons for point forces vs. distributed forces as described in the text for an equivalent EW shake. The left 3 plots present the computed displacements from the FEC for a point force scenario and a distributed force scenario, whereas the right 3 plots show them for a point couple and a distributed couple. The top 2 plots on each side show the non-nodal component displacements for a complete EW profile passing through the model's geometric center, while the bottom plot shows the displacements for an equivalent NS profile.

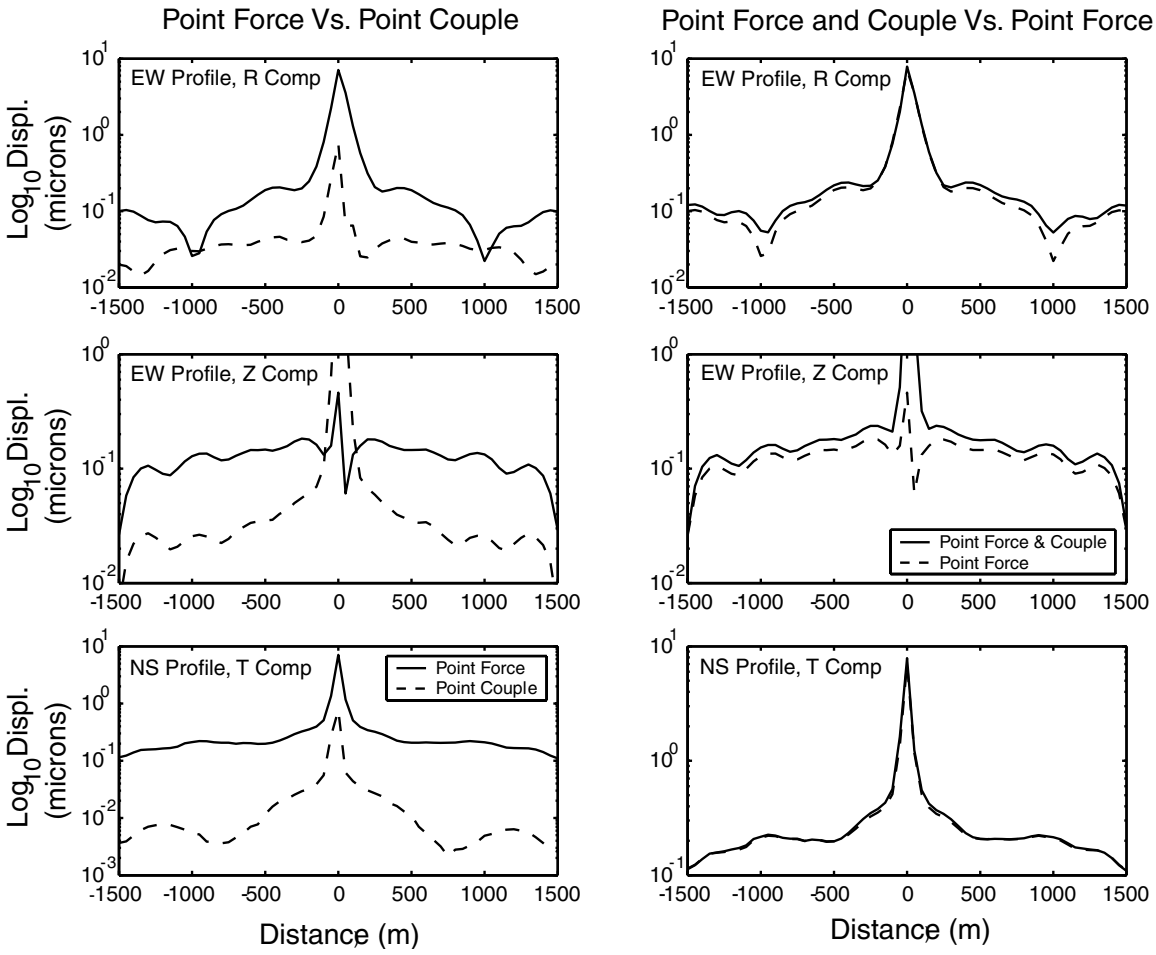

Figure 5.7 Same as Figure 5.6, except that the left 3 plots correspond to a comparison of 1) an applied point force and 2) a point couple and the right 3 plots compare those of 1) a jointly applied point force and couple, and 2) a point force by itself.

5.3 Velocity Model Results and Comparisons

The three velocity models given in Tables 5.2, 5.3, and 5.4 were run using the FEC. Velocity model Smooth was used as the test model for the FEC, and after it was run, an error in the estimation of the forces was discovered. This error was corrected for the other two models, and this produces a discrepancy in the forces used. The forces for each model are given in Table 5.5. The forces used for velocity models 2LayerA and 2LayerB are those given in Table 5.5, which were originally presented in Tables 3.4 and 3.5. It was shown in Section 5.2 that the total displacement field is dominated by the shear force, and since the difference in the forces for the EW shake for the various models is negligible, it is also assumed that the difference in the couples for the EW shake is unimportant. As a result, no force correction is performed for the EW shake. For the NS shake, it is found that the ratio of the two shear forces and the two couples are very similar. Therefore, for the NS shake, the synthetic displacements will be normalized by the ratio of the forces, and the estimated energy radiation will be normalized by this ratio squared, as this was the relationship between force and displacement and radiated energy derived for the theoretical half-space model in Chapter 3. These relationships between the applied forces and the generated displacements and the resulting energy radiation should still hold true for a layered medium, as the displacements amplitudes in the layered model should be linearly proportional to the applied force. For clarity, a * is used for any values normalized in this way.

Model Name	*EW Shake Shear Force* (N)	*EW Shake Couple* (Nm)	*NS Shake Shear Force* (N)	*NS Shake Couple* (Nm)
$2LayerA$	$1.66E5$	$5.37E6$	$3.84E5$	$1.21E7$
$2LayerB$	$1.66E5$	$5.37E6$	$3.84E5$	$1.21E7$
$Smooth$	$1.67E5$	$5.51E6$	$7.30E5$	$2.36E7$

Table 5.5 Forces applied for the different models. Note the difference between the forces for the Smooth model and the 2-layer models.

Using the FEC, synthetics are generated and errors are computed as discussed in Section 5.1. Table 5.6 lists the mean values for the phase error, displacement error, total error, and normalizing factor. All three models have similar average error values and normalizing factors, making it hard to decide which model is better, based on these simple quantities. For completeness, the individual quantities for each component for each run are also provided in Tables 5.9, 5.10, and 5.11 at the end of this section.

$Model$	E_P	$2\pi E_A$	E_T	N_F
$2LayerA$	1.68	1.45	3.13	1.34
$2LayerB$	2.14	0.93	3.07	1.71
$Smooth$	1.32	1.64	2.96	1.29^*

Table 5.6 Velocity model misfits for the different models run, when compared to the observations from Millikan Library. The * denotes that the average normalizing factor for the Smooth model is an approximation, as it was force corrected as stated in Section 5.3.

The radiated energy for each model, computed from the absorbing boundaries for those run on the FEC, and experimentally measured or theoretically estimated, are given for the models in Table 5.7. The results of four of the models presented in Table 5.7 are presented in Appendix C, and these are represented with a $^+$ superscript at the end of the model name. Furthermore, experimental estimates contain a ^{E} superscript, numerical estimates are denoted by a ^{N} superscript, and theoretical estimates are given with a ^{T} superscript. For the numerical models presented in this chapter and relating to the FEC, it should be noted that the estimated energy radiation is inversely correlated with the normalizing factor, and it is not surprising that the models with the lower normalizing factor possess the largest energy estimates, as they generate larger displacements. It can be seen from the error estimates that model 2LayerB fits the amplitudes better, but Figures 5.8 to 5.13 show that the velocity model is not correct as the phase velocity for the model is generally too fast (also shown by the phase error). This is easily observed because the phase values from

the synthetics are usually larger than those of the data (both of which have been unwrapped). This means that the phase for this model changes faster with distance, indicating a faster phase velocity than the observed one. As in Chapter 3, the faster the model velocities, the lower the energy radiation, and as a result this model only radiates about half the energy of the other two models.

It is difficult to differentiate between the other 2 numerical models presented in this chapter, as they generate similar energies, normalizing factors, and errors. However, it seems that the smooth model does a better job of generating the NS shake phase velocities, while model 2LayerA produces better matching displacements (shape wise) for the EW shake. Figures 5.8 to 5.13 show that both models do a good job of estimating the overall phase velocities, and therefore any inconsistencies with the amplitudes are due to spatial velocity variations which can not be incorporated into the simple velocity models employed here. The neglected soft layer on the upper few meters in the soil should also generate larger displacements, reconciling some of the differences between the computed and observed displacements, reducing the normalizing factors but maintaining the radiated energy estimates at a similar level or slightly higher. Now use the results provided in Table 5.7 to estimate the damping ratios for all the models presented in the table. Utilizing the method in Section 3.7 for estimating the building's damping, and the kinetic energy for the building for each shake from Tables 3.4 and 3.5, the damping estimates given in Table 5.8 are achieved. Furthermore, certain plots (4 for each a surface slice and a vertical cross section for each the EW and NS shakes) are provided in Figures 5.14 to 5.25 for the finite element run for the smooth model. It should be noted that the displacement plots for the NS shakes have not been corrected to the appropriate force, and instead, the raw computed FEM plots are presented. The scale on these plots is a logarithmic scale for the generated displacements, and the maximum is always -5, while the minimum is always -8.

As can be seen from Table 5.8, the observed damping values and the estimated damping values from the shaker are very similar. It should be noted that both of these estimates are from experimental techniques to measure the building's total

	$EW\ Energy\ Radiation\ (Watts)$	$NS\ Energy\ Radiation\ (Watts)$
$Shaker^{E}$	12.19	39.14
$Direct-Estimate^{E+}$	0.52	6.71
$2LayerA^{N}$	0.32	7.96
$2LayerA-Direct^{N+}$	0.30	7.50
$2LayerB^{N}$	0.22	3.72
$Smooth^{N}$	0.41	6.31*
$Half-Space^{T}$	0.23	3.64
$ImpedanceFunctionA1^{N+}$	0.78	8.80
$ImpedanceFunctionA2^{N+}$	0.77	8.16

Table 5.7 Energy radiation estimates from the Finite Element Code for the various velocity models, as well as the shaker power estimates (Shaker) from Chapter 6 and the half-space estimates from the second values in Equation 3.90 ("Half-Space"). The * denotes that the energy radiation estimate for the NS shake for the Smooth model is force normalized as mentioned in Section 5.3. Various models are presented in Appendix C and these are represented with a $^{+}$ superscript at the end of the model name. Furthermore, experimental estimates contain a ^{E} superscript, numerical estimates are denoted by a ^{N} superscript, and theoretical estimates are given with a ^{T} superscript.

damping, and therefore it is not surprising that the values are similar. The similarity in the measurements shows that the shaker values for both power and energy are very realistic. The direct-estimate provides an experimental measure of the radiation damping, to which all the other models can be compared to. This calculation is quite simple, and might also provide a realistic assessment of a building's radiation damping if data from a finite element calculation for a building undergoing some forcing is used. Moreover, the Half-Space and the 2LayerB models seems to underestimate the damping estimates. The Smooth and 2LayerA velocity models seem to be more representative of the soil conditions present at the building. The values for the 2LayerA model are verified by the simple calculations performed in Section C.2. Furthermore, the impedance function results provided in Section C.3 also provide

	ξ_{EW}	ξ_{NS}
$Observed^{E}$	1.63	1.65
$Shaker^{E}$	1.90	1.79
$Direct-Estimate^{E+}$	0.08	.31
$2LayerA^{N}$	0.05	0.36
$2LayerA-Direct^{N+}$	0.05	0.34
$2LayerB^{N}$	0.03	0.17
$Smooth^{N}$	0.06	0.29*
$Half-Space^{T}$	0.04	0.17
$ImpedanceFunctionA1^{N+}$	0.12	0.40
$ImpedanceFunctionA2^{N+}$	0.12	0.37

Table 5.8 Viscous damping estimates for all the models presented in this thesis. The Observed values are from the free amplitude decay of the building, the Shaker estimates are computed in Table 6.1, the Half-Space model values are calculated in Section 3.7, and the remaining three are computed from the finite element code. The * denotes that the energy radiation estimate for the NS shake for the Smooth model was force normalized as mentioned in Section 5.3. Various models are presented in Appendix C and these are represented with a $^{+}$ superscript at the end of the model name. Furthermore, experimental estimates contain a ^{E} superscript, numerical estimates are denoted by a ^{N} superscript, and theoretical estimates are given with a ^{T} superscript.

an independent check on the radiation energy estimates provided in this thesis. It therefore seems that for the NS shakes, approximately 20% of the library's total damping is due to energy radiation from the structure. For the EW shakes, only 4% of the damping seems to be due to energy radiation. The observations in Chapter 6 suggest that the estimated energy radiation for the EW shake should be higher, as otherwise the areal extent where the building is observed should be smaller. From the shaker power output and from the ratio of the shear forces that the building generates on the soil, the EW shakes output approximately 25% of the energy of a NS shake. If we believe both the EW and NS energy estimates from the FEC, then for the NS shake we can observe approximately 7 Watts at a distance of 390 km, while

for the EW shake we can see 0.4 Watts at a distance of nearly 270 km. The difference between these two powers is almost a factor of 20, while the distance difference for the observations is only a factor of 4. It therefore seems that only one of the the two energy estimates can be correct, and the large distances where the building can be observed supports the larger number. However, the measured displacements around the building generally match fairly well, suggesting that the numbers are correct as given. This is also supported by the results presented here from the various methods used to estimate the radiated energy. It is also possible that the different resistance mechanisms in the EW and NS direction for the building behave differently, with the EW dissipating more energy anelastically, which could account for the differences between the measured values and the estimated ones. There isn't enough data to fully resolve the problem, and the reason for the differences is left open to interpretation and for further research by perhaps adding strain meters inside the building to try and observe different behaviors. However, I believe that the radiation energies presented here are correct.

Dir, Line, Comp.	E_{Pi}	$2\pi E_{Ai}$	E_{Ti}	N_{Fi}
EW, EL, Radial	1.75	1.08	3.23	1.09
EW, EL, Vertical	2.50	1.00	3.75	1.32
EW, NL, Transverse	1.91	2.06	1.54	1.96
NS, EL, Transverse	1.82	0.95	3.85	0.45
NS, NL, Radial	0.92	2.76	3.38	0.88
NS, NL, Vertical	1.20	0.86	2.65	2.31

Table 5.9 Velocity model misfits for the individual components for the East and North lines for the smooth model. The data is presented similarly to that of Table 5.6, and the subscript i in the headers means that individual values are presented and not average values. The left column is to be read as follows: Shaking Direction, Instrument Line, and Observation Component.

Dir, Line, Comp.	E_{Pi}	$2\pi E_{Ai}$	E_{Ti}	N_{Fi}
EW, EL, Radial	2.79	0.44	3.23	1.10
EW, EL, Vertical	2.88	0.88	3.75	1.18
EW, NL, Transverse	1.13	0.41	1.54	2.21
NS, EL, Transverse	2.99	0.87	3.85	1.00
NS, NL, Radial	1.22	2.16	3.38	1.98
NS, NL, Vertical	1.80	0.85	2.65	2.79

Table 5.10 Same as Table 5.9, except for model 2LayerB.

Dir, Line, Comp.	E_{Pi}	$2\pi E_{Ai}$	E_{Ti}	N_{Fi}
EW, EL, Radial	1.73	1.77	3.51	0.84
EW, EL, Vertical	2.41	1.60	4.01	1.67
EW, NL, Transverse	0.42	1.39	1.81	1.74
NS, EL, Transverse	1.74	1.43	3.17	0.53*
NS, NL, Radial	0.91	2.42	3.33	0.93*
NS, NL, Vertical	0.69	1.22	1.92	2.04*

Table 5.11 Same as Table 5.9, except for model Smooth. The values with a star have been re-normalized as mentioned in the text.

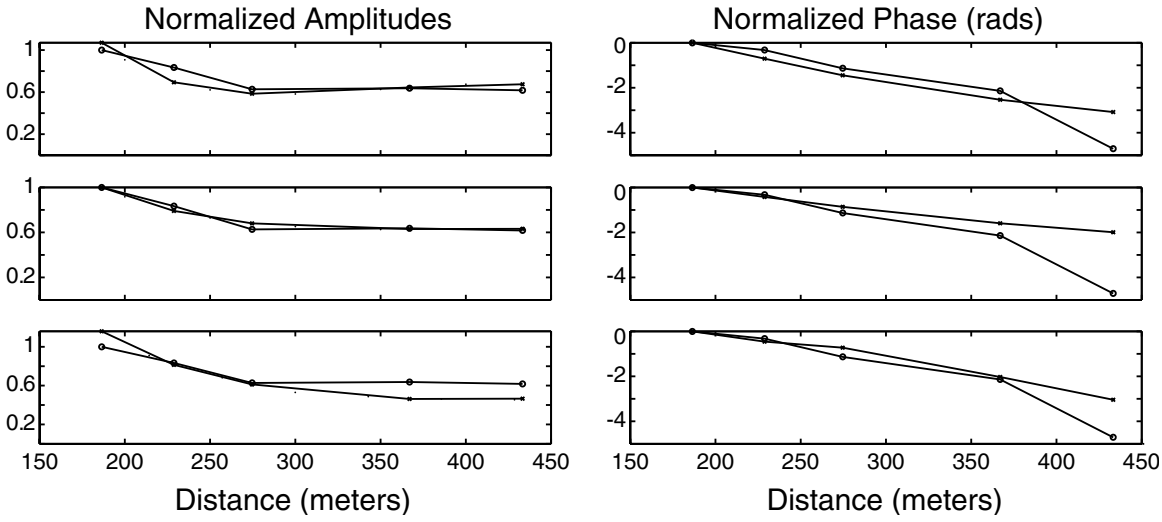

Figure 5.8 Normalized amplitude and phase measurements for an EW shake, along an East line, for the radial component, for the 3 different models run using the FEC. The left 3 plots present the normalized displacements data, while the right 3 plots show the normalized phase data. The top 2 panels correspond to the data for model 2LayerA, the middle 2 to model 2LayerB, and the bottom 3 to model Smooth. The observed data points are shown by the circles, while the data from synthetics is given by the x's (interpolated using a polynomial to fit the data at the nodes). For the amplitude plots, the displacements measured at the nodes are shown by dots in the plots.

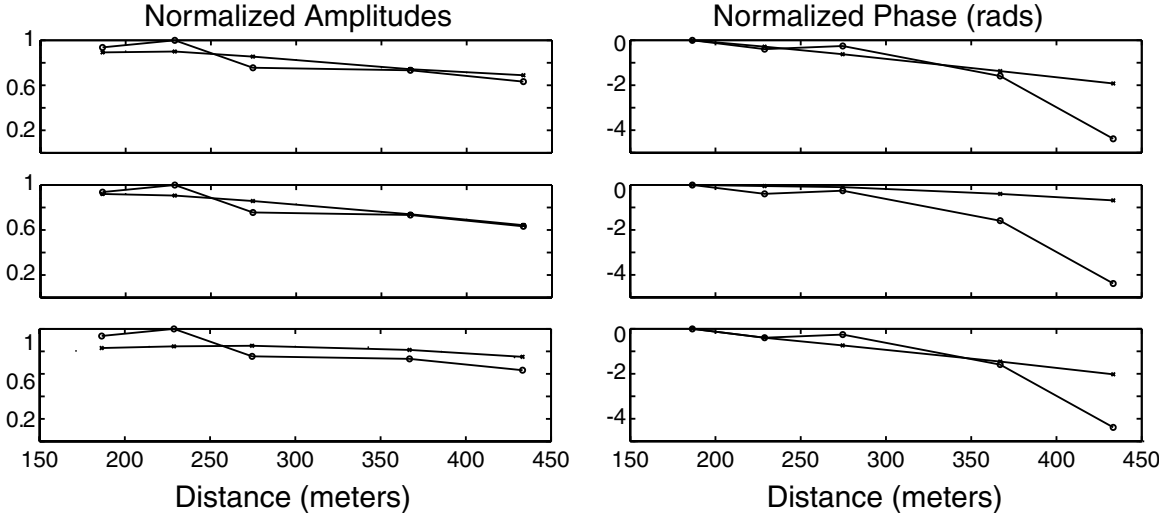

Figure 5.9 Same as Figure 5.8, except for an EW shake, along an East line, for the vertical component.

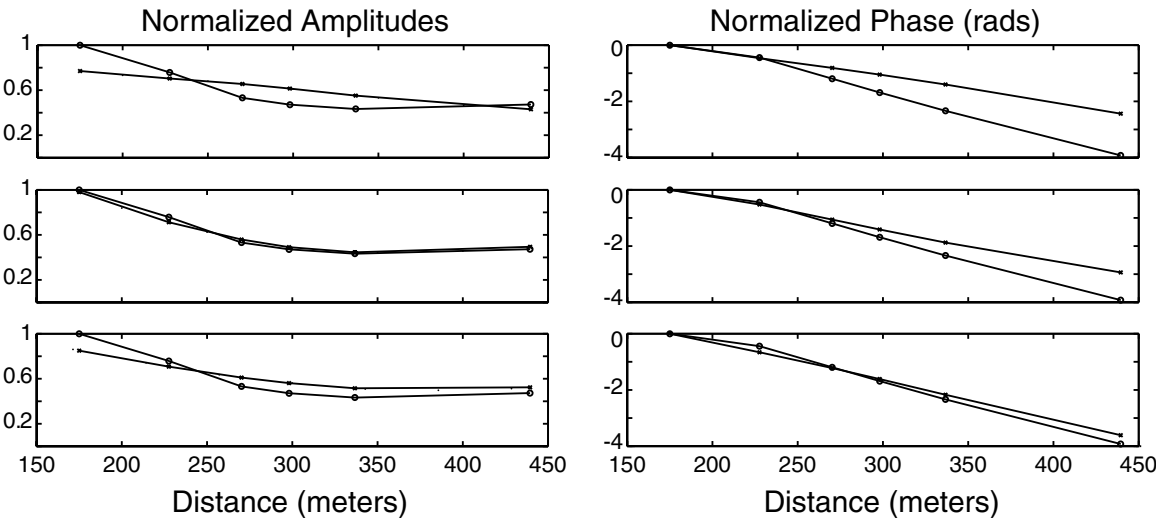

Figure 5.10 Same as Figure 5.8, except for an EW shake, along a North line, for the transverse component.

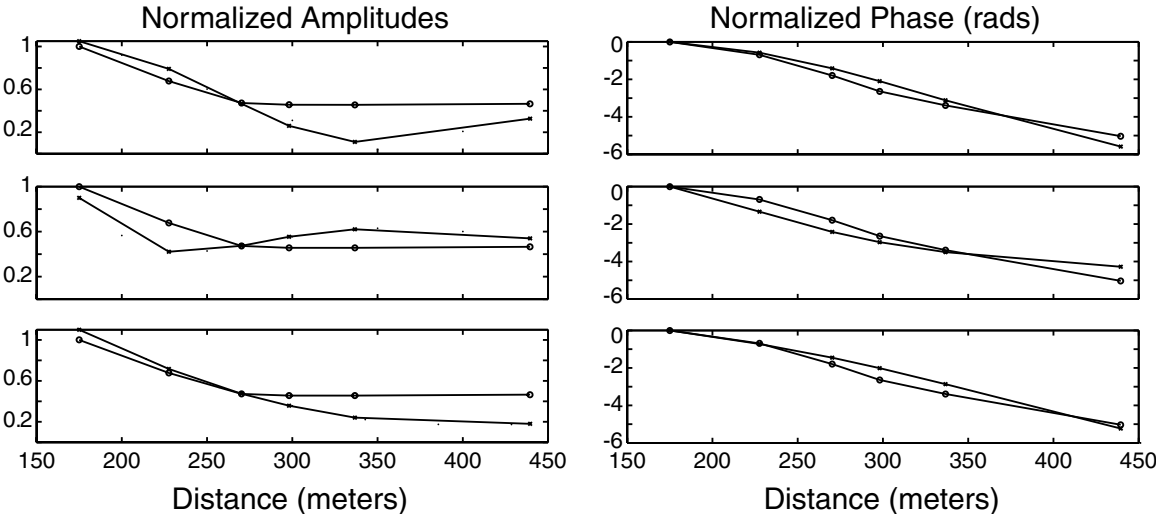

Figure 5.11 Same as Figure 5.8, except for a NS shake, along a North line, for the radial component.

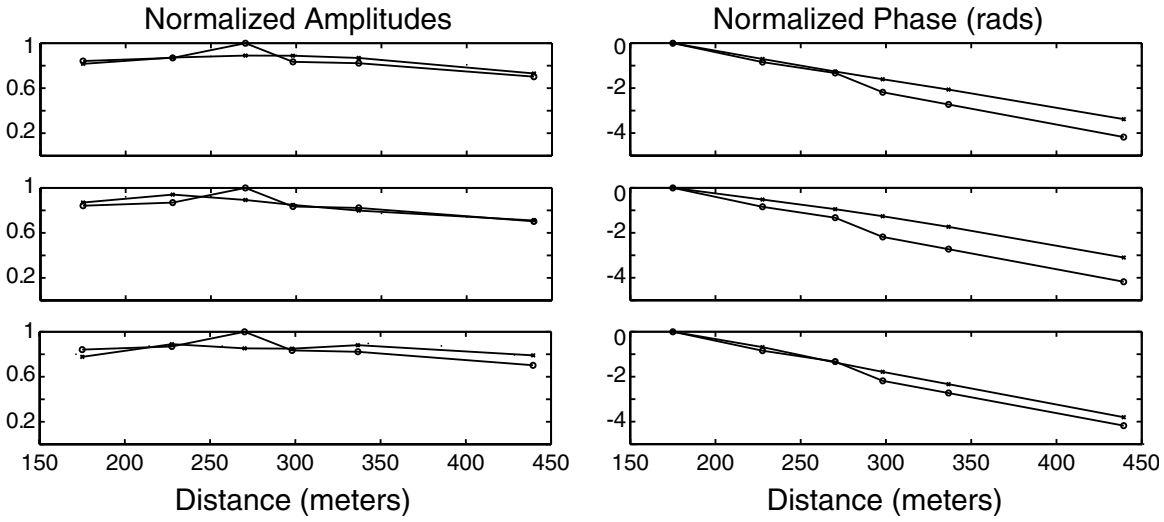

Figure 5.12 Same as Figure 5.8, except for a NS shake, along a North Line, for the vertical component.

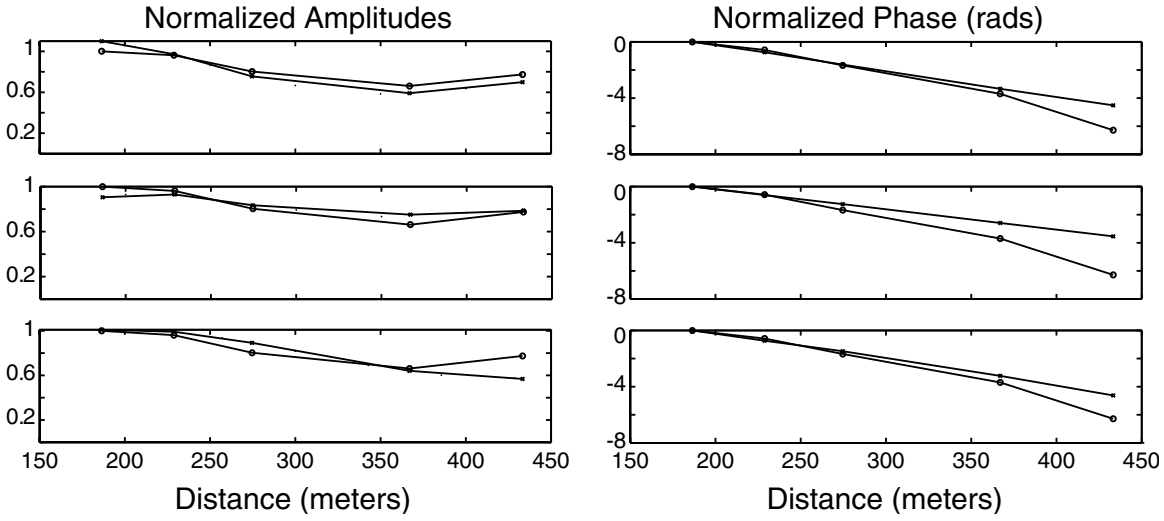

Figure 5.13 Same as Figure 5.8, except for a NS shake, along an East Line, for the transverse component.

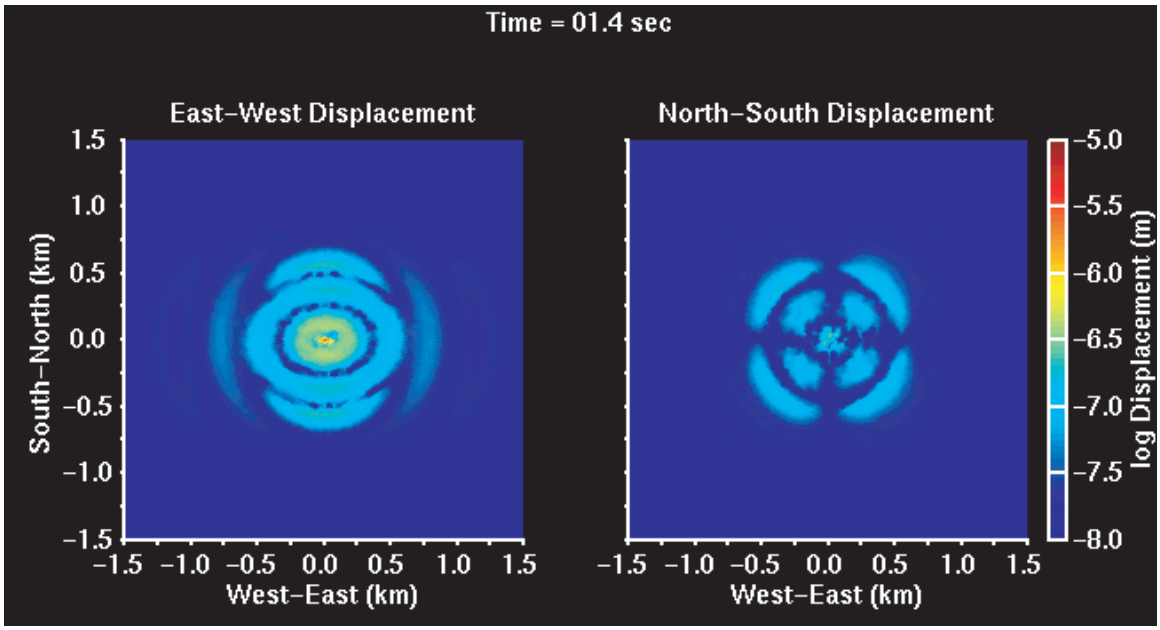

Figure 5.14 EW shake, FEM smooth model simulation at time 1.4 seconds. The left panel shows the east-west component and the right panel shows the north-south component at the surface.

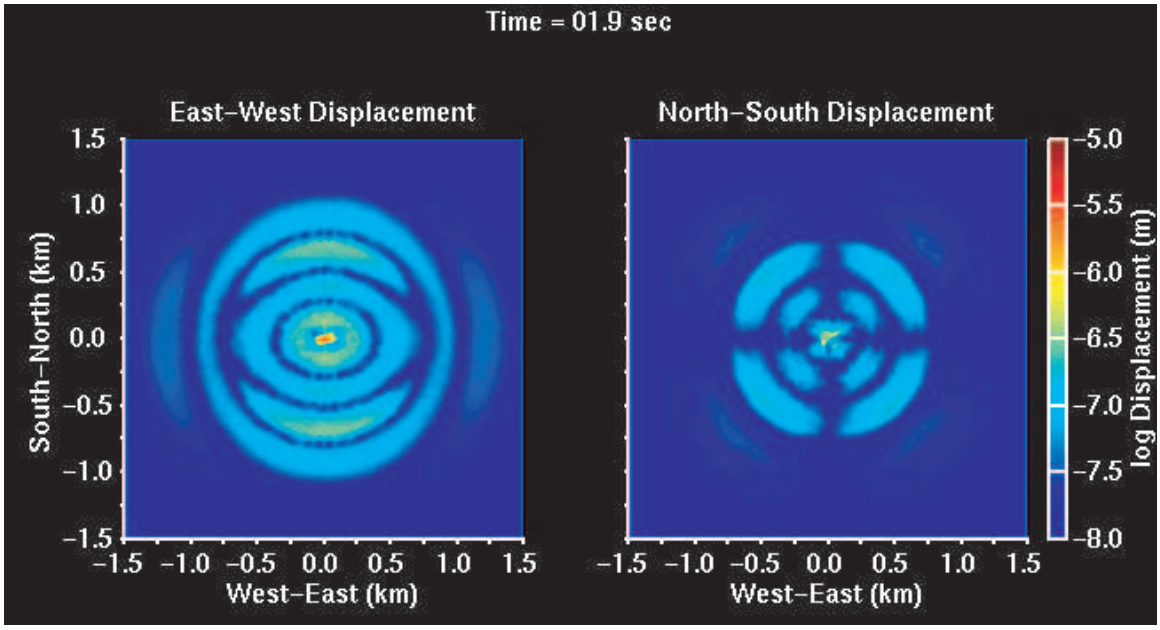

Figure 5.15 Same as Figure 5.14, at time 1.9 seconds.

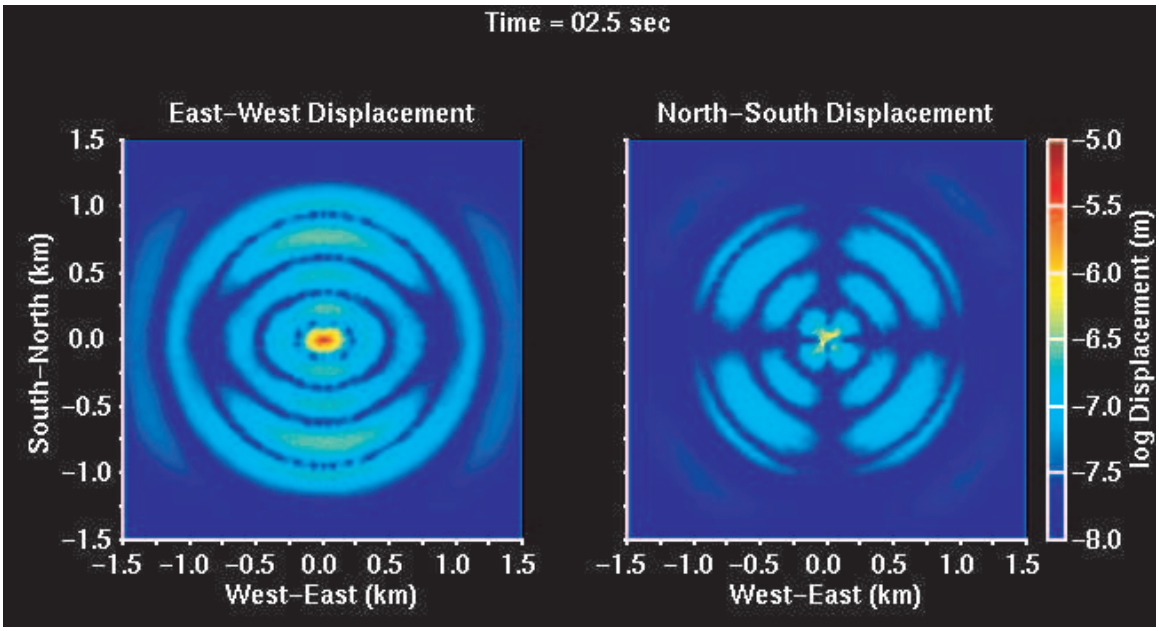

Figure 5.16 Same as Figure 5.14, at time 2.5 seconds.

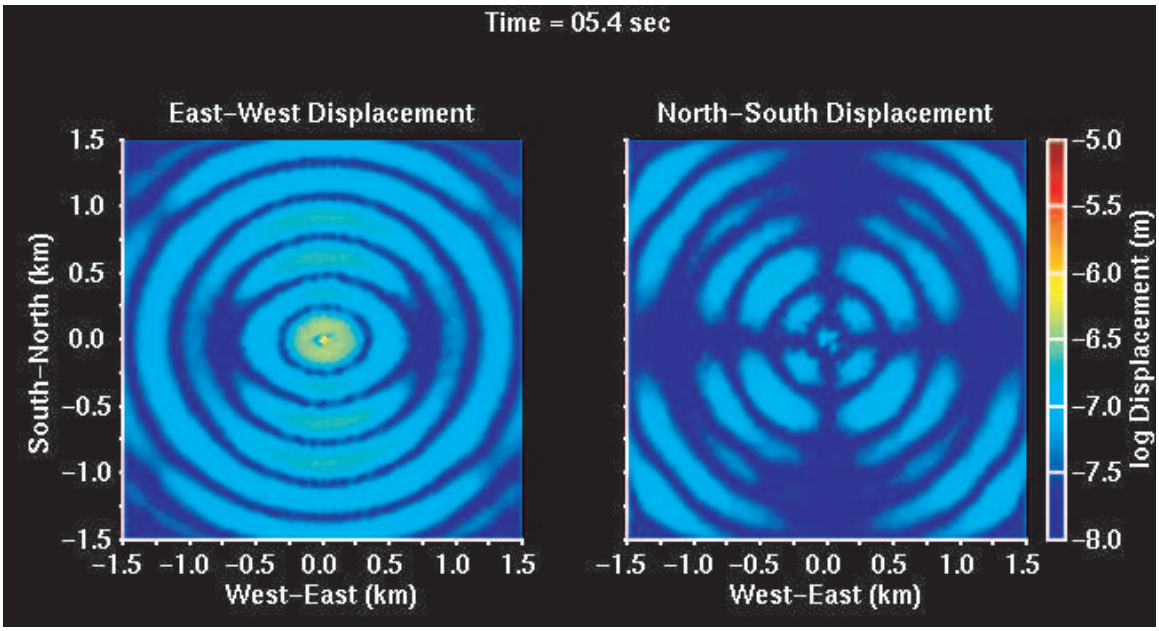

Figure 5.17 Same as Figure 5.14, at time 5.4 seconds.

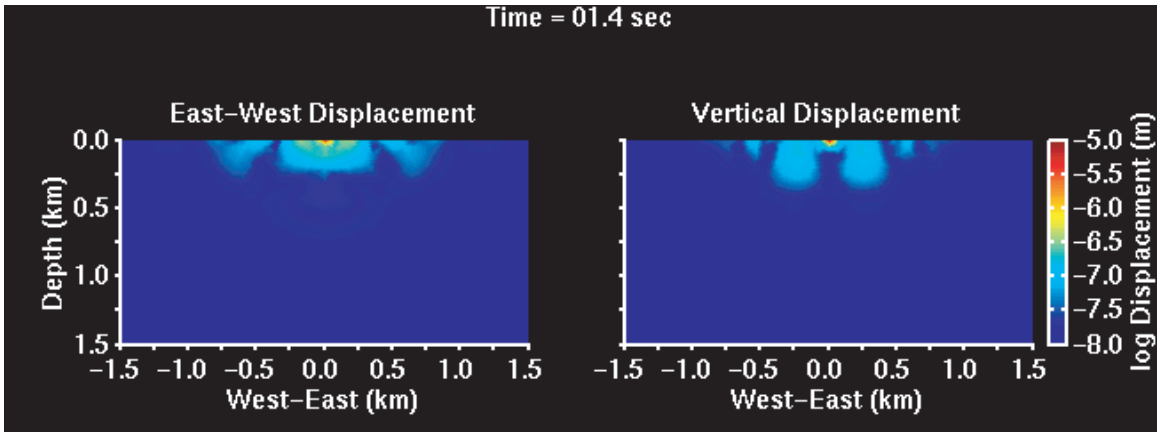

Figure 5.18 EW shake, FEM smooth model simulation at time 1.4 seconds. The left panel shows the east-west component and the right panel shows the vertical component for a EW vertical cross section through the central node.

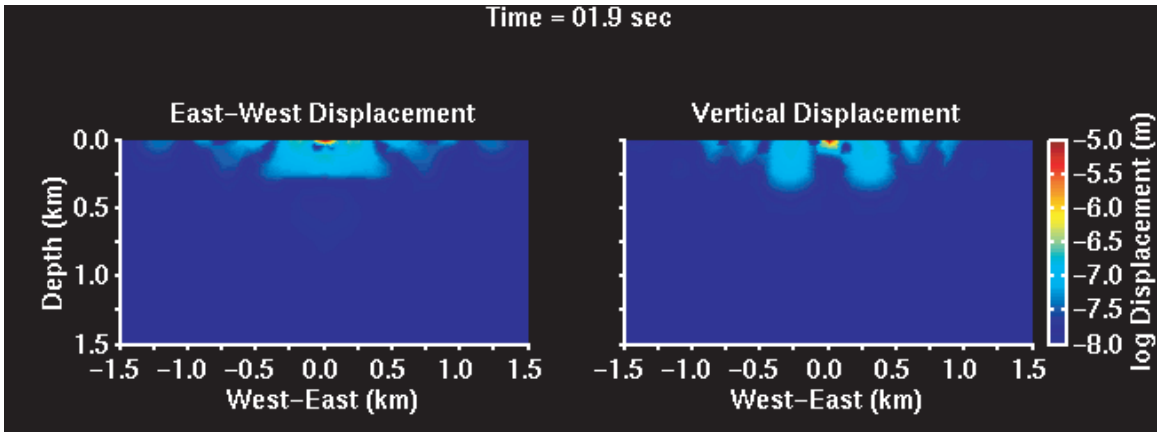

Figure 5.19 Same as Figure 5.18, at time 1.9 seconds.

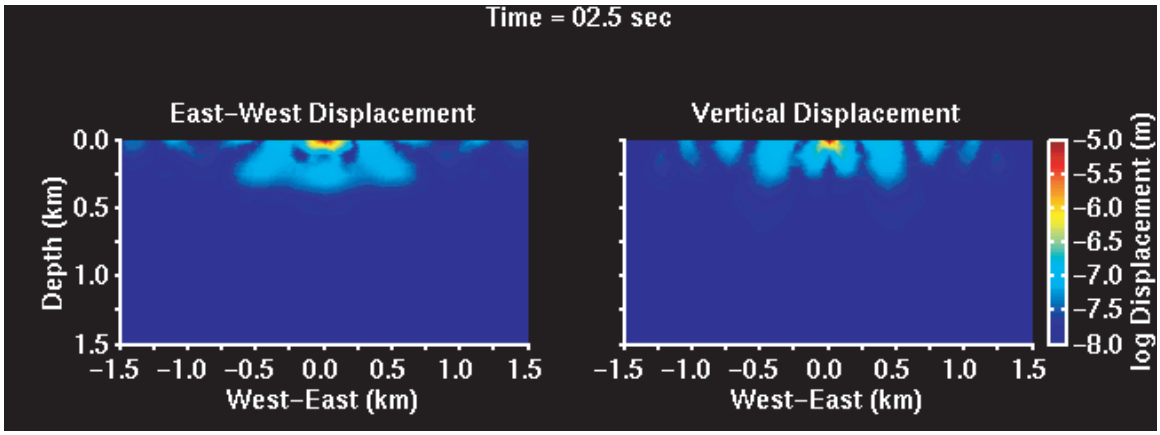

Figure 5.20 Same as Figure 5.18, at time 2.5 seconds.

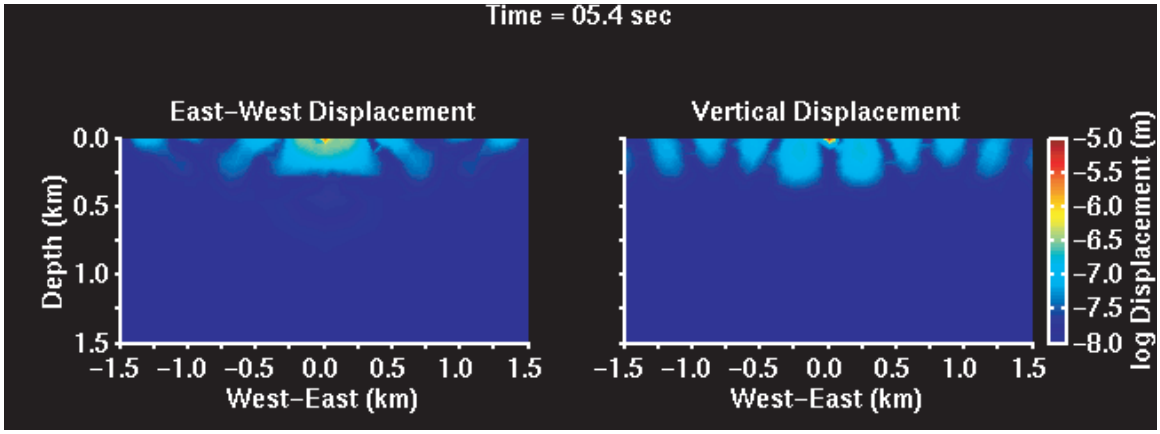

Figure 5.21 Same as Figure 5.18, at time 5.4 seconds.

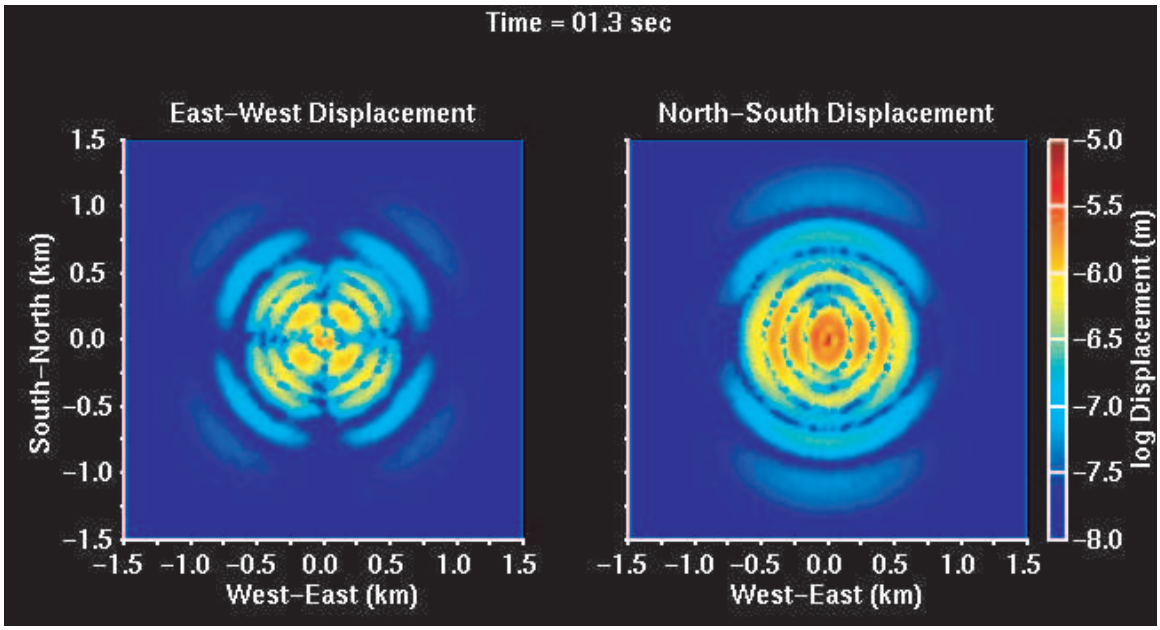

Figure 5.22 NS shake, FEM smooth model simulation at time 1.3 seconds. The left panel shows the east-west component and the right panel shows the north-south component at the surface.

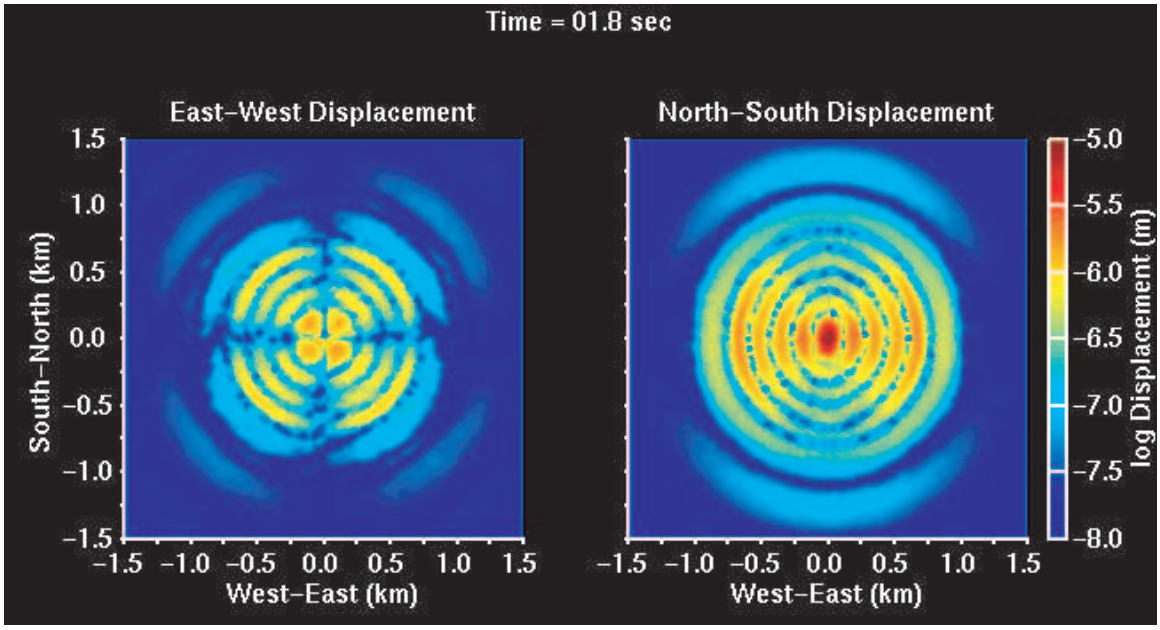

Figure 5.23 Same as Figure 5.22, at time 1.8 seconds.

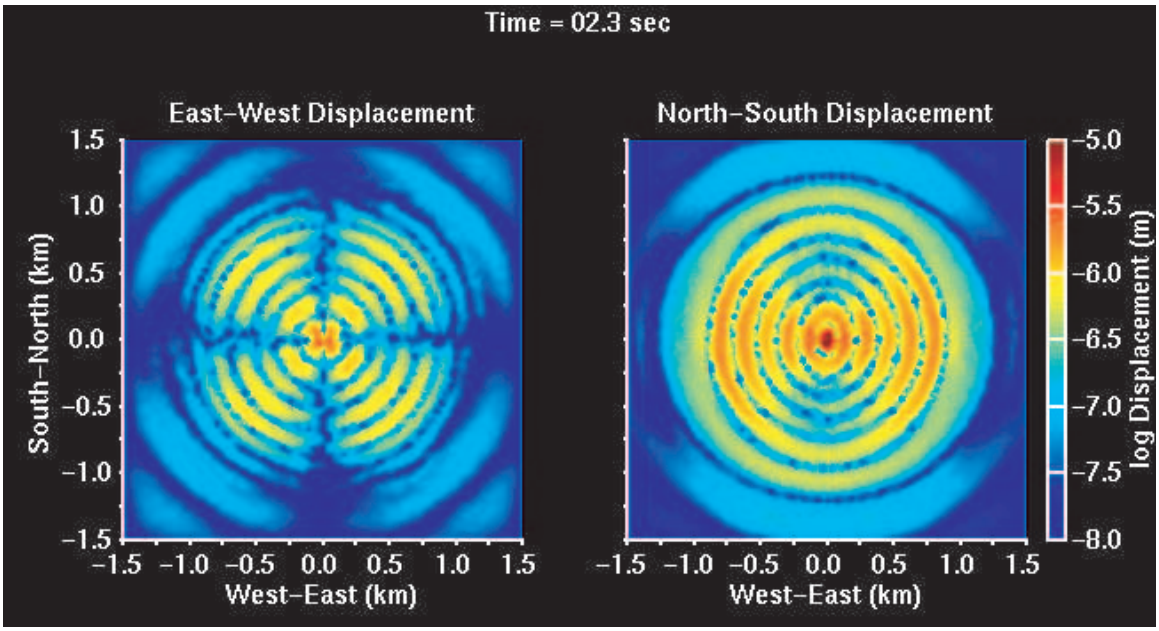

Figure 5.24 Same as Figure 5.22, at time 2.3 seconds.

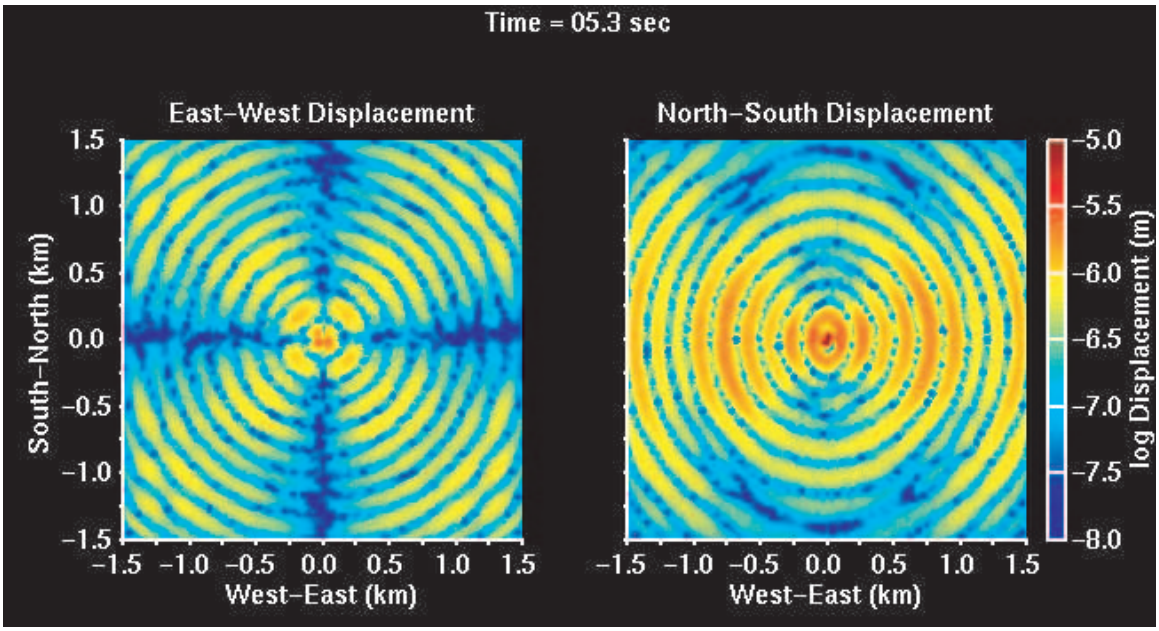

Figure 5.25 Same as Figure 5.22, at time 5.3 seconds.

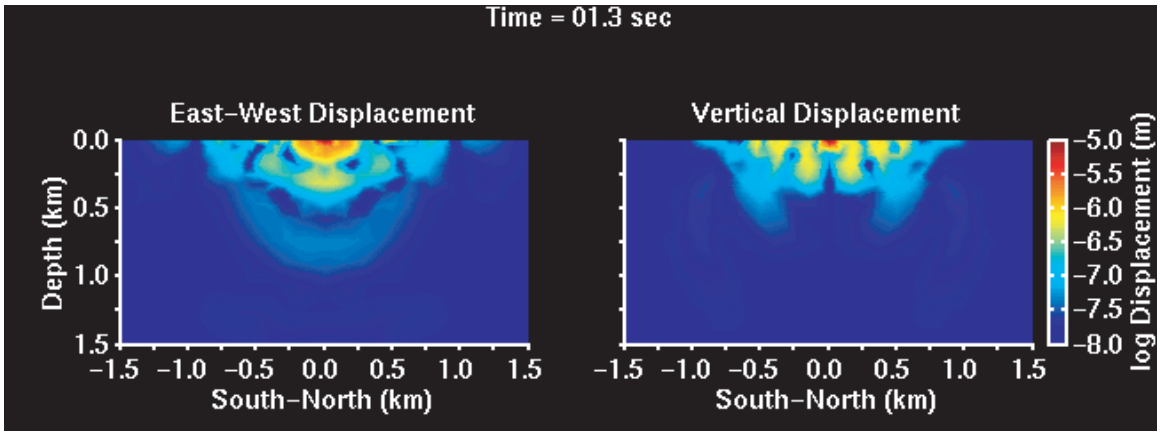

Figure 5.26 NS shake, FEM smooth model simulation at time 1.3 seconds. The left panel shows the east-west component and the right panel shows the vertical component for a NS vertical cross section through the central node.

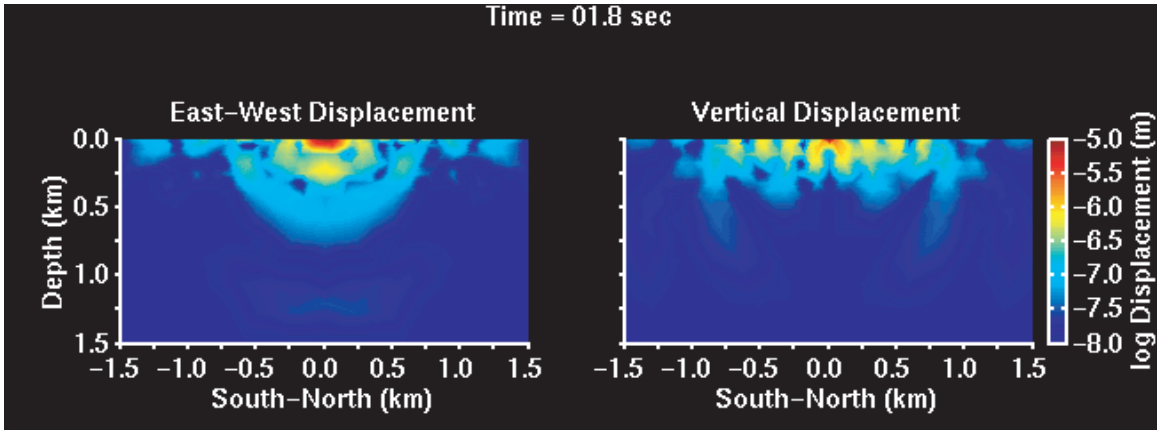

Figure 5.27 Same as Figure 5.26, at time 1.8 seconds.

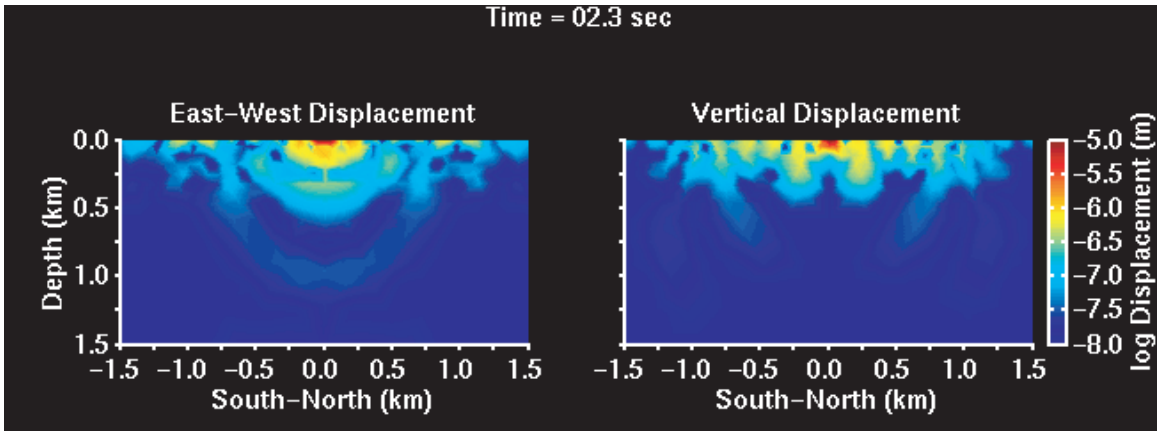

Figure 5.28 Same as Figure 5.26, at time 2.3 seconds.

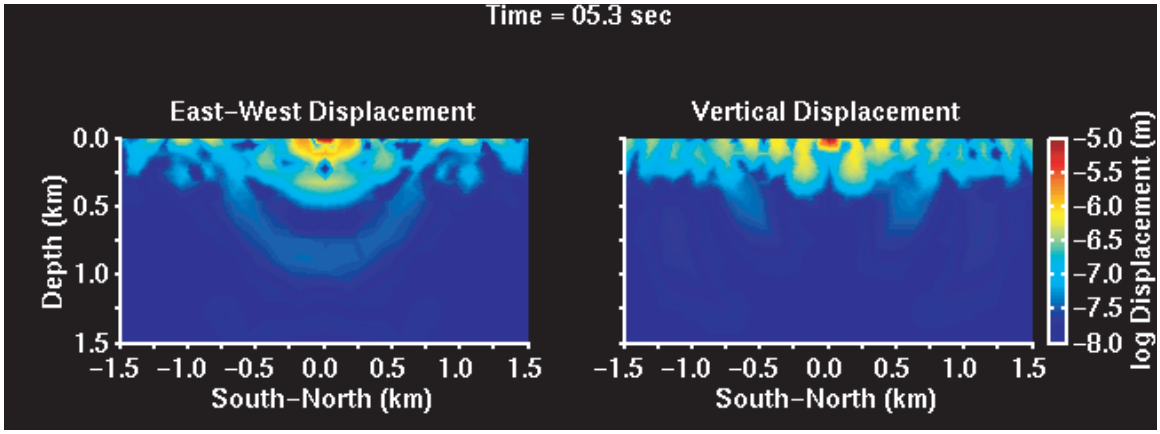

Figure 5.29 Same as Figure 5.26, at time 5.3 seconds.

Chapter 6

Regional Observations

The dynamic characteristics of Millikan Library and/or the building's soil structure interaction during forced excitations have been the subject of detailed studies by *Kuroiwa* (1969), *Jennings and Kuroiwa* (1968), *Luco et al.* (1975), *Foutch et al.* (1975), *Foutch* (1976), and *Luco et al.* (1986). Other studies have focused on the waves radiated by structures. *Luco et al.* (1975) collected data for waves radiated by Millikan Library up to a distance of 3 km in an experiment similar to this one. *Wong et al.* (1977) examined the behavior of radiated SH waves for the building in alluvium and rock sites within 5 km of the building, and also studied the effect of a surface depression on the generated wave field. In similar studies for the Volvi test site located near Thessaloniki, Greece, *Gueguen et al.* (2000) and *Cardenas et al.* (2000) observed and/or modelled radiated waves for distances up to a few hundred meters from the source. The main difference between these and the experiments performed for this thesis is temporal, as the experiments at the Volvi test site are transient in nature (free vibrations of the structure from pull-out tests), and my experiments focus on the steady-state motion generated from the forced vibration of a structure.

I performed four experiments utilizing Millikan Library as a harmonic seismic source during extended shaking periods (the duration ranged from four to six hours). Data was collected from (1) the southern California TriNet network (*Hauksson et al.*, 2001) for all four experiments, (2) the Berkeley Digital Seismic Network (BDSN) (*Uhrhammer et al.*, 1996) stations for the last two experiments, and (3) a USGS/Caltech accelerometer array of 36 accelerometers located in Millikan Library (*Bradford et al.*,

2004). The four hour experiments were conducted on August 3, 2001 (NS shaking, hereafter referred to as NS1) and February 18, 2002 (EW shaking, EW1). The six hour experiments were conducted on September 19, 2002 (EW2), and September 23, 2002 (NS2). A small earthquake occurred approximately 70 minutes after the start of the experiment on September 23, 2002, and as a result only the last four hours of the data are used to avoid data contamination from the earthquake. As previously shown in this thesis, the NS resonant frequency of the building is approximately 1.64 Hz, while the EW frequency is approximately 1.11 Hz.

6.1 Displacements

6.1.1 Method

The building's resonant frequencies were determined by performing a frequency sweep of the building (Resonant Amplification Method, *Clough and Penzien* (1993)), for which 0.01 Hz frequency increments were used. A plot of roof displacement (normalized by the excitation force) versus frequency is created, and the frequency with the largest normalized displacement corresponds to the structure's resonant frequency. A sample plot is provided in A. It should be noted that I am "resonant frequency" as it is commonly defined, namely, the frequency corresponding to the peak of the resonant amplification curve, which if determined using displacement is found by

$$\omega_D = \omega_0 \sqrt{1 - 2\xi^2}$$

where ω_D is the resonant frequency, $\omega_0 = \sqrt{k/m}$ is the undamped natural frequency of the structure, and ξ is the damping ratio. The resonant frequencies determined by this method are used as initial estimates for the experiment, and have been well documented for Millikan Library, most recently by this thesis, *Clinton et al.* (2004), and *Bradford et al.* (2004). However, to determine the building's resonant frequency at the time of testing, I set up a Kinemetrics Ranger seismometer (1 second pendulum, velocity transducer) connected to a readily visible analog chart recorder on the

library's roof. By monitoring the roof velocity as we vary the excitation frequency, we can find the frequency that corresponds to the building's maximum roof velocity. This frequency is slightly smaller than ω_D, but the difference between the two frequencies is less than 2% (*Kuroiwa*, 1969). However, since I do not correct for forcing while performing the experiment (the shaker force is proportional to the square of the forcing frequency), the frequency found during the experiment is close to the resonant frequency. All these frequencies are very closely spaced, and they can all be used interchangeably. Therefore, for the duration of this chapter, when I refer to the natural or resonant frequency of the structure, I refer to the resonant frequency found experimentally, using velocity measurements and without correcting for the applied force on the roof top.

The small amplitude of the generated waves at the large observation distances is often below the time domain noise level of the instruments recording the signal. Thus, the data was analyzed in the frequency domain by performing a fast Fourier transform (FFT) for a long time window during the building's forced excitation. Although the data should ideally be a monochromatic signal, Figure 6.1 shows that the FFT amplitude is not a delta function. Instead, the energy is spread over a narrow frequency band, which indicates that there are small changes in frequency with time. This broadening of the peak is probably due to the feedback mechanism in the shaker's controller. However, the width of the signal in the frequency domain is less than 0.006 Hz and most of the energy is usually concentrated in a band narrower than 0.002 Hz. This means that the signal is very narrow band and well controlled.

As a result of the signal's finite frequency content, an integration can be performed in the frequency domain around the frequency of excitation, to account for all of the energy radiated by the building for the duration of the shake. As Figure 6.1 qualitatively shows, the FFT amplitude spectra at all distances are similar in shape once the noise level is considered. I'll refer to this narrow frequency band containing most of the energy as the radiated spectral band (RSB) and the amplitude at each station of the FFT in this same band as the radiated spectra. The similarity in the radiated spectra is especially clear for stations MIK and PAS. Station MIK has a

three component Kinemetrics Episensor accelerometer located on the East side of the 9th floor of Millikan Library(*Clinton et al.*, 2004), and this data is used as the source spectrum and to determine the RSB. Station PAS contains an $STS-1$ broadband sensor, and it is located at a distance of 4.43 km WNW of the source.

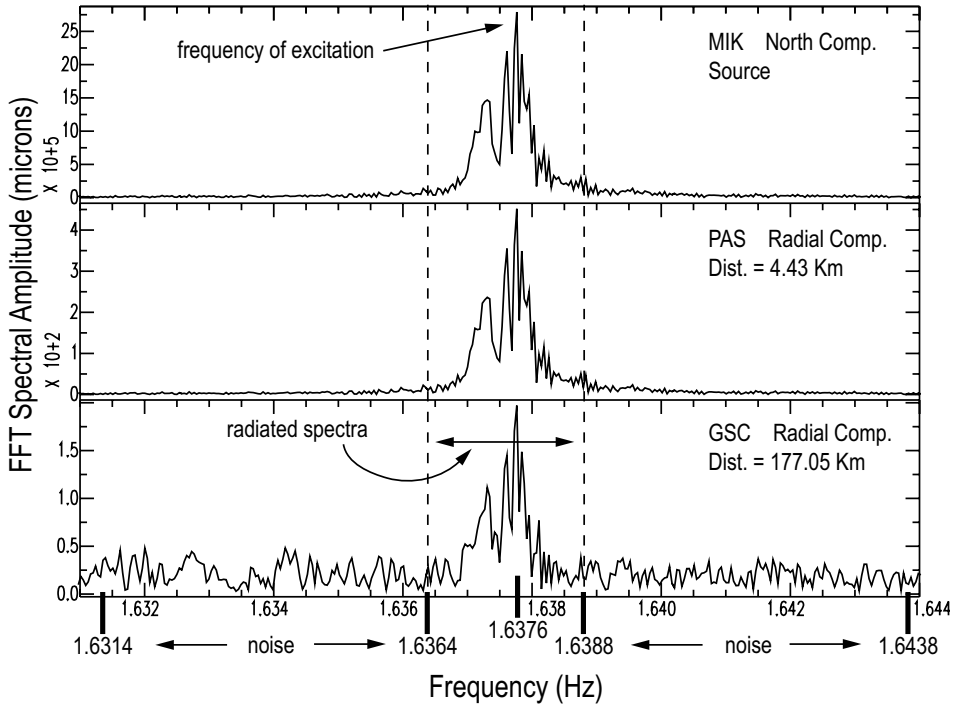

Figure 6.1 Spectral amplitudes at three TriNet stations: Millikan (MIK), Pasadena (PAS), and Goldstone (GSC). The data was recorded during a four hour forced vibration of Millikan Library for shake NS1, and the frequency of excitation was near 1.638 Hz. Notice the similarity in the three Fourier amplitude spectra, especially those at MIK and PAS, which have a very high signal-to-noise ratio. Station MIK is located on the 9th floor of Millikan Library, the source of the radiated signal.

To compute the time domain peak amplitude of the sinusoid generated by the forced vibration of Millikan Library at each station, I integrate the radiated spectra. However, it is necessary to remove the background spectral amplitude noise level from the station spectra, since signals at most of the stations are characterized by very low signal-to-noise levels. This procedure minimizes the influence of the variations in noise levels at the individual stations.

The integration is performed by utilizing a process similar to that used to generate a spectrogram. Starting a significant frequency interval away from the RSB, the FFT spectra is integrated over a moving frequency window as wide as the RSB. By performing an inverse FFT, this integral value is then transformed back into the time domain and stored in a vector, the frequency window moves by one sample, and the process is repeated until a significant frequency interval is achieved on both sides of the RSB. The individual time domain displacement values (from the IFFTs) are assigned the central frequency values of the integral window to track the locations of the original frequency values.

The background spectral noise level is determined from the frequencies immediately adjacent to and extending 0.05 Hz from the radiated spectra. The mean value for each of these noise ranges is determined, and both values are averaged to estimate the noise level for the radiated spectra, N. The chosen frequency range of 0.05 Hz is sufficiently broad for calculating the spectral amplitude noise level, as this frequency window is 20 times wider than the RSB. The mean standard deviation of the individual time domain values for these same frequency bands is considered to be the measurement error for the computed displacements, σ. Furthermore, the peak of the time domain values over the RSB corresponds to be the total signal amplitude, A_T. Therefore, to find the radiated signal amplitude, A_R, the noise level should be subtracted from the total signal amplitude as follows:

$$A_R = \sqrt{A_T^2 - N^2} \pm \sigma$$

This method is used to compute the amplitude of the harmonic, monochromatic source signal, A_R, at all of the TriNet stations where the building's excitation was observed, and only these stations will be presented in the data analysis.

6.1.2 Observations

In order to quantify the energy flux from the building, we estimate the mechanical power of the shaker by modelling the system as a damped linear oscillator with a

harmonic forcing function. We then compute the average power applied by the shaker by integrating the instantaneous power over a cycle period:

$$P_{avg} = \frac{1}{T}\int_0^T F(t)\dot{U}(t)\,dt$$

where T is the period of one oscillation cycle, ω is the forcing angular frequency (same as resonant frequency), $F(t)$ is the force applied by the shaker ($F_0\cos(\omega t - \delta)$), $U(t)$ is the displacement of the shaker ($U_0\cos\omega\tau$), $\dot{U}(\tau)$ the velocity, and δ is the phase difference between the shaker force and the building displacements. Performing the integral, we find that

$$P_{avg} = \frac{1}{2}\omega F_0 U_0 \sin\delta \tag{6.1}$$

Furthermore, $\delta = \frac{\pi}{2}$ for a damped linear oscillator that is forced at its resonant frequency. Upon substitution into Equation 6.1, the radiated power over a cycle is found to be

$$P_{avg} = \frac{1}{2}\omega F_0 U_0 \tag{6.2}$$

The vertical component and the horizontal component orthogonal to the shaking direction are small in amplitude and can be ignored in the calculation.

In Table 6.1, we show the maximum roof displacements, the maximum shaker forces for the excitation frequencies, and the resulting energy fluxes for the shaker inputs on the library. The maximum roof displacements are calculated from the roof-top instruments in the accelerometer array in Millikan Library. The mechanical power of the shaker is determined to be 12 Watts for an EW shake and 39 Watts for a NS shake. However, these estimates have been shown in Section 5.3 to be too large by a factor of two.

For Figures 6.2 through 6.8, the individual data-sets have been combined into a single data-set. The data-sets were merged by taking the mean radiated signal amplitudes (A_R) for stations with two readings, unless one measurement had at least

Shaking Direction	*Maximum Roof Displacement (mm)*	*Shaker Force (N)*	*Mechanical Power (Watts)*
EW	0.781	4507	12.19
NS	0.787	9662	39.14

Table 6.1 Estimated energy flux from Millikan Library under forced excitation for the EW and NS fundamental modes. The Maximum roof displacements are from accelerometers in the $9th$ floor in the direction of excitation, the shaker force is calculated from the shaker manual for the frequency of excitation (*Kinemetrics*, 1975), and the mechanical power is computed by estimating the average power per cycle of the shaker.

twice the signal-to-noise (STN) ratio ($\frac{A_R}{N}$)of the other measurement, in which case the one with the higher STN ratio was chosen over the other one. If only one reading was available, that reading was incorporated into the data-set. Furthermore, the data-set was limited to stations with at least a STN ratio of 0.5. The results for the individual shakes are provided in Tables 6.2 and 6.3. The results of our amplitude analysis are shown in Figure 6.2 and 6.3 for the combined data-sets, while Figures 6.4 and 6.5, which shows the interpolated (by Delauny triangulation) radiated displacement field for the NS and the EW shakes. Figures 6.2A-C, 6.3A-C, 6.4A-F, and 6.5A-F highlight the Los Angeles and San Fernando Valleys, as they show high amplitudes with respect to the surrounding regions. As the energy in the NS shake is greater than that for the EW shake, more TriNet stations record the building's signal. The NS shakes generate stronger signals primarily due to a difference in excitation forces for each of the natural frequencies. Even though the same load configuration (weight) is used in the shaker for all of the shakes, the excitation force of the shaker is proportional to the square of the shaking frequency. Thus the shaker will generate a force approximately 2.1 times larger for the NS frequency (1.64 Hz) than for the EW frequency (1.11 Hz). The shaker details are discussed in 2.1, as well as in *Kuroiwa* (1969), and *Bradford et al.* (2004). In principle, shakes in the individual excitation directions should be nearly identical. However, by comparing the individual amplitude plots, we see that there are differences between the two shaking experiments. These differences are most pronounced at the stations with the poorest signal-to-noise ratios; that is, the

differences reflect our ability to measure the size of the Millikan signal.

Experiment, Component	*Number of Observations*	*Distance Decay before R_T*	*Transition Distance R_T (Km)*	*Distance Decay after R_T*
$NS1, Radial$	60	$R^{-2.53}$	45	$R^{-1.19}$
$NS1, Transverse$	56	$R^{-2.49}$	50	$R^{-1.34}$
$NS1, Vertical$	47	$R^{-2.04}$	45	$R^{-1.20}$
$NS2, Radial$	43	$R^{-2.97}$	45	$R^{-0.94}$
$NS2, Transverse$	56	$R^{-2.85}$	45	$R^{-1.37}$
$NS2, Vertical$	35	$R^{-3.20}$	45	$R^{-1.26}$
$NSC, Radial$	73	$R^{-2.61}$	45	$R^{-1.13}$
$NSC, Transverse$	72	$R^{-2.60}$	50	$R^{-1.37}$
$NSC, Vertical$	57	$R^{-2.26}$	45	$R^{-1.15}$

Table 6.2 Distance decay rates and transition distances (R_T) for the NS shakes. The last three entries correspond to the lines of the combined data-set shown in Figure 6.7. R is the radial distance from Millikan Library, and NSC is the combined data-set.

Experiment, Component	*Number of Observations*	*Distance Decay before R_T*	*Transition Distance R_T (Km)*	*Distance Decay after R_T*
$EW1, Radial$	16	$R^{-2.10}$	45	$R^{-1.12}$
$EW1, Transverse$	13	$R^{-2.06}$	65	$R^{-1.20}$
$EW1, Vertical$	11	$R^{-1.00}$	30	$R^{-1.47}$
$EW2, Radial$	43	$R^{-1.11}$	30	$R^{-2.02}$
$EW2, Transverse$	49	$R^{-1.22}$	35	$R^{-2.44}$
$EW2, Vertical$	27	$R^{-0.87}$	40	$R^{-1.90}$
$EWC, Radial$	52	$R^{-0.57}$	30	$R^{-1.80}$
$EWC, Transverse$	56	$R^{-1.21}$	35	$R^{-2.37}$
$EWC, Vertical$	35	$R^{-0.98}$	40	$R^{-1.82}$

Table 6.3 Distance decay rates and transition distances (R_T) for the EW shakes. The last three entries correspond to the lines of the combined data-set shown in Figure 6.7. R is the radial distance from Millikan Library, and EWC is the combined data-set.

In addition to the energy radiated away from the building during our experiments, variations in the local background noise level also contribute to the difference in the

observed amplitudes, and on which stations the building's signal can be observed. The noise level is generally more important for stations further away from the building as these stations tend to have a lower signal-to-noise ratio. However, there are many stations located in the Los Angeles basin for which our signal is undetectable due to their high noise levels. The day to day noise level differences account for the small number of observations (16 for the radial, 13 for the transverse and 11 for the vertical components) for shake EW1 as compared to the last four hours of shake EW2 (43 for the radial, 49 for the transverse, and 27 for the vertical components). The mean noise level during shake EW1 for stations that observe the signal and that are located at distances greater than 100 km from the source, is on the order of 50% higher for the radial component, 250% higher for the transverse component, and 50% higher for the vertical component than the corresponding noise levels during shake EW2. The forces exerted by the shaker on the building for the two EW shakes differ only by 0.25%, with shake EW1 having the larger excitation force. Furthermore, since no obvious source differences exist between the EW shakes, the only reasonable explanation for the difference in the number of stations observing the signal is the noise level. The noise level varies for each station, and as a result, to properly construct a single amplitude map for each of the building's natural frequencies that incorporate the data presented in Figures 6.2 and 6.3, multiple experiments would ideally be performed, and the resulting amplitude maps averaged to form composite amplitude maps. These could then be used to obtain site amplification factors.

To compute the displacement fields from a forced excitation of Millikan Library, we only use those TriNet stations which have FFT amplitudes that visibly show the building's signal and with a radiated signal amplitude, A_R at least 50% larger than the background noise level, N. We then used a Delauney interpolation (triangle based cubic interpolation) to fit the logarithms of the maximum amplitudes in space. The logarithms of the amplitudes are used since this representation helps us to recognize amplitudes that depend on some power of distance. Each component (radial, transverse, and vertical) was treated independently to observe possible radiation patterns. As can be seen from Figures 6.2 through 6.5, there does not appear to be any

evident surface radiation pattern. We took the ratio of the radial versus the vertical component amplitudes to examine if we were observing surface waves regionally, but this ratio varies significantly from station to station, which implies that single outward-travelling fundamental Rayleigh waves are not being observed.

The distance dependence of the recorded displacements is shown in Figure 6.7. This plot contains a subset of the data presented in Figure 6.6, only including data for distances greater than 10 km from Millikan Library, to avoid biasing the linear fits near the source (due to a lack of azimuthal coverage for the stations close to the library). It is interesting to see that the smallest measured displacements are slightly smaller than the minimum reported resolution of $\sim$ 1x10^{-10} m (*Clinton and Heaton*, 2002) for an $STS-2$ seismometer for the frequencies of interest to us. To observe these very weak signals, we need to take the FFT of a long time window containing the building's monochromatic signal to observe these very weak signals.

Figure 6.6 is a plot of distance normalized displacement versus azimuth. As it clearly shows, there is no apparent radiation pattern for any of the components. The displacements shown have been corrected for distance (to 1 km) using the best fitting distance decay rates shown in Figure 6.7 and given in Tables 6.2 and 6.3, to be able to compare the relative displacements at different distances for each individual shake. If the distance correction is made assuming a single distance decay rate (instead of the distance decay rates determined using two separate sections shown in Figure 6.7), there is also no evident radiation pattern. Figure 6.9 shows the normalized distance decay rates for the individual shakes (in the same manner as in Figure 6.8), and each experiment is normalized independently. As a result, sometimes there is an offset between the two data-sets shown. The x's represent the first shake for that particular excitation direction, and the best-fit line is shown by a dashed line. Similarly, the o's represent the second shake (chronologically), and the vertical lines associated with each point are the error bars.

Figure 6.7 suggests a decrease in the distance decay rate at approximately 45 km (transition distance, R_T) for the NS shakes and 30 km for the EW shakes. The distance decay rates are approximately $R^{-2.4}$ ($r < 45$ km) and $R^{-1.6}$ ($r > 45$ km)

for the NS shakes ($f \sim 1.64$ Hz) and $R^{-1.0}$ ($r < 35$ km) and $R^{-1.9}$ ($r > 35$ km) for the EW shakes ($f \sim 1.11$ Hz). R_T is defined to be the distance at which the data shows a change in slope on a plot of logarithmic amplitude versus logarithmic distance. Its value is determined by minimizing the error between the fitted lines and the data, and varying R_T by 5 km steps. Furthermore, there is an objective measure to choosing the best fitting lines. The two lines must come close to intersecting near the transition distance in order to maintain continuity in the generated displacement field with distance. The data for shake EW1 is unreliable, as the number of stations that recorded the shake above the noise level is very small.

The slope changes in the data indicate that for a NS shake, once the waves travel to a distance greater than 45 km, they behave like lightly attenuated body waves, but at smaller distances the waves are attenuated much faster. The opposite seems to be true for an EW shake, but with a shorter transition distance. This behavior is complex and contradicts a ray theory explanation at the two frequencies at which the experiments were conducted. This suggests that more experiments should be performed to investigate whether the behavior for the amplitudes recorded for shake EW2 are anomalous, as the less reliable EW1 shake seems to indicate similar decay rate changes with distance to the NS shakes.

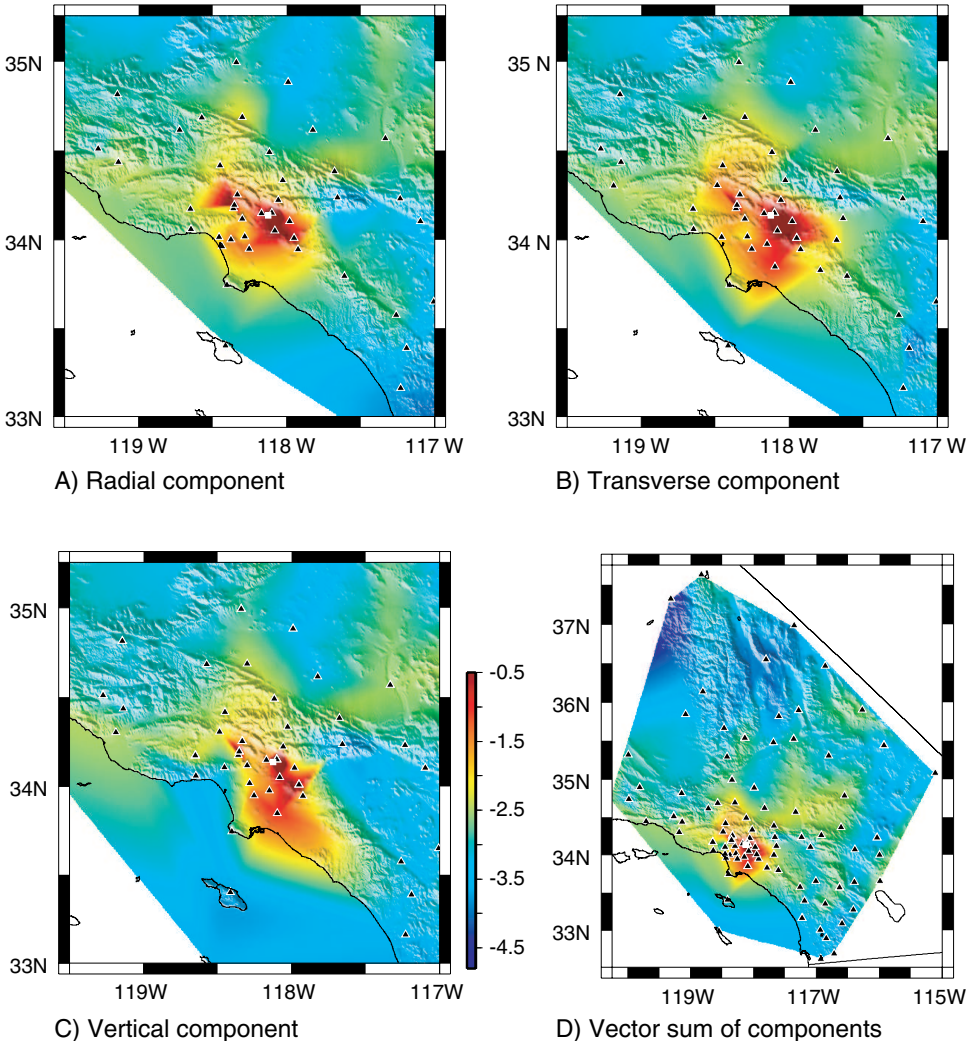

Figure 6.2 Map of Southern California with interpolated maximum displacement field for a combined data set derived from the two NS shakes (by Delauny triangulation), where the station measurements represent the mean observed displacements. Figures A-C show sub-section of the entire radiated field to highlight the Los Angeles and San Fernando basins, as they show higher displacements than the surrounding areas. Figure D shows the vector sum of all the components for a particular station where the library's signature is observed, and it shows the complete extent of the generated displacement field. The black triangles in the plots represent broadband TriNet stations, while the white square represents Millikan Library. The color bar shows displacements in microns scaled logarithmically (base 10), and is saturated at -0.5 (.316 microns). Note that no radiation pattern is evident.

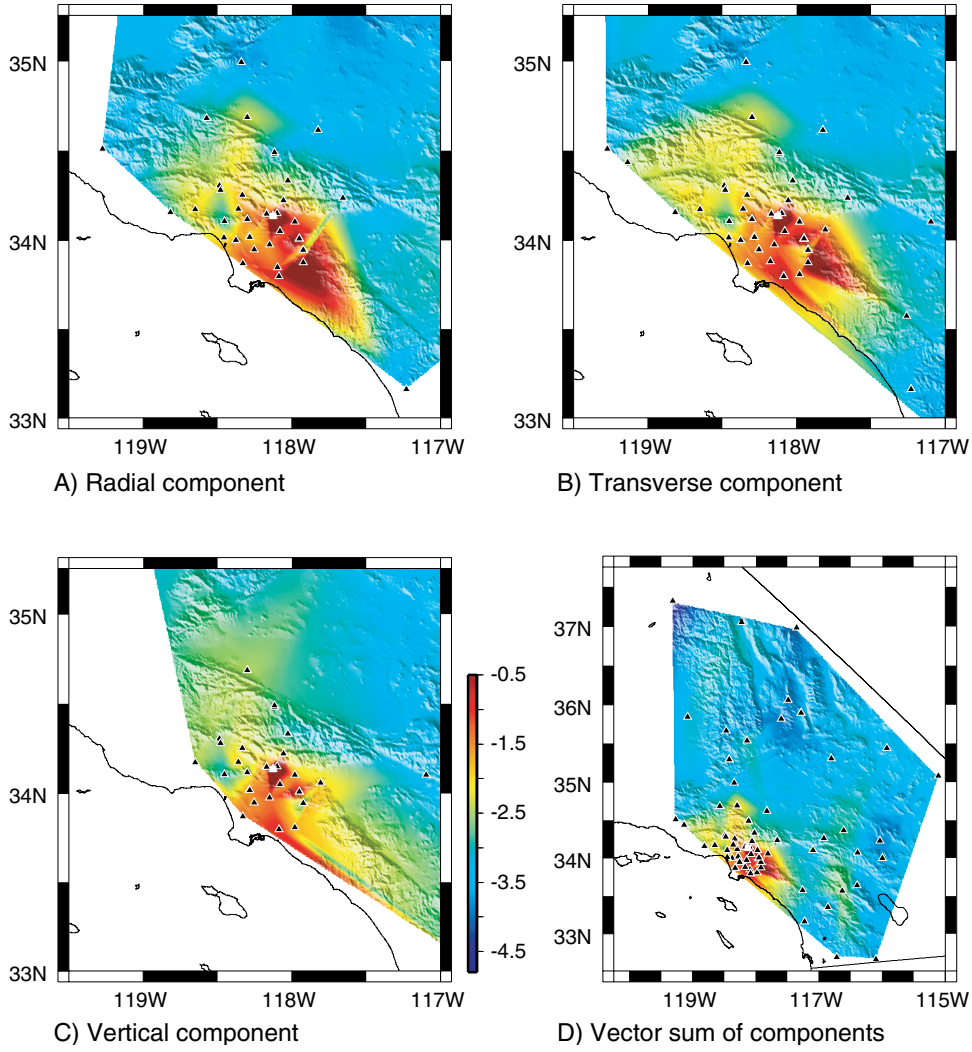

Figure 6.3 Same as Figure 6.2, except for the EW combined shakes.

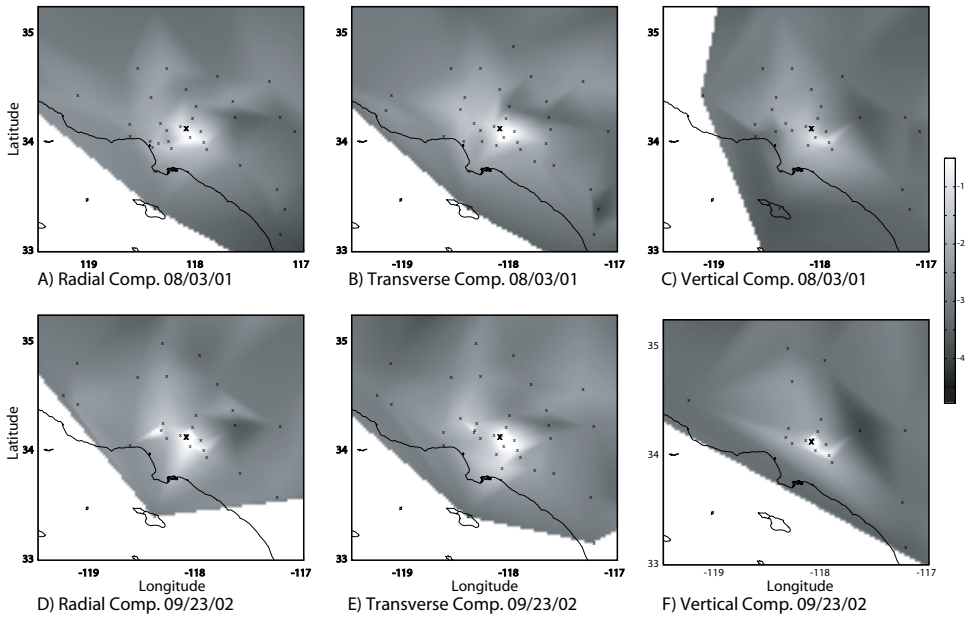

Figure 6.4 Map of Southern California with interpolated maximum displacement field for the individual data sets for the two NS shakes (by Delauny triangulation). Figures A-C and D-F show the same sub-sections as those presented in Figure 6.2 for NS1 and NS2 respectively. The black x's in the plots represent broadband TriNet stations, while the large black X represents Millikan Library. The color bar shows displacements in microns scaled logarithmically (base 10), and is saturated at -0.5 (.316 microns).

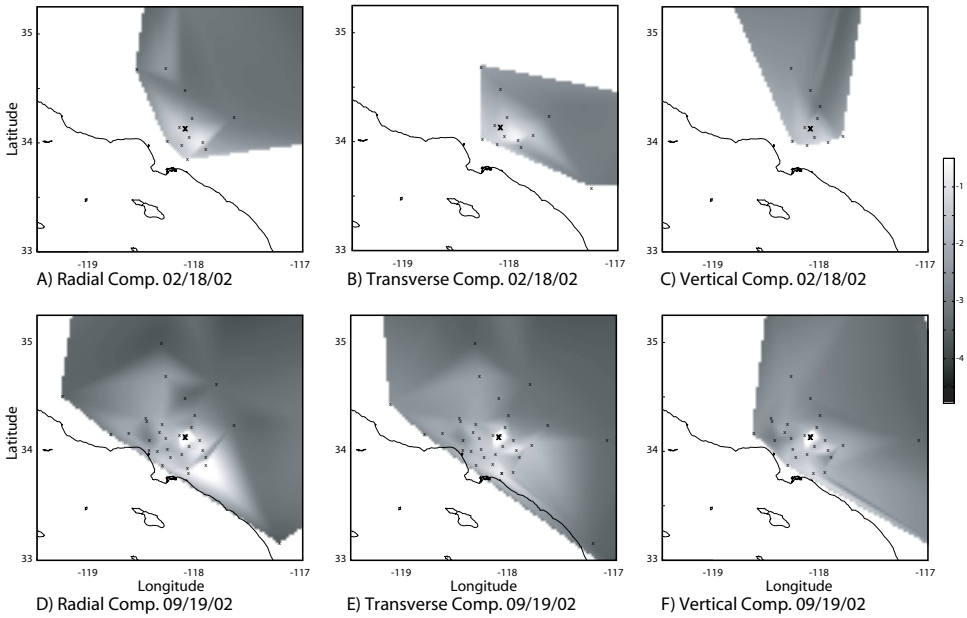

Figure 6.5 Same as Figure 6.4, except for the individual EW shakes.

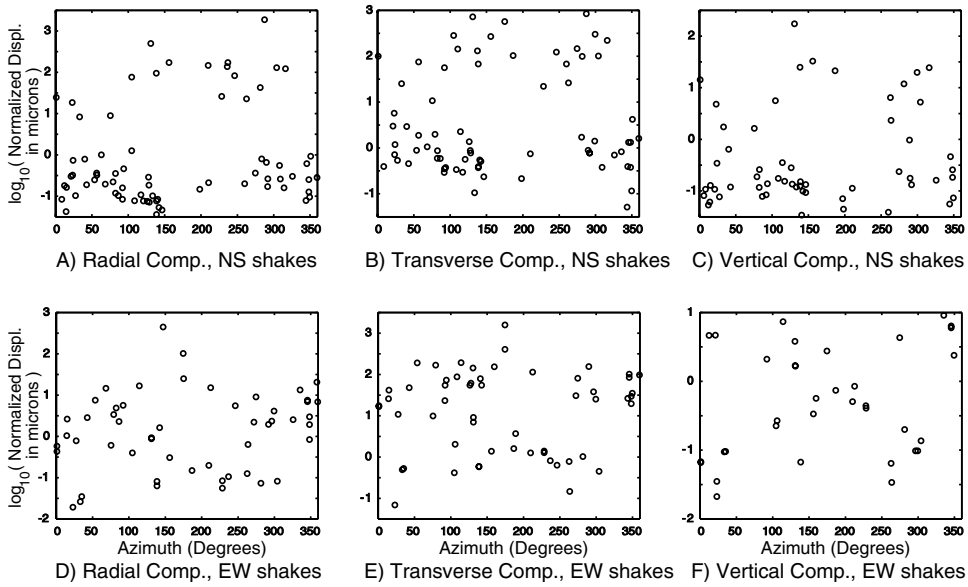

Figure 6.6 Azimuthal dependence of the displacements corrected for distance decay rates. Figures A-C are the data for the NS shakes; circles represent the mean observed displacements at the TriNet stations. Figures D-F are the same as figures A-C for the EW shakes. Figures A and D show the data for the radial component, figures B and E for the transverse component, and figures C and F for the vertical component. The displacements are given in microns. The data shown for each experiment has been corrected for its best distance decay rates as shown in Figure 6.7, to a distance of 1 km.

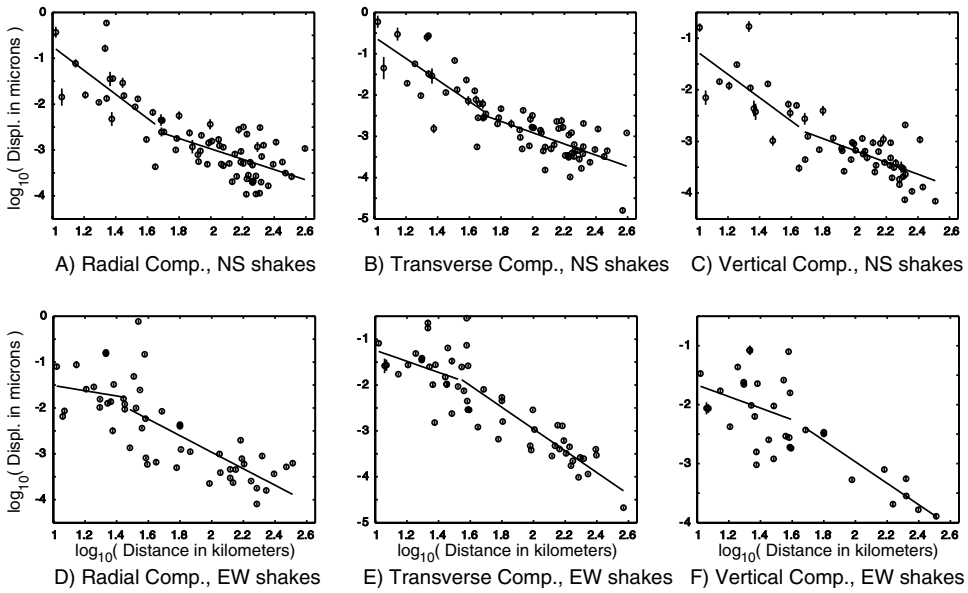

Figure 6.7 Displacement distance decay curves. Figures A-C present data for the NS shakes, with the circles representing the mean observed displacements at the TriNet stations for their respective shakes. Figures D-F are the same as figures A-C for the EW shakes. figures A and D show the data for the radial component, figures B and E for the transverse component, and figures C and F for the vertical component. Two independent lines were fit to the data (in log-log space), with the best fitting lines for each component and each shake shown in this plot. The displacements are given as the logarithm (base 10) of the displacement in microns. The error bars in the data represent the standard deviation of the noise level, as described in the method part of this article.

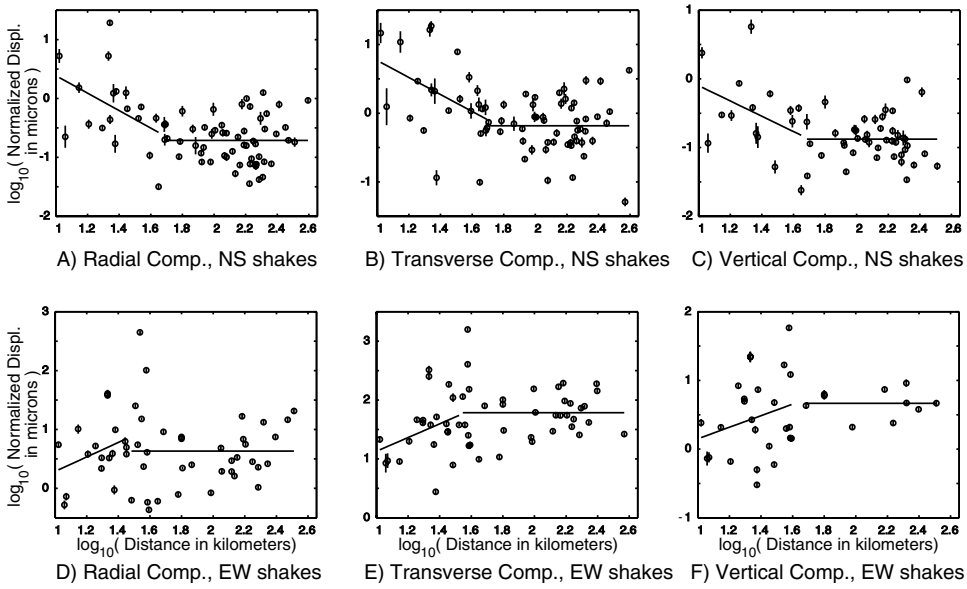

Figure 6.8 As Figure 6.7, except that the displacements for each shake have been corrected for the distance decay of the stations further than the transition distance (R_T) for the individual shakes. As a result, both shakes show a horizontal line for the fit of the stations past the transition distance. The displacements are given as the logarithm (base 10) of the displacement in microns, with a correction for the distance decay.

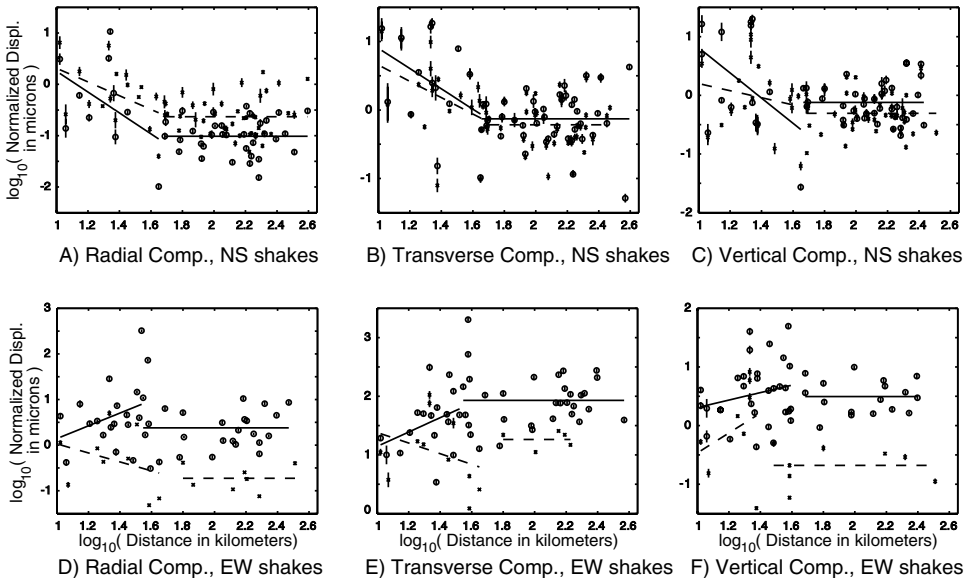

Figure 6.9 Same as Figure 6.8, except that the individual shakes are given in each plot. The x's represent the first shake for that particular excitation direction, and the best-fit line is shown by a dashed line. Similarly, the o's represent the second shake (chronologically), and the vertical lines associated with each point are the error bars. The normalization is done for each experiment independently, and as a result, an offset is common when the distance decay rates are significantly different for the two experiments.

6.2 Signal Velocities

6.2.1 Method and Results

Using the same data-sets described in the previous section, a method was devised to extract arrival times for the signal generated by the long shakes. If arrival times can be accurately determined for each station, it will then be possible to estimate signal velocities (as defined in *Brillouin* (1960)). These signal velocities can greatly improve our understanding of the travel paths for the observed waves, as well as help explain the kink in the displacement data in the previous section.

Due to the small signal-to-noise ratios, the data is again converted into the frequency domain to extract information from the observed sinusoids at each station. Utilizing the same method to compute the sinusoidal amplitudes as discussed in Section 6.1.1, I performed a running FFT (RFFT) on the data. The RFFT is modelled after a narrow frequency band spectrogram, and it involves a sliding window over the time domain trace. For each step in the time domain window, the FFT of the data within the sliding window is taken, and then the time domain sinusoidal amplitudes are computed for the RSB as previously discussed, creating an amplitude envelope function for the waveform. These envelope functions are then correlated with those of station MIK to estimate the signal arrival times.

Due to the large quantities of data involved, it is not feasible to perform the RFFT with one sample time steps, and therefore certain variables have to be chosen to speed up the process. These variables are the number of samples in the time domain to skip between each FFT, and also the length of the sliding time window. These two quantities were varied significantly, and a sliding time window 2100 seconds in duration in combination with skipping every 8 samples made the process feasible, given the available computation power. The 2100 seconds long sliding window is shorter than the noise window recorded prior and after each of the shakes (data window without the building's signal present), guaranteeing that the initial and final RFFT values are representative of the noise level for the station. This sliding window is also long enough to observe the building's signal at many of the stations where the

signal was observed using the entire 4 and 6 hour shakes in one long FFT. Utilizing a window this small is similar to performing only a 35 minute shake, which obviously decreases the signal-to-noise ratios in the FFTs as compared to those of the long shakes, but still generates envelope functions that are very similar to those of station MIK. The choice of the number of samples to skip depends on the desired accuracy, as the errors introduced by using larger numbers become larger. For a 20 sps datastream, as was used for this study, skipping 8 samples translates into a minimum error for the measured time shift of ± 0.2 seconds. However, for greater accuracy, the error can be minimized by decreasing the number of samples skipped.

Figure 6.10 shows the raw velocity traces (in counts) and the corresponding RFFTs for four TriNet stations. All RFFTs clearly have very similar characteristics, and the amplitude variations with time appear to correlate well for all the stations. However, the rise and fall time of the signal (the time it takes the signal to grow to the maximum envelope value and to fall to the noise level) varies between all stations. A similar variation in rise and fall time can be seen for the three different components at each station, which results in different signal velocities for each component from methods similar to and including the RFFT method. The source of this error is believed to be the different noise levels for the components as well as at each of the stations. Furthermore, the noise also leads to short period variations in the envelope functions, which further decreases the correlation accuracy.

In order to validate the results from the RFFT, they are compared with filtered time domain correlations for the same traces, and with hand-picked arrival times. The hand-picked arrival times are estimated by examining a variety of differently filtered data, as well as by utilizing all three components per station. Since the correlation methods allow each component to have a different arrival time, the data-set was limited to those stations for which at least two components had similar arrival time estimates for either the time domain correlations or for the RFFTs. The similar arrival times are then averaged per station and that number is considered to be the station's arrival time. The arrival times from these three methods were then transformed to signal velocities by taking the distance from source to station and dividing it by the

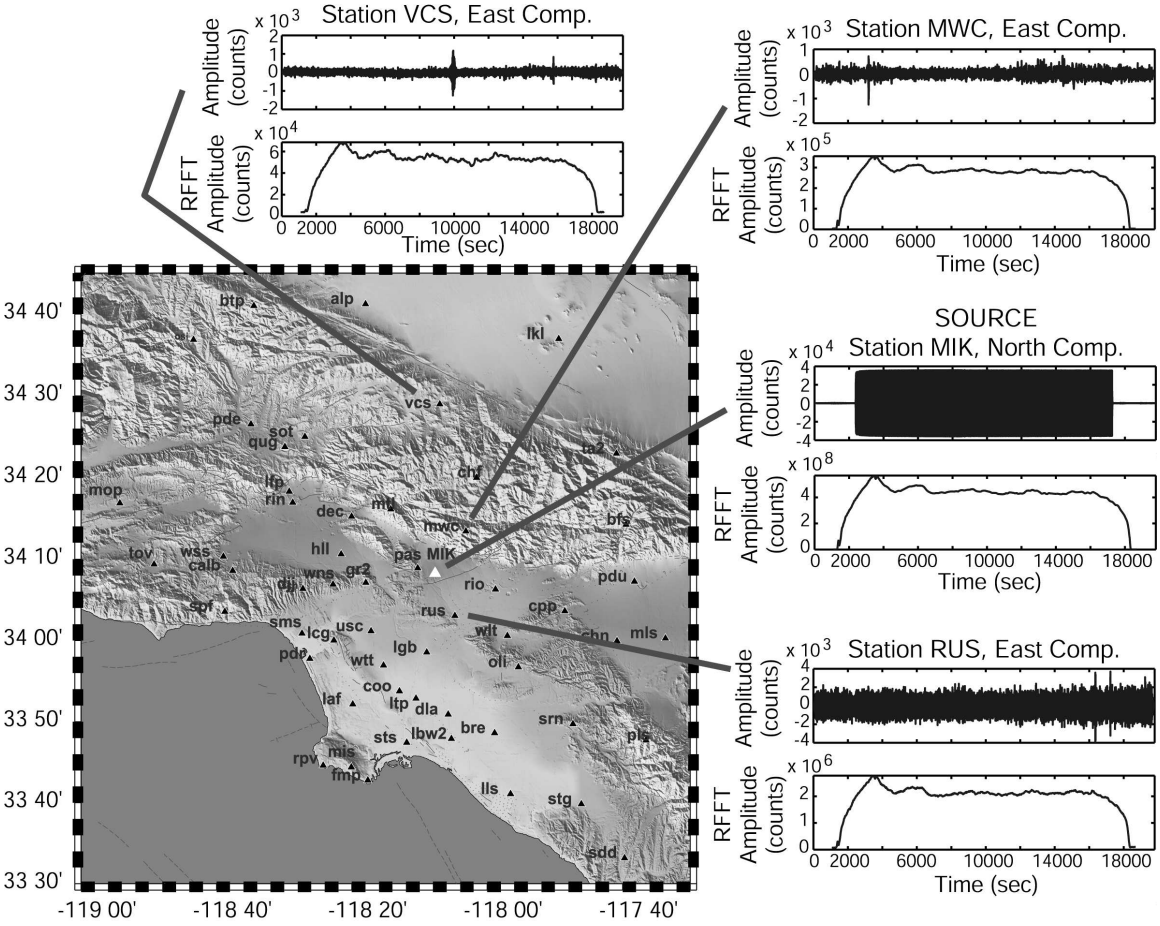

Figure 6.10 Running FFTs for four TriNet stations. The top trace for each station corresponds to the raw time domain velocity values for the station (in counts), while the bottom trace shows the RFFT that corresponds to each station. Station MIK is located on the 9th floor of Millikan Library, the source of the radiated signal.

arrival times. The signal velocities for shake NS1 are presented in Figure 6.11. There is some scatter to the data, but there is strong agreement for all three methods at distances smaller than 15 km from the source, indicating a velocity of approximately 600 m/s. Unfortunately, this distance is much smaller than the transition distance (R_T) observed in the previous section, and thus this data-set does not provide any information on the cause of the decay rate changes. However, the slow velocities at close distances agree with the results from Chapter 5, indicating that at these

distances the waves seem to be trapped in the upper few hundred meters.

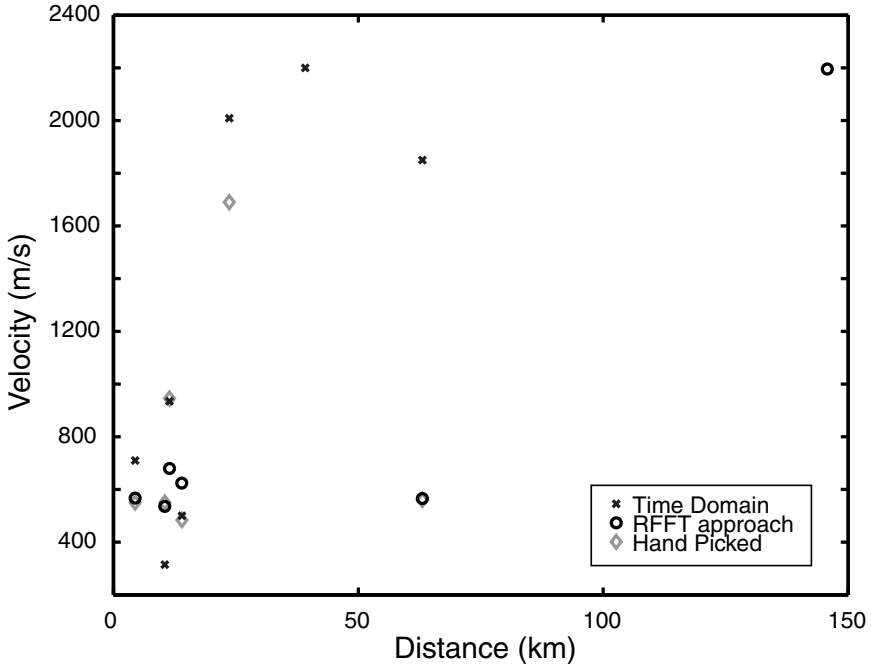

Figure 6.11 Signal velocities for stations which had two components with similar velocity values (using either the RFFT or the time domain correlations). The x's represent signal velocity measurements from time domain correlations, the circles from the RFFT method, and the diamonds are hand-picked signal velocity estimates.

6.3 Conclusions

The forced vibrations of Millikan Library generate very small displacements throughout Southern California, as can be seen in Figure 6.2. It is remarkable that such small building motions ($\sim$ 1.5 mm peak to peak at the roof) generate signals observable at distances close to 400 km. The building's signal can be observed at such great distances due to the constant monochromatic generation of waves by using the building's shaker. This steady nature of the generated waves is ideally suited for the use of Fourier transforms to analyze the data, which achieves higher resolution than would be expected from a time domain analysis. Furthermore, it is necessary to work in the

frequency domain, as the time domain signal is usually well below the ambient noise level and the instrument sensitivity.

Our analysis of the recorded waveforms shows that it is unlikely that surface waves are being observed, even though the building is in a good location to generate them (the surface). Since the geometric attenuation of surface waves is less than that of body waves, it is expected that surface waves be observed at the distances of observation. However, the observed decay rates are more characteristic of body rather than surface waves. An apparent decrease in the distance decay rates at a distance of approximately 45 km from the source is observed for the NS shakes, while the opposite seems to be occurring for the EW shakes. Further experiments are necessary to resolve the possible causes of this change in decay rates, as one of the four experiments suggests contradictory behavior to the other three experiments, and as a result, no explanation for the possible causes of the change in decay rates can be offered at this point in time. However, the signal velocities suggest that for stations at distances shorter than the transition distance are travelling in the upper few hundred meters of the crust. Perhaps at some distance, there is enough leakage of this energy into deeper layers travelling at different attenuation levels to be observable. The properties of the observed sinusoidal waves appear to change with frequency as well as with distance. The EW ($f \sim 1.11$ Hz) and the NS ($f \sim 1.64$ Hz) shakes produce different results, indicating a complex interaction of the waves with the crust. In principle, reciprocity could be used to infer how the fundamental modes of the library would be excited by sources located at the seismic stations.

This is the first time that vibrations from a building have been observed at such large distances. Since the building displacements are very small, the structure behaves linearly and no damage is incurred by the building. As a result, the same experiments can be repeated multiple times.

Appendix A

Millikan's Natural Frequencies below 9.5 Hz and Accelerometer Data

The following table lists the general location and instrument type of the FBAs located inside of Millikan Library at the time of the experiments. More precise locations can be found in the EERL report following the table. This report documents the dynamic properties of Millikan Library under forced excitations for frequencies less than 9.5 Hz. as well as a frequency sweep of the EW and NS directions. It is relevant to the context of this thesis, and as a result, it is included almost in its entirety and reproduced as published.

Floor	*FBA type*	*Orientation & Azimuth*	*Location within Building*
Bsmnt	*FBA* 11 – 1*g*	*Horizontal* 360	*North East corner*
Bsmnt	*FBA* 11 – 1*g*	*Vertical*	*North East corner*
Bsmnt	*FBA* 11 – 1*g*	*Horizontal* 270	*North East corner*
Bsmnt	*FBA* 11 – 1*g*	*Horizontal* 360	*North West corner*
Bsmnt	*FBA* 11 – 1*g*	*Vertical*	*North West corner*
Bsmnt	*FBA* 11 – 1*g*	*Vertical*	*South East corner*
1	*FBA* 11 – 1*g*	*Horizontal* 360	*East, access from Bsmnt*
1	*FBA* 11 – 1*g*	*Horizontal* 270	*West, electrical room*
1	*FBA* 11 – 1*g*	*Horizontal* 360	*West, electrical room*
2	*FBA* 11 – 1*g*	*Horizontal* 360	*East, small conf. room*
2	*FBA* 11 – 1*g*	*Horizontal* 270	*West, electrical room*
2	*FBA* 11 – 1*g*	*Horizontal* 360	*West, electrical room*
3	*FBA* 11 – 1*g*	*Horizontal* 360	*East*
3	*FBA* 11 – 1*g*	*Horizontal* 270	*West, electrical room*
3	*FBA* 11 – 1*g*	*Horizontal* 360	*West, electrical room*
4	*FBA* 11 – 1*g*	*Horizontal* 360	*East*
4	*FBA* 11 – 1*g*	*Horizontal* 270	*West, electrical room*
4	*FBA* 11 – 1*g*	*Horizontal* 360	*West, electrical room*
5	*FBA* 11 – 1*g*	*Horizontal* 360	*East*
5	*FBA* 11 – 1*g*	*Horizontal* 270	*West, electrical room*
5	*FBA* 11 – 1*g*	*Horizontal* 360	*West, electrical room*
6	*FBA* 11 – 1*g*	*Horizontal* 360	*East*
6	*FBA* 11 – 1*g*	*Horizontal* 270	*West, electrical room*
6	*FBA* 11 – 1*g*	*Horizontal* 360	*West, electrical room*
7	*FBA* 11 – 1*g*	*Horizontal* 360	*East*
7	*FBA* 11 – 2*g*	*Horizontal* 270	*West, electrical room*
7	*FBA* 11 – 2*g*	*Horizontal* 360	*West, electrical room*
8	*FBA* 11 – 2*g*	*Horizontal* 360	*East*
8	*FBA* 11 – 2*g*	*Horizontal* 270	*West, electrical room*
8	*FBA* 11 – 2*g*	*Horizontal* 360	*West, electrical room*
9	*FBA* 11 – 2*g*	*Horizontal* 360	*East*
9	*FBA* 11 – 2*g*	*Horizontal* 270	*West, electrical room*
9	*FBA* 11 – 2*g*	*Horizontal* 360	*West, electrical room*
Roof	*FBA* 11 – 2*g*	*Horizontal* 360	*East*
Roof	*FBA* 11 – 2*g*	*Horizontal* 270	*West, electrical room*
Roof	*FBA* 11 – 2*g*	*Horizontal* 360	*West, electrical room*

Table A.1 Accelerometer descriptions and locations for Millikan Library for the June 15, 1997 test date. The 36 channels are recorded using two 18 channel Mt. Whitney recorders.

CALIFORNIA INSTITUTE OF TECHNOLOGY

EARTHQUAKE ENGINEERING RESEARCH LABORATORY

RESULTS OF MILLIKAN LIBRARY FORCED VIBRATION TESTING

BY

S C BRADFORD, J F CLINTON, J FAVELA, T H HEATON

REPORT NO. EERL 2004-03

PASADENA, CALIFORNIA

FEBRUARY 2004

ACKNOWLEDGMENTS

The authors would like to acknowledge Arnie Acosta for data triggering and retrieval, and thank him for his support. We thank Caltech's Structural Monitoring Group for their input during this project, and we also thank the Southern California Earthquake Center and the Portable Broadband Instrumentation Center at the University of California Santa Barbara for the loan of the portable instrument. We acknowledge the SCEDC for the MIK data.

A report on research supported by the

CALIFORNIA INSTITUTE OF TECHNOLOGY

ABSTRACT

This report documents an investigation into the dynamic properties of Millikan Library under forced excitation. On July 10, 2002, we performed frequency sweeps from 1 Hz to 9.7 Hz in both the East-West (E-W) and North-South (N-S) directions using a roof level vibration generator. Natural frequencies were identified at 1.14 Hz (E-W fundamental mode), 1.67 Hz (N-S fundamental mode), 2.38 Hz (Torsional fundamental mode), 4.93 Hz (1^{st} E-W overtone), 6.57 Hz (1^{st} Torsional overtone), 7.22 Hz (1^{st} N-S overtone), and at 7.83 Hz (2^{nd} E-W overtone). The damping was estimated at 2.28% for the fundamental E-W mode and 2.39% for the N-S fundamental mode. On August 28, 2002, a modal analysis of each natural frequency was performed using the dense instrumentation network located in the building. For both the E-W and N-S fundamental modes, we observe a nearly linear increase in displacement with height, except at the ground floor which appears to act as a hinge. We observed little basement movement for the E-W mode, while in the N-S mode 30% of the roof displacement was due to basement rocking and translation. Both the E-W and N-S fundamental modes are best modeled by the first mode of a theoretical bending beam. The higher modes are more complex and not well represented by a simple structural system.

A:1 INTRODUCTION

This report documents the forced vibration testing of the Robert A. Millikan Memorial Library located on the California Institute of Technology campus. It also provides a historical backdrop to put our results in perspective.

During and immediately after the construction of the library in the late 1960s, numerous dynamic analyses were performed (Kuroiwa, 1967; Foutch et al, 1975; Trifunac, 1972; Teledyne-Geotech-West, 1972). In these analyses, fundamental modes and damping parameters were identified for the library, and higher order modes were suggested, but not investigated. It has been established that the fundamental frequencies of the library vary during strong motion (Luco et al, 1986; Clinton et al, 2004). Some drift in the long-term behavior of the building has also been observed in compiled reports of modal analysis from the CE180 class offered every year at Caltech (Clinton, 2004).

The temporal evolution of the building's dynamic behavior, as well as the much improved density and quality of instrumentation, led to an interest in a complete dynamic investigation into the properties of the system. Our experiments were designed to provide an updated account of the fundamental modes, and to identify and explore the higher order modes and modeshapes. A better understanding of the dynamic behavior of the Millikan Library will aid in the increased research being performed on the building, and provide a better understanding of the data currently being recorded by the instruments in the library.

An initial test was performed on July 10, 2002, for which we performed a full frequency sweep of the building (from 9.7Hz, the limit of the shaker, to 1Hz), in both the E-W and N-S directions. Frequencies of interest were explored in more detail, with a finer frequency spacing and different weight configurations, during a second test on August 28, 2002.

Figure A:1. Robert A. Millikan Memorial Library: View from the Northeast. The two dark colored walls in the foreground comprise the East shear wall.

A:2 MILLIKAN LIBRARY

The Millikan Library (Figure A:1) is a nine-story reinforced concrete building, approximately 44m tall, and 21m by 23m in plan. Figure A:2 shows plan views of the foundation and a typical floor, as well as cross-section views of the foundation and a N-S cross-section.

The building has concrete moment frames in both the E-W and N-S directions. In addition, there are shear walls on the East and West sides of the building that provide most of the stiffness in the N-S direction. Shear walls in the central core provide added stiffness in both directions. More detailed descriptions of the structural system may be found in Kuroiwa (1967), Foutch (1976), Luco et al. (1986), Favela (2004) and Clinton (2004).

A:2.1 Historical Information

The Millikan Library has been extensively monitored and instrumented since its completion in 1966 (Kuroiwa, 1967; Trifunac, 1972; Foutch, 1976; Luco et al, 1986; Chopra, 1995). Clinton et al. (2004)

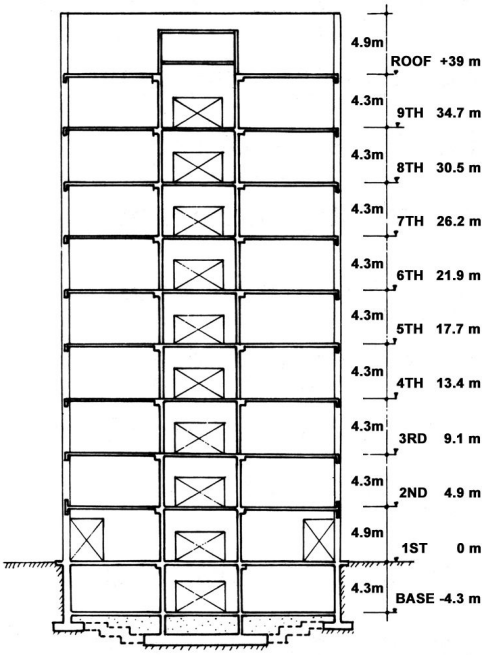

(a) North South Cross Section

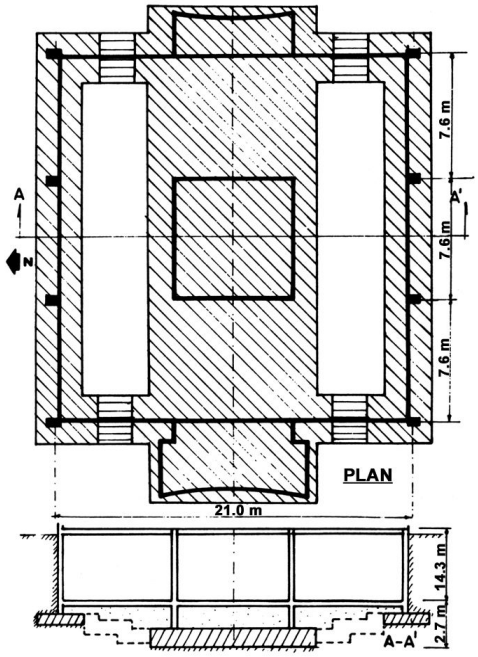

(b) Foundation Plan View and North-South Cross Section

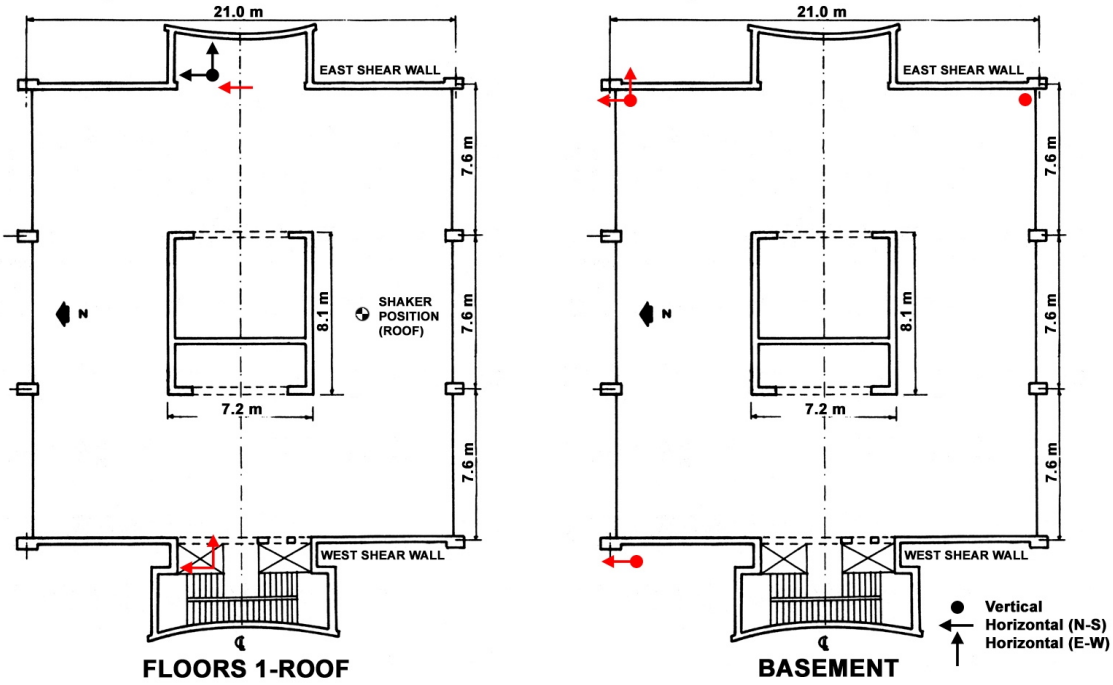

(c) Floor Plan and Instrumentation of Millikan Library, dense instrument array shown in red, station MIK (on 9th floor) shown in black. Shaker position (roof level) also shown.

Figure A:2. Millikan Library Diagrams

has summarized some of the previous data on Millikan Library's behavior under forced and ambient vibrations in Appendix A:6. The evolution of the building behavior, including some dramatic shifts in the fundamental modes, is documented in Clinton et al. (2004) and is reproduced here in Table A:2 and Figure A:3. A drop of 21% and 12% for the E-W and N-S fundamental modes since construction is noted. The primary cause for these shifts appears to be a permanent loss of structural stiffness which occurs during strong ground motions, most noticeably the San Fernando (1979) and Whittier Narrows (1987) events. Small fluctuations in natural frequencies have also been noted which can depend on weather conditions at the time of testing (Bradford and Heaton, 2004), in particular, the E-W and torsional fundamental frequencies have increased by $\sim$3% in the days following large rainfalls. The frequencies observed during ambient studies also differ from the frequencies observed during forced vibration tests (Clinton et al, 2004).

Event/Test	**East - West**				**North - South**			
	Nat Freq. *Hz*	**%diff1**	**%diff2**	**mx accn** cm/s^2	**Nat Freq.** *Hz*	**%diff1**	**%diff2**	**mx accn** cm/s^2
forced vibrations, 1967	1.45	-	-	**-**	1.90	-	-	**-**
Lytle Creek, 1970 M5.3, Δ=57km	1.30	10.3	10.3	**49**	1.88	1.1	1.1	**34**
San Fernando, 1971 M6.6, Δ=31km	1.0	31.0	31.0	**306**	1.64	13.7	13.7	**341**
forced vibrations, 1974	1.21	16.6	16.6	**-**	1.77	6.8	6.8	**-**
Whittier Narrows, 1987 M6.1, Δ=19km	1.00	31.0	17.4	**262**	1.33	30.0	24.9	**534**
forced vibrations, 1988	1.18	18.6	2.5	**-**	1.70	10.5	4.0	**-**
Sierra Madre, 1991M5.8, Δ=18km	0.92	36.6	22.0	**246**	1.39	26.8	18.2	**351**
forced vibrations, 1993	1.17	19.3	0.8	**-**	1.69	11.1	0.6	**-**
Northridge, 1994 M6.7, Δ=34km	0.94	35.2	19.7	**143**	1.33	30.0	21.3	**512**
forced vibrations, 1994	1.15	20.6	1.7	**-**	1.67	12.1	1.2	**-**
forced vibrations, 1995	1.15	20.6	0.0	**-**	1.68	11.6	-0.6	**-**
Beverly Hills, 2001 M4.2, Δ=26km	1.16	20.0	-0.9	**9.3**	1.68	11.6	0.0	**11.8**
forced vibrations, 2002 - Full Weights	1.11	23.4	3.5	**3.6**	1.64	13.7	2.4	**8.0**
- 1/2 weights	1.14	21.4	0.9	**1.9**	1.67	12.1	0.6	**4.1**
Big Bear, 2003 M5.4, Δ=119km	1.07	26.2	6.1	**14.2**	1.61	15.3	3.6	**22.6**

Table A:2. History of Millikan Library Strong Motion Behavior - Fundamental Modes. "%diff1" is the difference between the recorded frequency and that obtained in the first forced vibration tests (Kuroiwa, 1967). "%diff2" is the difference between the recorded frequency and that obtained in the most recent forced vibration test prior to the event. (adapted from Clinton, (2003))

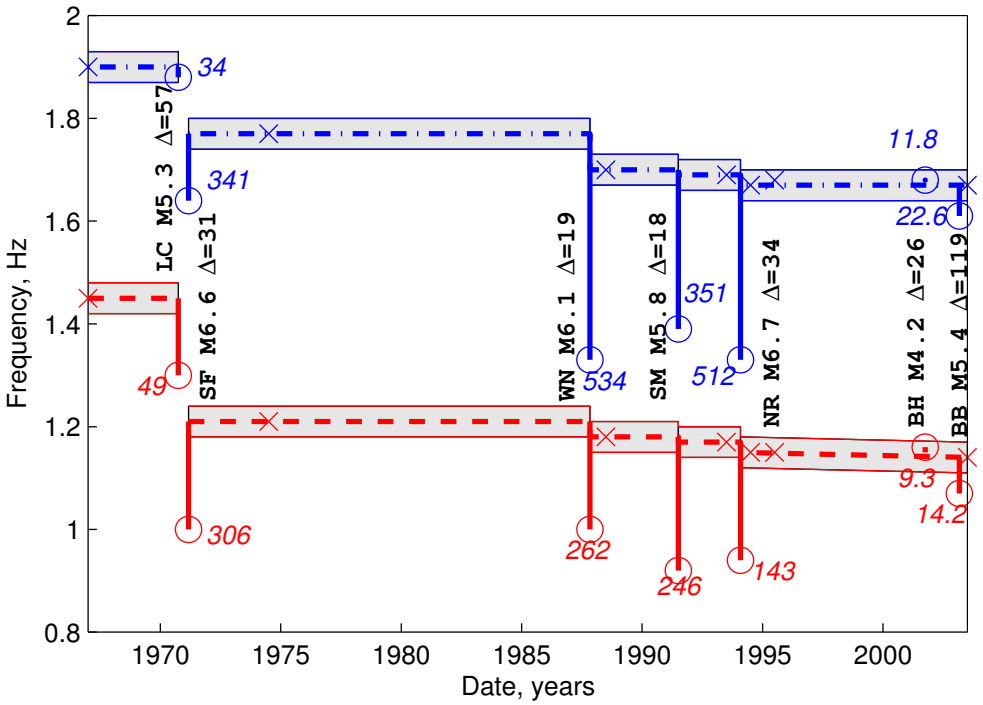

Figure A:3. Graphical depiction of Table A:2. Dashed lines represent the E-W natural frequencies and the dashed-dotted lines represent the N-S natural frequencies. Shaded area is the likely range of natural frequencies taking into consideration errors in measurement due to various factors - weight configuration in the shaker, weather conditions at the time of the test, and experimental error. Crosses indicate actual time forced test was made. Circles indicate natural frequency estimates from the strong motion record during earthquake events, and numbers in italics are peak acceleration recorded for the event (cm/s^2). [Earthquake Abbreviations: LC: Lytle Creek, SF: San Fernando, WN: Whittier Narrows, SM: Santa Monica, NR: Northridge, BH: Beverly Hills, BB: Big Bear] (adapted from Clinton, (2003))

A:2.2 Millikan Library Shaker

A Kinemetrics model VG-1 synchronized vibration generator ("shaker") was installed on the roof of Millikan Library in 1972 (Figure A:4). The shaker has two buckets that counter-rotate around a center spindle. These buckets can be loaded with different configurations of lead weights, and depending on the alignment of the buckets, the shaker can apply a sinusoidal force in any horizontal direction. The force (F_i) applied by the shaker in each of its configurations can be expressed as:

$$F_i = A_i f^2 \sin(2\pi f t) \qquad \begin{aligned} A_1 &= 235.73\ N \cdot sec^2 \\ A_2 &= 1518.67\ N \cdot sec^2 \\ A_3 &= 3575.89\ N \cdot sec^2 \end{aligned} \qquad \textbf{(A:1)}$$

Frequency, f, is in Hz; A_i (a shaker constant) is in N·sec^2; and the resulting force, F_i, is in units of N. Table A:3 lists the values of A_i and the limiting frequency for each weight configuration. For our test we used three shaker levels: A_3, full weights with the buckets loaded at 100% of capacity; A_2, an intermediate configuration with two large weights in each of the large weight sections of each bucket, corresponding to 42.5% of the mass of the full buckets; and A_1, empty buckets, which corresponds to a shake factor of 6.6% of the full weight configuration.

We can strongly excite the torsional modes through E-W shaking, as the shaker is located $\sim$6.1 meters to the South of the building's N-S line of symmetry (Figure A:2c). The shaker is located $\sim$0.3 meters to the East of the building's E-W centerline, and therefore we do not expect shaking in the N-S direction to effectively excite the building in torsion.

Figure A:4. Kinemetrics VG-1 Synchronized Vibration Generator (Shaker). The counter-rotating buckets, shown empty, can be loaded with different configurations of lead weights. The shaker is located on the roof of Millikan Library, as shown in Figure A:2.

Small Weights

Large Weights	0	1	2	3	4
0	**235.73 [9.7]**	429.31 [7.2]	622.88 [6.0]	816.45 [5.2]	1010.03 [4.7]
1	877.20 [5.0]	1070.77 [4.6]	1264.35 [4.2]	1457.92 [3.9]	1651.49 [3.7]
2	**1518.67 [3.8]**	1712.24 [3.6]	1905.81 [3.4]	2099.39 [3.3]	2292.96 [3.1]
3	2160.13 [3.2]	2353.71 [3.1]	2547.28 [3.0]	2740.85 [2.8]	2934.43 [2.8]
4	2801.60 [2.8]	2995.17 [2.7]	3188.75 [2.6]	3382.32 [2.6]	**3575.89 [2.5]**

Table A:3. Shaker constant, A_i (N·sec^2), and limiting frequencies [Hz] for different configurations of lead weights in the shaker. Bold type indicates the configurations used in these experiments.

A:2.3 Millikan Library Instrumentation

In 1996 the United States Geological Survey (USGS) and the Caltech Department of Civil Engineering installed a permanent dense array of uni-axial strong-motion instruments (1g and 2g Kinemetrics FBA-11s) in the Millikan Library, with 36 channels recording on two 19-bit 18-channel Mt. Whitney digitizers. The instruments are distributed throughout the building, with three horizontal accelerometers located on each floor and three vertical instruments in the basement. This dense array is recorded by the Mt. Whitney digitizer system, providing local hard-drive storage of triggered events. In 2001 a 3-component Episensor together with a 24-bit Q980 data logger was installed on the 9th floor. Data from this sensor is continuously telemetered to the Southern California Seismic Network (SCSN) as station MIK. Figure A:2c provides a schematic of the instrument locations.

A:3 FREQUENCY SWEEP

A frequency sweep of Millikan Library was performed on July 10, 2002. This test was designed to identify the natural frequencies and their damping; modeshapes would be determined with later detailed testing.The building response was recorded using the SCSN station MIK on the 9th floor, and a Mark Products L4C3D seismometer with a 16 bit Reftek recorder on the roof (provided by the Southern California Earthquake Center (SCEC) Portable Broadband Instrument Center located at U C Santa Barbara). We also used a Ranger seismometer with an oscilloscope at the roof level to provide an estimate of roof level response during our experiment.

We began with a N-S frequency sweep and the shaker set with empty buckets, starting near the frequency limit of the shaker at 9.7Hz. We held the frequency constant for approximately 60 seconds, to allow the building response to approach steady state, and then lowered the shaker frequency, in either .05Hz or .1Hz increments, again pausing for 60 seconds at each frequency. Once we reached 3.8Hz, we turned off the shaker, and loaded it with two large weights in each of the large weight compartments in each of the buckets (the intermediate 42.5% loading configuration). We then continued the frequency sweep from 3.7Hz to 1.5Hz. This procedure was repeated for the E-W direction — driving the empty shaker from 9.7Hz to 3.8Hz, then sweeping from 3.7Hz to 1Hz using the intermediate configuration.

Figure A:5 shows normalized peak displacement curves for the frequency sweeps. For each frequency, a representative section from the steady state portion of the data was selected, bandpass filtered (0.2Hz above and below each frequency, using a 2-pass 3-pole butterworth filter), and fit to a sine wave to estimate the exact frequency, amplitude, and phase. These sinusoidal amplitudes were then normalized by the applied shaker force for the particular frequency and weight combination (Equation A:1).

Furthermore, damping was determined by applying the half-power (band-width) method (Meirovitch, 1986). We estimated the peak displacement frequency from a cubic interpolation of the normalized data,

as our data sampling is somewhat sparse for a frequency/amplitude curve. As the higher modes have too much lower mode participation to determine the half-power points, damping was only determined for the fundamental modes. Damping is estimated to be 2.28%, 2.39% and 1.43% for the E-W, N-S and Torsional fundamental modes, respectively.

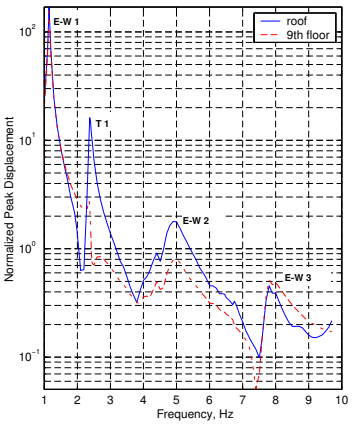

(a) East-West Response — East-West Excitation

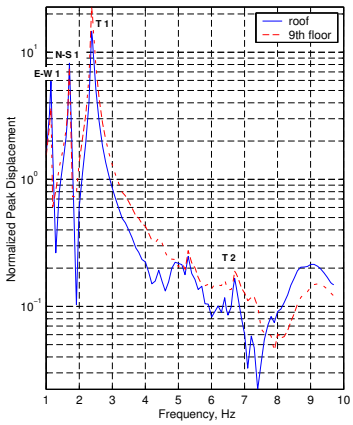

(b) North-South Response — East-West Excitation

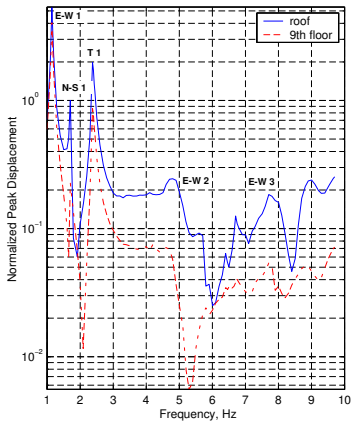

(c) Vertical Response — East-West Excitation

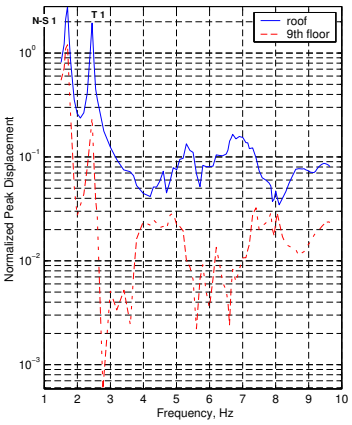

(d) East-West Response — North-South Excitation

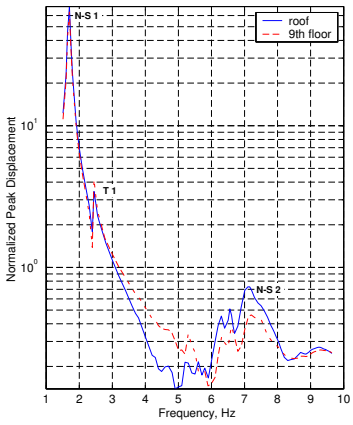

(e) North-South Response — North-South Excitation

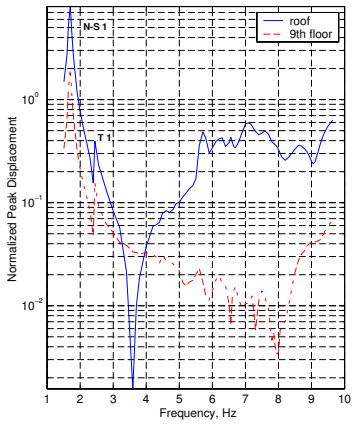

(f) Vertical Response — North-South Excitation

Figure A:5. Lin-Log normalized peak displacement curves for the frequency sweep performed on July 10, 2002. Amplitudes for E-W and N-S shaking are normalized by the force factor corresponding to the weight configuration and frequency, as calculated in Equation A:1. Roof response given by solid blue lines and station MIK (9th floor) response shown in dashed red lines.

A:4 MODESHAPE TESTING

We performed a forced excitation test of Millikan Library on August 18, 2002, recording data using the dense instrumentation network operated by the USGS and station MIK. We compare the behavior of the library with the behavior of uniform shear and bending beams (see Appendix A:5), but it is important to note that these are simple structural approximations which do not include the behavior of the foundation or the true structural system of the library.

Mode	Shake Direction/ Weight Configuration	Resonance Peak (Hz)	Normalized Roof Displacement [cm/N] x 10^{-7}	Percent Roof Displacement due to tilt and translation
Fundamental E-W	E-W / 100%	1.11	175(E-W)	3%
	E-W / 42.5%	1.14	180(E-W)	3%
Fundamental N-S	N-S / 100%	1.64	80(N-S)	30%
	N-S / 42.5%	1.67	80(N-S)	30%
Fundamental Torsion	E-W / 42.5%	2.38	25(N-S)	2% *
	N-S / 100%	2.35	5(N-S)	2% *
	N-S / 42.5%	2.38	5(N-S)	2% *
1st E-W Overtone	E-W / 6.6%	4.93	2(E-W)	1%
1st N-S Overtone	N-S / 6.6%	7.22	0.8(E-W)	-21%
1st Torsion Overtone	E-W / 6.6%	6.57	0.4(E-W) / 0.15(N-S)	23% *
	N-S / 6.6%	6.70	0.5(N-S)	23% *
2nd E-W Overtone	E-W / 6.6%	7.83	0.6(E-W)	0%

*: % of rotation recorded at roof due to basement rotation

Table A:4. Summary of Results for Modeshape Testing of August 28, 2002

A:4.1 Procedure and Data Reduction

We began the experiment with the shaker buckets fully loaded and set to excite the E-W direction. We excited the building at frequencies near the fundamental E-W and torsional modes, in frequency increments of .03-.05 Hz (again holding for 60s at each frequency to allow the building to approach steady-state response). With full buckets we then set the shaker to excite in the N-S direction to examine the fundamental N-S mode. We then repeated the excitation of the fundamental E-W, N-S and torsional

modes with the intermediate 42.5% weight configuration, to examine whether there is any shift in the natural frequencies depending on the exciting force. With empty shaker buckets, we excited the first and second E-W overtones, the first torsional overtone, and the first N-S overtone. Table A:4 summarizes our testing procedure and results.

There are two parallel arrays of instruments in the N-S direction: one set located on the east side of the library, and the other on the west side of the library, as shown in Figure A:2. In the E-W orientation there is one array, located on the west side of the building. The two N-S arrays are positioned towards the East and West edges of the building, far from the E-W centerline, while the E-W array on the west side of the building is located only 1m from the N-S centerline. Therefore, we expect to observe torsional response as strong, out of phase motion from the N-S arrays, with relatively small motion observed from the E-W array.

For each frequency, we selected a representative section from the the steady-state portion of the data, bandpassed the data (1/2 octave above and below each frequency using a 2-pass 2-pole butterworth filter) and integrated twice to obtain displacement values. We created resonance curves by fitting the displacement data to a sine wave to estimate frequency and amplitude, and then normalizing the response based on the applied force for each frequency and weight combination (Section A:2.2). The mode shape snapshots in Figures A:6 to A:11 depict the behavior of the building at the point of maximum roof displacement for each frequency. Using the geometry of the basement and the position of the vertical basement sensors, we were able to estimate the rigid body rocking of the building and use it to correct our mode shapes. The horizontal basement sensors were used to correct for rigid building translation. Our mode shape figures present the raw results from all three instrument arrays, and the corrected results with basement translation and rocking removed.

For the torsional modes, in Figures A:8 and A:11, we present a snapshot of the displacement records, and also provide a snapshot in terms of rotation angle, θ, at each floor. The rotation angle at each floor

was calculated by subtracting the western N-S array displacement values (D_2) from the eastern N-S array displacement values (D_1) and dividing by the E-W length ($L_{E\text{-}W}$) between the arrays (Equation A:2). For our rotation angle figures, we present the rotation angle at each floor, the basement rotation angle, and the rotation angle corrected for basement rotation.

$$\theta \approx \tan\theta = \frac{D_1 - D_2}{L_{E\text{-}W}} \qquad \textbf{(A:2)}$$

Two of the instruments in the Eastern N-S array malfunctioned, on floors 2 and 8, and as a result we show a linearly interpolated value for those floors in our mode shape diagrams.

A:4.2 Fundamental Modes

East-West Fundamental Mode

Figures A:6a and A:6b show the resonance curve obtained from forced E-W shaking with full weights and 42.5% weights respectively. Figures A:6c and A:6d present the respective mode shapes observed at the resonant frequencies for the different weight configurations. Shapes from all three sets of channels are shown on the same plot — the E-W response clearly dominates during E-W excitation. The observed mode shapes for different weight configurations are similar, but due to the non-linear force-response behavior of the building, the resonant frequency shifts from 1.11Hz with full weights to 1.14Hz with 42.5% weights. This shift in resonant frequency with respect to changing the applied force is small, and though obvious, is at the limit of the resolution of our survey.

Figures A:6c and A:6d show the mode shapes for both the raw displacements and the displacements corrected for translation and tilt. The mode shapes have a strong linear component, and closely resemble the theoretical mode shape for a bending beam, with the inclusion of the kink at the ground floor. See

Appendix A:5 for a brief summary and comparison of bending and shear beam behavior. Tilting and translation effects in this mode account for 3% of the roof displacement.

North-South Fundamental Mode

Figures A:7a and A:7d contain the resonance curves for N-S shaking with full weights and 42.5% weights, respectively. The fundamental N-S mode is also non-linear with respect to applied force, and we observe a resonant frequency shift from 1.64Hz for full weights to 1.67Hz with 42.5% weights. The mode shapes, Figure A:7c and Figure A:7d, are near identical, and show a more pronounced hinge behavior than the first E-W mode. When compared to the theoretical mode shapes of Appendix A:5, the observed shape most closely resembles theoretical bending beam behavior, differing near the ground floor due to the pronounced hinging behavior in this mode shape. We also observe that the two N-S arrays are exhibiting in-phase motion, and that the E-W response to N-S shaking is small, as expected. Foundation compliance becomes much more important for this mode, as we observe that $\sim$25% of the roof displacement is due to tilting of the library, and $\sim$5% is due to translation of the base of the library. Similar observations for the rigid-body rotation and translation of the building were made by Foutch et al. (1975).

Torsional Fundamental Mode

The fundamental torsional mode involves the twisting of the building and therefore has more complicated three-dimensional behavior. Due to the positioning of the instruments, a small amplitude response is observed from the accelerometers in the E-W array, while the two N-S arrays recorded a large amplitude out of phase response. Figure A:8a shows the resonance curve for the fundamental torsional mode. Figure A:8b gives the displacement records for the torsional mode shapes and Figure A:8c shows the torsional mode shapes in terms of twist angle, θ (as defined in Section A:2), instead of displacement.

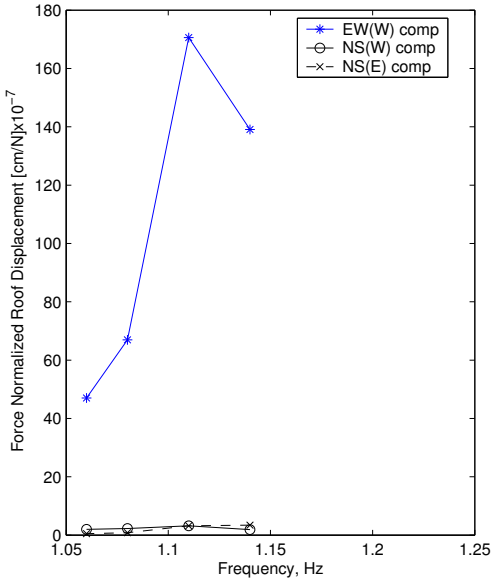

(a) Resonance curve for E-W Shaking, full weights

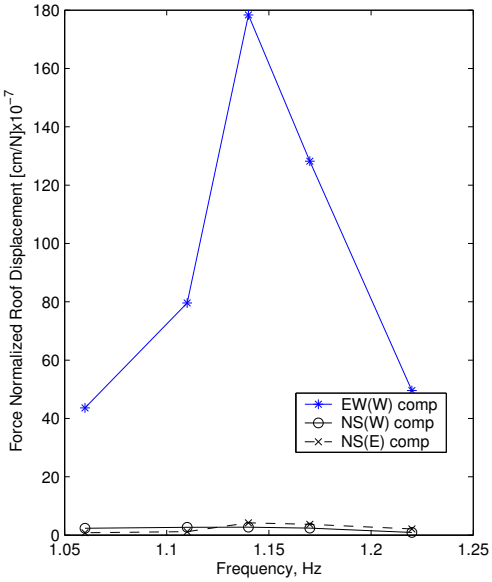

(b) Resonance curve for E-W Shaking, 42.5% weights

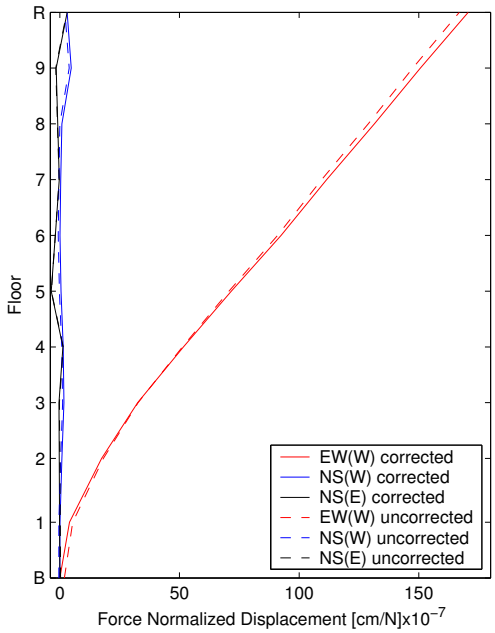

(c) Snapshot of building behavior at 1.11Hz, full weights, Force = 4,405.9N

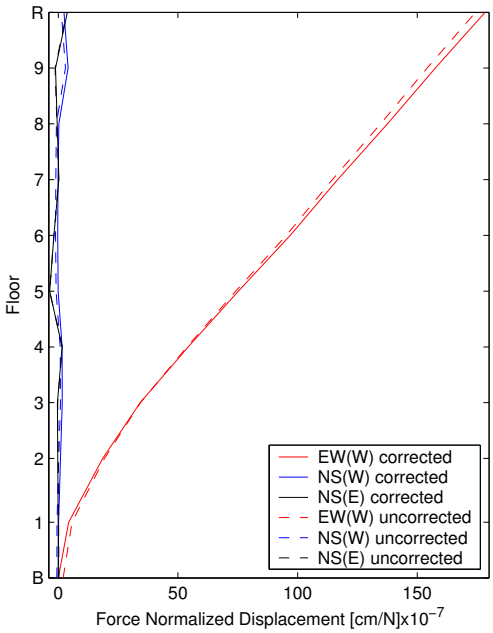

(d) Snapshot of building behavior at 1.14Hz, 42.5% weights, Force = 1,973.7N

Figure A:6. Resonance curves and mode shapes for the E-W fundamental mode under two loading conditions. Mode shapes are shown corrected for rigid body motion and uncorrected. The mode shapes and resonance curves are shown for the east-west array located on the west side of the building, EW(W); the western north-south array, NS(W); and the eastern north-south array, NS(E). Force is calculated as in Equation A:1, based on the frequency and loading configuration of the shaker.

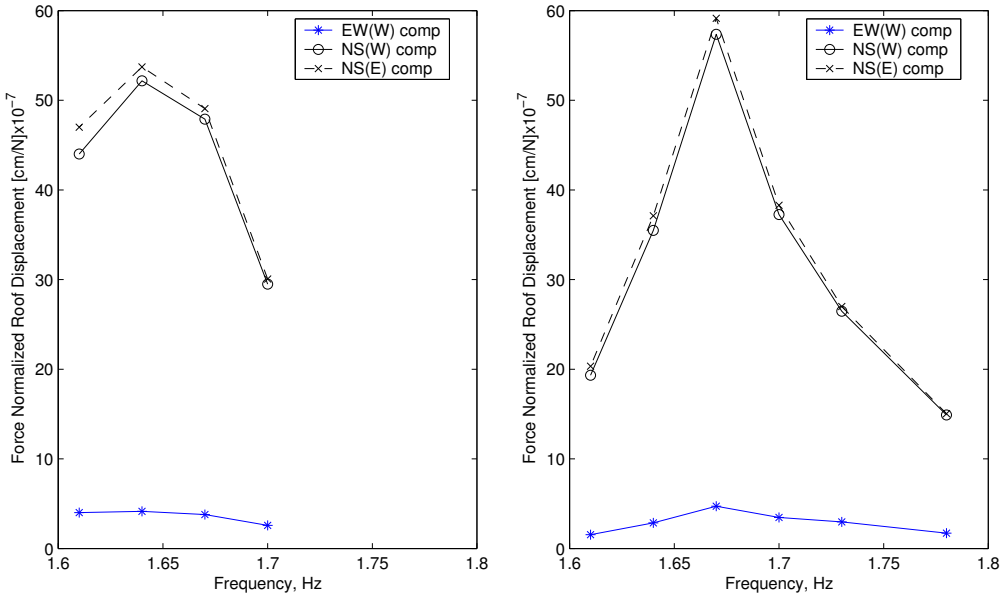

(a) Resonance curve for N-S Shaking, full weights

(b) Resonance curve for N-S Shaking, 42.5% weights

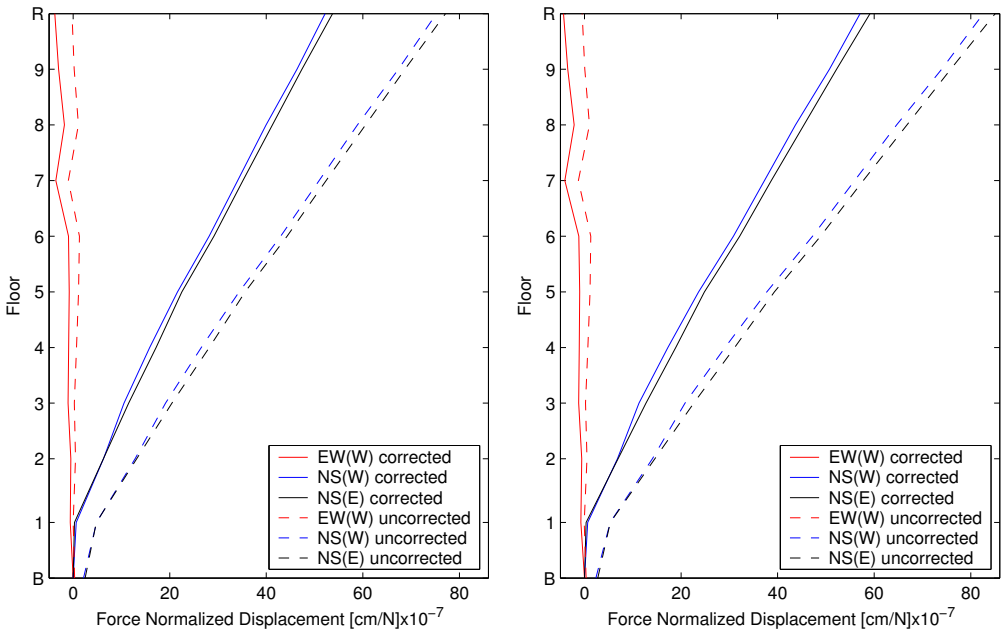

(c) Snapshot of building behavior at 1.64Hz, full weights, Force = 9,617.7N

(d) Snapshot of building behavior at 1.67Hz, 42.5% weights, Force = 4,235.4N

Figure A:7. Resonance curves and mode shapes for the N-S fundamental mode under two loading conditions. Mode shapes are shown corrected for rigid body motion and uncorrected. The mode shapes and resonance curves are shown for the east-west array, located on the west side of the building, EW(W); the western north-south array, NS(W); and the eastern north-south array, NS(E). Force is calculated as in Equation A:1, based on the frequency and loading configuration of the shaker.

In Figure A:8b the two N-S arrays display the expected out of phase displacements, although some asymmetry is observed.

A:4.3 Higher Order Modes

Prior to the installation of the dense instrument array, the higher order mode shapes were difficult to observe; determining the modeshapes and frequencies for these higher order modes was one of the primary goals of our suite of experiments.

Second and Third East-West Modes

The first E-W overtone (second E-W mode) has a broad resonance peak, with a maximum response at 4.93Hz (Figure A:9a). The mode shape, seen in Figure A:9c, is typical of the second mode shape of a beam in bending (Appendix A:5). The ratio of the frequency of the second mode to the first mode is 4.32, much lower than the theoretical ratio for a bending beam of 6.26. For comparison, the theoretical ratio for a shear beam is 3.

Also observed during our testing was the second E-W overtone (third E-W mode). Figure A:9b shows a resonance peak with a maximum response at 7.83Hz. The mode shape for this frequency is presented in Figure A:9d, and is typical of the second mode of a theoretical shear beam (Appendix A:5). The ratio of the frequency of the third mode to the second mode is 1.59, lower than the theoretical ratio for a bending beam of 2.80 and closer to the theoretical ratio for a shear beam of 1.67. The ratio of third mode to first mode frequencies for a bending beam is 17.55, the ratio for a shear beam is 5, and for our observed building behavior the ratio is 6.87.

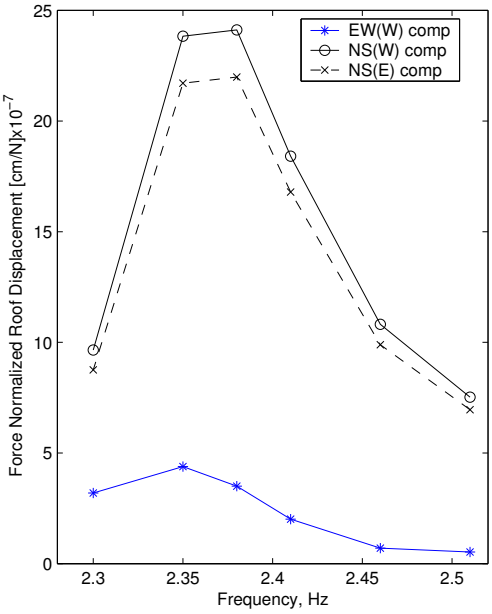

(a) Resonance curve for E-W Shaking, 42.5% weights

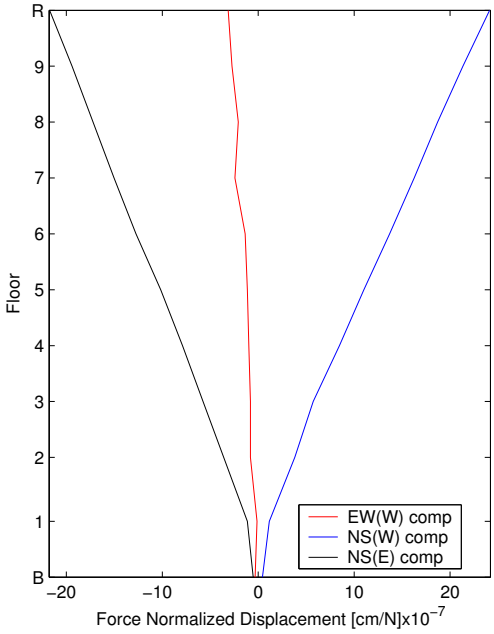

(b) Snapshot of building behavior at 2.38Hz, 42.5% weights, Force = 8,602.3N

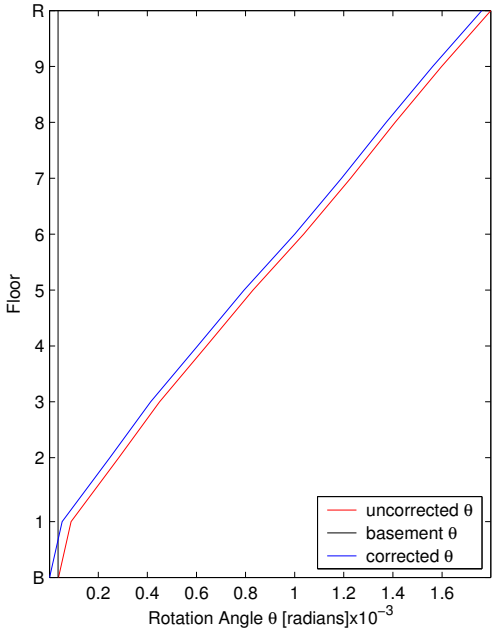

(c) Snapshot of building behavior in terms of rotation angle θ. Same configuration as in subfigure 8(b). The uncorrected snapshot is the rotation angle at each floor, calculated as in Equation A:2. The corrected snapshot is the basement rotation angle subtracted from the rotation angle at each floor.

Figure A:8. Resonance curves and mode shapes for the Torsional fundamental mode. Force is calculated as in Equation A:1, based on the frequency and loading configuration of the shaker.

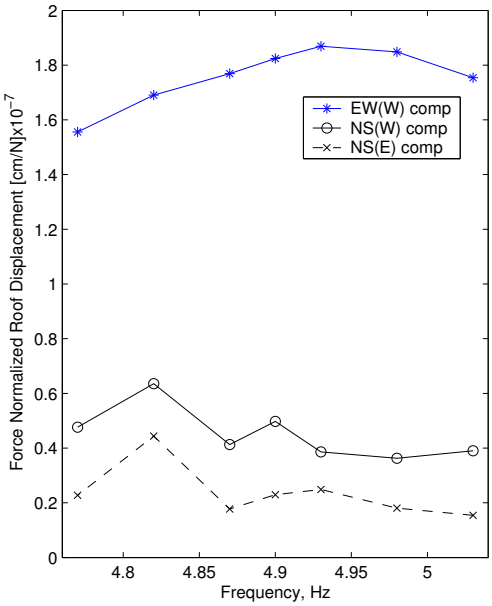

(a) Second E-W mode. Resonance curve for E-W Shaking, empty buckets

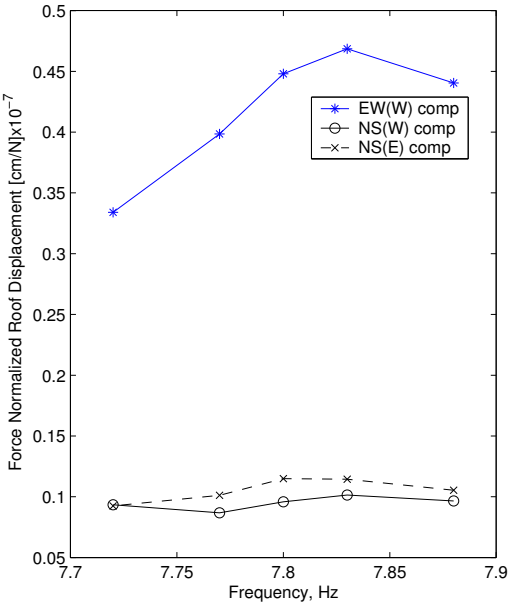

(b) Third E-W mode. Resonance curve for E-W shaking, empty buckets

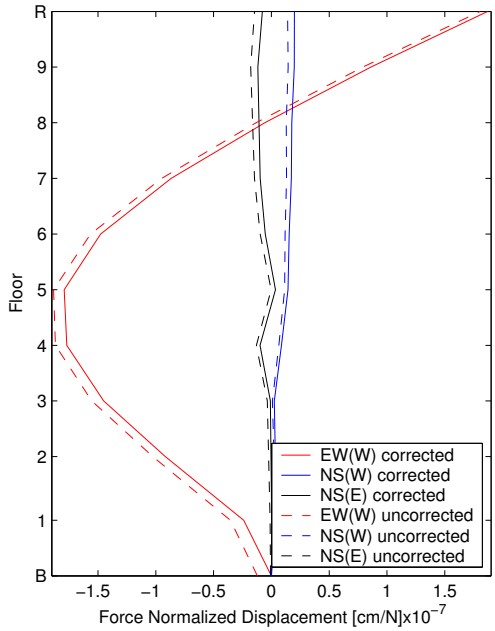

(c) Second E-W mode. Snapshot of building behavior at 4.93Hz, empty buckets, Force = 6,166.9N

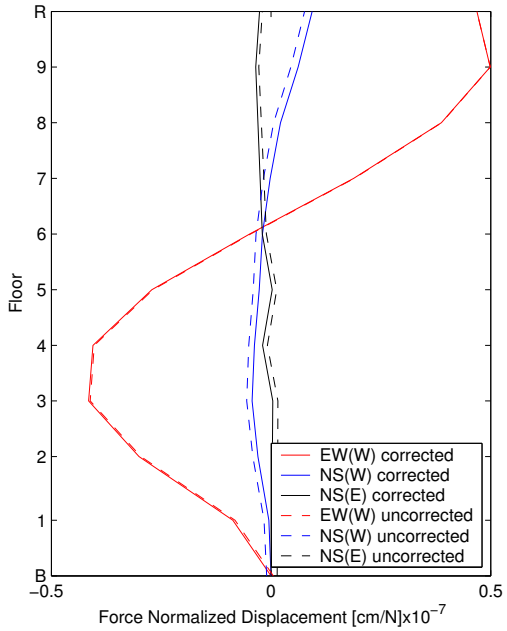

(d) Third E-W mode. Snapshot of building behavior at 7.83Hz, empty buckets, Force = 14,452.3N

Figure A:9. Second and third E-W modes (first and second E-W overtones). Resonance curves and mode shapes. Mode shapes are shown corrected for rigid body motion and uncorrected. The mode shapes and resonance curves are shown for the east-west array, located on the west side of the building, EW(W); the western north-south array, NS(W); and the eastern north-south array, NS(E). Force is calculated as in Equation A:1, based on the frequency and loading configuration of the shaker.

Second North-South Mode

As can be seen in Figure A:10a, the first N-S overtone (second N-S mode) also has a broad resonance peak. The resonance curves for the two N-S arrays did not have their peaks at the same frequency, so this test did not provide a single resonance peak. However, based on the frequency sweep of Section A:3, and the shapes of the two resonance curves, we selected 7.22Hz as the modal frequency. The mode shape at this frequency, shown in Figure A:10b, is qualitatively typical of a bending beam's second mode, but we see that the two N-S arrays have very different amplitudes with zero crossings at different heights. For the N-S second mode, the eastern and western arrays should have similar shapes and amplitudes (cf. the first N-S mode, Figure A:7), as the building is approximately symmetric. This implies that we did not excite the exact modal frequency, or that this mode has a more complicated three-dimensional response than the first N-S mode. The ratio of the frequency for the second mode (approximate) to the first mode is 4.32, which is close to the ratio of frequencies observed in E-W bending, and is also lower than the theoretical ratio for the first two modes of a bending beam.

Second Torsional Mode

The first torsional overtone was difficult to excite in the building, and difficult to observe. We excited the torsional mode using E-W excitation, and expected small torsional response on the E-W channels, and large out of phase response from the two N-S arrays. However, the observed response was dominated by E-W motion from the E-W shaking used to excite the system, which drove the building in a mode shape similar to that of the second E-W mode. We observed out of phase motion in the two N-S arrays, but the response of the N-S arrays was much smaller than the E-W response. Figure A:11a shows the response curve for this mode, which is dominated by the E-W motion. Figure A:11b shows the mode shapes, and Figure A:11c shows the response in terms of twist angle, θ, as defined in Section A:4.1. As with the N-S overtone, the resonance curve did not clearly identify a modal frequency, but we chose 6.57Hz as the

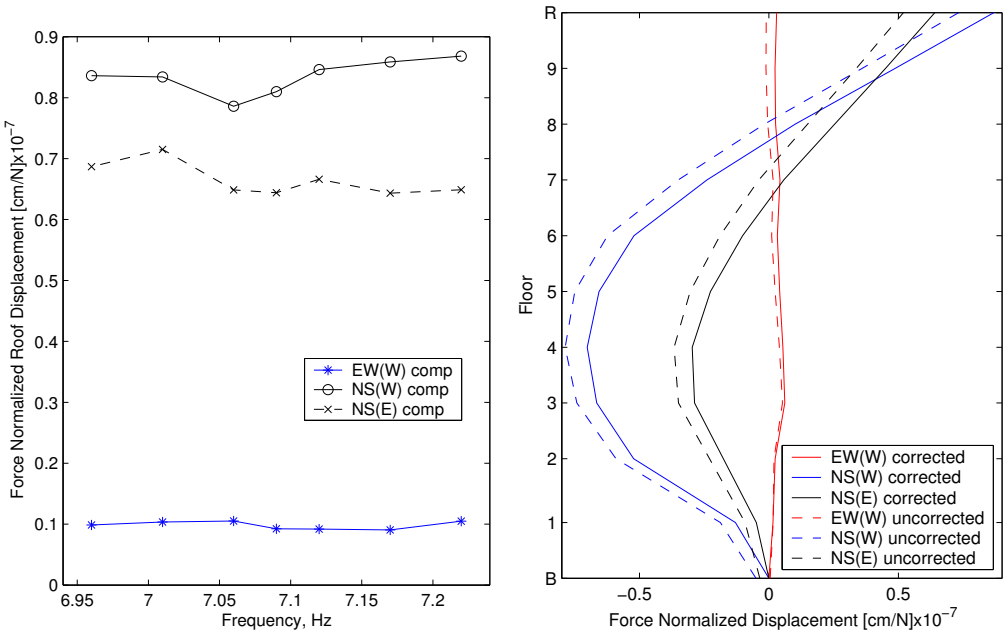

(a) Resonance curve for N-S shaking, empty buckets

(b) Snapshot of building behavior at 7.22Hz, empty buckets, Force = 12,288.2N

Figure A:10. Resonance curves and mode shapes for the second NS mode (first NS overtone). Mode shapes are shown corrected for rigid body motion and uncorrected. The mode shapes and resonance curves are shown for the east-west array, located on the west side of the building, EW(W); the western north-south array, NS(W); and the eastern north-south array, NS(E). Force is calculated as in Equation A:1, based on the frequency and loading configuration of the shaker.

frequency of interest based on the shapes of the resonance curves and the results of the frequency sweep of Section A:3.

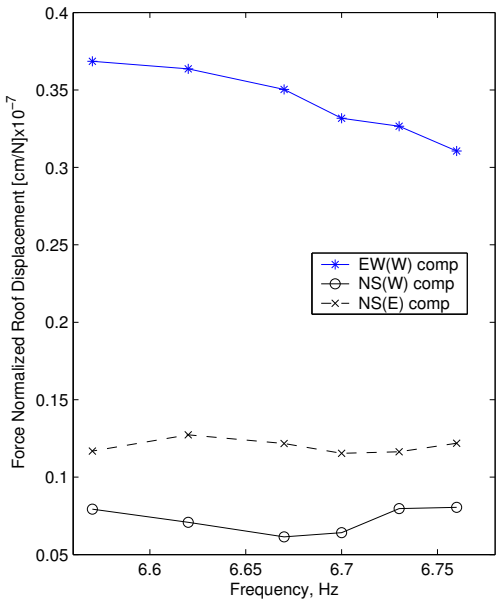

(a) Resonance curve for E-W shaking, empty buckets

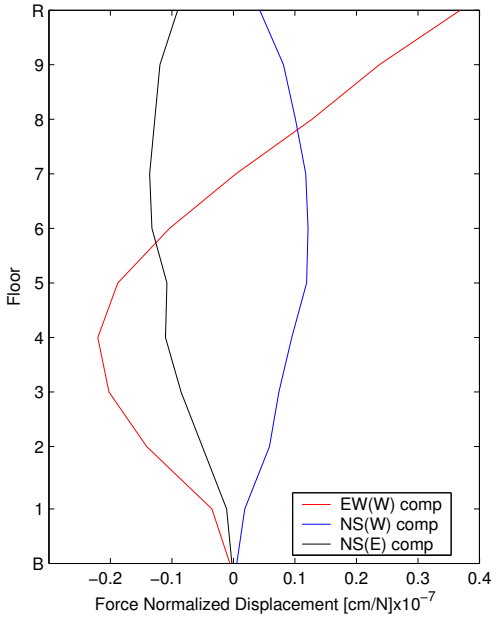

(b) Snapshot of building behavior at 6.57Hz, empty buckets, Force = 10,175.3N

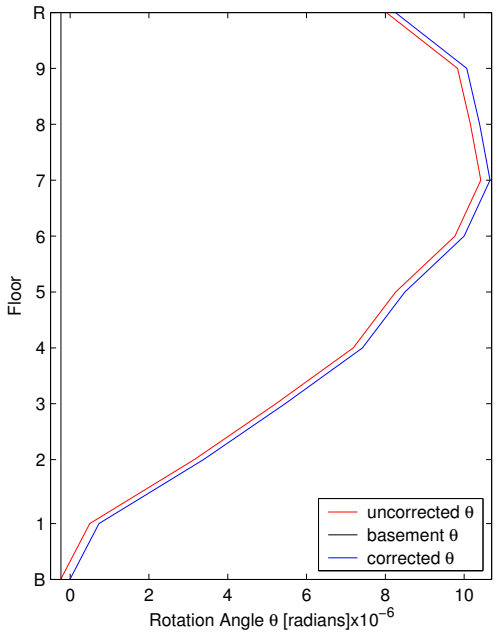

(c) Snapshot of building behavior in terms of rotation angle θ. Same configuration as in subfigure 11(b). The uncorrected snapshot is the rotation angle at each floor, calculated as in Equation A:2. The corrected snapshot is the basement rotation angle subtracted from the rotation angle at each floor.

Figure A:11. Resonance curves and mode shapes for the second Torsional mode (first Torsional overtone). Force is calculated as in Equation A:1, based on the frequency and loading configuration of the shaker.

A:4.4 Modeshapes Summary

Table A:5 contains a summary of the ratios of frequencies found for Millikan Library, along with theoretical results for bending and shear beams. Appendix A:5 presents a summary of theoretical bending and shear beam behavior. To further analyze the data, the mode shapes were fit using theoretical bending and shear beam behavior by a modified least squares method. Figures A:12 and A:13 show the results of the least squares curve-fitting for the E-W and N-S modes respectively. The experimental data and best fit are shown, along with the theoretical mode shapes which are scaled according to their participation in the best fit curve. Both the fundamental E-W and N-S modes, Figures A:12a and A:13a, are dominated by the bending component, as are the second E-W and N-S modes, Figures A:12b and A:13b. The third E-W mode was not matched well using the third theoretical bending and shear modes; a fit including the second theoretical bending and shear modes is presented in Figure A:12c, implying that the mode shape is best approximated by the second mode of a theoretical shear beam.

	Bending	Shear	Millikan E-W	Millikan N-S
ω_2/ω_1	6.26	3	4.32	4.32
ω_3/ω_1	17.55	5	6.87	N/A
ω_3/ω_2	2.8	1.67	1.57	N/A

Table A:5. Ratio of frequencies for bending beam behavior, shear beam behavior, and the observed behavior of Millikan Library.

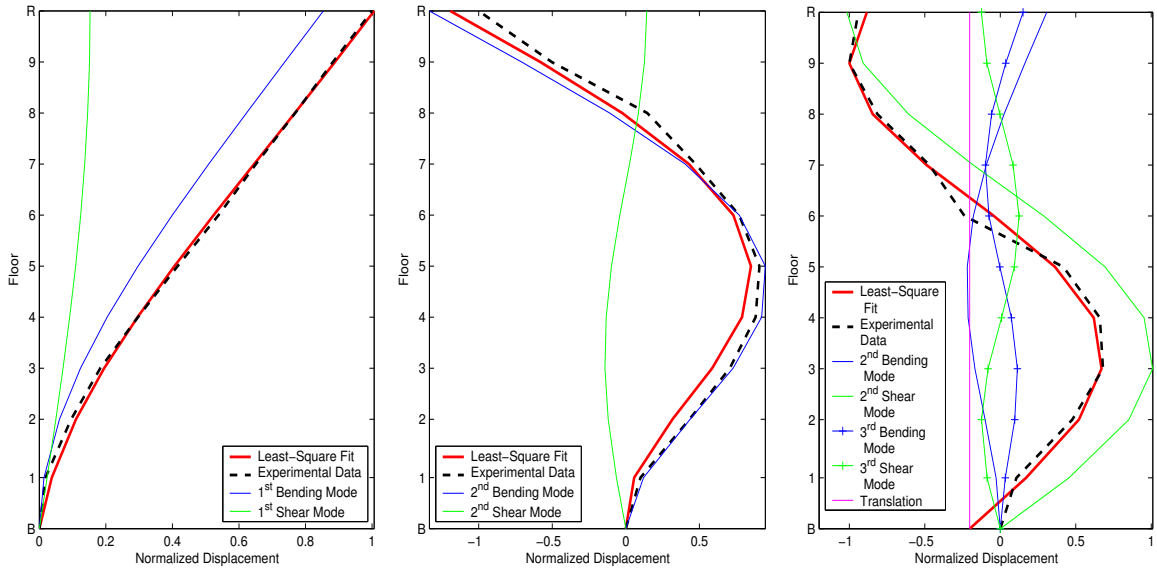

(a) Least square fit for fundamental E-W mode.

(b) Least square fit for second E-W mode (first E-W overtone).

(c) Least square fit for third E-W mode (second E-W overtone). Translational term included in curve-fitting to accommodate large kink at ground level.

Figure A:12. Least squares curve fitting for E-W modes. Tilt and translation removed.

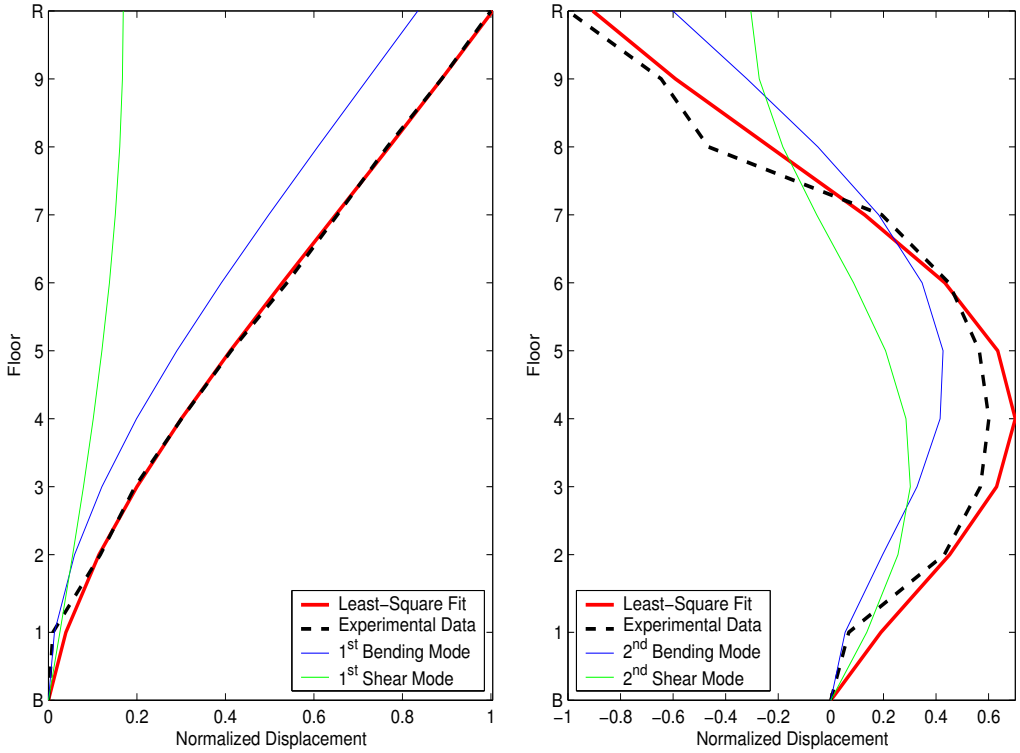

(a) Least square fit for fundamental N-S mode.

(b) Least square fit for second E-W mode (first E-W overtone).

Figure A:13. Least squares curve fitting for N-S modes. Tilt and translation removed.

A:5 THEORETICAL BEAM BEHAVIOR

Adapted from Meirovitch, (1986).

The mode shape and frequencies for a cantilevered (fixed-free) bending beam are found by solving the differential equation:

$$\frac{\partial^4 X(z)}{\partial z^4} - \beta^4 X(z) = 0 \quad \beta^4 = \frac{\omega^2 m}{EI}$$

m = Mass/Unit Length, E = Young's Modulus, I = Moment of Inertia

With the following boundary conditions:

$$X(0) = 0 \qquad \frac{\partial X(z)}{\partial z}|_{x=0} = 0 \qquad \text{At the fixed end}$$

$$\frac{\partial^2 X(z)}{\partial z^2}|_{x=L} = 0 \qquad \frac{\partial^3 X(z)}{\partial z^3}|_{x=L} = 0 \qquad \text{At the free end}$$

This leads to the characteristic equation:

$$\cos(\beta L)\cosh(\beta L) = -1$$

Which can be solved analytically to give the following values for the first three modes:

$$\begin{aligned} \text{Mode 1} : \beta_1 L &= 1.875 \\ \text{Mode 2} : \beta_2 L &= 4.694 \\ \text{Mode 3} : \beta_3 L &= 7.855 \\ \text{with } \omega_i &= \beta_i^2 \sqrt{\frac{EI}{mL^4}} \end{aligned}$$

The mode shapes are given by:

$$X_n(z) = C_1 \left[(\sin\beta_n z - \sinh\beta_n z) + \frac{(\cos\beta_n L + \cosh\beta_n L)}{(\sin\beta_n L - \sinh\beta_n L)} (\cos\beta_n z - \cosh\beta_n z) \right]$$

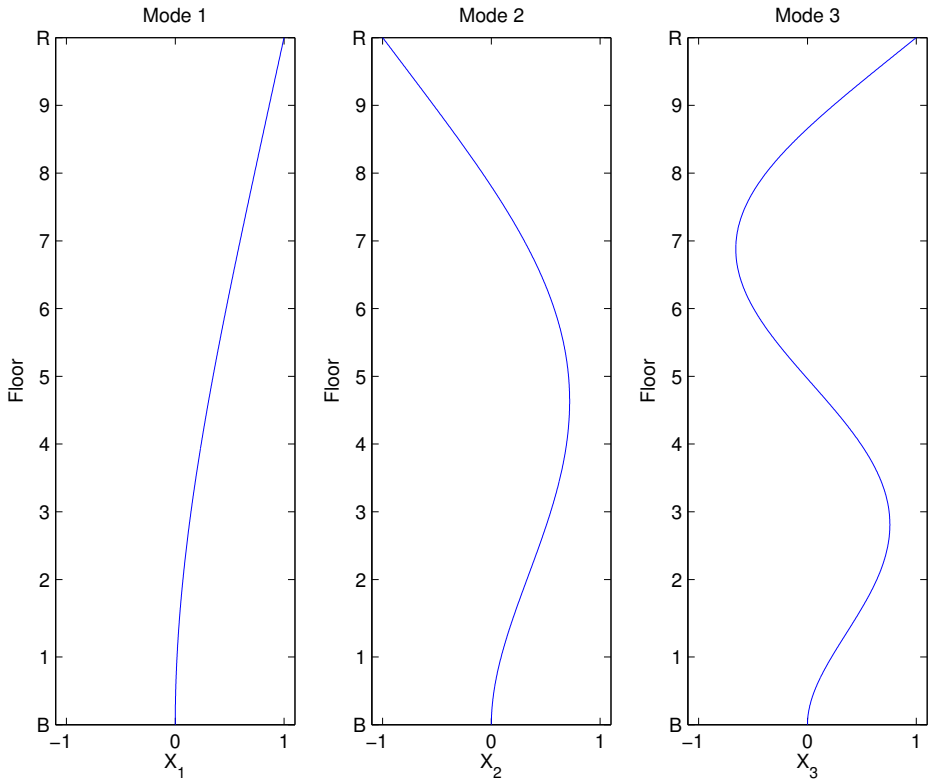

Figure A:14. From left to right, theoretical mode shapes for the fundamental mode (1st mode) and the first two overtones (2nd and 3rd modes) for a cantilevered bending beam. Mode shapes X_n are normalized such that the maximum displacement is equal to 1.

The first three modes are plotted in Figure A:14.

Theoretical shear beam behavior is as follows, with the deformed shape being portions of a sine curve:

$$X_n(z) = C_1 \left[(\sin \frac{(2n-1)\pi}{2} z) \right] \quad n = 1, 2, 3...$$

The first three modes are plotted in Figure A:15.

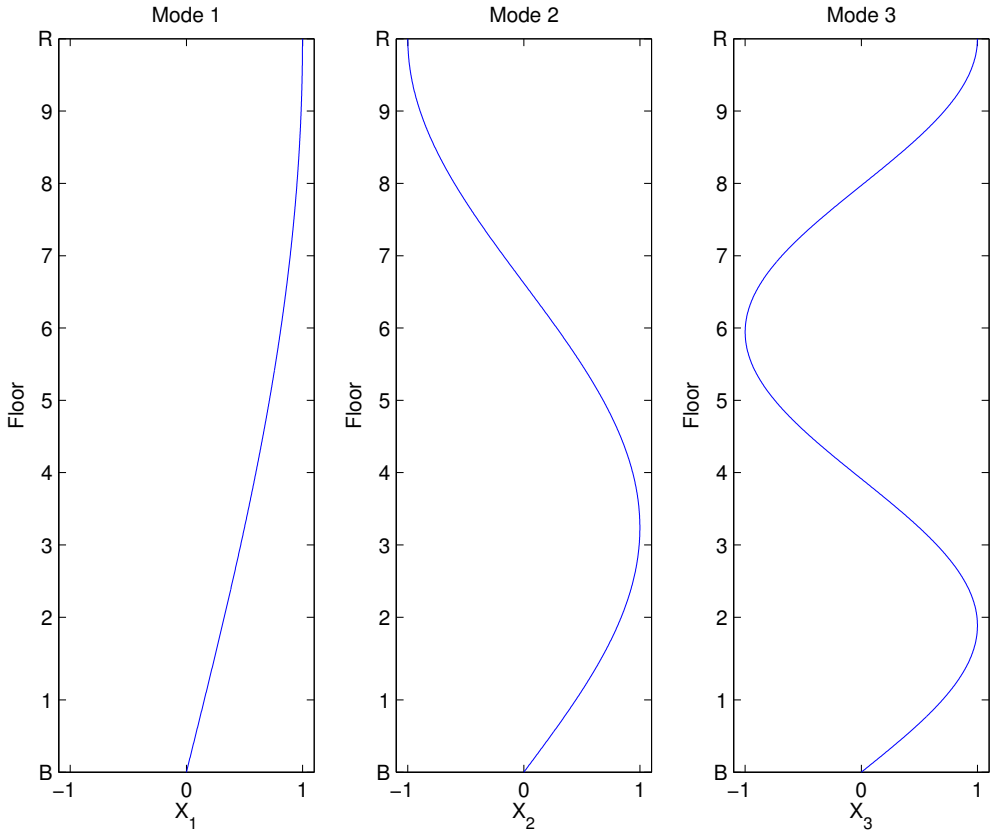

Figure A:15. From left to right, theoretical mode shapes for the fundamental mode (1st mode) and the first two overtones (2nd and 3rd modes) for a cantilevered shear beam. Mode shapes X_n are normalized such that the maximum displacement is equal to 1.

A:6 HISTORICAL SUMMARY OF MILLIKAN LIBRARY STUDIES

Adapted from Clinton (2004).

Tables A:6 and A:7 provide a summary of various studies into the frequencies and damping of Millikan Library. Table A:8 contains the references used to compile Tables A:6 and A:7. These studies include ambient and forced vibration testing, as well as data recorded from earthquake ground motions.

Test	East - West		North - South		Torsional		Remark
	f_0 [ζ_0]	f_1 [ζ_1]	f_0 [ζ_0]	f_1 [ζ_1]	f_0 [ζ_0]	f_1 [ζ_1]	
1966-1967[1]	1.46-1.51 [0.7-1.7]	6.2	1.89-1.98 [1.2-1.8]	-	2.84-2.90 [0.9-1.6]	-	A,F,M
Mar 1967[2]	1.49 [1.5]	6.1	1.91 [1.6]	-	2.88	-	A
Apr 1968[3]	1.45	6.1	1.89	9.18	2.87	9.62	A
Jul 1969[4]	1.45	5.90	1.89	9.10	-	-	A
Sep 12 1970[5]	1.30-1.50	-	1.90-2.10	-	-	-	E (LC)
Sep 12 1970[6]	1.30	-	1.88	-	-	-	E (LC)
~ M6.7 February 9 1971 San Fernando Earthquake (SF) @ 44km ~							
Feb 9 1971[5]	1.00-1.50	-	1.50-1.90	-	-	-	E (SF)
Feb 9 1971[7]	0.82-1.43 [1.0-13.0]	-	-	-	-	-	E (SF)
Feb 9 1971[8]	1.02-1.11 [3.5-5.5]	-	-	-	-	-	E (SF)
Feb 9 1971[9]	1.03 [0.07]	4.98 [0.06]	1.61 [0.06]	7.81 [0.06]	-	-	E (SF)
Feb 9 1971[10]	1.02 [0.06]	4.93 [0.05]	1.61 [0.06]	7.82 [0.05]	-	-	E (SF)
Feb 9 1971[6]	1.00	-	1.64	-	-	-	E (SF)
Feb 1971[11]	1.27 [2.5]	5.35 [0.9]	1.8 [3]	9.02 [0.2]	2.65 [2]	9.65 [0.5]	A
Feb 1971[4]	1.30	-	-	-	-	-	A
Dec 1972[4]	1.37	-	1.77	-	-	-	M
Apr 1973[12]	1.28 [1.3]	-	-	-	-	-	A
1974[13]	1.21	-	1.76	-	-	-	F
Jul 1975[14]	1.21 [1.8]	-	1.79 [1.8]	-	-	-	F
May 1976[9]	1.27	-	1.85	-	2.65	-	A
~ M6.1 October 1 1987 Whittier Narrows Earthquake (WN) @ 19km ~							
Oct 1 1987[10]	0.932 [0.04]	4.17 [0.08]	1.30 [0.06]	6.64 [0.18]	-	-	E (WN)
Oct 1 1987[6]	1.00	-	1.33	-	-	-	E (WN)
Oct 4 1987[10]	0.98	-	1.43	-	-	-	E(WN M5.3)
Oct 16 1987[10]	1.20	-	1.69	-	-	-	E(WN M2.8)
May 1988[11]	1.18	-	1.70	-	-	-	F
~ M5.8 June 28 1991 Sierra Madre Earthquake (SM) @ 18km ~							
June 28 1991[6]	0.92	-	1.39	-	-	-	E (SM)
May 1993[15]	1.17	-	1.69	-	2.44	-	F
~ M6.7 January 17 1994 Northridge Earthquake (N) @ 34km ~							
Jan 17 1994[6]	0.94	-	1.33	-	-	-	E (N)
Aug 2002[18]	1.14 [2.28]	4.93	1.67 [2.39]	7.22	2.38 [1.43]	6.57	F

Table A:6. Summary of Millikan Library Modal Frequency and Damping Analysis Experiments 1967-1994. f_o and f_1 are the fundamental frequency and the first overtone, in Hz. ζ_o and ζ_1 are the corresponding damping ratios, in %. References are found in Table A:8. A: Ambient, M: Man Excited, F: Forced Vibration, E: Earthquake Motions [LC: Lytle Creek Earthquake]

Test	East - West		North - South		Torsional		Remark
	f_0 [ζ_0]	f_1 [ζ_1]	f_0 [ζ_0]	f_1 [ζ_1]	f_0 [ζ_0]	f_1 [ζ_1]	
1966-1967[1]	1.46-1.51	6.2	1.89-1.98	-	2.84-2.90	-	A,F,M
	[0.7-1.7]		[1.2-1.8]		[0.9-1.6]		
Mar 1967[2]	1.49 [1.5]	6.1	1.91 [1.6]	-	2.88	-	A
∼ M6.7 February 9 1971 San Fernando Earthquake (SF) @ 44km ∼							
Feb 9 1971[6]	1.00	-	1.64	-	-	-	E (SF)
May 1976[9]	1.27	-	1.85	-	2.65	-	A
∼ M6.1 October 1 1987 Whittier Narrows Earthquake (WN) @ 19km ∼							
Oct 1 1987[10]	0.932 [0.04]	4.17 [0.08]	1.30 [0.06]	6.64 [0.18]	-	-	E (WN)
Oct 1 1987[6]	1.00	-	1.33	-	-	-	E (WN)
Oct 4 1987[10]	0.98	-	1.43	-	-	-	E(WN M5.3)
Oct 16 1987[10]	1.20	-	1.69	-	-	-	E(WN M2.8)
May 1988[11]	1.18	-	1.70	-	-	-	F
∼ M5.8 June 28 1991 Sierra Madre Earthquake (SM) @ 18km ∼							
June 28 1991[6]	0.92	-	1.39	-	-	-	E (SM)
May 1993[15]	1.17	-	1.69	-	2.44	-	F
∼ M6.7 January 17 1994 Northridge Earthquake (N) @ 34km ∼							
Jan 17 1994[6]	0.94	-	1.33	-	-	-	E (N)
Jan 19 1994[15]	1.13	-	1.65	-	2.39	-	F
Jan 20 1994[15]	1.13	4.40-4.90	1.65	8.22-8.24	2.39	-	A
	[1.2-2.1]	[1.0]	[0.7-1.5]	[0.2-0.3]	[0.3-0.5]		F
May 1994[16]	1.15 [1.38]	-	1.67 [1.46]	-	2.4 [1.18]	-	F
May 1995[16]	1.15 [1.44]	-	1.68 [1.25]	-	2.42 [1.15]	-	F
May 1998[16]	1.17 [1.4]	-	1.70 [1.3]	-	2.46	-	F
May 1998[16]	-	-	1.68	1.5	-	-	M
May 2000[16]	1.15 [3]	-	1.66 [3]	-	2.41 [2.5]	-	F
May 2000[16]	-	-	1.72 [0.8]	-	-	-	A
May 2001[16]	1.11 [3.25]	-	1.63 [3.69]	-	2.31 [2.9]	-	F
May 2001[16]	-	-	1.71 [1.2]	-	-	-	M
Dec 2001[17]	1.12 [1.63]	-	1.63 [1.65]	-	2.34	-	F
Sep 9 2001[6]	1.16	-	1.68	-	-	-	E (BH M4.2)
Aug 2002[18]	1.14 [2.28]	4.93	1.67 [2.39]	7.22	2.38 [1.43]	6.57	F
Feb 22 2003[6]	1.07	-	1.61	-	-	-	E (BB M5.4)

Table A:7. Summary of Millikan Library Modal Frequency and Damping Analysis Experiments 1987-2003. f_o and f_1 are the fundamental frequency and the first overtone, in Hz. ζ_o and ζ_1 are the corresponding damping ratios, in %. References are found in Table A:8. A: Ambient, M: Man Excited, F: Forced Vibration, E: Earthquake Motions [BH: Beverly Hills Earthquake, BB: Big Bear Earthquake]

Footnote #	Reference	Remarks
1	Kuroiwa (1967)	*forced, ambient, man excitations*
		— during and immediately after construction, Library not full
2	Blandford et al. (1968)	*ambient*
3	Jennings and Kuroiwa (1968)	*ambient*
4	Udwadia and Trifunac (1973)	*ambient*
5	Udwadia and Trifunac (1974)	*Lytle Creek, San Fernando*
		— based on transfer functions
6	Clinton et al. (2004)	*Earthquakes*
		— estimated from strong motion records
7	Iemura and Jennings (1973)	*San Fernando*
8	Udwadia and Marmarelis (1976)	*San Fernando*
		— based on linear model
9	McVerry (1980)	*SanFernando; ambient*
10	Beck and Chan (1995)	*SanFernando, Whittier MODEID*
11	Teledyne-Geotech-West (1972)	*ambient - 1mth after San Fernando*
		— Also Vertical $f_0 = 3-4Hz$*, high* ζ.
12	Udwadia and Marmarelis (1976)	*San Fernando*
13	Foutch et al. (1975)	*forced*
14	Luco et al. (1987)	*forced*
15	Beck et al. (1994)	*forced, ambient*
		— Also Jan 20 Ambient test: EW3 at 7.83Hz
16	CE180 Caltech - various students	*forced*
17	Favela, personal communication	*forced*
18	This report, Bradford et al. (2004)	*forced*
		— Also EW3 at 7.83Hz

Table A:8. References which correspond to footnote numbers in Tables A:6 and A:7.

Appendix B

Millikan Roof Calibration

The details for the short period L4C-3D seismometer calibrations performed on the roof of Millikan Library are provided in this appendix. Two calibration experiments were performed, the first one on May 4, 2000 and the second one on May 6, 2000. They will be referred to as calibration 1 and calibration 2, respectively. Both calibrations used the exact same instrument configuration, given in Figure B.1, while the frequencies used varied.

The instruments were calibrated with respect to each other on the roof of Millikan Library, while it was excited at frequencies similar to its natural frequencies. All the instruments were set along an East-West line, while the building was only excited in the North-South direction to minimize excitation of torsional motions in the building. As a result, the North component of the seismometers contains the highest amplitude data. Under these conditions, and due to the position of the shaker, it is expected that all the instruments should have the same phase and amplitude for the calibration, since the floor slabs move in-plane (*Foutch*, 1976) and can be considered rigid (*Kuroiwa*, 1969).

As can be seen from Figures B.3 and B.4 and from Tables B.3 through B.44, better agreement between instruments was achieved when deconvolving the nominal response of the L4C-3D seismometer from the raw waveforms than when each instrument's response (as calibrated by SCEC) was deconvolved. This can be qualitatively observed in Figures B.2 and B.3, that show that the waveforms in Figure B.2 are more similar than those in Figure B.3. This indicates that the precision in the individual

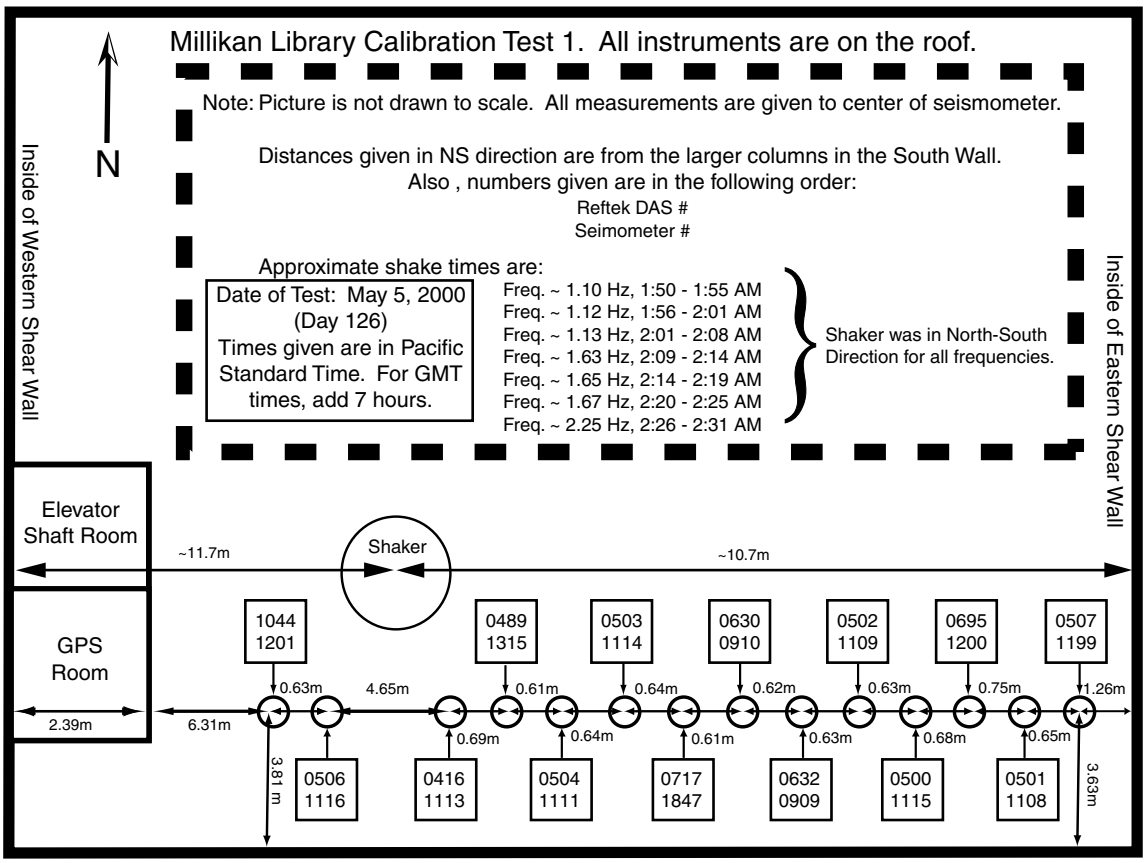

Figure B.1 Seismometer set up for calibration experiments conducted on the roof of Millikan Library.

responses is not accurate enough to justify their use over the nominal response for L4C-3D seismometers.

The calibration experiments were performed for periods close to the natural period of the seismometers, which is the range in which the phase of the instrument response changes most rapidly. As a result, if the individual seismometer responses are used to process the data, errors in the calculation of the responses will be most evident near the natural frequency. For waveforms recorded at frequencies near the seismometer's natural frequency, small errors in the responses will affect the phase and amplitude of the waveforms if the instrument responses are deconvolved from the signal. Figures B.4 through B.9 show the SCEC calculated amplitude and phase responses for all of the instruments used. From these figures, it can be seen that the amplitude differences

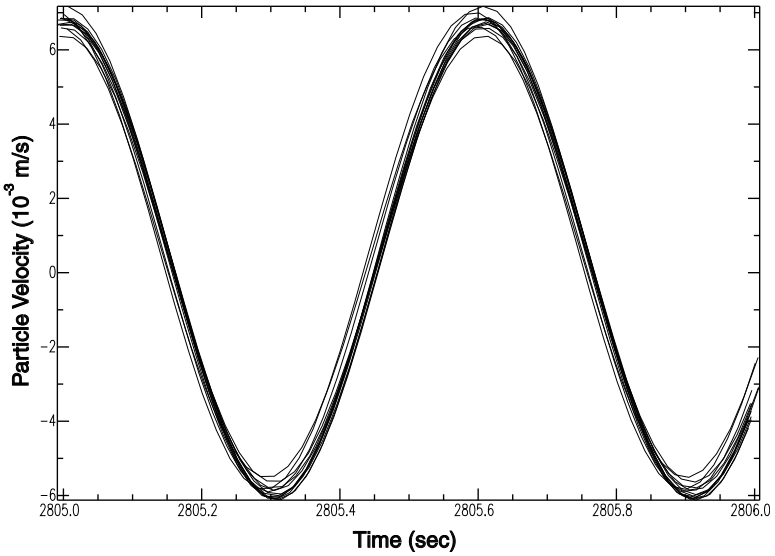

Figure B.2 North component particle velocities for the L4C-3D seismometers used in the roof calibration after removing the nominal instrument response. Excitation in the NS direction.

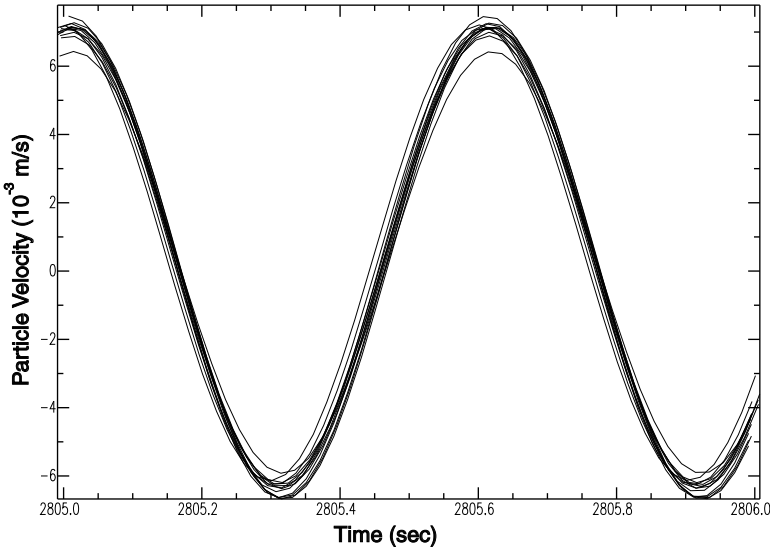

Figure B.3 North component particle velocities for the L4C-3D seismometers used in the roof calibration after removing the individual SCEC determined instrument responses. Excitation in the NS direction.

for small frequency changes for frequencies between 1.0 and 2.5 Hz are not going to be as noticeable as the phase changes for these same frequencies. Furthermore, it should be noted that the waveforms from a single seismometer were excluded from

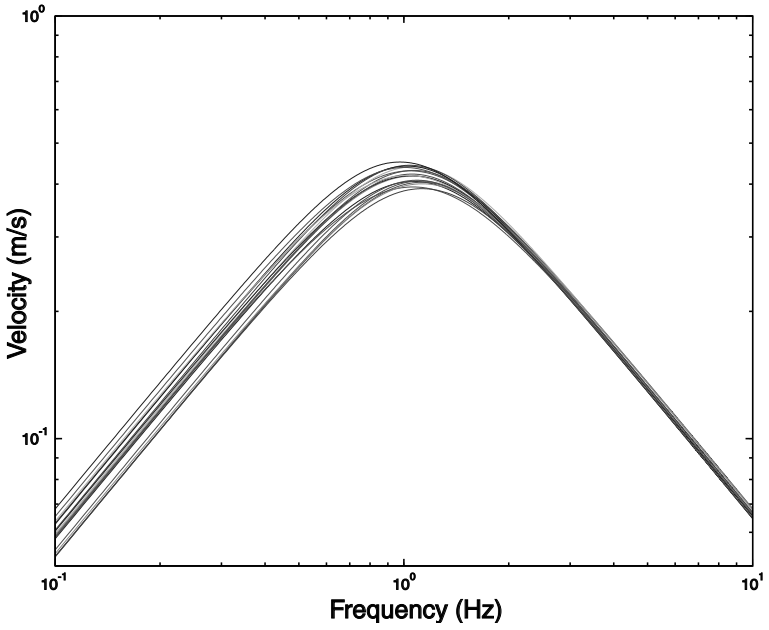

Figure B.4 SCEC calculated velocity responses for the north component of the L4C-3D seismometers used for the Millikan experiments.

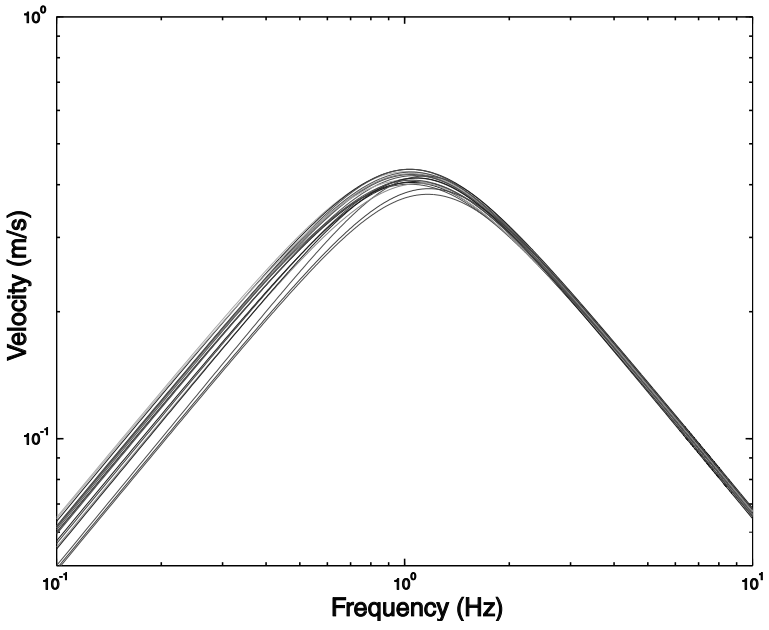

Figure B.5 SCEC calculated velocity responses for the east component of the L4C-3D seismometers used for the Millikan experiments.

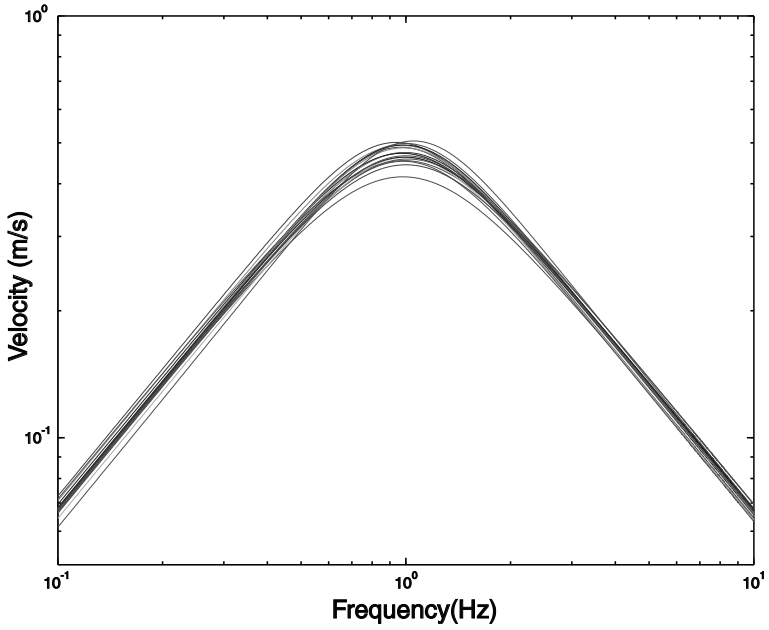

Figure B.6 SCEC calculated velocity responses for the vertical component of the L4C-3D seismometers used for the Millikan experiments.

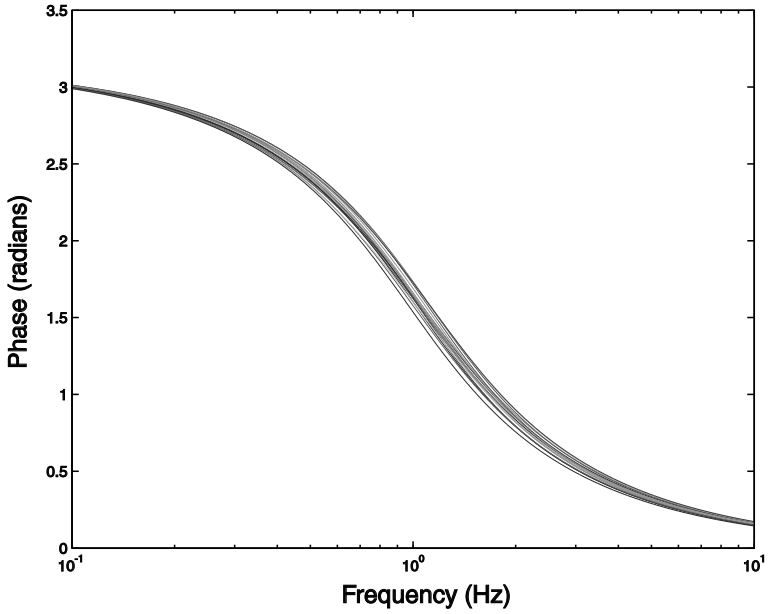

Figure B.7 SCEC calculated phase responses for the north component of the L4C-3D seismometers used for the Millikan experiments.

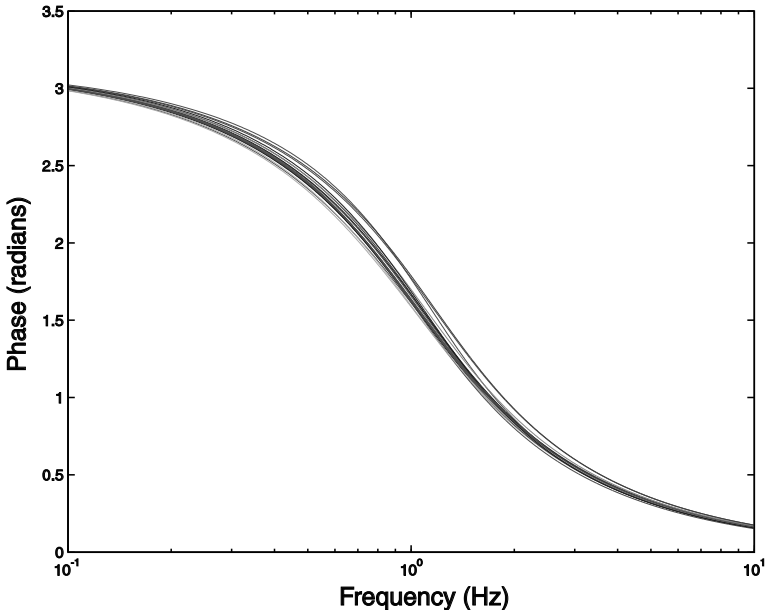

Figure B.8 SCEC calculated phase responses for the east component of the L4C-3D seismometers used for the Millikan experiments.

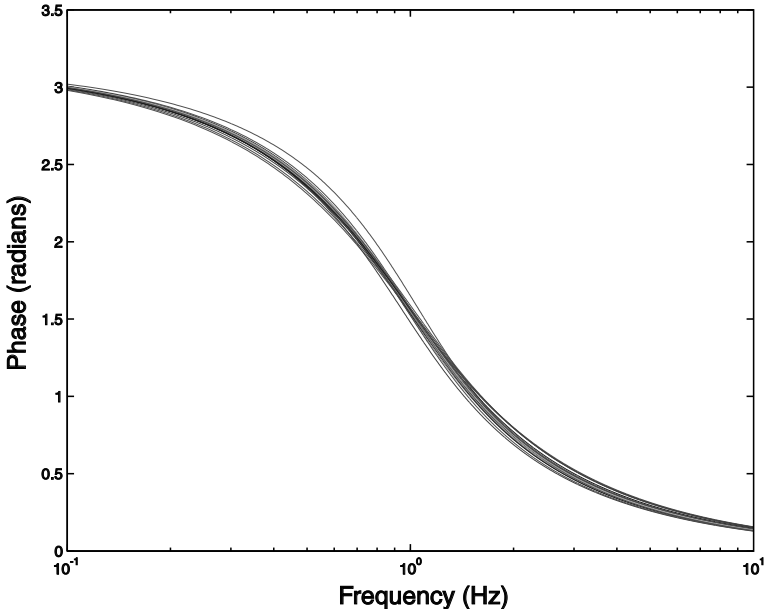

Figure B.9 SCEC calculated phase responses for the vertical component of the L4C-3D seismometers used for the Millikan experiments.

Figures B.2 and B.3, as it malfunctioned due to soft springs, causing its response to deviate significantly from the mean. As a result, it was not used for the Millikan II experiment, and it was excluded from the analysis performed for Tables B.3 through B.44.

The data presented in the Tables B.3 to B.44 is listed by component for each excitation frequency, and given are mean signal phase (in radians), median signal phase (in radians), phase variance (in radians), mean signal amplitude (in m/s), median signal amplitude (in m/s), and signal amplitude variance (in m/s). The amplitude values are given in m/s for all of the table values, except for the values listed under "raw responses", which are given in counts. Fourteen seismometers were used for the roof calibration, and of the seismometers given in Tables B.1 and B.2, the instruments not used for the calibration are the seismometers numbered 1110, 1112, 1316, and 1848.

The amplitudes used to make Tables B.1 through B.44 are calculated utilizing a Fourier transform in SAC, by calculating the energy contained in the peak of the excitation frequency as described in Section 6.1.1. The phases are calculated relative to a particular seismometer's (SCEC seismometer # 1847, referred to as the fixed seismometer) phase, and the process utilized is outlined below and carried out in Matlab:

- For the following process, the sinusoidal phase of each waveform was computed with respect to the reference seismometer, and both traces have the same sampling rate of 50 sps.

- Once the appropriate instrument response was deconvolved from the waveforms, the changing seismometer waveform was re-sampled to match the sampling points (in time) of the reference trace.

- Then, the same 150 second trace was cut from all of the records (in the section containing the frequency being studied), and waveforms were normalized by their respective mean maximum amplitude. This allows for the assumption that both records have the same amplitude.

- Next, the two traces were subtracted from each other, and the mean maximum amplitude of the resulting sinusoid is computed, and referred to as A in the following step.

- Since it is easier to measure amplitudes than phases, the trigonometric identity

$$\sin\alpha - \sin\beta = 2 * \cos(\frac{1}{2}(\alpha+\beta)) * \sin(\frac{1}{2}(\alpha-\beta)) \tag{B.1}$$

was exploited to compute the relative phases of the recorded waveforms by performing an amplitude calculation. If the following relationships are used:

$$\begin{aligned} \alpha &= \omega t - \phi_1 \\ \beta &= \omega t - \phi_2 \\ \phi_1 &= 0 \\ \phi_2 &<< 1 \end{aligned}$$

Then, Equation B.1 can be written as follows

$$\begin{aligned} \sin\alpha - \sin\beta &= A \sin B \\ &= 2\cos(\omega t - \phi_2))\sin(\frac{\phi_2}{2}) \end{aligned}$$

and the amplitude terms can be equated, resulting in the following equation for the relative phase of the original waveform.

$$\phi_2 = 2\arcsin(\frac{A}{2}) \tag{B.2}$$

There are four scenarios for the presented data, and they are labelled as follows: Nominal response (the nominal L4C-3D instrument response is deconvolved from the raw waveforms. The poles used are $-4.44 \pm 4.44i$); Median response (the median L4C-3D instrument responses as given by SCEC are deconvolved from the raw data. The

poles used are $-4.9755 \pm 4.4672i$); Raw response (there has been no processing for the raw response, and as a result of the amplitudes being in counts, the amplitudes are much bigger than for the other 3 cases); and Individual response (the individual L4C-3D instrument responses given by SCEC are deconvolved from the raw waveforms). Both the poles and the seismometer's generator constant are given in Table B.1, and they were acquired from the PBIC's (Portable Broadband Instrument Center) web page for both positive and negative calibration pulses (the process is described on their web page, http://www.crustal.ucsb.edu/scec/pbic/). When deconvolving the instrument responses, two zeros were used (to achieve velocity measurements), and the median seismometer generator constant of the individual SCEC responses was used for both nominal and the median responses. Furthermore, the instruments used by SCEC's PBIC have different generator constant values than the typically produced L4C-3D seismometers (Aaron Martin, personal communication, 1998). Therefore it was necessary to estimate the generator constant, which I took to be the median (417.574 counts/volt) of the 3 channels from the 18 different L4C-3D seismometers used in this study, for both the positive and negative calibration pulses, as reproduced in Tables B.1 and B.2.

For calibration 1, the following frequencies were excited (in Hz): 1.105, 1.120, 1.126, 1.627, 1.651, 1.672, 2.249. For calibration 2, the following frequencies were excited (in Hz): 1.117, 1.627, 1.651, 1.672, 1.700, 2.252, 2.356. The main trends to notice in Tables B.3 through B.44 are:

- The phase variances for the nominal, median, and raw responses are very similar, and in general smaller than the phase variances calculated for the individual responses. This is more evident for the North component.

- The amplitude variances are generally smaller for the nominal responses, but the differences between the three comparable cases (nominal, median, and individual responses) is less than a factor of two.

From Tables B.3 to B.44, it is evident that the phase and the phase variances for the nominal responses match those of the raw responses. The raw responses are the

PBIC seismometer number	*East comp. constant*	*East comp. poles*	*North comp. constant*	*North comp. poles*	*Vertical comp. constant*	*Vertical comp. poles*
0909	413.21	$-5.10 \pm 4.14i$	416.72	$-5.10 \pm 4.70i$	420.08	$-4.44 \pm 4.39i$
0910	417.85	$-5.47 \pm 4.87i$	415.23	$-5.32 \pm 4.04i$	404.23	$-4.90 \pm 3.73i$
1108	421.83	$-5.22 \pm 3.88i$	404.32	$-5.01 \pm 4.87i$	405.31	$-4.44 \pm 4.29i$
1109	421.56	$-4.98 \pm 4.30i$	419.60	$-4.97 \pm 4.41i$	417.00	$-4.24 \pm 4.37i$
1110	425.67	$-5.05 \pm 4.40i$	425.13	$-5.00 \pm 4.22i$	428.42	$-4.77 \pm 4.22i$
1111	419.81	$-4.94 \pm 4.06i$	426.16	$-4.83 \pm 4.63i$	406.79	$-4.35 \pm 4.39i$
1112	412.16	$-4.95 \pm 4.61i$	411.31	$-4.66 \pm 4.58i$	402.31	$-4.02 \pm 4.32i$
1113	419.04	$-5.11 \pm 4.42i$	416.56	$-5.01 \pm 4.30i$	412.45	$-4.39 \pm 4.27i$
1114	405.62	$-4.90 \pm 5.26i$	410.08	$-4.83 \pm 4.55i$	421.90	$-4.18 \pm 4.67i$
1115	432.14	$-4.95 \pm 4.24i$	409.96	$-4.68 \pm 4.41i$	417.90	$-4.18 \pm 4.56i$
1116	413.19	$-4.75 \pm 4.43i$	417.31	$-4.86 \pm 4.62i$	394.97	$-4.07 \pm 4.53i$
1199	427.40	$-4.98 \pm 4.29i$	417.80	$-5.19 \pm 4.82i$	434.91	$-4.83 \pm 3.88i$
1200	423.05	$-5.26 \pm 4.51i$	420.74	$-5.35 \pm 4.67i$	412.38	$-4.27 \pm 4.48i$
1201	418.31	$-4.95 \pm 4.33i$	417.64	$-4.75 \pm 4.17i$	429.62	$-4.22 \pm 5.09i$
1315	417.50	$-5.09 \pm 3.83i$	420.17	$-5.01 \pm 4.03i$	400.64	$-4.35 \pm 4.51i$
1316	427.88	$-5.46 \pm 4.98i$	421.23	$-5.40 \pm 4.59i$	421.41	$-4.81 \pm 4.05i$
1847	406.38	$-4.90 \pm 4.76i$	408.94	$-4.51 \pm 4.14i$	419.35	$-4.59 \pm 4.24i$
1848	423.38	$-5.09 \pm 4.22i$	406.63	$-4.99 \pm 4.70i$	416.28	$-4.49 \pm 4.40i$

Table B.1 Individual instrument responses from positive calibration pulses for the 18 L4C-3D seismometers used for the performed experiments. Given are values for the seismometer's poles and generator constant for each of the seismometer's components.

waveforms that the instruments were actually recording at the time of the experiment, and the data for them represent the highest accuracy that should be expected from the instruments. Furthermore, the particle velocity variances (amplitudes) for the nominal responses were also the lowest (excluding the raw response calculations which are on a different scale). Therefore, for convenience, I choose to deconvolve the nominal response from the waveforms when an L4C-3D seismometer is used in this thesis.

PBIC seismometer number	*East comp. constant*	*East comp. poles*	*North comp. constant*	*North comp. poles*	*Vertical comp. constant*	*Vertical comp. poles*
0909	413.36	$-5.23 \pm 4.33i$	414.27	$-5.12 \pm 4.34i$	421.79	$-5.06 \pm 5.71i$
0910	412.06	$-5.04 \pm 4.26i$	423.41	$-5.57 \pm 4.26i$	410.22	$-5.39 \pm 4.77i$
1108	415.00	$-5.20 \pm 4.36i$	410.71	$-4.65 \pm 4.06i$	398.22	$-5.04 \pm 5.68i$
1109	424.57	$-4.96 \pm 4.20i$	410.39	$-5.10 \pm 5.38i$	419.37	$-5.04 \pm 5.80i$
1110	422.90	$-5.04 \pm 4.54i$	435.10	$-5.11 \pm 4.16i$	444.44	$-5.23 \pm 4.59i$
1111	429.08	$-5.22 \pm 4.41i$	423.58	$-4.81 \pm 4.77i$	415.54	$-5.06 \pm 5.46i$
1112	410.00	$-4.83 \pm 4.52i$	414.98	$-5.05 \pm 5.19i$	403.03	$-4.68 \pm 5.90i$
1113	412.99	$-4.98 \pm 4.50i$	422.79	$-5.04 \pm 4.11i$	416.77	$-4.93 \pm 5.26i$
1114	416.95	$-4.69 \pm 4.45i$	406.16	$-5.08 \pm 5.16i$	411.93	$-4.87 \pm 6.45i$
1115	429.41	$-4.93 \pm 4.31i$	416.03	$-4.93 \pm 4.66i$	408.46	$-4.88 \pm 6.19i$
1116	413.38	$-4.89 \pm 4.69i$	421.25	$-4.79 \pm 4.42i$	399.62	$-4.79 \pm 5.72i$
1199	426.79	$-5.07 \pm 4.48i$	420.98	$-4.92 \pm 4.38i$	442.48	$-5.32 \pm 4.94i$
1200	423.15	$-5.08 \pm 3.98i$	436.06	$-5.83 \pm 4.53i$	417.81	$-4.98 \pm 5.78i$
1201	418.55	$-5.26 \pm 4.86i$	413.95	$-5.22 \pm 5.18i$	422.94	$-5.01 \pm 6.63i$
1315	417.05	$-5.38 \pm 4.46i$	420.99	$-5.17 \pm 4.26i$	403.44	$-5.10 \pm 5.84i$
1316	426.69	$-4.90 \pm 3.93i$	421.39	$-5.17 \pm 4.12i$	431.94	$-5.35 \pm 4.78i$
1847	406.37	$-4.50 \pm 4.21i$	405.35	$-4.80 \pm 4.63i$	429.16	$-5.03 \pm 4.63i$
1848	412.07	$-4.78 \pm 4.12i$	409.64	$-4.75 \pm 4.26i$	419.94	$-5.02 \pm 5.06i$

Table B.2 Individual instrument responses from negative calibration pulses for the 18 L4C-3D seismometers used for the performed experiments. Given are values for the seismometer's poles and generator constant for each of the seismometer's components.

East Comp. *Freq = 1.105 Hz*	*Nominal* *Response*	*Median* *Response*	*Raw* *Response*	*Individual* *Response*
Mean Phase	$-2.0485 * 10^{-1}$	$-2.0402 * 10^{-1}$	$-2.0915 * 10^{-1}$	$-1.6297 * 10^{-1}$
Median Phase	$-2.2117 * 10^{-1}$	$-2.2043 * 10^{-1}$	$-2.2413 * 10^{-1}$	$-1.7129 * 10^{-1}$
Phase Variance	$3.2345 * 10^{-3}$	$3.2370 * 10^{-3}$	$3.2196 * 10^{-3}$	$1.0002 * 10^{-2}$
Mean Amp.	$5.6476 * 10^{-5}$	$6.2693 * 10^{-5}$	$1.8258 * 10^{-2}$	$6.2594 * 10^{-5}$
Median Amp.	$5.6340 * 10^{-5}$	$6.2541 * 10^{-5}$	$1.8215 * 10^{-2}$	$6.3084 * 10^{-5}$
Amp. Variance	$3.5981 * 10^{-11}$	$4.4343 * 10^{-11}$	$3.7619 * 10^{-6}$	$5.1533 * 10^{-11}$

Table B.3 East component data properties for seismometer calibration 1 at a frequency of 1.105 Hz. Phase values in radians, amplitude values in m/s (raw response in counts).

North Comp. *Freq = 1.105 Hz*	*Nominal* *Response*	*Median* *Response*	*Raw* *Response*	*Individual* *Response*
Mean Phase	$2.3064 * 10^{-2}$	$2.3065 * 10^{-2}$	$2.3054 * 10^{-2}$	$2.3466 * 10^{-2}$
Median Phase	$2.0295 * 10^{-2}$	$2.0295 * 10^{-2}$	$2.0318 * 10^{-2}$	$3.1832 * 10^{-3}$
Phase Variance	$2.0333 * 10^{-3}$	$2.0333 * 10^{-3}$	$2.0329 * 10^{-3}$	$6.0934 * 10^{-3}$
Mean Amp.	$1.0976 * 10^{-4}$	$1.2185 * 10^{-4}$	$: 3.5489 * 10^{-2}$	$1.2310 * 10^{-4}$
Median Amp.	$1.0857 * 10^{-4}$	$1.2052 * 10^{-4}$	$; 3.5100 * 10^{-2}$	$1.2412 * 10^{-4}$
Amp. Variance	$2.2179 * 10^{-11}$	$2.7330 * 10^{-11}$	$2.3154 * 10^{-6}$	$2.8170 * 10^{-11}$

Table B.4 North component data properties for seismometer calibration 1 at a frequency of 1.105 Hz. Phase values in radians, amplitude values in m/s (raw response in counts).

Vert. Comp. *Freq = 1.105 Hz*	*Nominal* *Response*	*Median* *Response*	*Raw* *Response*	*Individual* *Response*
Mean Phase	$2.0429 * 10^{-1}$	$1.8785 * 10^{-1}$	$1.8794 * 10^{-1}$	$3.5573 * 10^{-1}$
Median Phase	$1.8340 * 10^{-1}$	$1.8338 * 10^{-1}$	$1.8353 * 10^{-1}$	$3.1377 * 10^{-1}$
Phase Variance	$4.1585 * 10^{-2}$	$4.6360 * 10^{-2}$	$4.6362 * 10^{-2}$	$3.3444 * 10^{-2}$
Mean Amp.	$2.2577 * 10^{-5}$	$2.5063 * 10^{-5}$	$7.3010 * 10^{-3}$	$2.2168 * 10^{-5}$
Median Amp.	$1.1889 * 10^{-5}$	$1.3198 * 10^{-5}$	$3.8427 * 10^{-3}$	$1.2293 * 10^{-5}$
Amp. Variance	$3.9815 * 10^{-10}$	$4.9064 * 10^{-10}$	$4.1626 * 10^{-5}$	$3.6075 * 10^{-10}$

Table B.5 Vertical component data properties for seismometer calibration 1 at a frequency of 1.105 Hz. Phase values in radians, amplitude values in m/s (raw response in counts).

East Comp. *Freq = 1.117 Hz*	*Nominal* *Response*	*Median* *Response*	*Raw* *Response*	*Individual* *Response*
Mean Phase	$-2.4612 * 10^{-1}$	$-2.4599 * 10^{-1}$	$-2.4697 * 10^{-1}$	$-2.1623 * 10^{-1}$
Median Phase	$-2.4925 * 10^{-1}$	$-2.4910 * 10^{-1}$	$-2.5023 * 10^{-1}$	$-2.2790 * 10^{-1}$
Phase Variance	$6.3028 * 10^{-3}$	$6.2886 * 10^{-3}$	$6.3700 * 10^{-3}$	$7.0523 * 10^{-3}$
Mean Amp.	$8.2905 * 10^{-5}$	$9.1920 * 10^{-5}$	$2.7009 * 10^{-2}$	$9.1774 * 10^{-5}$
Median Amp.	$8.2640 * 10^{-5}$	$9.1628 * 10^{-5}$	$2.6921 * 10^{-2}$	$9.2837 * 10^{-5}$
Amp. Variance	$5.9984 * 10^{-11}$	$7.3736 * 10^{-11}$	$6.3653 * 10^{-6}$	$8.7986 * 10^{-11}$

Table B.6 East component data properties for seismometer calibration 2 at a frequency of 1.117 Hz. Phase values in radians, amplitude values in m/s (raw response in counts).

North Comp. *Freq = 1.117 Hz*	*Nominal* *Response*	*Median* *Response*	*Raw* *Response*	*Individual* *Response*
Mean Phase	$-2.0365 * 10^{-2}$	$-2.0364 * 10^{-2}$	$-2.0366 * 10^{-2}$	$-3.1421 * 10^{-3}$
Median Phase	$-3.9051 * 10^{-2}$	$-3.9049 * 10^{-2}$	$-3.9050 * 10^{-2}$	$-4.5184 * 10^{-2}$
Phase Variance	$5.6950 * 10^{-3}$	$5.6953 * 10^{-3}$	$5.6949 * 10^{-3}$	$1.1695 * 10^{-3}$
Mean Amp.	$1.4830 * 10^{-4}$	$1.6442 * 10^{-4}$	$4.8312 * 10^{-2}$	$1.6611 * 10^{-4}$
Median Amp.	$1.4647 * 10^{-4}$	$1.6240 * 10^{-4}$	$4.7715 * 10^{-2}$	$1.6740 * 10^{-4}$
Amp. Variance	$4.0010 * 10^{-11}$	$4.9182 * 10^{-11}$	$4.2427 * 10^{-6}$	$5.0926 * 10^{-11}$

Table B.7 North component data properties for seismometer calibration 2 at a frequency of 1.117 Hz. Phase values in radians, amplitude values in m/s (raw response in counts).

Vert. Comp. *Freq = 1.117 Hz*	*Nominal* *Response*	*Median* *Response*	*Raw* *Response*	*Individual* *Response*
Mean Phase	$1.3492 * 10^{-1}$	$1.3491 * 10^{-1}$	$1.3500 * 10^{-1}$	$2.6805 * 10^{-1}$
Median Phase	$1.0055 * 10^{-1}$	$1.0056 * 10^{-1}$	$1.0068 * 10^{-1}$	$2.3036 * 10^{-1}$
Phase Variance	$2.9430 * 10^{-2}$	$2.9428 * 10^{-2}$	$2.9441 * 10^{-2}$	$2.8207 * 10^{-2}$
Mean Amp.	$3.0183 * 10^{-5}$	$3.3464 * 10^{-5}$	$9.8338 * 10^{-3}$	$2.9633 * 10^{-5}$
Median Amp.	$1.6563 * 10^{-5}$	$1.8363 * 10^{-5}$	$5.3989 * 10^{-3}$	$1.6668 * 10^{-5}$
Amp. Variance	$7.0771 * 10^{-10}$	$8.6996 * 10^{-10}$	$7.5117 * 10^{-5}$	$6.4070 * 10^{-10}$

Table B.8 Vertical component data properties for seismometer calibration 2 at a frequency of 1.117 Hz. Phase values in radians, amplitude values in m/s (raw response in counts).

East Comp. Freq = 1.120 Hz	*Nominal Response*	*Median Response*	*Raw Response*	*Individual Response*
Mean Phase	$-2.0558 * 10^{-1}$	$-2.0538 * 10^{-1}$	$-2.0598 * 10^{-1}$	$-1.7477 * 10^{-1}$
Median Phase	$-2.1224 * 10^{-1}$	$-2.1200 * 10^{-1}$	$-2.1185 * 10^{-1}$	$-1.5962 * 10^{-1}$
Phase Variance	$3.7923 * 10^{-3}$	$3.7927 * 10^{-3}$	$5.0471 * 10^{-3}$	$5.0471 * 10^{-3}$
Mean Amp.	$7.3545 * 10^{-5}$	$8.1504 * 10^{-5}$	$2.4019 * 10^{-2}$	$8.1371 * 10^{-5}$
Median Amp.	$7.3565 * 10^{-5}$	$8.1526 * 10^{-5}$	$2.4024 * 10^{-2}$	$8.2665 * 10^{-5}$
Amp. Variance	$3.5308 * 10^{-11}$	$4.3366 * 10^{-11}$	$3.7645 * 10^{-6}$	$5.3895 * 10^{-11}$

Table B.9 East component data properties for seismometer calibration 1 at a frequency of 1.120 Hz. Phase values in radians, amplitude values in m/s (raw response in counts).

North Comp. Freq = 1.120 Hz	*Nominal Response*	*Median Response*	*Raw Response*	*Individual Response*
Mean Phase	$2.6106 * 10^{-2}$	$2.6107 * 10^{-2}$	$2.6104 * 10^{-2}$	$3.8058 * 10^{-2}$
Median Phase	$1.8387 * 10^{-2}$	$1.8386 * 10^{-2}$	$1.8386 * 10^{-2}$	$3.4410 * 10^{-2}$
Phase Variance	$2.3474 * 10^{-3}$	$2.3475 * 10^{-3}$	$2.3474 * 10^{-3}$	$6.6036 * 10^{-3}$
Mean Amp.	$1.1478 * 10^{-4}$	$1.2720 * 10^{-4}$	$3.7490 * 10^{-2}$	$1.2850 * 10^{-4}$
Median Amp.	$1.1358 * 10^{-4}$	$1.2587 * 10^{-4}$	$3.7099 * 10^{-2}$	$1.2964 * 10^{-4}$
Amp. Variance	$2.3847 * 10^{-11}$	$2.9294 * 10^{-11}$	$2.5432 * 10^{-6}$	$2.9811 * 10^{-11}$

Table B.10 North component data properties for seismometer calibration 1 at a frequency of 1.120 Hz. Phase values in radians, amplitude values in m/s (raw response in counts).

Vert. Comp. Freq = 1.120 Hz	*Nominal Response*	*Median Response*	*Raw Response*	*Individual Response*
Mean Phase	$2.2719 * 10^{-1}$	$2.2718 * 10^{-1}$	$2.2716 * 10^{-1}$	$3.8264 * 10^{-1}$
Median Phase	$2.1105 * 10^{-1}$	$2.1105 * 10^{-1}$	$2.1103 * 10^{-1}$	$3.3233 * 10^{-1}$
Phase Variance	$4.6565 * 10^{-2}$	$4.6567 * 10^{-2}$	$4.6550 * 10^{-2}$	$3.6267 * 10^{-2}$
Mean Amp.	$2.2974 * 10^{-5}$	$2.5460 * 10^{-5}$	$7.5053 * 10^{-3}$	$2.2552 * 10^{-5}$
Median Amp.	$1.2286 * 10^{-5}$	$1.3615 * 10^{-5}$	$4.0152 * 10^{-3}$	$1.2814 * 10^{-5}$
Amp. Variance	$4.3005 * 10^{-10}$	$5.2817 * 10^{-10}$	$4.5879 * 10^{-5}$	$3.8980 * 10^{-10}$

Table B.11 Vertical component data properties of seismometer calibration 1 at a frequency of 1.120 Hz. Phase values in radians, amplitude values in m/s (raw response in counts).

East Comp. *Freq = 1.126 Hz*	*Nominal* *Response*	*Median* *Response*	*Raw* *Response*	*Individual* *Response*
Mean Phase	$-2.5313 * 10^{-1}$	$-2.5303 * 10^{-1}$	$-2.5382 * 10^{-1}$	$-2.2127 * 10^{-1}$
Median Phase	$-2.6247 * 10^{-1}$	$-2.6235 * 10^{-1}$	$-2.6328 * 10^{-1}$	$-2.0639 * 10^{-1}$
Phase Variance	$3.8708 * 10^{-3}$	$3.8720 * 10^{-3}$	$3.8633 * 10^{-3}$	$5.1788 * 10^{-3}$
Mean Amp.	$8.3572 * 10^{-5}$	$9.2547 * 10^{-5}$	$2.7406 * 10^{-2}$	$9.2395 * 10^{-5}$
Median Amp.	$8.3959 * 10^{-5}$	$9.2976 * 10^{-5}$	$2.7532 * 10^{-2}$	$9.4098 * 10^{-5}$
Amp. Variance	$3.5141 * 10^{-11}$	$4.3093 * 10^{-11}$	$3.7806 * 10^{-6}$	$5.5736 * 10^{-11}$

Table B.12 East component data properties for seismometer calibration 1 at a frequency of 1.126 Hz. Phase values in radians, amplitude values in m/s (raw response in counts).

North Comp. *Freq = 1.126 Hz*	*Nominal* *Response*	*Median* *Response*	*Raw* *Response*	*Individual* *Response*
Mean Phase	$2.5989 * 10^{-2}$	$2.5990 * 10^{-2}$	$2.5986 * 10^{-2}$	$3.7557 * 10^{-2}$
Median Phase	$1.8161 * 10^{-2}$	$1.8162 * 10^{-2}$	$1.8154 * 10^{-2}$	$3.4859 * 10^{-2}$
Phase Variance	$2.4085 * 10^{-3}$	$2.4085 * 10^{-3}$	$2.4085 * 10^{-3}$	$6.5992 * 10^{-3}$
Mean Amp.	$1.1757 * 10^{-4}$	$1.3019 * 10^{-4}$	$3.8556 * 10^{-2}$	$1.3152 * 10^{-4}$
Median Amp.	$1.1639 * 10^{-4}$	$1.2889 * 10^{-4}$	$3.8172 * 10^{-2}$	$1.3265 * 10^{-4}$
Amp. Variance	$2.4850 * 10^{-11}$	$3.0477 * 10^{-11}$	$2.6720 * 10^{-6}$	$3.0784 * 10^{-11}$

Table B.13 North component data properties for seismometer calibration 1 at a frequency of 1.126 Hz. Phase values in radians, amplitude values in m/s (raw response in counts).

Vert. Comp. *Freq = 1.126 Hz*	*Nominal* *Response*	*Median* *Response*	*Raw* *Response*	*Individual* *Response*
Mean Phase	$2.4167 * 10^{-1}$	$2.4166 * 10^{-1}$	$2.5813 * 10^{-1}$	$3.9795 * 10^{-1}$
Median Phase	$2.2818 * 10^{-1}$	$2.2817 * 10^{-1}$	$2.2824 * 10^{-1}$	$3.4130 * 10^{-1}$
Phase Variance	$4.9492 * 10^{-2}$	$4.9489 * 10^{-2}$	$4.2861 * 10^{-2}$	$3.8124 * 10^{-2}$
Mean Amp.	$2.3231 * 10^{-5}$	$2.5725 * 10^{-5}$	$7.6185 * 10^{-3}$	$2.2801 * 10^{-5}$
Median Amp.	$1.2568 * 10^{-5}$	$1.3917 * 10^{-5}$	$4.1218 * 10^{-3}$	$1.3111 * 10^{-5}$
Amp. Variance	$4.4878 * 10^{-10}$	$5.5037 * 10^{-10}$	$4.8267 * 10^{-5}$	$4.0686 * 10^{-10}$

Table B.14 Vertical component data properties for seismometer calibration 1 at a frequency of 1.126 Hz. Phase values in radians, amplitude values in m/s (raw response in counts).

East Comp. *Freq = 1.627 Hz*	*Nominal* *Response*	*Median* *Response*	*Raw* *Response*	*Individual* *Response*
Mean Phase	$-1.0646 * 10^{0}$	$-1.0646 * 10^{0}$	$-1.0648 * 10^{0}$	$-1.0511 * 10^{0}$
Median Phase	$-6.6329 * 10^{-1}$	$-6.6330 * 10^{-1}$	$-6.6330 * 10^{-1}$	$-7.1423 * 10^{-1}$
Phase Variance	$8.6222 * 10^{-1}$	$8.6228 * 10^{-1}$	$8.6132 * 10^{-1}$	$8.6132 * 10^{-1}$
Mean Amp.	$5.7955 * 10^{-5}$	$6.1195 * 10^{-5}$	$2.2624 * 10^{-2}$	$6.1238 * 10^{-5}$
Median Amp.	$5.1219 * 10^{-5}$	$5.4083 * 10^{-5}$	$1.9994 * 10^{-2}$	$5.6699 * 10^{-5}$
Amp. Variance	$7.1420 * 10^{-10}$	$7.9632 * 10^{-10}$	$1.0880 * 10^{-4}$	$8.0195 * 10^{-10}$

Table B.15 East component data properties for seismometer calibration 1 at a frequency of 1.627 (A) Hz. Phase values in radians, amplitude values in m/s (raw response in counts).

North Comp. *Freq = 1.627 Hz*	*Nominal* *Response*	*Median* *Response*	*Raw* *Response*	*Individual* *Response*
Mean Phase	$-7.3976 * 10^{-2}$	$-7.3975 * 10^{-2}$	$-7.3975 * 10^{-2}$	$-6.5858 * 10^{-2}$
Median Phase	$-6.6030 * 10^{-2}$	$-6.6030 * 10^{-2}$	$-6.6028 * 10^{-2}$	$-6.4533 * 10^{-2}$
Phase Variance	$3.4339 * 10^{-3}$	$3.4339 * 10^{-3}$	$3.4335 * 10^{-3}$	$4.2130 * 10^{-3}$
Mean Amp.	$4.0299 * 10^{-3}$	$4.2552 * 10^{-3}$	$1.5731 * 10^{0}$	$4.2815 * 10^{-3}$
Median Amp.	$4.0541 * 10^{-3}$	$4.2808 * 10^{-3}$	$1.5826 * 10^{0}$	$4.2823 * 10^{-3}$
Amp. Variance	$1.2212 * 10^{-8}$	$1.3615 * 10^{-8}$	$1.8605 * 10^{-3}$	$1.9676 * 10^{-8}$

Table B.16 North component data properties for seismometer calibration 1 at a frequency of 1.627 (A) Hz. Phase values in radians, amplitude values in m/s (raw response in counts).

Vert. Comp. *Freq = 1.627 Hz*	*Nominal* *Response*	*Median* *Response*	*Raw* *Response*	*Individual* *Response*
Mean Phase	$-6.2740 * 10^{-3}$	$-6.2744 * 10^{-3}$	$-6.2808 * 10^{-3}$	$1.6273 * 10^{-1}$
Median Phase	$-5.3833 * 10^{-2}$	$-5.3832 * 10^{-2}$	$-5.3828 * 10^{-2}$	$1.5422 * 10^{-1}$
Phase Variance	$1.5582 * 10^{-2}$	$1.5581 * 10^{-2}$	$1.5580 * 10^{-2}$	$1.1442 * 10^{-2}$
Mean Amp.	$4.7506 * 10^{-4}$	$5.0163 * 10^{-4}$	$1.8545 * 10^{-1}$	$4.7612 * 10^{-4}$
Median Amp.	$4.8672 * 10^{-4}$	$5.1394 * 10^{-4}$	$1.8999 * 10^{-1}$	$4.7823 * 10^{-4}$
Amp. Variance	$2.2797 * 10^{-9}$	$2.5417 * 10^{-9}$	$3.4739 * 10^{-4}$	$1.8012 * 10^{-9}$

Table B.17 Vertical component data properties for seismometer calibration 1 at a frequency of 1.627 (A) Hz. Phase values in radians, amplitude values in m/s (raw response in counts).

East Comp. *Freq = 1.627 Hz*	*Nominal* *Response*	*Median* *Response*	*Raw* *Response*	*Individual* *Response*
Mean Phase	$-1.0646 * 10^{0}$	$-1.0939 * 10^{0}$	$-1.0937 * 10^{0}$	$-1.0821 * 10^{0}$
Median Phase	$-6.3649 * 10^{-1}$	$-6.3651 * 10^{-1}$	$-6.3646 * 10^{-1}$	$-6.8738 * 10^{-1}$
Phase Variance	$1.0675 * 10^{0}$	$1.0675 * 10^{0}$	$1.0670 * 10^{0}$	$1.0657 * 10^{0}$
Mean Amp.	$9.2738 * 10^{-5}$	$9.7912 * 10^{-5}$	$3.6212 * 10^{-2}$	$9.7885 * 10^{-5}$
Median Amp.	$7.9699 * 10^{-5}$	$8.4144 * 10^{-5}$	$3.1122 * 10^{-2}$	$8.2301 * 10^{-5}$
Amp. Variance	$1.4754 * 10^{-9}$	$1.6447 * 10^{-9}$	$2.2491 * 10^{-4}$	$1.6247 * 10^{-9}$

Table B.18 East component data properties for seismometer calibration 2 at a frequency of 1.627 (B) Hz. Phase values in radians, amplitude values in m/s (raw response in counts).

North Comp. *Freq = 1.627 Hz*	*Nominal* *Response*	*Median* *Response*	*Raw* *Response*	*Individual* *Response*
Mean Phase	$6.2578 * 10^{-2}$	$6.2579 * 10^{-2}$	$6.2571 * 10^{-2}$	$6.3386 * 10^{-2}$
Median Phase	$4.9828 * 10^{-2}$	$4.9828 * 10^{-2}$	$4.9828 * 10^{-2}$	$2.4135 * 10^{-2}$
Phase Variance	$1.2441 * 10^{-2}$	$1.2441 * 10^{-2}$	$1.2439 * 10^{-2}$	$1.4400 * 10^{-2}$
Mean Amp.	$7.4242 * 10^{-3}$	$7.8385 * 10^{-3}$	$2.8988 * 10^{0}$	$7.8867 * 10^{-3}$
Median Amp.	$7.4292 * 10^{-3}$	$7.8437 * 10^{-3}$	$2.9007 * 10^{0}$	$7.8843 * 10^{-3}$
Amp. Variance	$3.9904 * 10^{-8}$	$4.4480 * 10^{-8}$	$6.0823 * 10^{-3}$	$6.4170 * 10^{-8}$

Table B.19 North component data properties for seismometer calibration 2 at a frequency of 1.627 (B) Hz. Phase values in radians, amplitude values in m/s (raw response in counts).

Vert. Comp. *Freq = 1.627 Hz*	*Nominal* *Response*	*Median* *Response*	*Raw* *Response*	*Individual* *Response*
Mean Phase	$1.4319 * 10^{-1}$	$1.4319 * 10^{-1}$	$1.4317 * 10^{-1}$	$2.6749 * 10^{-1}$
Median Phase	$1.0409 * 10^{-1}$	$1.0409 * 10^{-1}$	$1.0409 * 10^{-1}$	$2.4602 * 10^{-1}$
Phase Variance	$1.2811 * 10^{-2}$	$1.2811 * 10^{-2}$	$1.2807 * 10^{-2}$	$1.0259 * 10^{-2}$
Mean Amp.	$8.2266 * 10^{-4}$	$8.6856 * 10^{-4}$	$3.2122 * 10^{-1}$	$8.2517 * 10^{-4}$
Median Amp.	$8.0285 * 10^{-4}$	$8.4765 * 10^{-4}$	$3.1350 * 10^{-1}$	$8.0860 * 10^{-4}$
Amp. Variance	$7.3838 * 10^{-9}$	$8.2307 * 10^{-9}$	$1.1254 * 10^{-3}$	$7.2050 * 10^{-9}$

Table B.20 Vertical component data properties for seismometer calibration 2 at a frequency of 1.627 (B) Hz. Phase values in radians, amplitude values in m/s (raw response in counts).

East Comp. *Freq = 1.651 Hz*	*Nominal* *Response*	*Median* *Response*	*Raw* *Response*	*Individual* *Response*
Mean Phase	$-7.8148 * 10^{-1}$	$-7.8146 * 10^{-1}$	$-7.8147 * 10^{-1}$	$-7.6852 * 10^{-1}$
Median Phase	$-3.5483 * 10^{-1}$	$-3.5483 * 10^{-1}$	$-3.5483 * 10^{-1}$	$-3.7544 * 10^{-1}$
Phase Variance	$8.3098 * 10^{-1}$	$8.3094 * 10^{-1}$	$8.3093 * 10^{-1}$	$8.3213 * 10^{-1}$
Mean Amp.	$8.9615 * 10^{-5}$	$9.4472 * 10^{-5}$	$3.5111 * 10^{-2}$	$9.4546 * 10^{-5}$
Median Amp.	$8.7449 * 10^{-5}$	$9.2189 * 10^{-5}$	$3.4262 * 10^{-2}$	$9.4025 * 10^{-5}$
Amp. Variance	$1.7085 * 10^{-9}$	$1.8988 * 10^{-9}$	$2.6225 * 10^{-4}$	$1.9097 * 10^{-9}$

Table B.21 East component data properties for seismometer calibration 1 at a frequency of 1.651 (A) Hz. Phase values in radians, amplitude values in m/s (raw response in counts).

North Comp. *Freq = 1.651 Hz*	*Nominal* *Response*	*Median* *Response*	*Raw* *Response*	*Individual* *Response*
Mean Phase	$2.9872 * 10^{-2}$	$2.9872 * 10^{-2}$	$2.9873 * 10^{-2}$	$3.8073 * 10^{-2}$
Median Phase	$3.5082 * 10^{-2}$	$3.5081 * 10^{-2}$	$3.5083 * 10^{-2}$	$4.1554 * 10^{-2}$
Phase Variance	$3.7730 * 10^{-3}$	$3.7730 * 10^{-3}$	$3.7733 * 10^{-3}$	$4.4132 * 10^{-3}$
Mean Amp.	$6.1929 * 10^{-3}$	$6.5286 * 10^{-3}$	$2.4264 * 10^{0}$	$6.5676 * 10^{-3}$
Median Amp.	$6.2215 * 10^{-3}$	$6.5587 * 10^{-3}$	$2.4376 * 10^{0}$	$6.5560 * 10^{-3}$
Amp. Variance	$2.8139 * 10^{-8}$	$3.1272 * 10^{-8}$	$4.3196 * 10^{-3}$	$4.5210 * 10^{-8}$

Table B.22 North component data properties for seismometer calibration 1 at a frequency of 1.651 (A) Hz. Phase values in radians, amplitude values in m/s (raw response in counts).

Vert. Comp. *Freq = 1.651 Hz*	*Nominal* *Response*	*Median* *Response*	*Raw* *Response*	*Individual* *Response*
Mean Phase	$1.0602 * 10^{-1}$	$1.0602 * 10^{-1}$	$1.0602 * 10^{-1}$	$2.7444 * 10^{-1}$
Median Phase	$5.6983 * 10^{-2}$	$5.6983 * 10^{-2}$	$5.6983 * 10^{-2}$	$2.5435 * 10^{-1}$
Phase Variance	$2.0368 * 10^{-2}$	$2.0367 * 10^{-2}$	$2.0367 * 10^{-2}$	$1.6054 * 10^{-2}$
Mean Amp.	$6.7781 * 10^{-4}$	$7.1455 * 10^{-4}$	$2.6557 * 10^{-1}$	$6.8018 * 10^{-4}$
Median Amp.	$6.5348 * 10^{-4}$	$6.8890 * 10^{-4}$	$2.5604 * 10^{-1}$	$6.3762 * 10^{-4}$
Amp. Variance	$7.0343 * 10^{-9}$	$7.8175 * 10^{-9}$	$1.0798 * 10^{-3}$	$7.1925 * 10^{-9}$

Table B.23 Vertical component data properties for seismometer calibration 1 at a frequency of 1.651 (A) Hz. Phase values in radians, amplitude values in m/s (raw response in counts).

East Comp. *Freq = 1.651 Hz*	*Nominal* *Response*	*Median* *Response*	*Raw* *Response*	*Individual* *Response*
Mean Phase	$-1.0450 * 10^{0}$	$-1.0450 * 10^{0}$	$-1.0450 * 10^{0}$	$-1.0322 * 10^{0}$
Median Phase	$-4.7962 * 10^{-1}$	$-4.7962 * 10^{-1}$	$-4.7955 * 10^{-1}$	$-5.0367 * 10^{-1}$
Phase Variance	$1.1452 * 10^{0}$	$1.1453 * 10^{0}$	$1.1454 * 10^{0}$	$1.1475 * 10^{0}$
Mean Amp.	$8.2589 * 10^{-5}$	$8.7054 * 10^{-5}$	$3.2372 * 10^{-2}$	$8.7049 * 10^{-5}$
Median Amp.	$7.6261 * 10^{-5}$	$8.0382 * 10^{-5}$	$2.9892 * 10^{-2}$	$8.0898 * 10^{-5}$
Amp. Variance	$1.1581 * 10^{-9}$	$1.2867 * 10^{-9}$	$1.7800 * 10^{-4}$	$1.2736 * 10^{-9}$

Table B.24 East component data properties for seismometer calibration 2 at a frequency of 1.651 (B) Hz. Phase values in radians, amplitude values in m/s (raw response in counts).

North Comp. *Freq = 1.651 Hz*	*Nominal* *Response*	*Median* *Response*	*Raw* *Response*	*Individual* *Response*
Mean Phase	$-4.0293 * 10^{-2}$	$-4.0296 * 10^{-2}$	$-4.0291 * 10^{-2}$	$3.8073 * 10^{-2}$
Median Phase	$-5.4426 * 10^{-2}$	$-5.4425 * 10^{-2}$	$-5.4423 * 10^{-2}$	$4.1554 * 10^{-2}$
Phase Variance	$1.3703 * 10^{-2}$	$1.3702 * 10^{-2}$	$1.3702 * 10^{-2}$	$1.5519 * 10^{-2}$
Mean Amp.	$6.7568 * 10^{-3}$	$7.1220 * 10^{-3}$	$2.4264 * 10^{0}$	$7.1645 * 10^{-3}$
Median Amp.	$6.7621 * 10^{-3}$	$7.1276 * 10^{-3}$	$2.4376 * 10^{0}$	$7.1649 * 10^{-3}$
Amp. Variance	$3.2106 * 10^{-8}$	$3.5674 * 10^{-8}$	$4.3196 * 10^{-3}$	$5.1700 * 10^{-8}$

Table B.25 North component data properties for seismometer calibration 2 at a frequency of 1.651 (B) Hz. Phase values in radians, amplitude values in m/s (raw response in counts).

Vert. Comp. *Freq = 1.651 Hz*	*Nominal* *Response*	*Median* *Response*	*Raw* *Response*	*Individual* *Response*
Mean Phase	$4.9185 * 10^{-2}$	$4.9178 * 10^{-2}$	$4.9188 * 10^{-2}$	$1.7151 * 10^{-1}$
Median Phase	$2.0919 * 10^{-3}$	$2.0898 * 10^{-3}$	$2.0968 * 10^{-3}$	$1.3438 * 10^{-1}$
Phase Variance	$1.5499 * 10^{-2}$	$1.5498 * 10^{-2}$	$1.5499 * 10^{-2}$	$1.3305 * 10^{-2}$
Mean Amp.	$7.1533 * 10^{-4}$	$7.5400 * 10^{-4}$	$2.8042 * 10^{-1}$	$7.1812 * 10^{-4}$
Median Amp.	$6.9167 * 10^{-4}$	$7.2905 * 10^{-4}$	$2.7114 * 10^{-1}$	$6.8981 * 10^{-4}$
Amp. Variance	$1.1225 * 10^{-8}$	$1.2472 * 10^{-8}$	$1.7250 * 10^{-3}$	$1.1833 * 10^{-8}$

Table B.26 Vertical component data properties for seismometer calibration 2 at a frequency of 1.651 (B) Hz. Phase values in radians, amplitude values in m/s (raw response in counts).

East Comp. *Freq = 1.672 Hz*	*Nominal* *Response*	*Median* *Response*	*Raw* *Response*	*Individual* *Response*
Mean Phase	$-7.9289 * 10^{-1}$	$-7.9290 * 10^{-1}$	$-7.9290 * 10^{-1}$	$-7.8056 * 10^{-1}$
Median Phase	$-3.8091 * 10^{-1}$	$-3.8090 * 10^{-1}$	$-3.8092 * 10^{-1}$	$-3.8401 * 10^{-1}$
Phase Variance	$7.9629 * 10^{-1}$	$7.9634 * 10^{-1}$	$7.9631 * 10^{-1}$	$7.9848 * 10^{-1}$
Mean Amp.	$7.4852 * 10^{-5}$	$7.8802 * 10^{-5}$	$2.9416 * 10^{-2}$	$7.8864 * 10^{-5}$
Median Amp.	$7.5919 * 10^{-5}$	$7.9924 * 10^{-5}$	$2.9834 * 10^{-2}$	$7.9268 * 10^{-5}$
Amp. Variance	$1.2349 * 10^{-9}$	$1.3686 * 10^{-9}$	$1.9073 * 10^{-4}$	$1.3739 * 10^{-9}$

Table B.27 East component data properties for seismometer calibration 1 at a frequency of 1.672 (A) Hz. Phase values in radians, amplitude values in m/s (raw response in counts).

North Comp. *Freq = 1.672 Hz*	*Nominal* *Response*	*Median* *Response*	*Raw* *Response*	*Individual* *Response*
Mean Phase	$-7.3043 * 10^{-2}$	$-7.3043 * 10^{-2}$	$-7.3042 * 10^{-2}$	$-6.4357 * 10^{-2}$
Median Phase	$-6.8674 * 10^{-2}$	$-6.8674 * 10^{-2}$	$-6.8674 * 10^{-2}$	$-5.9332 * 10^{-2}$
Phase Variance	$3.8243 * 10^{-3}$	$3.8243 * 10^{-3}$	$3.8246 * 10^{-3}$	$4.4564 * 10^{-3}$
Mean Amp.	$5.0360 * 10^{-3}$	$5.3017 * 10^{-3}$	$1.9790 * 10^{0}$	$5.3326 * 10^{-3}$
Median Amp.	$5.0638 * 10^{-3}$	$5.3310 * 10^{-3}$	$1.9900 * 10^{0}$	$5.3165 * 10^{-3}$
Amp. Variance	$1.8219 * 10^{-8}$	$2.0192 * 10^{-8}$	$2.8136 * 10^{-3}$	$2.9290 * 10^{-8}$

Table B.28 North component data properties for seismometer calibration 1 at a frequency of 1.672 (A) Hz. Phase values in radians, amplitude values in m/s (raw response in counts).

Vert. Comp. *Freq = 1.672 Hz*	*Nominal* *Response*	*Median* *Response*	*Raw* *Response*	*Individual* *Response*
Mean Phase	$1.0533 * 10^{-2}$	$1.0534 * 10^{-2}$	$1.0534 * 10^{-1}$	$1.5316 * 10^{-1}$
Median Phase	$-4.5763 * 10^{-2}$	$-4.5763 * 10^{-2}$	$-4.5762 * 10^{-2}$	$1.2733 * 10^{-1}$
Phase Variance	$2.4874 * 10^{-2}$	$2.4874 * 10^{-2}$	$2.4873 * 10^{-2}$	$2.9451 * 10^{-2}$
Mean Amp.	$5.3254 * 10^{-4}$	$5.6064 * 10^{-4}$	$2.0927 * 10^{-1}$	$5.3473 * 10^{-4}$
Median Amp.	$5.2171 * 10^{-4}$	$5.4924 * 10^{-4}$	$2.0502 * 10^{-1}$	$5.1311 * 10^{-4}$
Amp. Variance	$7.5859 * 10^{-9}$	$8.4076 * 10^{-9}$	$1.1715 * 10^{-3}$	$7.9745 * 10^{-9}$

Table B.29 Vertical component data properties for seismometer calibration 1 at a frequency of 1.672 (A) Hz. Phase values in radians, amplitude values in m/s (raw response in counts).

East Comp. *Freq = 1.672 Hz*	*Nominal* *Response*	*Median* *Response*	*Raw* *Response*	*Individual* *Response*
Mean Phase	$-8.5317 * 10^{-1}$	$-8.5327 * 10^{-1}$	$-8.5326 * 10^{-1}$	$-8.4088 * 10^{-1}$
Median Phase	$-2.9846 * 10^{-1}$	$-2.9848 * 10^{-1}$	$-2.9849 * 10^{-1}$	$-3.2172 * 10^{-1}$
Phase Variance	$1.1684 * 10^{0}$	$1.1688 * 10^{0}$	$1.1687 * 10^{0}$	$1.1721 * 10^{0}$
Mean Amp.	$6.6223 * 10^{-5}$	$6.9714 * 10^{-5}$	$2.6029 * 10^{-2}$	$6.9715 * 10^{-5}$
Median Amp.	$5.7568 * 10^{-5}$	$6.0603 * 10^{-5}$	$2.2628 * 10^{-2}$	$6.3423 * 10^{-5}$
Amp. Variance	$7.1825 * 10^{-10}$	$7.9596 * 10^{-10}$	$1.1099 * 10^{-4}$	$7.8784 * 10^{-10}$

Table B.30 East component data properties for seismometer calibration 2 at a frequency of 1.672 (B) Hz. Phase values in radians, amplitude values in m/s (raw response in counts).

North Comp. *Freq = 1.672 Hz*	*Nominal* *Response*	*Median* *Response*	*Raw* *Response*	*Individual* *Response*
Mean Phase	$6.6702 * 10^{-2}$	$6.6706 * 10^{-2}$	$6.6705 * 10^{-2}$	$6.6891 * 10^{-2}$
Median Phase	$5.1123 * 10^{-2}$	$5.1120 * 10^{-2}$	$5.1115 * 10^{-2}$	$2.6869 * 10^{-2}$
Phase Variance	$1.5311 * 10^{-2}$	$1.5312 * 10^{-2}$	$1.5312 * 10^{-2}$	$1.6994 * 10^{-2}$
Mean Amp.	$5.3219 * 10^{-3}$	$5.6024 * 10^{-3}$	$2.0918 * 10^{0}$	$5.6349 * 10^{-3}$
Median Amp.	$5.3329 * 10^{-3}$	$5.6140 * 10^{-3}$	$2.0962 * 10^{0}$	$5.6384 * 10^{-3}$
Amp. Variance	$1.9517 * 10^{-8}$	$2.1630 * 10^{-8}$	$3.0154 * 10^{-3}$	$3.1338 * 10^{-8}$

Table B.31 North component data properties for seismometer calibration 2 at a frequency of 1.672 (B) Hz. Phase values in radians, amplitude values in m/s (raw response in counts).

Vert. Comp. *Freq = 1.672 Hz*	*Nominal* *Response*	*Median* *Response*	*Raw* *Response*	*Individual* *Response*
Mean Phase	$1.6577 * 10^{-1}$	$1.6578 * 10^{-1}$	$1.6577 * 10^{-1}$	$2.8699 * 10^{-1}$
Median Phase	$1.1246 * 10^{-1}$	$1.1247 * 10^{-1}$	$1.1245 * 10^{-1}$	$2.4081 * 10^{-1}$
Phase Variance	$1.9662 * 10^{-2}$	$1.9665 * 10^{-2}$	$1.9663 * 10^{-2}$	$1.7678 * 10^{-2}$
Mean Amp.	$5.4728 * 10^{-4}$	$5.7612 * 10^{-4}$	$2.1512 * 10^{-1}$	$5.4970 * 10^{-4}$
Median Amp.	$5.4363 * 10^{-4}$	$5.7229 * 10^{-4}$	$2.1369 * 10^{-1}$	$5.3860 * 10^{-4}$
Amp. Variance	$1.0580 * 10^{-8}$	$1.1725 * 10^{-8}$	$1.6348 * 10^{-3}$	$1.1175 * 10^{-8}$

Table B.32 Vertical component data properties for seismometer calibration 2 at a frequency of 1.672 (B) Hz. Phase values in radians, amplitude values in m/s (raw response in counts).

East Comp. *Freq = 1.700 Hz*	*Nominal* *Response*	*Median* *Response*	*Raw* *Response*	*Individual* *Response*
Mean Phase	$-7.6014 * 10^{-1}$	$-7.6016 * 10^{-1}$	$-7.6014 * 10^{-1}$	$-7.4860 * 10^{-1}$
Median Phase	$-2.2405 * 10^{-1}$	$-2.2405 * 10^{-1}$	$-2.2405 * 10^{-1}$	$-2.4851 * 10^{-1}$
Phase Variance	$1.1843 * 10^{0}$	$1.1844 * 10^{0}$	$1.1843 * 10^{0}$	$1.1888 * 10^{0}$
Mean Amp.	$5.0905 * 10^{-5}$	$5.3492 * 10^{-5}$	$2.0083 * 10^{-2}$	$5.3493 * 10^{-5}$
Median Amp.	$4.5082 * 10^{-5}$	$4.7373 * 10^{-5}$	$1.7784 * 10^{-2}$	$4.7977 * 10^{-5}$
Amp. Variance	$4.3521 * 10^{-10}$	$4.8058 * 10^{-10}$	$6.7730 * 10^{-5}$	$4.7478 * 10^{-10}$

Table B.33 East component data properties for seismometer calibration 2 at a frequency of 1.700 Hz. Phase values in radians, amplitude values in m/s (raw response in counts).

North Comp. *Freq = 1.700 Hz*	*Nominal* *Response*	*Median* *Response*	*Raw* *Response*	*Individual* *Response*
Mean Phase	$6.5199 * 10^{-2}$	$6.5199 * 10^{-2}$	$6.5197 * 10^{-2}$	$6.9197 * 10^{-2}$
Median Phase	$2.8702 * 10^{-2}$	$2.8702 * 10^{-2}$	$2.8697 * 10^{-2}$	$2.0428 * 10^{-2}$
Phase Variance	$1.7570 * 10^{-2}$	$1.7570 * 10^{-2}$	$1.7569 * 10^{-2}$	$1.8871 * 10^{-2}$
Mean Amp.	$3.9189 * 10^{-3}$	$4.1181 * 10^{-3}$	$1.5461 * 10^{0}$	$4.1411 * 10^{-3}$
Median Amp.	$3.9449 * 10^{-3}$	$4.1454 * 10^{-3}$	$1.5564 * 10^{0}$	$4.1400 * 10^{-3}$
Amp. Variance	$1.0347 * 10^{-8}$	$1.1425 * 10^{-8}$	$1.6106 * 10^{-3}$	$1.6455 * 10^{-8}$

Table B.34 North component data properties for seismometer calibration 2 at a frequency of 1.700 Hz. Phase values in radians, amplitude values in m/s (raw response in counts).

Vert. Comp. *Freq = 1.700 Hz*	*Nominal* *Response*	*Median* *Response*	*Raw* *Response*	*Individual* *Response*
Mean Phase	$1.9114 * 10^{-1}$	$1.9114 * 10^{-1}$	$1.9114 * 10^{-1}$	$3.1004 * 10^{-1}$
Median Phase	$1.3473 * 10^{-1}$	$1.3473 * 10^{-1}$	$1.3474 * 10^{-1}$	$2.4231 * 10^{-1}$
Phase Variance	$3.2734 * 10^{-2}$	$3.2734 * 10^{-2}$	$3.2736 * 10^{-2}$	$3.1613 * 10^{-2}$
Mean Amp.	$3.8554 * 10^{-4}$	$4.0513 * 10^{-4}$	$1.5210 * 10^{-1}$	$3.8755 * 10^{-4}$
Median Amp.	$3.9146 * 10^{-4}$	$4.1135 * 10^{-4}$	$1.5444 * 10^{-1}$	$3.9138 * 10^{-4}$
Amp. Variance	$9.5834 * 10^{-9}$	$1.0582 * 10^{-8}$	$1.4919 * 10^{-3}$	$1.0055 * 10^{-8}$

Table B.35 Vertical component data properties for seismometer calibration 2 at a frequency of 1.700 Hz. Phase values in radians, amplitude values in m/s (raw response in counts).

East Comp. *Freq = 2.249 Hz*	*Nominal* *Response*	*Median* *Response*	*Raw* *Response*	*Individual* *Response*
Mean Phase	$2.6998 * 10^{0}$	$2.7003 * 10^{0}$	$2.7001 * 10^{0}$	$2.7030 * 10^{0}$
Median Phase	$2.7714 * 10^{0}$	$2.7715 * 10^{0}$	$2.7712 * 10^{0}$	$2.7447 * 10^{0}$
Phase Variance	$5.8678 * 10^{-2}$	$5.8765 * 10^{-2}$	$5.8766 * 10^{-2}$	$5.5038 * 10^{-2}$
Mean Amp.	$5.0965 * 10^{-5}$	$5.2366 * 10^{-5}$	$2.0866 * 10^{-2}$	$5.2473 * 10^{-5}$
Median Amp.	$4.9008 * 10^{-5}$	$5.0355 * 10^{-5}$	$2.0065 * 10^{-2}$	$5.1770 * 10^{-5}$
Amp. Variance	$3.6101 * 10^{-10}$	$3.8114 * 10^{-10}$	$6.0522 * 10^{-5}$	$3.8216 * 10^{-10}$

Table B.36 East component data properties for seismometer calibration 1 at a frequency of 2.249 Hz. Phase values in radians, amplitude values in m/s (raw response in counts).

North Comp. *Freq = 2.249 Hz*	*Nominal* *Response*	*Median* *Response*	*Raw* *Response*	*Individual* *Response*
Mean Phase	$-9.1935 * 10^{-2}$	$-9.1936 * 10^{-2}$	$-9.1934 * 10^{-2}$	$-9.9537 * 10^{-2}$
Median Phase	$-6.9926 * 10^{-2}$	$-6.9932 * 10^{-2}$	$-6.9927 * 10^{-2}$	$-8.7031 * 10^{-2}$
Phase Variance	$7.2299 * 10^{-3}$	$7.2297 * 10^{-3}$	$7.2303 * 10^{-3}$	$7.1553 * 10^{-3}$
Mean Amp.	$5.4718 * 10^{-4}$	$5.6223 * 10^{-4}$	$2.2403 * 10^{-1}$	$5.6359 * 10^{-4}$
Median Amp.	$5.4145 * 10^{-4}$	$5.5634 * 10^{-4}$	$2.2169 * 10^{-1}$	$5.5655 * 10^{-4}$
Amp. Variance	$6.6585 * 10^{-10}$	$7.0297 * 10^{-10}$	$1.1162 * 10^{-4}$	$7.6256 * 10^{-10}$

Table B.37 North component data properties for seismometer calibration 1 at a frequency of 2.249 Hz. Phase values in radians, amplitude values in m/s (raw response in counts).

Vert. Comp. *Freq = 2.249 Hz*	*Nominal* *Response*	*Median* *Response*	*Raw* *Response*	*Individual* *Response*
Mean Phase	$1.0674 * 10^{0}$	$1.0677 * 10^{0}$	$1.0680 * 10^{0}$	$1.1403 * 10^{0}$
Median Phase	$-1.2323 * 10^{-2}$	$-1.2325 * 10^{-2}$	$-1.2317 * 10^{-2}$	$1.4631 * 10^{-1}$
Phase Variance	$2.3565 * 10^{0}$	$2.3574 * 10^{0}$	$2.3588 * 10^{0}$	$2.3903 * 10^{0}$
Mean Amp.	$9.4668 * 10^{-5}$	$9.7271 * 10^{-5}$	$3.8760 * 10^{-2}$	$9.4986 * 10^{-5}$
Median Amp.	$6.5436 * 10^{-5}$	$6.7235 * 10^{-5}$	$2.6793 * 10^{-2}$	$6.6017 * 10^{-5}$
Amp. Variance	$9.1377 * 10^{-9}$	$9.6471 * 10^{-9}$	$1.5317 * 10^{-3}$	$9.2708 * 10^{-9}$

Table B.38 Vertical component data properties for seismometer calibration 1 at a frequency of 2.249 Hz. Phase values in radians, amplitude values in m/s (raw response in counts).

East Comp. *Freq = 2.252 Hz*	*Nominal* *Response*	*Median* *Response*	*Raw* *Response*	*Individual* *Response*
Mean Phase	$2.2376 * 10^{0}$	$2.2383 * 10^{0}$	$2.2382 * 10^{0}$	$2.2407 * 10^{0}$
Median Phase	$2.7271 * 10^{0}$	$2.7283 * 10^{0}$	$2.7280 * 10^{0}$	$2.7294 * 10^{0}$
Phase Variance	$2.5221 * 10^{0}$	$2.5234 * 10^{0}$	$2.5234 * 10^{0}$	$2.5186 * 10^{0}$
Mean Amp.	$9.1470 * 10^{-5}$	$9.3977 * 10^{-5}$	$3.7458 * 10^{-2}$	$9.4155 * 10^{-5}$
Median Amp.	$8.8676 * 10^{-5}$	$9.1107 * 10^{-5}$	$3.6315 * 10^{-2}$	$9.3514 * 10^{-5}$
Amp. Variance	$6.6109 * 10^{-10}$	$6.9781 * 10^{-10}$	$1.1087 * 10^{-4}$	$7.0003 * 10^{-10}$

Table B.39 East component data properties for seismometer calibration 2 at a frequency of 2.252 Hz. Phase values in radians, amplitude values in m/s (raw response in counts).

North Comp. *Freq = 2.252 Hz*	*Nominal* *Response*	*Median* *Response*	*Raw* *Response*	*Individual* *Response*
Mean Phase	$-5.9356 * 10^{-2}$	$-5.9354 * 10^{-2}$	$-5.9358 * 10^{-2}$	$-7.2693 * 10^{-2}$
Median Phase	$-9.7874 * 10^{-2}$	$-9.7874 * 10^{-2}$	$-9.7881 * 10^{-2}$	$-1.0323 * 10^{-1}$
Phase Variance	$3.1619 * 10^{-2}$	$3.1620 * 10^{-2}$	$3.1617 * 10^{-2}$	$3.3705 * 10^{-2}$
Mean Amp.	$6.7488 * 10^{-4}$	$6.9338 * 10^{-4}$	$2.7637 * 10^{-1}$	$6.9507 * 10^{-4}$
Median Amp.	$6.5875 * 10^{-4}$	$6.7681 * 10^{-4}$	$2.6976 * 10^{-1}$	$6.8355 * 10^{-4}$
Amp. Variance	$2.0762 * 10^{-9}$	$2.1915 * 10^{-9}$	$3.4818 * 10^{-4}$	$2.3055 * 10^{-9}$

Table B.40 North component data properties for seismometer calibration 2 at a frequency of 2.252 Hz. Phase values in radians, amplitude values in m/s (raw response in counts).

Vert. Comp. *Freq = 2.252 Hz*	*Nominal* *Response*	*Median* *Response*	*Raw* *Response*	*Individual* *Response*
Mean Phase	$6.3153 * 10^{-1}$	$6.3134 * 10^{-1}$	$6.3124 * 10^{-1}$	$7.3051 * 10^{-1}$
Median Phase	$-6.4229 * 10^{-3}$	$-6.4195 * 10^{-3}$	$-6.4188 * 10^{-3}$	$1.1589 * 10^{-1}$
Phase Variance	$2.9003 * 10^{0}$	$2.8990 * 10^{0}$	$2.8988 * 10^{0}$	$2.9249 * 10^{0}$
Mean Amp.	$1.2227 * 10^{-4}$	$1.2562 * 10^{-4}$	$5.0072 * 10^{-2}$	$1.2268 * 10^{-4}$
Median Amp.	$7.8171 * 10^{-5}$	$8.0313 * 10^{-5}$	$3.2011 * 10^{-2}$	$8.0452 * 10^{-5}$
Amp. Variance	$1.6683 * 10^{-8}$	$1.7610 * 10^{-8}$	$2.7977 * 10^{-3}$	$1.6921 * 10^{-8}$

Table B.41 Vertical component data properties for seismometer calibration 2 at a frequency of 2.252 Hz. Phase values in radians, amplitude values in m/s (raw response in counts).

East Comp. *Freq = 2.356 Hz*	*Nominal* *Response*	*Median* *Response*	*Raw* *Response*	*Individual* *Response*
Mean Phase	$1.5890 * 10^{0}$	$1.5890 * 10^{0}$	$1.5889 * 10^{0}$	$1.5908 * 10^{0}$
Median Phase	$1.5816 * 10^{0}$	$1.5816 * 10^{0}$	$1.5816 * 10^{0}$	$1.5838 * 10^{0}$
Phase Variance	$4.2312 * 10^{-2}$	$4.2298 * 10^{-2}$	$4.2314 * 10^{-2}$	$4.0556 * 10^{-2}$
Mean Amp.	$4.6614 * 10^{-4}$	$4.7771 * 10^{-4}$	$1.9146 * 10^{-1}$	$4.7847 * 10^{-4}$
Median Amp.	$4.7109 * 10^{-4}$	$4.8278 * 10^{-4}$	$1.9349 * 10^{-1}$	$4.8109 * 10^{-4}$
Amp. Variance	$4.1587 * 10^{-10}$	$4.3674 * 10^{-10}$	$7.0199 * 10^{-5}$	$4.2102 * 10^{-10}$

Table B.42 East component data properties for seismometer calibration 2 at a frequency of 2.356 Hz. Phase values in radians, amplitude values in m/s (raw response in counts).

North Comp. *Freq = 2.356 Hz*	*Nominal* *Response*	*Median* *Response*	*Raw* *Response*	*Individual* *Response*
Mean Phase	$-5.6585 * 10^{-2}$	$-5.6580 * 10^{-2}$	$-5.6588 * 10^{-2}$	$-6.5500 * 10^{-2}$
Median Phase	$7.3410 * 10^{-2}$	$7.3415 * 10^{-2}$	$7.3408 * 10^{-2}$	$-1.8956 * 10^{-3}$
Phase Variance	$2.7988 * 10^{-1}$	$2.7989 * 10^{-1}$	$2.7987 * 10^{-1}$	$2.7214 * 10^{-1}$
Mean Amp.	$5.8473 * 10^{-4}$	$5.9923 * 10^{-4}$	$2.4017 * 10^{-1}$	$6.0029 * 10^{-4}$
Median Amp.	$5.5917 * 10^{-4}$	$5.7303 * 10^{-4}$	$2.2969 * 10^{-1}$	$5.6289 * 10^{-4}$
Amp. Variance	$7.3419 * 10^{-9}$	$7.7105 * 10^{-9}$	$1.2395 * 10^{-3}$	$7.6037 * 10^{-9}$

Table B.43 North component data properties for seismometer calibration 2 at a frequency of 2.356 Hz. Phase values in radians, amplitude values in m/s (raw response in counts).

Vert. Comp. *Freq = 2.356 Hz*	*Nominal* *Response*	*Median* *Response*	*Raw* *Response*	*Individual* *Response*
Mean Phase	$1.2339 * 10^{0}$	$1.2339 * 10^{0}$	$1.2339 * 10^{0}$	$1.2984 * 10^{0}$
Median Phase	$9.6412 * 10^{-1}$	$9.6413 * 10^{-1}$	$9.6411 * 10^{-1}$	$9.9333 * 10^{-1}$
Phase Variance	$9.7288 * 10^{-1}$	$9.7302 * 10^{-1}$	$9.7291 * 10^{-1}$	$9.4797 * 10^{-1}$
Mean Amp.	$1.4106 * 10^{-4}$	$1.4456 * 10^{-4}$	$5.7940 * 10^{-2}$	$1.4161 * 10^{-4}$
Median Amp.	$8.0675 * 10^{-5}$	$8.2677 * 10^{-5}$	$3.3132 * 10^{-2}$	$8.0369 * 10^{-5}$
Amp. Variance	$2.4436 * 10^{-8}$	$2.5663 * 10^{-8}$	$4.1238 * 10^{-3}$	$2.4874 * 10^{-8}$

Table B.44 Vertical component data properties for seismometer calibration 2 at a frequency of 2.356 Hz. Phase values in radians, amplitude values in m/s (raw response in counts).

Appendix C

More Power Radiation Estimates

The following sections show power estimates from 3 different methods utilizing Equation 6.1 to compute the power for each of the methods. The values calculated here are incorporated in the results presented in Section 5.3. When a velocity model is needed for the following calculations, the properties used for the half-space are those of the top layer of model "2LayerA".

C.1 Direct Method from Millikan Library Acceleration Data

For an EW shake, the maximum sinusoidal displacements and phases are presented in Table C.1 for the shake performed May 19, 2001. The average values for the NS shake (as there are 2 accelerometers per floor) are presented in Table C.2. As mentioned in Appendix A, the 36 accelerometers in Millikan Library are recorded by two Mt. Whitney recorders. Those accelerometers in the basement, 1^{st}, 2^{nd}, 6^{th}, and 7^{th} floors are in one box, and the others are in the second box. As a result of the timing malfunctions between the two recorders, when the records for each recorder are interpreted, the records for each recorder seem to have very different phases, even though they should have very similar phases. As can be seen from Tables C.1 and C.2, the records for the roof, 9^{th}, 8^{th}, and 5^{th} floor have very similar phases. Furthermore, the records for the 7^{th}, and 6^{th} floor also have very similar phases. For the purposes of estimating the energy radiation of Millikan Library, it will be assumed that the

records for the roof and those for the 7^{th} floor have the same phase. It can then be noticed that the top 5 floors, those with the largest displacements, have similar phases. Since these floors will account for most of the force being applied at the base, if the phase of the 7^{th} floor is used as the phase of the shear force at the base, and if the displacement for the basement is used as the displacement caused by the shear forces given in Section 3.6. By using Equation 6.1, it can estimated that the power radiated by Millikan Library is as follows for an EW shake

$$\begin{aligned} P_{EW} &= \frac{1}{2}(2\pi)(1.1133\ Hz.)(1.66E+5\ N)(8.98E-6\ m)(\sin(5.73^o)) \\ &= 0.52\ Watts \end{aligned} \tag{C.1}$$

where the phase angle is found by subtracting the phase for the basement record from that of the 7^{th} floor record. Similarly for the NS shake,

$$\begin{aligned} P_{NS} &= \frac{1}{2}(2\pi)(1.638\ Hz.)(3.84E+5\ N)(2.434E-5\ m)(\sin(8.02^o)) \\ &= 6.71\ Watts \end{aligned} \tag{C.2}$$

These estimates will be referred to as the "direct estimate".

C.2 FEM Central Node Estimate

The power radiated by the FEM calculation as calculated in Section 5.3 can also be estimated using the shear force applied at the central node and by utilizing the generated displacements. This calculation is only presented for the "2LayerA" model, as the calculation is very similar for the other finite element models. Furthermore, the power radiation for the applied moment is ignored, as it accounts for $\frac{1}{30}$ of the generated power for both the EW and NS shakes. In order to compute the phase

Floor	*Displacement (m)*	*Phase (rads)*
Basement	$8.982 * 10^{-6}$	2.406
*Floor*1	$2.499 * 10^{-5}$	2.476
*Floor*2	$8.468 * 10^{-5}$	2.504
*Floor*3	$1.516 * 10^{-4}$	-1.862
*Floor*4	$2.389 * 10^{-4}$	-1.859
*Floor*5	$3.291 * 10^{-4}$	-1.860
*Floor*6	$4.242 * 10^{-4}$	2.511
*Floor*7	$5.128 * 10^{-4}$	2.511
*Floor*8	$6.044 * 10^{-4}$	-1.856
*Floor*9	$6.918 * 10^{-4}$	-1.856
Roof	$7.811 * 10^{-4}$	-1.853

Table C.1 Displacement and phase data for an EW shake of Millikan Library in May 19, 2001. The excitation frequency is 1.1133 Hz. The phases are all relative to an arbitrary point in time for all the records. Due to an error in the Kinemetrics Mt. Whitney recorders, the timing of the two recording boxes is not the same. As a result, there appear to be two different phases present for the same shake, but they should all be very similar in values. In case one recorder box fails, the components for the different floors are staggered between the two boxes.

Floor	*Displacement (m)*	*Phase (rads)*
Basement	$2.434 * 10^{-5}$	-2.512
*Floor*1	$5.059 * 10^{-5}$	-2.436
*Floor*2	$1.433 * 10^{-4}$	-2.389
*Floor*3	$2.041 * 10^{-4}$	-1.902
*Floor*4	$2.817 * 10^{-4}$	-1.896
*Floor*5	$3.608 * 10^{-4}$	-1.889
*Floor*6	$4.481 * 10^{-4}$	-2.373
*Floor*7	$5.239 * 10^{-4}$	-2.376
*Floor*8	$6.191 * 10^{-4}$	-1.879
*Floor*9	$7.044 * 10^{-4}$	-1.876
Roof	$7.870 * 10^{-4}$	-1.876

Table C.2 Same as Table C.2 except for a NS shake and the excitation frequency is 1.638 Hz.

difference between the applied force and the node displacement, 21 points (time step = 0.1 seconds) were taken in the center of the records (approximately 2 cycles) and a sinusoid fit to both time series.

Shake	*Generated Displacement (m)*	*Phase Difference(rads)*
$EWshake$	$6.204 * 10^{-6}$	0.082
$NSshake$	$1.521 * 10^{-5}$	0.252

Table C.3 Maximum generated displacement and phase data in the direction of shaking for the EW and NS shake FEM simulations. The excitation frequency is 1.12 $Hz.$ in the EW shaking direction and 1.64 $Hz.$ in the NS shaking direction. The phase differences are between the generated synthetic and the applied force.

Using the displacement and phase values in Table C.3 and the shear forces previously used, the radiated power can be estimated as follows for an EW shake

$$\begin{aligned} P_{EW} &= \frac{1}{2}(2\pi)(1.12\ Hz.)(1.66E+5\ N)(6.20E-6\ m)(\sin(4.70^o)) \\ &= 0.30\ Watts \end{aligned} \tag{C.3}$$

where the phase angle is found by subtracting the phase for the basement record from that of the 7^{th} floor record. Similarly for the NS shake,

$$\begin{aligned} P_{NS} &= \frac{1}{2}(2\pi)(1.64\ Hz.)(3.84E+5\ N)(1.52E-5\ m)(\sin(14.44^o)) \\ &= 7.50\ Watts \end{aligned} \tag{C.4}$$

These estimates will be referred to as the "2LayerA-Direct". It should be noted that these power estimates are very close to those calculated in Section 5.3 by using the absorbing boundaries to compute the radiated power from the point force and couple using the finite element code of *Aagaard* (1999).

C.3 Impedance Function Estimates

This section focuses on using the results of the impedance function method to estimate the power radiated from Millikan Library, and as a result, the method itself is not summarized here. While there are many technical papers on the subject, for a summary of the method of impedance functions refer to *Wong and Luco* (1978), *Crouse et al.* (1990), *Wong et al.* (1988), and *Mita and Luco* (1989). For the following discussion, it is assumed that the rotation caused by a horizontal force on a foundation, causes very small rotations. As a result, the equations describing the displacement of the foundation in the direction of the force simplify to

$$F_i = \mu L k_{ii} U_i \tag{C.5}$$

where F_i is the applied force, μ is the shear modulus, k_{ii} is the impedance matrix component relating to the horizontal force in the direction of the force, U_i is the displacement of the foundation due to the force, and L is a measure of length for the foundation given by

$$L = \sqrt{\frac{BC}{\pi}} \tag{C.6}$$

where B and C are the lengths of the rectangular foundation. It should be noted that k_{ii} is complex and from it one can obtain the phase difference between the applied force and the generated motion. For Millikan Library, $B = 69\ ft$ and $B = 74\ ft$, which leads to an $L \approx 12.3m$. Utilizing the soil properties for the top layer of model "2LayerA" as those for the half-space ($V_S = 376$ m/s, $V_P = 770$ m/s, and $\rho = 1907\ Kg/m^3$), it can be computed that $\nu \approx 0.34$ and that $\mu \approx 2.7E+8$ Pascals. Furthermore, the dimensionless frequencies for Millikan can be estimated from

$$A = \frac{\omega L}{V_S} \tag{C.7}$$

to be

$$A_{EW} = 0.225 \qquad A_{NS} = 0.33 \tag{C.8}$$

for the EW shakes (Freq. $\sim$ 1.12 Hz.) and for the NS shakes (Freq. $\sim$ 1.64 Hz.), respectively.

C.3.1 Impedance Functions from *Wong and Luco* (1978)

From the tables given in *Wong and Luco* (1978), assuming 0% damping for the soil, $\nu = \frac{1}{3}$, and assuming a square foundation for Millikan Library, for $A = 0$ and $A = 0.5$

$$k_{ii} = 4.90 + 0.0i \qquad k_{ii} = 4.89 + 1.45i \tag{C.9}$$

for $A = 0$ and $A = 0.5$ respectively. Interpolating linearly between the two data points for the respective dimensionless frequencies, one gets that

$$k_{EW} = 4.90 + 0.653i \qquad k_{NS} = 4.90 + 0.957i \tag{C.10}$$

Taking the magnitude of k, we can find that

$$k_{EW} = 4.94 \qquad k_{NS} = 4.99 \tag{C.11}$$

and that the phase angle between force and displacement, one can estimate the phase angle to be

$$\delta_{EW} = 7.59^o \qquad \delta_{NS} = 11.05^o \tag{C.12}$$

Solving for the displacement of the foundation, U_i, and using the parameters given here and the shear forces for the EW and NS shakes

$$F_{EW} = 1.66E + 5\ N \qquad F_{NS} = 3.84E + 5\ N \tag{C.13}$$

the foundation displacements can be estimated by

$$U_i = \frac{F_i}{\mu L k_{ii}} \tag{C.14}$$

and therefore,

$$U_{EW} = 1.01E-5\ m \qquad U_{NS} = 2.32E-5\ m \tag{C.15}$$

Applying these numbers into the equation for power given in Equation 6.1, it is estimated that the building radiates

$$P_{EW} = 0.78\ Watts \qquad P_{NS} = 8.80\ Watts \tag{C.16}$$

These estimates will be referred to as the "ImpedanceFunctionA1".

C.3.2 Impedance Functions from *Mita and Luco* (1989)

Now use the same method, but for the results of *Mita and Luco* (1989) for an embedded foundation with the ratios similar to those of Millikan library, where the ratio of the embedment to half the building's width is approximately equal to $\frac{2}{3}$. Also, assume a very small damping, and keep the same notation given above. By utilizing the plots given in *Mita and Luco* (1989), one can estimate the following values of k_{ii} for the appropriate dimensionless frequencies

$$k_{EW} = 9.30 + 2.36i \qquad k_{NS} = 9.30 + 3.40i \tag{C.17}$$

Taking the magnitude of k, we can find that

$$k_{EW} = 9.59 \qquad k_{NS} = 9.90 \tag{C.18}$$

and that the phase angle between force and displacement, one can estimate the phase

angle to be

$$\delta_{EW} = 14.24^o \qquad \delta_{NS} = 20.08^o \tag{C.19}$$

Solving for the displacement of the foundation, U_i, and using the parameters given here and the shear forces for the EW and NS shakes

$$F_{EW} = 1.66E + 5\ N \qquad F_{NS} = 3.84E + 5\ N \tag{C.20}$$

the foundation displacements can be estimated by

$$U_i = \frac{F_i}{\mu L k_{ii}} \tag{C.21}$$

and therefore,

$$U_{EW} = 5.34E - 6\ m \qquad U_{NS} = 1.20E - 5\ m \tag{C.22}$$

Applying these numbers into the equation for power given in Equation 6.1, it is estimated that the building should radiate

$$P_{EW} = 0.77\ Watts \qquad P_{NS} = 8.16\ Watts \tag{C.23}$$

These estimates will be referred to as the "ImpedanceFunctionA2".

Appendix D

Steepest Descent Method

The following is a description of the steepest descent method used to solve the problems in Sections 3.2 and 3.3. To solve for the displacement field, we will encounter integrals of the form of Equations D.1 and D.2 (*Miller and Pursey*, 1954)

$$\psi_0 = \int_0^\infty e^{-z\sqrt{\zeta^2-m^2}}\zeta E(\zeta)J_0(r\zeta)\,d\zeta \tag{D.1}$$

$$\psi_1 = \int_0^\infty e^{-z\sqrt{\zeta^2-m^2}}\zeta^2 E(\zeta)J_1(r\zeta)\,d\zeta \tag{D.2}$$

where $E(\zeta)$ is an even function, and $J_0(r\zeta)$ and $J_1(r\zeta)$ are cylindrical Bessel functions, m is the saddle point (to be determined later), r is the radial distance along the surface, and z is the depth ($r = R\sin\theta$, $z = R\cos\theta$ in polar coordinates). It should be noted that these Bessel functions are related by Equation D.3 (*Gradshteyn and Ryzhjk*, 1995)

$$J_1(x) = -\frac{d}{dx}J_0(x) \tag{D.3}$$

Therefore, once the solution to Equation D.1 is determined, it can be differentiated to obtain the solution to Equation D.2. However, I will solve the ψ_1 integral by both taking the derivative of Equation D.1 and by independently solving Equation D.2. The latter aproach avoids taking derivatives that are difficult to simplify using Mathematica. I then use the independent derivation of the ψ_1 integral to compute additional

integrals that will be encountered in the following sections.

D.0.3 Integral Involving Cylindrical Bessel Function J_0

Starting with Equation D.1, using the fact that $E(\zeta)$ is even and making the following integral substitution for the Bessel function,

$$J_0(x) = \frac{2}{\pi}\int_0^\infty e^{-\xi^2}\left[\frac{e^{i\left(x-\frac{\pi}{4}\right)}}{\sqrt{2x+i\xi^2}} + \frac{e^{-i\left(x-\frac{\pi}{4}\right)}}{\sqrt{2x-i\xi^2}}\right] d\xi \tag{D.4}$$

as described in equation 109 of *Miller and Pursey* (1954), yields

$$\psi_0 = \frac{2e^{\frac{-i\pi}{4}}}{\pi}\int_{-\infty}^\infty e^{Rf(\zeta)}\zeta E(\zeta)\left[\int_0^\infty \frac{e^{-\xi^2}}{\sqrt{2R\zeta\sin\theta+i\xi^2}}\,d\xi\right] d\zeta \tag{D.5}$$

where polar coordinates have been introduced for r ($r = R\sin\theta$) and z ($z = R\cos\theta$), and the exponent is given by (*Miller and Pursey*, 1954)

$$f(\zeta) = i\zeta\sin\theta - \sqrt{\zeta^2-m^2}\cos\theta \tag{D.6}$$

First, work with the integral in brackets. Let

$$I_0 = \int_0^\infty \frac{e^{-\xi^2}}{\sqrt{2R\zeta\sin\theta+i\xi^2}}\,d\xi \tag{D.7}$$

Note that I_0 and I_1 are used to refer to integrals of the above form, and should not be associated with the modified Bessel functions. The substitution of

$$x(\xi) = \frac{i\xi^2}{2R\zeta\sin\theta} = \gamma\xi^2 \tag{D.8}$$

where $\gamma = \frac{i}{2R\zeta\sin\theta}$, is used to simplify equations that follow. Plugging into D.7 gives

$$I_0 = \frac{1}{\sqrt{2R\zeta\sin\theta}}\int_0^\infty \frac{e^{-\xi^2}}{\sqrt{1+x(\xi)}}\,d\xi \tag{D.9}$$

By using the binomial theorem, it can be shown (*Gradshteyn and Ryzhjk*, 1995) that

$$(1+x)^{-1/2} = \sum_{j=0}^{\infty} \frac{\Gamma(\frac{1}{2})x^j}{\Gamma(\frac{1}{2}-j)j!} \tag{D.10}$$

where $\Gamma(z)$ is the Gamma function defined by

$$\Gamma(z) = \int_0^{\infty} t^{z-1}e^{-t}dt \tag{D.11}$$

Equation D.9 can now be rewritten as

$$I_0 = \frac{1}{\sqrt{2R\zeta\sin\theta}} \int_0^{\infty} \sum_{j=0}^{\infty} \frac{\Gamma(\frac{1}{2})x(\xi)^j}{\Gamma(\frac{1}{2}-j)j!} e^{-\xi^2}\, d\xi \tag{D.12}$$

After term by term integration, Equation D.12 reduces to

$$I_0 = \frac{1}{\sqrt{2R\zeta\sin\theta}} \sum_{j=0}^{\infty} \frac{\Gamma(\frac{1}{2})\gamma^j}{\Gamma(\frac{1}{2}-j)j!} \int_0^{\infty} \xi^{2j}e^{-\xi^2}\, d\xi \tag{D.13}$$

Utilizing Equation D.11, we know that

$$\int_0^{\infty} \xi^{2j}e^{-\xi^2}d\xi = \frac{\Gamma(j+\frac{1}{2})}{2} \tag{D.14}$$

where j is a positive integer. With the appropriate substitutions for the Gamma functions, Equation D.13 reduces to the following infinite sum

$$I_0 = \frac{\sqrt{\pi}}{\sqrt{8R\zeta\sin\theta}} \sum_{j=0}^{\infty} \frac{[(2j)!]^2 e^{\frac{-i\pi j}{2}}}{2^{5j}(j!)^3(R\zeta\sin\theta)^j} \tag{D.15}$$

Substituting this result into the definition of ψ_0 (Equation D.5) and integrating term by term, gives

$$\psi_0 = \frac{1}{\sqrt{2\pi R\sin\theta}} \sum_{j=0}^{\infty} \frac{[(2j)!]^2 e^{-i\frac{\pi}{4}(2j+1)}}{2^{(5j)}\ (j!)^3(R\sin\theta)^j} \int_{-\infty}^{\infty} \zeta^{(\frac{1}{2}-j)}E(\zeta)e^{Rf(\zeta)}\, d\zeta \tag{D.16}$$

The method of steepest descent can be applied to solve the remaining integral,

$$I^{SD} = \int_{-\infty}^{\infty} \zeta^{(\frac{1}{2}-j)} E(\zeta) e^{Rf(\zeta)}\, d\zeta \tag{D.17}$$

Note that $f(\zeta)$ depends on m, which takes on the values of either h or k, depending on the type of wave being studied (P or S, respectively). In order to apply the steepest descent method, the extremum of Equation D.6 must be found (*Bender and Orszag*, 1978; *Miller and Pursey*, 1954). Equating the first derivative of $f(\zeta)$ to zero,

$$f'(\zeta) = i\sin\theta - \frac{\zeta\cos\theta}{\sqrt{\zeta^2 - m^2}} = 0 \tag{D.18}$$

gives the saddle points to be

$$\zeta_0 = \pm m\sin\theta \tag{D.19}$$

The negative saddle point, $\zeta_0 = -m\sin\theta$, has to be chosen, as substituting both possible saddle points into $f'(\zeta)$ shows that only the negative saddle point is a solution. Applying the negative saddle point and taking the necessary derivatives of ζ, the following results are obtained

$$f(\zeta_0) = -im \tag{D.20}$$

$$f'(\zeta_0) = 0 \tag{D.21}$$

$$f''(\zeta_0) = \frac{i}{m\cos^2\theta} \tag{D.22}$$

Following *Miller and Pursey* (1954), the path of integration must be deformed "into a contour C which passes through the saddle-point and is such that $f(\zeta) - f(\zeta_0)$ is real and negative or zero on C". As in *Miller and Pursey* (1954), now define

$$f(\zeta) - f(\zeta_0) \equiv -\tau^2 \tag{D.23}$$

which solving for $f(\zeta)$ results in

$$f(\zeta) = -im - \tau^2 \tag{D.24}$$

for values of ζ on C and where τ is small. From Equation D.23, τ vanishes only when $\zeta = \zeta_0$. Substituting Equation D.24 into D.17 and changing variables from ζ to τ, and deforming the contour (*Miller and Pursey*, 1954),

$$I_C^{SD} = \oint_C \zeta^{(\frac{1}{2}-j)} E(\zeta) e^{Rf(\zeta)}\, d\zeta$$

yields,

$$\begin{aligned} I_j^{SD} &= \int_{-\infty}^{\infty} e^{R(-im-\tau^2)} \left[\zeta(\tau)^{(\frac{1}{2}-j)} E(\zeta(\tau)) \frac{d\zeta}{d\tau} \right] d\tau \\ &= e^{-imR} \int_{-\infty}^{\infty} e^{-R\tau^2} \left[\zeta(\tau)^{(\frac{1}{2}-j)} E(\zeta(\tau)) \zeta'(\tau) \right] d\tau \end{aligned} \tag{D.25}$$

Letting

$$g_j(\tau) = \zeta(\tau)^{(\frac{1}{2}-j)} E(\zeta(\tau)) \zeta'(\tau) \tag{D.26}$$

gives a similar result to that of *Miller and Pursey* (1954)

$$I_j^{SD} = e^{-imR} \int_{-\infty}^{\infty} e^{-R\tau^2} g_j(\tau)\, d\tau \tag{D.27}$$

where it can be shown by substituting Equation D.6 into Equation D.24 and solving for $\zeta(\tau)$ that

$$\zeta(\tau) = -m \sin\theta + i\tau^2 \sin\theta + \tau \cos\theta \sqrt{\tau^2 + 2im} \tag{D.28}$$

where the positive root for the square root term was taken, since τ takes on all real values.

Departing from the single term asymptotic expansion of *Miller and Pursey* (1954), a complete solution is generated by Taylor expanding $g_j(\tau)$ around τ equal to zero. This yields

$$\begin{aligned} g_j(\tau) &= g_j(0) + g_j'(0)\tau + \frac{g_j''(0)}{2}\tau^2 + \cdots \\ &= \sum_{n=0}^{\infty} \frac{g_j^n(0)}{n!}\tau^n \end{aligned} \tag{D.29}$$

where $g_j^n(0)$ represents the n^{th} derivative of $g_j(0)$, $\frac{\partial^n}{\partial \tau^n} g_j(0)$. Note that $g_j^n(0)$ is a function of θ, but its dependence will be suppressed for notational convenience. Substituting Equation D.29 into the steepest descent integral and performing term by term integration yields

$$I_j^{SD} = e^{-imR} \sum_{n=0}^{\infty} \frac{g_j^n(0)}{n!} \int_{-\infty}^{\infty} e^{-R\tau^2} \tau^n \, d\tau \tag{D.30}$$

For this integral, the odd terms of n vanish due to symmetry over an even interval. Letting $n \rightarrow 2n$, and utilizing Equation D.14, leads to

$$\int_{-\infty}^{\infty} e^{-R\tau^2} \tau^{2n} \, d\tau = \frac{\Gamma(n+\frac{1}{2})}{R^{(n+\frac{1}{2})}} \tag{D.31}$$

then, the steepest descent integral reduces to

$$I_j^{SD} = e^{-imR} \sum_{n=0}^{\infty} \frac{g_j^{2n}(0)\ \Gamma(n+\frac{1}{2})}{(2n)!\ R^{(n+\frac{1}{2})}} \tag{D.32}$$

When this result is substituted into Equation D.16, the original integral for ψ_0 reduces to a double infinite sum,

$$\psi_0 = \frac{e^{-imR}}{R\sqrt{2\pi \sin\theta}} \sum_{j=0}^{\infty} \sum_{n=0}^{\infty} \frac{[(2j)!]^2 e^{-i\frac{\pi}{4}(2j+1)}\ g_j^{2n}(0)\ \Gamma(n+\frac{1}{2})}{2^{(5j)}\ (j!)^3\ (2n)!\ (R\sin\theta)^j\ R^n} \tag{D.33}$$

Recalling (*Gradshteyn and Ryzhjk*, 1995) the convolution formula for double sums

$$\sum_{j=0}^{\infty}\sum_{n=0}^{\infty} a_j\, b_n \;=\; \sum_{j=0}^{\infty}\sum_{n=0}^{j} a_n\, b_{j-n} \tag{D.34}$$

and applying it to Equation D.33, to group all the powers of R, yields

$$\psi_0 \;=\; \frac{e^{-imR}}{R\sqrt{2\pi\sin\theta}}\sum_{j=0}^{\infty}\sum_{n=0}^{j}\frac{[(2n)!]^2 e^{-i\frac{\pi}{4}(2n+1)}\; g_n^{2j-2n}(0)\;\Gamma(j-n+\frac{1}{2})}{2^{(5n)}\;(n!)^3\;(2j-2n)!\;R^j\;(\sin\theta)^n} \tag{D.35}$$

Now let

$$a_{jn} \;=\; \frac{[(2n)!]^2 e^{-i\frac{\pi}{4}(2n+1)}\;\Gamma(j-n+\frac{1}{2})}{\sqrt{2\pi}\;2^{(5n)}\;(n!)^3\;(2j-2n)!} \tag{D.36}$$

and

$$G_{jn}(\theta) \;=\; \frac{g_n^{2j-2n}(0)}{(\sin\theta)^{n+\frac{1}{2}}} \tag{D.37}$$

This simplifies the form of Equation D.35 to

$$\psi_0 \;=\; \sum_{j=0}^{\infty}\sum_{n=0}^{j} a_{jn}\,\frac{e^{-imR}}{R^{j+1}}\,G_{jn}(\theta) \tag{D.38}$$

and provides a complete answer to the integral posed in Equation D.1, which will be used to compute the radiation patterns in the following sections.

D.0.4 Integral Involving Cylindrical Bessel Function J_1

D.0.4.1 Solution Utilizing the Derivative of the Bessel Function

As previously mentioned, the solution to Equation D.2 can be determined by taking the derivative of Equation D.38 by recalling that the cylindrical Bessel functions J_0 and J_1 are related by Equation D.3. Noting that Equations D.1 and D.2 only have a radial dependence on the Bessel function, the solution to ψ_1 can be derived by taking

the derivative of the solution to ψ_0 with respect to r. Therefore,

$$\psi_1 = -\frac{d\,\psi_0(r,\theta)}{dr} = -\Big[\frac{d\,\psi_0(R,\theta)}{dR}\frac{dR}{dr} + \frac{d\psi_0(R,\theta)}{d\theta}\frac{d\theta}{dr}\Big] \tag{D.39}$$

The second equation is due to the application of the chain rule using spherical coordinates, with the knowledge that

$$R^2 = r^2 + z^2 \qquad \text{and} \qquad \tan\theta = \frac{r}{z}$$

the derivatives in Equation D.39 are given by

$$\frac{dR}{dr} = \sin\theta \qquad \text{and} \qquad \frac{d\theta}{dr} = \frac{\cos\theta}{R}$$

Substituting the respective derivatives into Equation D.39 gives

$$\psi_1(R,\theta) = -\left[\sin\theta\,\frac{d\psi_0}{dR} + \frac{\cos\theta}{R}\,\frac{d\psi_0}{d\theta}\right] \tag{D.40}$$

Now, taking the appropriate derivatives of ψ_0 as it appears in Equation D.38, and differentiating term by term, it can be shown that

$$\frac{d\psi_0(R,\theta)}{dR} = \sum_{j=0}^{\infty}\sum_{n=0}^{j} a_{jn}\,\frac{g(0)_n^{(2j-2n)}}{\sin\theta^{(n+\frac{1}{2})}}\,\frac{e^{-imR}}{R^{j+2}}[-imR-(j+1)] \tag{D.41}$$

$$\frac{d\psi_0(R,\theta)}{d\theta} = \sum_{j=0}^{\infty}\sum_{n=0}^{j} a_{jn}\,\frac{e^{-imR}}{R^{j+1}}\left[\frac{\frac{dg(0)_n^{(2j-2n)}}{d\theta}}{\sin\theta^{(n+\frac{1}{2})}} - \frac{(n+\frac{1}{2})g(0)_n^{(2j-2n)}\,\cos\theta}{\sin\theta^{(n+\frac{3}{2})}}\right] \tag{D.42}$$

Substituting these derivatives into Equation D.40, yields the solution to the ψ_1 integral

$$\begin{aligned}\psi_1(R,\theta) = \sum_{j=0}^{\infty}\sum_{n=0}^{j}\frac{a_{jn}\,e^{-imR}}{R^{j+2}}\Bigg[&\frac{g(0)_n^{(2j-2n)}}{\sin\theta^{(n-\frac{1}{2})}}\,(imR+j+1)\;+\\ &-\frac{\cos\theta}{\sin\theta^{n+\frac{1}{2}}}\frac{dg(0)_n^{(2j-2n)}}{d\theta} + \frac{(n+\frac{1}{2})g(0)_n^{(2j-2n)}\,\cos^2\theta}{\sin\theta^{(n+\frac{3}{2})}}\Bigg]\end{aligned} \tag{D.43}$$

However, the displacement fields to be derived will be solved using Mathematica, which has problems reducing/simplifying many terms. The derivatives in Equation D.43 will present a problem when trying to simplify the solution, and as a result, the ψ_1 integral will also be solved similarly to the ψ_0 integral.

D.0.4.2 Independent Derivation of Solution

Recalling the equation for the Integral Bessel Function given in Equation D.4, and as in Equation D.3, multiplying by -1 and differentiating with respect to x yields the Integral Bessel Function for $J_1(x)$

$$\begin{aligned} J_1(x) = -\frac{d}{dx}J_0(x) &= -\frac{2}{\pi}\int_0^\infty e^{-\zeta^2}\left[\frac{ie^{i\left(x-\frac{\pi}{4}\right)}}{\sqrt{2x+i\zeta^2}} - \frac{ie^{-i\left(x-\frac{\pi}{4}\right)}}{\sqrt{2x-i\zeta^2}}\right]d\zeta + \\ &\quad \frac{2}{\pi}\int_0^\infty e^{-\zeta^2}\left[\frac{e^{i\left(x-\frac{\pi}{4}\right)}}{(2x+i\zeta^2)^{3/2}} + \frac{e^{-i\left(x-\frac{\pi}{4}\right)}}{(2x-i\zeta^2)^{3/2}}\right]d\zeta \end{aligned} \tag{D.44}$$

Substituting Equation D.44 into Equation D.2, as in *Miller and Pursey* (1954) simplifies ψ_1 to

$$\begin{aligned} \psi_1 &= -\frac{2ie^{\frac{-i\pi}{4}}}{\pi}\int_{-\infty}^\infty e^{Rf(\zeta)}\zeta^2 E(\zeta)\left[\int_0^\infty \frac{e^{-\xi^2}}{\sqrt{2R\zeta\sin\theta+i\xi^2}}\,d\xi\right]d\zeta \; + \\ &\quad \frac{2e^{\frac{-i\pi}{4}}}{\pi}\int_{-\infty}^\infty e^{Rf(\zeta)}\zeta^2 E(\zeta)\left[\int_0^\infty \frac{e^{-\xi^2}}{(2R\zeta\sin\theta+i\xi^2)^{\frac{3}{2}}}\,d\xi\right]d\zeta \end{aligned} \tag{D.45}$$

The top integral has already been solved for when solving for ψ_0, and therefore only the bottom integral has to be solved. To solve this integral, the method shown in Section D.0.3 will be followed, with only minor differences. Rewriting Equation D.7 by using the change of variable, $y = R\zeta\sin\theta$, gives

$$I_0 = \int_0^\infty \frac{e^{-\xi^2}}{\sqrt{2y+i\xi^2}}\,d\xi \tag{D.46}$$

differentiating with respect to y, yields

$$I_0' = \frac{\partial I_0(y)}{\partial y} = \int_0^\infty -\frac{e^{-\xi^2}}{(2y + i\xi^2)^{3/2}}\, d\xi \tag{D.47}$$

substituting Equations D.46 and D.47 into Equation D.45 simplifies to

$$\psi_1 = -\frac{2e^{\frac{-i\pi}{4}}}{\pi} \int_{-\infty}^{\infty} e^{Rf(\zeta)} \zeta^2 E(\zeta)\, [iI_0(r\zeta) + I_0'(r\zeta)]\, d\zeta \tag{D.48}$$

From Equation D.15 it is known that I_0 reduces to

$$I_0 = \sqrt{\frac{\pi}{8}} \sum_{j=0}^{\infty} \frac{[(2j)!]^2\, e^{\frac{-i\pi j}{2}}}{2^{5j}(j!)^3\, y^{(j+\frac{1}{2})}} \tag{D.49}$$

where the substitution $y = R\zeta \sin\theta$ was used. Taking the derivative with respect to y of Equation D.49, gives

$$I_0' = -\sqrt{\frac{\pi}{8}} \sum_{j=0}^{\infty} \frac{[(2j)!]^2 (j + \frac{1}{2})\, e^{\frac{-i\pi j}{2}}}{2^{5j}(j!)^3\, y^{(j+\frac{3}{2})}} \tag{D.50}$$

and therefore, Equation D.48 reduces to

$$\psi_1 = -\frac{e^{\frac{-i\pi}{4}}}{\sqrt{2\pi}} \sum_{j=0}^{\infty} \frac{[(2j)!]^2 e^{\frac{-i\pi j}{2}}}{2^{5j}(j!)^3} \int_{-\infty}^{\infty} e^{Rf(\zeta)} \zeta^2 E(\zeta) \left[\frac{-i}{(r\zeta)^{j+\frac{1}{2}}} + \frac{j + \frac{1}{2}}{(r\zeta)^{j+\frac{3}{2}}}\right] d\zeta \tag{D.51}$$

where again, the exponent is given by

$$f(\zeta) = i\zeta \sin\theta - \sqrt{\zeta^2 - m^2}\cos\theta \tag{D.52}$$

substituting Equation D.52 into Equation D.51, yields

$$\begin{aligned} \psi_1 = \frac{-1}{\sqrt{2\pi}} \sum_{j=0}^{\infty} \frac{[(2j)!]^2 e^{\frac{-i\pi}{4}(2j+1)}}{2^{5j}(j!)^3} \Bigg[& \int_{-\infty}^{\infty} \left(\frac{-i}{(R\sin\theta)^{j+\frac{1}{2}}}\right) \zeta^{(\frac{3}{2}-j)}\, E(\zeta)\, e^{Rf(\zeta)} + \\ & \int_{-\infty}^{\infty} \left(\frac{(j + \frac{1}{2})}{(R\sin\theta)^{j+\frac{3}{2}}}\right) \zeta^{(\frac{1}{2}-j)}\, E(\zeta)\, e^{Rf(\zeta)} \Bigg] d\zeta \end{aligned} \tag{D.53}$$

which has the same form as ψ_0 in Equation D.16, and the previous definition of I^{SD} in Equation D.17 is still valid, and can be used in the second integral. For the first integral, define

$$I_j^{SD2} = \int_{-\infty}^{\infty} \zeta^{(\frac{3}{2}-j)} E(\zeta) e^{Rf(\zeta)}\, d\zeta \tag{D.54}$$

and recall from Equation D.25 that

$$I_j^{SD} = \int_{-\infty}^{\infty} \zeta^{(\frac{1}{2}-j)} E(\zeta) e^{Rf(\zeta)}\, d\zeta$$

It can be seen that $I_j^{SD} = I_{j+1}^{SD2}$, and therefore Equation D.53 reduces to

$$\psi_1 = \frac{-1}{\sqrt{2\pi}} \sum_{j=0}^{\infty} \frac{[(2j)!]^2 e^{\frac{-i\pi}{4}(2j+1)}}{2^{5j}(j!)^3} \left[\frac{-i\, I_j^{SD2}}{(R\sin\theta)^{j+\frac{1}{2}}} + \frac{(j+\frac{1}{2})\, I_{j+1}^{SD2}}{(R\sin\theta)^{j+\frac{3}{2}}} \right] \tag{D.55}$$

Again, the method of steepest descent needs to be applied to solve the I^{SD2} integral, and by repeating the process described in Equations D.17 through D.32, it can be derived that

$$I_j^{SD2} = e^{-imR} \sum_{n=0}^{\infty} \frac{g_j^{2n}(0)\, \Gamma(n+\frac{1}{2})}{(2n)!\, R^{(n+\frac{1}{2})}} \tag{D.56}$$

where $g_j(\tau)$ is given by

$$g_j(\tau) = \zeta(\tau)^{(\frac{3}{2}-j)} E(\zeta(\tau)) \zeta'(\tau) \tag{D.57}$$

Therefore, with these definitions, Equation D.55 can be rewritten as

$$\begin{aligned} \psi_1 = & -\frac{i\, e^{-imR}}{\sqrt{2\pi}} \sum_{j=0}^{\infty} \sum_{n=0}^{\infty} \frac{\Gamma(n+\frac{1}{2})\, [(2j)!]^2 e^{-i\frac{\pi}{4}(2j+1)}\, g_j^{2n}(0)}{2^{(5j)}\, (j!)^3\, (2n)!\, R^{j+n+1}\, (\sin\theta)^{(j+\frac{1}{2})}} + \\ & \frac{e^{-imR}}{\sqrt{2\pi}} \sum_{j=0}^{\infty} \sum_{n=0}^{\infty} \frac{\Gamma(n+\frac{1}{2})\, [(2j)!]^2 e^{-i\frac{\pi}{4}(2j+1)}\, (j+\frac{1}{2})\, g_{j+1}^{2n}(0)}{2^{(5j)}\, (j!)^3\, (2n)!\, R^{j+n+2}\, (\sin\theta)^{(j+\frac{3}{2})}} \end{aligned} \tag{D.58}$$

Applying the convolution formula for double sums (Equation D.34), to Equation D.58, yields

$$\begin{aligned}\psi_1 &= -\frac{i\,e^{-imR}}{\sqrt{2\pi}}\sum_{j=0}^{\infty}\sum_{n=0}^{j}\frac{\Gamma(j-n+\frac{1}{2})\,[(2n)!]^2 e^{-i\frac{\pi}{4}(2n+1)}\,g_n^{2j-2n}(0)}{2^{(5n)}\,(n!)^3\,(2j-2n)!\,R^{j+1}\,(\sin\theta)^{n+\frac{1}{2}}}+ \\ &\quad \frac{e^{-imR}}{\sqrt{2\pi}}\sum_{j=0}^{\infty}\sum_{n=0}^{j}\frac{\Gamma(j-n+\frac{1}{2})\,[(2n)!]^2 e^{-i\frac{\pi}{4}(2n+1)}\,(n+\frac{1}{2})\,g_{n+1}^{2j-2n}(0)}{2^{(5n)}\,(n!)^3\,(2j-2n)!\,R^{j+2}\,(\sin\theta)^{n+\frac{3}{2}}}\end{aligned} \tag{D.59}$$

Now define

$$L_{jn}(\theta) = \frac{g_{n+1}^{2j-2n}(0)}{(\sin\theta)^{n+\frac{3}{2}}} \tag{D.60}$$

$$H_{jn}(\theta) = \frac{g_n^{2j-2n}(0)}{(\sin\theta)^{n+\frac{1}{2}}} \tag{D.61}$$

where

$$g_n^{2j-2n}(0) = \left[\frac{\partial^{2j-2n}}{\partial\tau^{2j-2n}}g_n(\tau,\theta)\right]_{\tau=0} \tag{D.62}$$

Applying these substitutions simplifies the form of Equation D.59 to

$$\psi_1 = \sum_{j=0}^{\infty}\sum_{n=0}^{j} -i\,a_{jn}\,H_{jn}\,\frac{e^{-imR}}{R^{j+1}} + \sum_{j=0}^{\infty}\sum_{n=0}^{j}(n+\frac{1}{2})\,a_{jn}\,L_{jn}\,\frac{e^{-imR}}{R^{j+2}} \tag{D.63}$$

where

$$a_{jn} = \frac{[(2n)!]^2 e^{-i\frac{\pi}{4}(2n+1)}\,\Gamma(j-n+\frac{1}{2})}{\sqrt{2\pi}\,2^{(5n)}\,(n!)^3\,(2j-2n)!} \tag{D.64}$$

and grouping all terms of equal powers of R, yields

$$\psi_1 = \sum_{j=0}^{\infty}\frac{e^{-imR}}{R^{j+1}}\left[-i\sum_{n=0}^{j}a_{jn}\,H_{jn} + \sum_{n=0}^{j-1}(n+\frac{1}{2})\,a_{j-1,n}\,L_{j-1\,n}\right] \tag{D.65}$$

where $a_{-1,0} \equiv 0$.

For complete examples of the application of these integrals in Mathematica (version 4), refer to Appendix E.

Appendix E

Mathematica Codes

Included in this appendix are the details of the displacement field computations using Mathematica, including the Mathematica output. The code provided here works in Mathematica 4, and has not been tested or applied in any other version of Mathematica. All of the variables presented here have been normalized by h (the compressional wavenumber), so as to non-dimensionalize all of the integrals.

The notation in this section might not match that presented in Appendix D, as Mathematica does not allow the use of indices. However, the notation is very close to that used in Appendix D, while the step by step process shown here is exactly that given in Appendix D. The following pages are printouts of the Mathematica code used to generate the solution, and each page was printed individually. As a result, you will notice that the file "header" has the Mathematica file name on the top left corner and the page number (always 1) on the top right corner. Furthermore, the darker text is the code that I typed in, while the lighter colored text following it is the Mathematica output. Note that only the output for the lines without semicolons at the end are provided.

The process used to solve for each of the body-wave displacement fields derived in Sections 3.2 and 3.3 is very similar. Both of the displacement fields are comprised of multiple integrals that are given in the individual solutions, but which can be classified as one of two integrals, those solved in Appendix D involving the Bessel functions J_0 or J_1. The mathematica code that follows, solves the individual integrals provided for each displacement field. The order of the solutions for the integrals is the exact same

order that is presented in Sections 3.2 and 3.3 for the integrals. Since each solution is classified as a J_0 or J_1 integral, the code that follows has a header for each integral being solved, and the headers $J0\alpha$, $J0\beta$, $J1\alpha$, or $J1\beta$ are used. These headers should help the reader identify which integral is being solved. For example, a $J0\alpha$ header solves a J_0 integral that contains an $e^{-\alpha z}$ exponential in the integral (compressional waves). Similarly, a $J0\beta$ header solves a J_0 integral that contains an $e^{-\beta z}$ (shear waves), a $J1\alpha$ header solves a J_1 integral that contains an $e^{-\alpha z}$ (compressional waves), and a $J1\beta$ header solves a J_1 integral that contains an $e^{-\beta z}$ (shear waves).

Moreover, at the beginning of each displacement field, an equation is given that relates to the integral solution given in Sections 3.2 and 3.3, where each integral is replaced by 4 or 5 letter code. In the following , a ? denotes a component. Therefore, $U?$ can represent either U_r, U_ϕ, or U_z. The number following the ? tells what type of Bessel function integral was solved; a 1 informs the reader that a J_1 integral is solved, while a 0 tells us that a J_0 integral is involved. Also, the Greek letter following this number (either an α or a β) tells us if the integral involved contains an exponential of the type $e^{-\alpha z}$ or $e^{-\beta z}$. If there is more than one integral that fits this 4 letter description, then a fifth number is used, where a 1 represents the first integral that fits the 4 letter code description, and a 2 the second. Furthermore, if the integral solution is multiplied by a $\frac{1}{r}$ term (mentioned in the equation at the beginning of each displacement field), then a variable named "*segundo*" is set equal to zero to ignore all the second-order terms, as the $\frac{1}{r}$ makes them third order in r and the process presented here focuses only on the first and second-order terms in r.

Now that a general description has been provided for all the terms, since the process for computing the displacement is the same, a detailed description of a J_0 and a J_1 solution follows. The reader will notice that the code for all J_0 terms is the same, with some minor differences. These will occur in the bold text that is given in a gray color. The black bold text does not change for each type of integral. In the following mathematica codes, ϵ corresponds to a normalized building radius, r_0. However, the term in front of the integral is not normalized as it is presented here (as the terms cancel out), and therefore the ϵs and the $r_0 s$ are allowed to coexist in the

same equation to maintain the same form of the equation presented in Sections 3.2 and 3.3.

E.1 Detailed Explanation of the Codes

E.1.1 Detailed Explanation of J_0 Codes

(*————————————————-*)

(* J0α *)

(*————————————————-*)

Clear[R, θ, Λ, z, z1, F, EE, a00, a10, a11, m, segundo, g, τ, Ig, ddg, g2, G00, G10, G11, IG00, IG10, IG11, A00, temp1, A00ϵ 3, A10, A11, Ur0α]

$-->$ clears a bunch of variables to be used in this integral solution.

z=-m*Sin[θ] + I*τ^2* Sin[θ] + τ * Cos[θ] * Sqrt [τ^2 + 2*I*m];

$-->$ directly from Equation D.28.

z1=Simplify[D[z,τ]];

$-->$ take a derivative of z with respect to τ.

F=(Λ^2 - 2*z^2)-4*z^2*Sqrt[(z^2-1)]*Sqrt[(z^2-Λ^2)];

$-->$ normalized Rayleigh equation, Equation 3.18.

EE=(2*z*Sin[ϵ*z]*Sqrt[z^2-Λ^2]/F;

$-->$ E($\zeta(\tau)$) from Equation D.26. Varies depending on integral being solved, therefore appears in gray in Mathematica text.

a00=Exp[-I*Pi/4]* Gamma[1/2] / Sqrt[2*Pi];

a10=Exp[-I*Pi/4]* Gamma[3/2] / (2*Sqrt[2*Pi]);

a11=4*Exp[-3*I*Pi/4]* Gamma[1/2] / (2^5*Sqrt[2*Pi]);

$-->$ all three terms are a_{ij} from Equation D.36.

m=1;

−− > m=1 for an α integral, and m=Λ for a β integral.

segundo=1;

−− > segundo=0 for terms with a $\frac{1}{r}$ term in the solution of $U_?$, and 1 otherwise.

g=$z^{(3/2-1)}$*EE*z1; (* for j=1*)

Ig=$z^{(3/2-2)}$*EE*z1; (* for j=2*)

−− > from Equation D.26, plugging in j=1 or j=2.

g2=Normal[Series[g,{ϵ,0,1}]];

−− > first term of Taylor series for g, needed in next step.

dgg=D[D[g2,τ],τ];

−− > second derivative of g2 with respect to τ. Needed for Equation D.37 when j-n$\neq$0.

τ=0;

−− > from Equation D.24, as τ is small. However, must apply after all derivatives are taken.

G00=(1/Sin[θ]$^{(1/2)}$) * g;

G10=(1/Sin[θ]$^{(1/2)}$) * dgg;

G11=(1/Sin[θ]$^{(3/2)}$) * Ig;

−− > from Equation D.37, where the 2 numbers following the G represent the 2 indices (i,j) in Equation D.37.

IG00=Exp[-I*m*R]*a00*G00/R;

IG10=Exp[-I*m*R]*a10*G10/(R^2);

IG11=Exp[-I*m*R]*a11*G11/(R^2);

−− > from Equation D.38, where each term indicates the contribution to the total sum of ψ_0 from G00, G10, and G11.

A00 = Simplify[Normal[Series[IG00,{ϵ,0,1}]], 0$\leq \theta$ && $\theta \leq \pi/2$ && 0 $\leq \Lambda$]

−− > Taylor expands in r_0 (ϵ) and gives the $\frac{r_0}{R}$ term for Ur0α, which is then

divided by r_0. Output is printed at the bottom of the code, as there is no semi-colon used.

temp1 = Coefficient[Normal[Series[IG00,{ϵ,0,3}]], ϵ^3];

A00ϵ3 = segundo*Simplify[temp1*ϵ^3, 0$\leq$ θ && $\theta \leq \pi/2$ && 0 $\leq \Lambda$];

$-->$ expands in r_0 and gives the $\frac{r_0^3}{R}$ term for Ur0α, which is then divided by r_0.

A10 = segundo * IG10;

A11 = segundo * Simplify[Normal[Series[IG11,{ϵ,0,1}]], 0$\leq$ θ && $\theta \leq \pi/2$ && 0 $\leq \Lambda$];

$-->$ The two $\frac{1}{R^2}$ generated from the summation in Equation D.38.

Ur0α = A00 + segundo * (A00ϵ3 + A10 + A11);

$-->$ sums all 3 terms. No output provided as it is messy and long.

E.1.2 Detailed Explanation of J_1 Codes

(*————————————————-*)

(* J1α *)

(*————————————————-*)

Clear[R, θ, Λ, z, z1, F, EE, a00, a10, a11, m, segundo, g, τ, Ig, ddg, g2, G00, G10, G11, IG00, IG10, IG11, A00, temp1, A00ϵ 3, A10, A11, Ur0α]

$-->$ clears a bunch of variables to be used in this integral solution.

z=-m*Sin[θ] + I*τ^2* Sin[θ] + τ * Cos[θ] * Sqrt [τ^2 + 2*I*m];

$-->$ directly from Equation D.28.

z1=Simplify[D[z,τ]];

$-->$ take a derivative of z with respect to τ.

F=(Λ^2 - 2*z^2)-4*z^2*Sqrt[(z^2-1)]*Sqrt[(z^2-Λ^2)];

−− > normalized Rayleigh equation, Equation 3.18.

EE=(2*z*Sin[ϵ*z]*Sqrt[z^2-Λ^2]/F;

−− > E($\zeta(\tau)$) from Equation D.54. Varies depending on integral being solved, therefore appears in gray in Mathematica text.

a00=Exp[-I*Pi/4]* Gamma[1/2] / Sqrt[2*Pi];

a10=Exp[-I*Pi/4]* Gamma[3/2] / (2*Sqrt[2*Pi]);

a11=4*Exp[-3*I*Pi/4]* Gamma[1/2] / (2^5*Sqrt[2*Pi]);

−− > all three terms are a_{ij} from Equation D.64.

m=1;

−− > m=1 for an α integral, and m=Λ for a β integral.

segundo=1;

−− > segundo=0 for terms with a $\frac{1}{r}$ term in the solution of U$_?$, and 1 otherwise.

gH=$z^{(3/2-1)}$*EE*z1; (* for j=1*) IgH=$z^{(3/2-2)}$*EE*z1; (* for j=2*)

−− > from Equation D.61, plugging in j=1 or j=2.

gH2=Normal[Series[gH,{ϵ,0,1}]];

−− > first term of Taylor series for gH, needed in next step.

dggH=D[D[gH2,τ],τ];

−− > second derivative of gH2 with respect to τ. Needed for Equation D.61 when j-n$\neq$0.

gL=$z^{(3/2-1)}$*EE*z1; (* for j=1*)

−− > from Equation D.60, plugging in j=1.

τ=0;

−− > from Equation D.24, as τ is small. However, must apply after all derivatives are taken.

H00=(1/Sin[θ]$^{(1/2)}$) * gH;

H10=(1/Sin[θ]$^{(1/2)}$) * dggH;

H11=(1/Sin[θ]$^{(3/2)}$) * IgH;

$--> $ from Equation D.61, where the 2 numbers following the H represent the 2 indices (i,j) in Equation D.61.

L00=(1/Sin[θ]$^{(3/2)}$) * gL;

$--> $ from Equation D.60, where the 2 numbers following the L represent the 2 indices (i,j) in Equation D.60.

IH00=Exp[-I*m*R]*a00*H00/R;

IH10=Exp[-I*m*R]*a10*H10/(R^2);

IH11=Exp[-I*m*R]*a11*H11/(R^2);

$--> $ from Equation D.65, where each term indicates the contribution to the total sum of ψ_1 from G00, G10, and G11.

IL00=Exp[-I*m*R]*a00*L00/R;

$--> $ from Equation D.65, where the term indicates the contribution to the total sum of ψ_1 from L00.

A00 = Simplify[Normal[Series[IH00,{ϵ,0,1}]], 0$\leq \theta$ && $\theta \leq \pi/2$ && 0 $\leq \Lambda$]

$--> $ Taylor expands in r_0 (ϵ) and gives the $\frac{r_0}{R}$ term for Ur1α, which is then divided by r_0. Output is printed at the bottom of the code, as there is no semi-colon used.

temp1 = Coefficient[Normal[Series[IH00,{ϵ,0,3}]], ϵ^3];

A00ϵ3 = segundo*Simplify[temp1*ϵ^3, 0$\leq \theta$ && $\theta \leq \pi/2$ && 0 $\leq \Lambda$];

$--> $ expands in r_0 and gives the $\frac{r_0^3}{R}$ term for Ur0α, which is then divided by r_0.

A10 = segundo * IH10;

A11 = segundo * Simplify[Normal[Series[IH11,{ϵ,0,1}]], 0$\leq \theta$ && $\theta \leq \pi/2$ && 0

$\leq \Lambda$];

B00 = segundo * Simplify[Normal[Series[IL00,{ϵ,0,1}]], 0$\leq \theta$ && $\theta \leq \pi/2$ && 0 $\leq \Lambda$];

$-->$ The two $\frac{1}{R^2}$ generated from the summation in Equation D.38.

Ur1α = A00 + segundo * (A00ϵ3 + A10 + A11 B00)

$-->$ sums all 3 terms. The output provided for this line is the same as before, as segundo = 0.

E.2 Derivation of Displacement Field for Shearing Motion

```
(*   ON BODY WAVES FROM THE SHEARING
 MOTION OF A RIGID DISK ON A HALF SPACE
 Calculation of Dispalcement in the little
 r direction, in cylindrical coordinates
  Ur= P*Sin[ϕ]/(2*π*ro*μ) (-Ur0α +
   Ur1α/r + Ur1β1/r + Ur0β - Ur1β2/r)
*)

(*_____________________________________
  ____________________________________  *)
(*                                      J0α
                                        *)
(*_____________________________________
  ____________________________________  *)
```

```
Clear[R, θ, Λ, z, z1, F, EE, a00, a10, a11, m, segundo, g, τ, Ig, ddg,
   g2, G00, G10, G11, IG00, IG10, IG11, A00, temp1, A00ϵ3, A10, A11, Ur0α];

z = -m*Sin[θ] + I*τ^2*Sin[θ] + τ*Cos[θ]*Sqrt[τ^2 + 2*I*m];
z1 = Simplify[D[z, τ]];
F = (Λ^2 - 2*z^2)^2 - 4*z^2*Sqrt[(z^2 - 1)]*Sqrt[(z^2 - Λ^2)];
EE = 2*z*Sin[ϵ*z]*Sqrt[z^2 - Λ^2] / F;

a00 = Exp[-I*Pi/4] Gamma[1/2] / Sqrt[2*Pi];
a10 = Exp[-I*Pi/4]*Gamma[3/2] / (2*Sqrt[2*Pi] );
a11 = 4*Exp[-3*I*Pi/4]*Gamma[1/2] / (2^5*Sqrt[2*Pi] );

m = 1;
segundo = 1;
g = z^(3/2 - 1)*EE*z1;   (* for j=1 *)
Ig = z^(3/2 - 2)*EE*z1;   (* for j=2 *)
g2 = Normal[Series[g, {ϵ, 0, 1}]];
ddg = D[D[g2, τ], τ];

τ = 0;

G00 = (1/Sin[θ]^(1/2))*g;
G10 = (1/Sin[θ]^(1/2))*ddg;
G11 = (1/Sin[θ]^(3/2))*Ig;

IG00 = Exp[-I*m*R]*a00*G00/R;
IG10 = Exp[-I*m*R]*a10*G10/(R^2);
IG11 = Exp[-I*m*R]*a11*G11/(R^2);

A00 = Simplify[Normal[Series[IG00, {ϵ, 0, 1}]], 0 ≤ θ && θ ≤ π/2 && 0 ≤ Λ]

temp1 = Coefficient[Normal[Series[IG00, {ϵ, 0, 3}]], ϵ^3];
A00ϵ3 = segundo*Simplify[temp1*ϵ^3, 0 ≤ θ && θ ≤ π/2 && 0 ≤ Λ];

A10 = segundo*IG10;
A11 = segundo*Simplify[Normal[Series[IG11, {ϵ, 0, 1}]], 0 ≤ θ && θ ≤ π/2 && 0 ≤ Λ];

Ur0α = A00 + segundo*(A00ϵ3 + A10 + A11);
```

$$\frac{(1-i)\,(-1)^{3/4}\,e^{-iR}\,\epsilon\,\cos[\theta]\,\sqrt{1-2\Lambda^2-\cos[2\theta]}\,\sin[\theta]^2}{R\left(\Lambda^4+4\sin[\theta]^4-4\sin[\theta]^2\left(\Lambda^2+i\cos[\theta]\sqrt{-\Lambda^2+\sin[\theta]^2}\right)\right)}$$

```
(*_____________________________________________________________
  ____________________________________________________________  *)
(*                                                              J0α
                                                                  *)
(*_____________________________________________________________
  ____________________________________________________________  *)

Clear[R, θ, Λ, z, z1, F, EE, a00, a10, a11, m, segundo, g, τ, Ig, ddg,
   g2, G00, G10, G11, IG00, IG10, IG11, A00, temp1, A00ϵ3, A10, A11, Ur0α];

z = -m * Sin[θ] + I * τ^2 * Sin[θ] + τ * Cos[θ] * Sqrt[τ^2 + 2 * I * m];
z1 = Simplify[D[z, τ]];
F = (Λ^2 - 2 * z^2)^2 - 4 * z^2 * Sqrt[(z^2 - 1)] * Sqrt[(z^2 - Λ^2)];
EE = 2 * z * Sin[ϵ * z] * Sqrt[z^2 - Λ^2] / F;

a00 = Exp[-I * Pi / 4] Gamma[1 / 2] / Sqrt[2 * Pi];
a10 = Exp[-I * Pi / 4] * Gamma[3 / 2] / (2 * Sqrt[2 * Pi] );
a11 = 4 * Exp[-3 * I * Pi / 4] * Gamma[1 / 2] / (2^5 * Sqrt[2 * Pi] );

m = 1;
segundo = 1;
g = z^(3 / 2 - 1) * EE * z1;   (* for j=1 *)
Ig = z^(3 / 2 - 2) * EE * z1;   (* for j=2 *)
g2 = Normal[Series[g, {ϵ, 0, 1}]];
ddg = D[D[g2, τ], τ];

τ = 0;

G00 = (1 / Sin[θ]^(1 / 2)) * g;
G10 = (1 / Sin[θ]^(1 / 2)) * ddg;
G11 = (1 / Sin[θ]^(3 / 2)) * Ig;

IG00 = Exp[-I * m * R] * a00 * G00 / R;
IG10 = Exp[-I * m * R] * a10 * G10 / ( R^2);
IG11 = Exp[-I * m * R] * a11 * G11 / ( R^2);

A00 = Simplify[Normal[Series[IG00, {ϵ, 0, 1}]], 0 ≤ θ && θ ≤ π / 2 && 0 ≤ Λ]

temp1 = Coefficient[Normal[Series[IG00, {ϵ, 0, 3}]], ϵ^3];
A00ϵ3 = segundo * Simplify[temp1 * ϵ^3, 0 ≤ θ && θ ≤ π / 2 && 0 ≤ Λ];

A10 = segundo * IG10;
A11 = segundo * Simplify[Normal[Series[IG11, {ϵ, 0, 1}]], 0 ≤ θ && θ ≤ π / 2 && 0 ≤ Λ];

Ur0α = A00 + segundo * (A00ϵ3 + A10 + A11);
```

$$\frac{(1-i)\,(-1)^{3/4}\,e^{-i\,R}\,\epsilon\,\text{Cos}[\theta]\,\sqrt{1-2\,\Lambda^2-\text{Cos}[2\,\theta]}\,\text{Sin}[\theta]^2}{R\left(\Lambda^4+4\,\text{Sin}[\theta]^4-4\,\text{Sin}[\theta]^2\left(\Lambda^2+i\,\text{Cos}[\theta]\,\sqrt{-\Lambda^2+\text{Sin}[\theta]^2}\right)\right)}$$

```
(*____ ____ ____ ____ ____ ____ ____ ____ ____ ____ ____ ____ ____ ____ ____
  ____ ____ ____ ____ ____ ____ ____ ____ ____ ____ ____ ____ ____ ____ ____ ____ _   *)
(*                                                                    J1α
                                                                   *)
(*____ ____ ____ ____ ____ ____ ____ ____ ____ ____ ____ ____ ____
  ____ ____ ____ ____ ____ ____ ____ ____ ____ ____ ____ ____ ____ ____ ____ ____   *)

Clear[R, θ, Λ, z, z1, F, EE, a00, a10, a11, m, segundo, gH, τ, IgH, ddgH, gH2, gL, H00,
   H10, H11, L00, IH00, IH10, IH11, IL00, A00, temp1, A00ϵ3, A10, A11, B00, Ur1α];

 z = -m * Sin[θ] + I * τ^2 * Sin[θ] + τ * Cos[θ] * Sqrt[τ^2 + 2 * I * m];
 z1 = Simplify[D[z, τ]];
 F = (Λ^2 - 2 * z^2)^2 - 4 * z^2 * Sqrt[(z^2 - 1)] * Sqrt[(z^2 - Λ^2)];
 EE = 2 * Sin[ϵ * z] * Sqrt[z^2 - Λ^2] / (z * F);

 a00 = Exp[-I * Pi / 4] Gamma[1 / 2] / Sqrt[2 * Pi];
 a10 = Exp[-I * Pi / 4] * Gamma[3 / 2] / (2 * Sqrt[2 * Pi] );
 a11 = 4 * Exp[-3 * I * Pi / 4] * Gamma[1 / 2] / (2^5 * Sqrt[2 * Pi] );

 m = 1;
 segundo = 0;
 gH = z^(3 / 2 - 0) * EE * z1;   (* for j=0 *)
 IgH = z^(3 / 2 - 1) * EE * z1;   (* for j=1 *)
 gH2 = Normal[Series[gH, {ϵ, 0, 1}]];
 ddgH  = D[D[gH2, τ], τ];

 gL = z^(3 / 2 - 1) * EE * z1;   (* for j=1 *)

 τ = 0;

 H00  =  (1 / Sin[θ]^(1 / 2)) * gH;
 H10  =  (1 / Sin[θ]^(1 / 2)) * ddgH;
 H11  =  (1 / Sin[θ]^(3 / 2)) * IgH;

 L00  =  (1 / Sin[θ]^(3 / 2)) * gL;

 IH00 = -I * Exp[-I * m * R] * a00 * H00 / R;
 IH10 = -I * Exp[-I * m * R] * a10 * H10 / ( R^2);
 IH11 = -I * Exp[-I * m * R] * a11 * H11 / ( R^2);

 IL00 = Exp[-I * m * R] * a00 * L00 / (2 * R^2);

 A00 = Simplify[Normal[Series[IH00, {ϵ, 0, 1}]], 0 ≤ θ && θ ≤ π / 2 && 0 ≤ Λ]

 temp1 = segundo * Coefficient[Normal[Series[IH00, {ϵ, 0, 3}]], ϵ^3];
 A00ϵ3 = segundo * Simplify[temp1 * ϵ^3, 0 ≤ θ && θ ≤ π / 2 && 0 ≤ Λ];

 A10 = segundo * IH10;
 A11 = segundo * Simplify[Normal[Series[IH11, {ϵ, 0, 1}]], 0 ≤ θ && θ ≤ π / 2 && 0 ≤ Λ];

 B00 = segundo * Simplify[Normal[Series[IL00, {ϵ, 0, 1}]], 0 ≤ θ && θ ≤ π / 2 && 0 ≤ Λ];

 Ur1α = A00 + segundo * (A00ϵ3 + A10 + A11 + B00)
```

$$\frac{(1+\mathrm{i})\,(-1)^{3/4}\,\mathrm{e}^{-\mathrm{i}\,R}\,\epsilon\,\mathrm{Cos}[\theta]\,\sqrt{1-2\,\Lambda^2-\mathrm{Cos}[2\,\theta]}\,\mathrm{Sin}[\theta]}{R\left(\Lambda^4+4\,\mathrm{Sin}[\theta]^4-4\,\mathrm{Sin}[\theta]^2\left(\Lambda^2+\mathrm{i}\,\mathrm{Cos}[\theta]\,\sqrt{-\Lambda^2+\mathrm{Sin}[\theta]^2}\right)\right)}$$

$$\frac{(1+\mathrm{i})\,(-1)^{3/4}\,\mathrm{e}^{-\mathrm{i}\,R}\,\epsilon\,\mathrm{Cos}[\theta]\,\sqrt{1-2\,\Lambda^2-\mathrm{Cos}[2\,\theta]}\,\mathrm{Sin}[\theta]}{R\left(\Lambda^4+4\,\mathrm{Sin}[\theta]^4-4\,\mathrm{Sin}[\theta]^2\left(\Lambda^2+\mathrm{i}\,\mathrm{Cos}[\theta]\,\sqrt{-\Lambda^2+\mathrm{Sin}[\theta]^2}\right)\right)}$$

```
(*_____________________________________________________________
  _____________________________________________________________  *)
(*                                                                J1β
                                                                  *)
(*_____________________________________________________________
  _____________________________________________________________  *)
Clear[R, θ, Λ, z, z1, F, EE, a00, a10, a11, m, segundo, gH, τ, IgH, ddgH, gH2, gL, H00,
   H10, H11, L00, IH00, IH10, IH11, IL00, A00, temp1, A00ϵ3, A10, A11, B00, Ur1β1];

z = -m * Sin[θ] + I * τ^2 * Sin[θ] + τ * Cos[θ] * Sqrt[τ^2 + 2 * I * m];
z1 = Simplify[D[z, τ]];
F = (Λ^2 - 2 * z^2)^2 - 4 * z^2 * Sqrt[(z^2 - 1)] * Sqrt[(z^2 - Λ^2)];
EE = Sin[ϵ * z] / (z^3 * Sqrt[z^2 - Λ^2]);

a00 = Exp[-I * Pi / 4] Gamma[1 / 2] / Sqrt[2 * Pi];
a10 = Exp[-I * Pi / 4] * Gamma[3 / 2] / (2 * Sqrt[2 * Pi] );
a11 = 4 * Exp[-3 * I * Pi / 4] * Gamma[1 / 2] / (2^5 * Sqrt[2 * Pi] );

m = Λ;
segundo = 0;
gH = z^(3 / 2 - 0) * EE * z1;   (* for j=0 *)
IgH = z^(3 / 2 - 1) * EE * z1;   (* for j=1 *)
gH2 = Normal[Series[gH, {ϵ, 0, 1}]];
ddgH = D[D[gH2, τ], τ];

gL = z^(3 / 2 - 1) * EE * z1;   (* for j=1 *)

τ = 0;

H00 = (1 / Sin[θ]^(1 / 2)) * gH;
H10 = (1 / Sin[θ]^(1 / 2)) * ddgH;
H11 = (1 / Sin[θ]^(3 / 2)) * IgH;

L00 = (1 / Sin[θ]^(3 / 2)) * gL;

IH00 = -I * Exp[-I * m * R] * a00 * H00 / R;
IH10 = -I * Exp[-I * m * R] * a10 * H10 / ( R^2);
IH11 = -I * Exp[-I * m * R] * a11 * H11 / ( R^2);

IL00 = Exp[-I * m * R] * a00 * L00 / (2 * R^2);

A00 = Simplify[Normal[Series[IH00, {ϵ, 0, 1}]], 0 ≤ θ && θ ≤ π / 2 && 0 ≤ Λ]

temp1 = segundo * Coefficient[Normal[Series[IH00, {ϵ, 0, 3}]], ϵ^3];
A00ϵ3 = segundo * Simplify[temp1 * ϵ^3, 0 ≤ θ && θ ≤ π / 2 && 0 ≤ Λ];

A10 = segundo * IH10;
A11 = segundo * Simplify[Normal[Series[IH11, {ϵ, 0, 1}]], 0 ≤ θ && θ ≤ π / 2 && 0 ≤ Λ];

B00 = segundo * Simplify[Normal[Series[IL00, {ϵ, 0, 1}]], 0 ≤ θ && θ ≤ π / 2 && 0 ≤ Λ];

Ur1β1 = A00 + segundo * (A00ϵ3 + A10 + A11 + B00)
```

$$\frac{i\, e^{-i\, R\, \Lambda}\, \epsilon\, \text{Csc}[\theta]}{R\, \Lambda}$$

$$\frac{i\, e^{-i\, R\, \Lambda}\, \epsilon\, \text{Csc}[\theta]}{R\, \Lambda}$$

```
(*_____________________________________________
  ___________________________________________  *)
(*                                             J0β
                                                 *)
(*_____________________________________________
  ___________________________________________  *)
Clear[R, θ, Λ, z, z1, F, EE, a00, a10, a11, m, segundo, g, τ, Ig, ddg, g2,
   G00, G10, G11, IG00, IG10, IG11, A00, temp1, A00ϵ3, A10, A11, Ur0β];

 z = -m * Sin[θ] + I * τ^2 * Sin[θ] + τ * Cos[θ] * Sqrt[τ^2 + 2 * I * m];
 z1 = Simplify[D[z, τ]];
 F = (Λ^2 - 2 * z^2)^2 - 4 * z^2 * Sqrt[(z^2 - 1)] * Sqrt[(z^2 - Λ^2)];
 EE = (2 * z^2 - Λ^2) * Sqrt[z^2 - Λ^2] * Sin[ϵ * z] / (z * F);

 a00 = Exp[-I * Pi / 4] Gamma[1 / 2] / Sqrt[2 * Pi];
 a10 = Exp[-I * Pi / 4] * Gamma[3 / 2] / (2 * Sqrt[2 * Pi] );
 a11 = 4 * Exp[-3 * I * Pi / 4] * Gamma[1 / 2] / (2^5 * Sqrt[2 * Pi] );

 m = Λ;
 segundo = 1;
 g = z^(3 / 2 - 1) * EE * z1;   (* for j=1 *)
 Ig = z^(3 / 2 - 2) * EE * z1;   (* for j=2 *)
 g2 = Normal[Series[g, {ϵ, 0, 1}]];
 ddg = D[D[g2, τ], τ];

 τ = 0;

 G00 = (1 / Sin[θ]^(1 / 2)) * g;
 G10 = (1 / Sin[θ]^(1 / 2)) * ddg;
 G11 = (1 / Sin[θ]^(3 / 2)) * Ig;

 IG00 = Exp[-I * m * R] * a00 * G00 / R;
 IG10 = Exp[-I * m * R] * a10 * G10 / ( R^2);
 IG11 = Exp[-I * m * R] * a11 * G11 / ( R^2);

 A00 = Simplify[Normal[Series[IG00, {ϵ, 0, 1}]], 0 ≤ θ && θ ≤ π / 2 && 0 ≤ Λ]

 temp1 = segundo * Coefficient[Normal[Series[IG00, {ϵ, 0, 3}]], ϵ^3];
 A00ϵ3 = segundo * Simplify[temp1 * ϵ^3, 0 ≤ θ && θ ≤ π / 2 && 0 ≤ Λ];
 A10 = segundo * IG10;
 A11 = segundo * Simplify[Normal[Series[IG11, {ϵ, 0, 1}]], 0 ≤ θ && θ ≤ π / 2 && 0 ≤ Λ];

 Ur0β = A00 + segundo * (A00ϵ3 + A10 + A11);
```

$$\frac{e^{-i R \Lambda}\, \epsilon\, \Lambda \cos[\theta]^2 \cos[2\theta]}{R\left(\Lambda + 4\Lambda \sin[\theta]^4 - 4 \sin[\theta]^2 \left(\Lambda + i \cos[\theta] \sqrt{-1 + \Lambda^2 \sin[\theta]^2}\right)\right)}$$

```
(*_____________________________________________________________________
  _____________________________________________________________________ *)
(*                                                                J1β
                                                                   *)
(*_____________________________________________________________________
  _____________________________________________________________________ *)
Clear[R, θ, Λ, z, z1, F, EE, a00, a10, a11, m, segundo, gH, τ,
   IgH, ddgH, gH2, gL, H00, H10, H11, L00, IH00, IH10, IH11,
   IL00, A00, temp1, A00ϵ3, A10, A11, B00, temp2, B00ϵ3, Ur1β2];

 z = -m * Sin[θ] + I * τ^2 * Sin[θ] + τ * Cos[θ] * Sqrt[τ^2 + 2 * I * m];
 z1 = Simplify[D[z, τ]];
 F = (Λ^2 - 2 * z^2)^2 - 4 * z^2 * Sqrt[(z^2 - 1)] * Sqrt[(z^2 - Λ^2)];
 EE = (2 * z^2 - Λ^2) * Sqrt[z^2 - Λ^2] * Sin[ϵ * z] / (z^3 * F);

 a00 = Exp[-I * Pi / 4] Gamma[1 / 2] / Sqrt[2 * Pi];
 a10 = Exp[-I * Pi / 4] * Gamma[3 / 2] / (2 * Sqrt[2 * Pi] );
 a11 = 4 * Exp[-3 * I * Pi / 4] * Gamma[1 / 2] / (2^5 * Sqrt[2 * Pi] );

 m = Λ;
 segundo = 0;
 gH = z^(3 / 2 - 0) * EE * z1;   (* for j=0 *)
 IgH = z^(3 / 2 - 1) * EE * z1;   (* for j=1 *)
 gH2 = Normal[Series[gH, {ϵ, 0, 1}]];
 ddgH  = D[D[gH2, τ], τ];

 gL = z^(3 / 2 - 1) * EE * z1;   (* for j=1 *)

 τ = 0;

 H00  =  (1 / Sin[θ]^(1 / 2)) * gH;
 H10  =  (1 / Sin[θ]^(1 / 2)) * ddgH;
 H11  =  (1 / Sin[θ]^(3 / 2)) * IgH;

 L00  =  (1 / Sin[θ]^(3 / 2)) * gL;

 IH00 = -I * Exp[-I * m * R] * a00 * H00 / R;
 IH10 = -I * Exp[-I * m * R] * a10 * H10 / ( R^2);
 IH11 = -I * Exp[-I * m * R] * a11 * H11 / ( R^2);

 IL00 = Exp[-I * m * R] * a00 * L00 / (2 * R^2);

 A00 = Simplify[Normal[Series[IH00, {ϵ, 0, 1}]], 0 ≤ θ && θ ≤ π / 2 && 0 ≤ Λ]

 temp1 = segundo * Coefficient[Normal[Series[IH00, {ϵ, 0, 3}]], ϵ^3];
 A00ϵ3 = segundo * temp1 * ϵ^3;

 A10 = segundo * IH10;
 A11 = segundo * Normal[Series[IH11, {ϵ, 0, 1}]];

 B00 = segundo * Normal[Series[IL00, {ϵ, 0, 1}]];

 Ur1β2 = A00 + segundo * (A00ϵ3 + A10 + A11 + B00)
```

$$\frac{\mathrm{i}\, e^{-\mathrm{i}\, R\, \Lambda}\, \epsilon\, \mathrm{Cos}[\theta]\, \mathrm{Cos}[2\,\theta]\, \mathrm{Cot}[\theta]}{R\left(\Lambda + 4\,\Lambda\, \mathrm{Sin}[\theta]^4 - 4\, \mathrm{Sin}[\theta]^2 \left(\Lambda + \mathrm{i}\, \mathrm{Cos}[\theta] \sqrt{-1 + \Lambda^2\, \mathrm{Sin}[\theta]^2}\right)\right)}$$

$$\frac{\mathrm{i}\, e^{-\mathrm{i}\, R\, \Lambda}\, \epsilon\, \mathrm{Cos}[\theta]\, \mathrm{Cos}[2\,\theta]\, \mathrm{Cot}[\theta]}{R\left(\Lambda + 4\,\Lambda\, \mathrm{Sin}[\theta]^4 - 4\, \mathrm{Sin}[\theta]^2 \left(\Lambda + \mathrm{i}\, \mathrm{Cos}[\theta] \sqrt{-1 + \Lambda^2\, \mathrm{Sin}[\theta]^2}\right)\right)}$$

```
(*_____________________________________________________________
  ____________________________________________________________ *)
(*                    Ur Summation of all sub-
 components                                                  *)
(*_____________________________________________________________
  ____________________________________________________________ *)

Clear[Ur, Urtotal, co1, co2, co3, co4, co5, co6]

Urtotal = P * Sin[ϕ] / (2 * π * μ * ro) * ( -Ur0α + Ur0β + (Ur1α + Ur1β1 - Ur1β2) / (R * Sin[θ]) ) ;

co1 = Simplify[
  Coefficient[Urtotal, P * ϵ^1 * Sin[ϕ] / (μ * ro) * Exp[-I * R] / R], 0 ≤ θ && θ ≤ π / 2 && 0 ≤ Λ]
co2 = Simplify[Coefficient[Urtotal, P * ϵ^3 * Sin[ϕ] / (μ * ro) * Exp[-I * R] / R],
   0 ≤ θ && θ ≤ π / 2 && 0 ≤ Λ];
co3 = Simplify[Coefficient[Urtotal, P * ϵ^1 * Sin[ϕ] / (μ * ro) * Exp[-I * Λ * R] / R],
  0 ≤ θ && θ ≤ π / 2 && 0 ≤ Λ]
co4 = Simplify[Coefficient[Urtotal, P * ϵ^3 * Sin[ϕ] / (μ * ro) * Exp[-I * Λ * R] / R],
   0 ≤ θ && θ ≤ π / 2 && 0 ≤ Λ];
co5 = Coefficient[Urtotal, P * ϵ^1 * Sin[ϕ] / (μ * ro) * Exp[-I * Λ * R] / R^2];
co6 = Coefficient[Urtotal, P * ϵ^1 * Sin[ϕ] / (μ * ro) * Exp[-I * R] / R^2];


Ur = P * ϵ^1 * Sin[ϕ] / (μ * ro) * Exp[-I * R] / R * co1 + P * ϵ^3 * Sin[ϕ] / (μ * ro) *
    Exp[-I * R] / R * co2 + P * ϵ^1 * Sin[ϕ] / (μ * ro) * Exp[-I * Λ * R] / R * co3 +
   P * ϵ^3 * Sin[ϕ] / (μ * ro) * Exp[-I * Λ * R] / R * co4 + P * ϵ^1 * Sin[ϕ] / (μ * ro) *
    Exp[-I * Λ * R] / R^2 * co5 + P * ϵ^1 * Sin[ϕ] / (μ * ro) * Exp[-I * R] / R^2 * co6;
```

$$-\frac{\left(\frac{1}{2}-\frac{i}{2}\right)(-1)^{3/4}\,\text{Cos}[\theta]\,\sqrt{1-2\Lambda^2-\text{Cos}[2\theta]}\,\text{Sin}[\theta]^2}{\pi\left(\Lambda^4+4\,\text{Sin}[\theta]^4-4\,\text{Sin}[\theta]^2\left(\Lambda^2+i\,\text{Cos}[\theta]\,\sqrt{-\Lambda^2+\text{Sin}[\theta]^2}\right)\right)}$$

$$\frac{\Lambda\,\text{Cos}[\theta]^2\,\text{Cos}[2\theta]}{2\pi\left(\Lambda+4\,\Lambda\,\text{Sin}[\theta]^4-4\,\text{Sin}[\theta]^2\left(\Lambda+i\,\text{Cos}[\theta]\,\sqrt{-1+\Lambda^2\,\text{Sin}[\theta]^2}\right)\right)}$$

```
(* Calculation of Dispalcement
 in the little ϕ direction,
in cylindrical coordinates

  Uϕ= P*Cos[ϕ]/(2*Pi*μ*ro)*
  (-Ur1α + Uϕ0B - Uϕ1β + Ur1β2 )
*)

(*_____________________________________________
  ____________________________________________ *)
(*                                          J0β
                                              *)
(*_____________________________________________
  ____________________________________________ *)

Clear[R, θ, Λ, z, z1, F, EE, a00, a10, a11, m, segundo, g, τ, Ig, ddg,
   g2, G00, G10, G11, IG00, IG10, IG11, A00, temp1, A00ϵ3, A10, A11, Uϕ0β];

 z = -m*Sin[θ] + I*τ^2*Sin[θ] + τ*Cos[θ]*Sqrt[τ^2 + 2*I*m];
 z1 = Simplify[D[z, τ]];
 F = (Λ^2 - 2*z^2)^2 - 4*z^2*Sqrt[(z^2 - 1)]*Sqrt[(z^2 - Λ^2)];
 EE = Sin[ϵ*z] / (z*Sqrt[z^2 - Λ^2]);

 a00 = Exp[-I*Pi/4] Gamma[1/2] / Sqrt[2*Pi];
 a10 = Exp[-I*Pi/4]*Gamma[3/2] / (2*Sqrt[2*Pi] );
 a11 = 4*Exp[-3*I*Pi/4]*Gamma[1/2] / (2^5*Sqrt[2*Pi] );

 m = Λ;
 segundo = 1;
 g = z^(3/2 - 1)*EE*z1;   (* for j=1 *)
 Ig = z^(3/2 - 2)*EE*z1;   (* for j=2 *)
 g2 = Normal[Series[g, {ϵ, 0, 1}]];
 ddg = D[D[g2, τ], τ];

 τ = 0;

 G00 = (1/Sin[θ]^(1/2))*g;
 G10 = (1/Sin[θ]^(1/2))*ddg;
 G11 = (1/Sin[θ]^(3/2))*Ig;

 IG00 = Exp[-I*m*R]*a00*G00/R;
 IG10 = Exp[-I*m*R]*a10*G10/(R^2);
 IG11 = Exp[-I*m*R]*a11*G11/(R^2);

 A00 = Simplify[Normal[Series[IG00, {ϵ, 0, 1}]], 0 ≤ θ && θ ≤ π/2 && 0 ≤ Λ]

 temp1 = segundo*Coefficient[Normal[Series[IG00, {ϵ, 0, 3}]], ϵ^3];
 A00ϵ3 = segundo*Simplify[temp1*ϵ^3, 0 ≤ θ && θ ≤ π/2 && 0 ≤ Λ]
 A10 = segundo*Simplify[IG10, 0 ≤ θ && θ ≤ π/2 && 0 ≤ Λ]
 A11 = segundo*Simplify[Normal[Series[IG11, {ϵ, 0, 1}]], 0 ≤ θ && θ ≤ π/2 && 0 ≤ Λ]

 Uϕ0β = A00 + segundo*(A00ϵ3 + A10 + A11)
```

$$\frac{e^{-i R \Lambda} \epsilon}{R}$$

$$-\frac{e^{-i R \Lambda} \epsilon^3 \Lambda^2 \text{Sin}[\theta]^2}{6 R}$$

$$-\frac{i e^{-i R \Lambda} \epsilon \text{Csc}[\theta]^2}{8 R^2 \Lambda}$$

$$\frac{i e^{-i R \Lambda} \epsilon \text{Csc}[\theta]^2}{8 R^2 \Lambda}$$

$$\frac{e^{-i R \Lambda} \epsilon}{R} - \frac{e^{-i R \Lambda} \epsilon^3 \Lambda^2 \text{Sin}[\theta]^2}{6 R}$$

```
(*_____________________________________________________________
  ____________________________________________________________ *)
(*                                                          J1β
                                                              *)
(*_____________________________________________________________
  ____________________________________________________________ *)

Clear[R, θ, Λ, z, z1, F, EE, a00, a10, a11, m, segundo, gH, τ, IgH, ddgH, gH2, gL, H00,
   H10, H11, L00, IH00, IH10, IH11, IL00, A00, temp1, A00ϵ3, A10, A11, B00, Uϕ1β];

z = -m * Sin[θ] + I * τ^2 * Sin[θ] + τ * Cos[θ] * Sqrt[τ^2 + 2 * I * m];
z1 = Simplify[D[z, τ]];
F = (Λ^2 - 2 * z^2)^2 - 4 * z^2 * Sqrt[(z^2 - 1)] * Sqrt[(z^2 - Λ^2)];
EE = Sin[ϵ * z] / (z^3 * Sqrt[z^2 - Λ^2]);

a00 = Exp[-I * Pi / 4] Gamma[1 / 2] / Sqrt[2 * Pi];
a10 = Exp[-I * Pi / 4] * Gamma[3 / 2] / (2 * Sqrt[2 * Pi] );
a11 = 4 * Exp[-3 * I * Pi / 4] * Gamma[1 / 2] / (2^5 * Sqrt[2 * Pi] );

m = Λ;
segundo = 0;
gH = z^(3 / 2 - 0) * EE * z1;   (* for j=0 *)
IgH = z^(3 / 2 - 1) * EE * z1;   (* for j=1 *)
gH2 = Normal[Series[gH, {ϵ, 0, 1}]];
ddgH = D[D[gH2, τ], τ];

gL = z^(3 / 2 - 1) * EE * z1;   (* for j=1 *)

τ = 0;

H00 = (1 / Sin[θ]^(1 / 2)) * gH;
H10 = (1 / Sin[θ]^(1 / 2)) * ddgH;
H11 = (1 / Sin[θ]^(3 / 2)) * IgH;

L00 = (1 / Sin[θ]^(3 / 2)) * gL;

IH00 = -I * Exp[-I * m * R] * a00 * H00 / R;
IH10 = -I * Exp[-I * m * R] * a10 * H10 / ( R^2);
IH11 = -I * Exp[-I * m * R] * a11 * H11 / ( R^2);

IL00 = Exp[-I * m * R] * a00 * L00 / (2 * R^2);

A00 = Simplify[Normal[Series[IH00, {ϵ, 0, 1}]], 0 ≤ θ && θ ≤ π / 2 && 0 ≤ Λ]

temp1 = segundo * Coefficient[Normal[Series[IH00, {ϵ, 0, 3}]], ϵ^3];
A00ϵ3 = segundo * Simplify[temp1 * ϵ^3, 0 ≤ θ && θ ≤ π / 2 && 0 ≤ Λ];

A10 = segundo * IH10;
A11 = segundo * Simplify[Normal[Series[IH11, {ϵ, 0, 1}]], 0 ≤ θ && θ ≤ π / 2 && 0 ≤ Λ];

B00 = segundo * Simplify[Normal[Series[IL00, {ϵ, 0, 1}]], 0 ≤ θ && θ ≤ π / 2 && 0 ≤ Λ];

Uϕ1β = A00 + segundo * (A00ϵ3 + A10 + A11 + B00)
```

$$\frac{i\, e^{-i R \Lambda}\, \epsilon\, \text{Csc}[\theta]}{R \Lambda}$$

$$\frac{i\, e^{-i R \Lambda}\, \epsilon\, \text{Csc}[\theta]}{R \Lambda}$$

```
(*_____________________________________________
  _____________________________________________ *)
(*                 Uϕ Summation of all sub-
 components                                    *)
(*_____________________________________________
  _____________________________________________ *)

Clear[Uϕ, Uϕtotal, co1, co2, co3, co4, co5, co6]

Uϕtotal = P * Cos[ϕ] / (2 * π * μ * ro) * ( Uϕ0β + (-Ur1α - Uϕ1β + Ur1β2) / (R * Sin[θ])) ;

co1 = Simplify[
    Coefficient[Uϕtotal, P * ϵ^1 * Cos[ϕ] / (μ * ro) * Exp[-I * R] / R], 0 ≤ θ && θ ≤ π / 2 && 0 ≤ Λ];
co2 = Simplify[Coefficient[Uϕtotal, P * ϵ^3 * Cos[ϕ] / (μ * ro) * Exp[-I * R] / R],
    0 ≤ θ && θ ≤ π / 2 && 0 ≤ Λ];
co3 = Simplify[Coefficient[Uϕtotal, P * ϵ^1 * Cos[ϕ] / (μ * ro) * Exp[-I * Λ * R] / R],
  0 ≤ θ && θ ≤ π / 2 && 0 ≤ Λ]
co4 = Simplify[Coefficient[Uϕtotal, P * ϵ^3 * Cos[ϕ] / (μ * ro) * Exp[-I * Λ * R] / R],
  0 ≤ θ && θ ≤ π / 2 && 0 ≤ Λ]
co5 = Coefficient[Uϕtotal, P * ϵ^1 * Cos[ϕ] / (μ * ro) * Exp[-I * Λ * R] / R^2]
co6 = Coefficient[Uϕtotal, P * ϵ^1 * Cos[ϕ] / (μ * ro) * Exp[-I * R] / R^2]


Uϕ = P * ϵ^1 * Cos[ϕ] / (μ * ro) * Exp[-I * R] / R * co1  + P * ϵ^3 * Cos[ϕ] / (μ * ro) *
     Exp[-I * R] / R * co2 + P * ϵ^1 * Cos[ϕ] / (μ * ro) * Exp[-I * Λ * R] / R * co3 +
   P * ϵ^3 * Cos[ϕ] / (μ * ro) * Exp[-I * Λ * R] / R * co4 + P * ϵ^1 * Cos[ϕ] / (μ * ro) *
    Exp[-I * Λ * R] / R^2 * co5 + P * ϵ^1 * Cos[ϕ] / (μ * ro) * Exp[-I * R] / R^2 * co6;
```

$$\frac{1}{2\pi}$$

$$-\frac{\Lambda^2 \operatorname{Sin}[\theta]^2}{12\pi}$$

$$-\frac{i \operatorname{Csc}[\theta]^2}{2\pi\Lambda} + \frac{i \operatorname{Cos}[2\theta] \operatorname{Cot}[\theta]^2}{2\pi\left(\Lambda + 4\Lambda \operatorname{Sin}[\theta]^4 - 4 \operatorname{Sin}[\theta]^2 \left(\Lambda + i \operatorname{Cos}[\theta] \sqrt{-1 + \Lambda^2 \operatorname{Sin}[\theta]^2}\right)\right)}$$

$$-\frac{\left(\frac{1}{2} + \frac{i}{2}\right) (-1)^{3/4} \operatorname{Cos}[\theta] \sqrt{1 - 2\Lambda^2 - \operatorname{Cos}[2\theta]}}{\pi\left(\Lambda^4 + 4 \operatorname{Sin}[\theta]^4 - 4 \operatorname{Sin}[\theta]^2 \left(\Lambda^2 + i \operatorname{Cos}[\theta] \sqrt{-\Lambda^2 + \operatorname{Sin}[\theta]^2}\right)\right)}$$

```
(* Calculation of Dispalcement
 in the little z direction,
 in cylindrical coordinates
  Uz= P*r0*Sin[ϕ]/μ (Uz1α - Uz1β)    *)

(*_____________________________________________
 __________________________________________________________ *)
(*                                                    J1α
                                                   *)
(*_____________________________________________
 __________________________________________________________ *)

Clear[R, θ, Λ, z, z1, F, EE, a00, a10, a11, m, segundo, gH, τ, IgH, ddgH, gH2, gL, H00,
  H10, H11, L00, IH00, IH10, IH11, IL00, A00, temp1, A00ϵ3, A10, A11, B00, Uz1α];

z = -m * Sin[θ] + I * τ^2 * Sin[θ] + τ * Cos[θ] * Sqrt[τ^2 + 2 * I * m];
z1 = Simplify[D[z, τ]];
F = (Λ^2 - 2 * z^2)^2 - 4 * z^2 * Sqrt[(z^2 - 1)] * Sqrt[(z^2 - Λ^2)];
EE = 2 * Sin[ϵ * z] * Sqrt[z^2 - 1] * Sqrt[z^2 - Λ^2] / (z * F);

a00 = Exp[-I * Pi / 4] Gamma[1 / 2] / Sqrt[2 * Pi];
a10 = Exp[-I * Pi / 4] * Gamma[3 / 2] / (2 * Sqrt[2 * Pi] );
a11 = 4 * Exp[-3 * I * Pi / 4] * Gamma[1 / 2] / (2^5 * Sqrt[2 * Pi] );

m = 1;
segundo = 1;
gH = z^(3 / 2 - 0) * EE * z1;   (* for j=0 *)
IgH = z^(3 / 2 - 1) * EE * z1;   (* for j=1 *)
gH2 = Normal[Series[gH, {ϵ, 0, 1}]];
ddgH  = D[D[gH2, τ], τ];

gL = z^(3 / 2 - 1) * EE * z1;   (* for j=1 *)

τ = 0;

H00  =  (1 / Sin[θ]^(1 / 2)) * gH;
H10  =  (1 / Sin[θ]^(1 / 2)) * ddgH;
H11  =  (1 / Sin[θ]^(3 / 2)) * IgH;

L00  =  (1 / Sin[θ]^(3 / 2)) * gL;

IH00 = -I * Exp[-I * m * R] * a00 * H00 / R;
IH10 = -I * Exp[-I * m * R] * a10 * H10 / ( R^2);
IH11 = -I * Exp[-I * m * R] * a11 * H11 / ( R^2);

IL00 = Exp[-I * m * R] * a00 * L00 / (2 * R^2);

A00 = Simplify[Normal[Series[IH00, {ϵ, 0, 1}]], 0 ≤ θ && θ ≤ π / 2 && 0 ≤ Λ]

temp1 = segundo * Coefficient[Normal[Series[IH00, {ϵ, 0, 3}]], ϵ^3];
A00ϵ3 = segundo * Simplify[temp1 * ϵ^3, 0 ≤ θ && θ ≤ π / 2 && 0 ≤ Λ];

A10 = segundo * IH10;
A11 = segundo * Simplify[Normal[Series[IH11, {ϵ, 0, 1}]], 0 ≤ θ && θ ≤ π / 2 && 0 ≤ Λ];

B00 = segundo * Simplify[Normal[Series[IL00, {ϵ, 0, 1}]], 0 ≤ θ && θ ≤ π / 2 && 0 ≤ Λ];

Uz1α = A00 + segundo * (A00ϵ3 + A10 + A11 + B00);
```

$$-\frac{(1-\mathbb{i})\ (-1)^{3/4}\ \mathbb{e}^{-\mathbb{i}\,R}\ \epsilon\ \mathrm{Cos}[\theta]^{2}\ \sqrt{1-2\,\Lambda^{2}-\mathrm{Cos}[2\,\theta]}\ \mathrm{Sin}[\theta]}{R\left(\Lambda^{4}+4\,\mathrm{Sin}[\theta]^{4}-4\,\mathrm{Sin}[\theta]^{2}\left(\Lambda^{2}+\mathbb{i}\,\mathrm{Cos}[\theta]\,\sqrt{-\Lambda^{2}+\mathrm{Sin}[\theta]^{2}}\right)\right)}$$

$$-\frac{(1-\mathrm{i})\,(-1)^{3/4}\,e^{-\mathrm{i}\,R\,\epsilon}\,\mathrm{Cos}[\theta]^2\,\sqrt{1-2\,\Lambda^2-\mathrm{Cos}[2\,\theta]}\;\mathrm{Sin}[\theta]}{R\left(\Lambda^4+4\,\mathrm{Sin}[\theta]^4-4\,\mathrm{Sin}[\theta]^2\left(\Lambda^2+\mathrm{i}\,\mathrm{Cos}[\theta]\,\sqrt{-\Lambda^2+\mathrm{Sin}[\theta]^2}\right)\right)}$$

```
(*_____________________________________________________
  _________________________________________________________   *)
(*                                                        J1β
                                                         *)
(*_____________________________________________________
  _________________________________________________________   *)
```

```
Clear[R, θ, Λ, z, z1, F, EE, a00, a10, a11, m, segundo, gH, τ, IgH, ddgH, gH2, gL, H00,
   H10, H11, L00, IH00, IH10, IH11, IL00, A00, temp1, A00ϵ3, A10, A11, B00, Uz1β];

 z = -m * Sin[θ] + I * τ^2 * Sin[θ] + τ * Cos[θ] * Sqrt[τ^2 + 2 * I * m];
 z1 = Simplify[D[z, τ]];
 F = (Λ^2 - 2 * z^2)^2 - 4 * z^2 * Sqrt[(z^2 - 1)] * Sqrt[(z^2 - Λ^2)];
 EE = Sin[ϵ * z] * (2 * z^2 - 1 Λ^2) / (z * F);

 a00 = Exp[-I * Pi / 4] Gamma[1 / 2] / Sqrt[2 * Pi];
 a10 = Exp[-I * Pi / 4] * Gamma[3 / 2] / (2 * Sqrt[2 * Pi] );
 a11 = 4 * Exp[-3 * I * Pi / 4] * Gamma[1 / 2] / (2^5 * Sqrt[2 * Pi] );

 m = Λ;
 segundo = 1;
 gH = z^(3 / 2 - 0) * EE * z1;   (* for j=0 *)
 IgH = z^(3 / 2 - 1) * EE * z1;   (* for j=1 *)
 gH2 = Normal[Series[gH, {ϵ, 0, 1}]];
 ddgH  = D[D[gH2, τ], τ];

 gL = z^(3 / 2 - 1) * EE * z1;   (* for j=1 *)

 τ = 0;

 H00  =  (1 / Sin[θ]^(1 / 2)) * gH;
 H10  =  (1 / Sin[θ]^(1 / 2)) * ddgH;
 H11  =  (1 / Sin[θ]^(3 / 2)) * IgH;

 L00  =  (1 / Sin[θ]^(3 / 2)) * gL;

 IH00 = -I * Exp[-I * m * R] * a00 * H00 / R;
 IH10 = -I * Exp[-I * m * R] * a10 * H10 / ( R^2);
 IH11 = -I * Exp[-I * m * R] * a11 * H11 / ( R^2);

 IL00 = Exp[-I * m * R] * a00 * L00 / (2 * R^2);

 A00 = Simplify[Normal[Series[IH00, {ϵ, 0, 1}]], 0 ≤ θ && θ ≤ π / 2 && 0 ≤ Λ]

 temp1 = segundo * Coefficient[Normal[Series[IH00, {ϵ, 0, 3}]], ϵ^3];
 A00ϵ3 = segundo * Simplify[temp1 * ϵ^3, 0 ≤ θ && θ ≤ π / 2 && 0 ≤ Λ];

 A10 = segundo * IH10;
 A11 = segundo * Simplify[Normal[Series[IH11, {ϵ, 0, 1}]], 0 ≤ θ && θ ≤ π / 2 && 0 ≤ Λ];

 B00 = segundo * Simplify[Normal[Series[IL00, {ϵ, 0, 1}]], 0 ≤ θ && θ ≤ π / 2 && 0 ≤ Λ];

 Uz1β = A00 + segundo * (A00ϵ3 + A10 + A11 + B00);
```

$$\frac{e^{-\mathrm{i}\,R\,\Lambda}\,\epsilon\,\Lambda\,\mathrm{Sin}[4\,\theta]}{4\,R\left(\Lambda+4\,\Lambda\,\mathrm{Sin}[\theta]^4-4\,\mathrm{Sin}[\theta]^2\left(\Lambda+\mathrm{i}\,\mathrm{Cos}[\theta]\,\sqrt{-1+\Lambda^2\,\mathrm{Sin}[\theta]^2}\right)\right)}$$

```
(*_____________________________________________________________
  _____________________________________________________________ *)
(*                    Uz Summation of all sub-
 components                                                    *)
(*_____________________________________________________________
  _____________________________________________________________ *)

Clear[co1, co2, co3, co4, co5, co6, Uz, Uztotal]

Uztotal = P * Sin[ϕ] / (2 * π * μ * ro) * ( Uz1α - Uz1β );

co1 = Simplify[
  Coefficient[Uztotal, P * ϵ^1 * Sin[ϕ] / (μ * ro) * Exp[-I * R] / R], 0 ≤ Θ && Θ ≤ π / 2 && 0 ≤ Λ]
co2 = Simplify[Coefficient[Uztotal, P * ϵ^3 * Sin[ϕ] / (μ * ro) * Exp[-I * R] / R],
   0 ≤ Θ && Θ ≤ π / 2 && 0 ≤ Λ];
co3 = FullSimplify[Coefficient[Uztotal, P * ϵ^1 * Sin[ϕ] / (μ * ro) * Exp[-I * Λ * R] / R],
  0 ≤ Θ && Θ ≤ π / 2 && 0 ≤ Λ]
co4 = FullSimplify[Coefficient[Uztotal, P * ϵ^3 * Sin[ϕ] / (μ * ro) * Exp[-I * Λ * R] / R],
   0 ≤ Θ && Θ ≤ π / 2 && 0 ≤ Λ];
co5 = Coefficient[Uztotal, P * ϵ^1 * Sin[ϕ] / (μ * ro) * Exp[-I * Λ * R] / R^2];
co6 = Coefficient[Uztotal, P * ϵ^1 * Sin[ϕ] / (μ * ro) * Exp[-I * R] / R^2];


Uz = P * ϵ^1 * Sin[ϕ] / (μ * ro) * Exp[-I * R] / R * co1 + P * ϵ^3 * Sin[ϕ] / (μ * ro) *
    Exp[-I * R] / R * co2 + P * ϵ^1 * Sin[ϕ] / (μ * ro) * Exp[-I * Λ * R] / R * co3 +
   P * ϵ^3 * Sin[ϕ] / (μ * ro) * Exp[-I * Λ * R] / R * co4 + P * ϵ^1 * Sin[ϕ] / (μ * ro) *
    Exp[-I * Λ * R] / R^2 * co5 + P * ϵ^1 * Sin[ϕ] / (μ * ro) * Exp[-I * R] / R^2 * co6;
```

$$-\frac{\left(\frac{1}{2}-\frac{i}{2}\right)(-1)^{3/4}\,\text{Cos}[\Theta]^2\,\sqrt{1-2\Lambda^2-\text{Cos}[2\Theta]}\,\text{Sin}[\Theta]}{\pi\left(\Lambda^4+4\,\text{Sin}[\Theta]^4-4\,\text{Sin}[\Theta]^2\left(\Lambda^2+i\,\text{Cos}[\Theta]\,\sqrt{-\Lambda^2+\text{Sin}[\Theta]^2}\right)\right)}$$

$$\frac{\Lambda\,\text{Sin}[4\Theta]}{-8\pi\Lambda\,\text{Cos}[2\Theta]^2+32\,i\,\pi\,\text{Cos}[\Theta]\,\text{Sin}[\Theta]^2\,\sqrt{-1+\Lambda^2\,\text{Sin}[\Theta]^2}}$$

```
(*    TRANSFORMATION
 FROM CYLINDRICAL TO
 SPHERICAL COORDINATES    *)
```

```
Clear[UR, co1, co2, co3, co4, co5, co6, URtotal]

URtotal = Ur * Sin[θ] + Uz * Cos[θ];

co1 = Simplify[
  Coefficient[URtotal, P * ϵ^1 * Sin[ϕ] / (μ * ro) * Exp[-I * R] / R], 0 ≤ θ && θ ≤ π / 2 && 0 ≤ Λ]
co2 = Simplify[Coefficient[URtotal, P * ϵ^3 * Sin[ϕ] / (μ * ro) * Exp[-I * R] / R],
  0 ≤ θ && θ ≤ π / 2 && 0 ≤ Λ]
co3 = Simplify[Coefficient[URtotal, P * ϵ^1 * Sin[ϕ] / (μ * ro) * Exp[-I * Λ * R] / R],
  0 ≤ θ && θ ≤ π / 2 && 0 ≤ Λ]
co4 = Simplify[Coefficient[URtotal, P * ϵ^3 * Sin[ϕ] / (μ * ro) * Exp[-I * Λ * R] / R],
  0 ≤ θ && θ ≤ π / 2 && 0 ≤ Λ]
co5 = Coefficient[URtotal, P * ϵ^1 * Sin[ϕ] / (μ * ro) * Exp[-I * Λ * R] / R^2];
co6 = Coefficient[URtotal, P * ϵ^1 * Sin[ϕ] / (μ * ro) * Exp[-I * R] / R^2];

UR = P * ϵ^1 * Sin[ϕ] / (μ * ro) * Exp[-I * R] / R * co1 + P * ϵ^3 * Sin[ϕ] / (μ * ro) *
     Exp[-I * R] / R * co2 + P * ϵ^1 * Sin[ϕ] / (μ * ro) * Exp[-I * Λ * R] / R * co3 +
    P * ϵ^3 * Sin[ϕ] / (μ * ro) * Exp[-I * Λ * R] / R * co4 + P * ϵ^1 * Sin[ϕ] / (μ * ro) *
     Exp[-I * Λ * R] / R^2 * co5 + P * ϵ^1 * Sin[ϕ] / (μ * ro) * Exp[-I * R] / R^2 * co6;


Clear[Uθ, co1, co2, co3, co4, co5, co6, Uθtotal]

Uθtotal = Ur * Cos[θ] - Uz * Sin[θ];

co1 = Simplify[
  Coefficient[Uθtotal, P * ϵ^1 * Sin[ϕ] / (μ * ro) * Exp[-I * R] / R], 0 ≤ θ && θ ≤ π / 2 && 0 ≤ Λ]
co2 = Simplify[Coefficient[Uθtotal, P * ϵ^3 * Sin[ϕ] / (μ * ro) * Exp[-I * R] / R],
  0 ≤ θ && θ ≤ π / 2 && 0 ≤ Λ]
co3 = Simplify[Coefficient[Uθtotal, P * ϵ^1 * Sin[ϕ] / (μ * ro) * Exp[-I * Λ * R] / R],
  0 ≤ θ && θ ≤ π / 2 && 0 ≤ Λ]
co4 = Simplify[Coefficient[Uθtotal, P * ϵ^3 * Sin[ϕ] / (μ * ro) * Exp[-I * Λ * R] / R],
  0 ≤ θ && θ ≤ π / 2 && 0 ≤ Λ]
co5 = Coefficient[Uθtotal, P * ϵ^1 * Sin[ϕ] / (μ * ro) * Exp[-I * Λ * R] / R^2];
co6 = Coefficient[Uθtotal, P * ϵ^1 * Sin[ϕ] / (μ * ro) * Exp[-I * R] / R^2];

Uθ = P * ϵ^1 * Sin[ϕ] / (μ * ro) * Exp[-I * R] / R * co1 + P * ϵ^3 * Sin[ϕ] / (μ * ro) *
     Exp[-I * R] / R * co2 + P * ϵ^1 * Sin[ϕ] / (μ * ro) * Exp[-I * Λ * R] / R * co3 +
    P * ϵ^3 * Sin[ϕ] / (μ * ro) * Exp[-I * Λ * R] / R * co4 + P * ϵ^1 * Sin[ϕ] / (μ * ro) *
     Exp[-I * Λ * R] / R^2 * co5 + P * ϵ^1 * Sin[ϕ] / (μ * ro) * Exp[-I * R] / R^2 * co6;
```

$$-\frac{\left(\frac{1}{2}-\frac{i}{2}\right)(-1)^{3/4}\cos[\theta]\sqrt{1-2\Lambda^2-\cos[2\theta]}\sin[\theta]}{\pi\left(\Lambda^4+4\sin[\theta]^4-4\sin[\theta]^2\left(\Lambda^2+i\cos[\theta]\sqrt{-\Lambda^2+\sin[\theta]^2}\right)\right)}$$

$$\frac{\left(\frac{1}{12}-\frac{i}{12}\right)(-1)^{3/4}\cos[\theta]\sqrt{1-2\Lambda^2-\cos[2\theta]}\sin[\theta]^3}{\pi\left(\Lambda^4+4\sin[\theta]^4-4\sin[\theta]^2\left(\Lambda^2+i\cos[\theta]\sqrt{-\Lambda^2+\sin[\theta]^2}\right)\right)}$$

```
0

0

0
```

$$0$$

$$\frac{\Lambda\,(\text{Cos}[\theta]+\text{Cos}[3\,\theta])}{4\,\pi\left(\Lambda+4\,\Lambda\,\text{Sin}[\theta]^4-4\,\text{Sin}[\theta]^2\left(\Lambda+\text{i}\,\text{Cos}[\theta]\,\sqrt{-1+\Lambda^2\,\text{Sin}[\theta]^2}\right)\right)}$$

$$-\frac{\Lambda^3\,(\text{Cos}[\theta]+\text{Cos}[3\,\theta])\,\text{Sin}[\theta]^2}{12\,\pi\left(\Lambda-\text{i}\,\sqrt{2}\,\text{Cos}[\theta]\,\sqrt{-2+\Lambda^2-\Lambda^2\,\text{Cos}[2\,\theta]}+\text{i}\,\sqrt{2}\,\sqrt{-2+\Lambda^2-\Lambda^2\,\text{Cos}[2\,\theta]}\,\text{Cos}[3\,\theta]+\Lambda\,\text{Cos}[4\,\theta]\right)}$$

E.3 Derivation of Displacement Field for Rocking Motion

```
(*   ON BODY WAVES FROM THE ROCKING
 MOTION OF A RIGID DISK ON A HALF SPACE

 Calculation of Dispalcement in the little
 r direction, in cylindrical coordinates
  Ur= -K*r0*Sin[ϕ]/μ
  (-Ur1α/r - Ur1β/r + Ur0α + Ur0β)
*)

(*_____________________________________
  ____________________________________  *)
(*                J1α                  *)
(*_____________________________________
  ____________________________________  *)

Clear[R, θ, Λ, z, z1, F, EE, a00, a10, a11, m, segundo, gH, τ, IgH, ddgH, gH2, gL, H00,
   H10, H11, L00, IH00, IH10, IH11, IL00, A00, temp1, A00ϵ4, A10, A11, B00, Ur1α];

z = -m*Sin[θ] + I*τ^2*Sin[θ] + τ*Cos[θ]*Sqrt[τ^2 + 2*I*m];
z1 = Simplify[D[z, τ]];
F = (Λ^2 - 2*z^2)^2 - 4*z^2*Sqrt[(z^2 - 1)]*Sqrt[(z^2 - Λ^2)];
EE = (Λ^2 - 2*z^2)*(Sin[ϵ*z] - ϵ*z*Cos[ϵ*z])/(ϵ*z^3*F);

a00 = Exp[-I*Pi/4] Gamma[1/2]/Sqrt[2*Pi];
a10 = Exp[-I*Pi/4]*Gamma[3/2]/(2*Sqrt[2*Pi] );
a11 = 4*Exp[-3*I*Pi/4]*Gamma[1/2]/(2^5*Sqrt[2*Pi] );

m = 1;
segundo = 0;
gH = z^(3/2 - 0)*EE*z1;   (* for j=0 *)
IgH = z^(3/2 - 1)*EE*z1;   (* for j=1 *)
gH2 = Normal[Series[gH, {ϵ, 0, 2}]];
ddgH = D[D[gH2, τ], τ];

gL = z^(3/2 - 1)*EE*z1;   (* for j=1 *)

τ = 0;

H00 = (1/Sin[θ]^(1/2))*gH;
H10 = (1/Sin[θ]^(1/2))*ddgH;
H11 = (1/Sin[θ]^(3/2))*IgH;

L00 = (1/Sin[θ]^(3/2))*gL;

IH00 = -I*Exp[-I*m*R]*a00*H00/R;
IH10 = -I*Exp[-I*m*R]*a10*H10/(R^2);
IH11 = -I*Exp[-I*m*R]*a11*H11/(R^2);

IL00 = Exp[-I*m*R]*a00*L00/(2*R^2);

A00 = Simplify[Normal[Series[IH00, {ϵ, 0, 2}]], 0 ≤ θ && θ ≤ π/2 && 0 ≤ Λ]

temp1 = segundo*Coefficient[Normal[Series[IH00, {ϵ, 0, 4}]], ϵ^4];
A00ϵ4 = segundo*Simplify[temp1*ϵ^4, 0 ≤ θ && θ ≤ π/2 && 0 ≤ Λ];

A10 = segundo*IH10;
A11 = segundo*Simplify[Normal[Series[IH11, {ϵ, 0, 2}]], 0 ≤ θ && θ ≤ π/2 && 0 ≤ Λ];

B00 = segundo*Simplify[Normal[Series[IL00, {ϵ, 0, 2}]], 0 ≤ θ && θ ≤ π/2 && 0 ≤ Λ];

Ur1α = A00 + segundo*(A00ϵ4 + A10 + A11 + B00)
```

$$\frac{\left(\frac{1}{3}+\frac{i}{3}\right)(-1)^{3/4}\, e^{-i R}\,\epsilon^2\,\text{Cos}[\theta]\,\left(-1+\Lambda^2+\text{Cos}[2\theta]\right)\text{Sin}[\theta]}{\sqrt{2}\,R\left(\Lambda^4+4\,\text{Sin}[\theta]^4-4\,\text{Sin}[\theta]^2\left(\Lambda^2+i\,\text{Cos}[\theta]\sqrt{-\Lambda^2+\text{Sin}[\theta]^2}\right)\right)}$$

$$\frac{\left(\frac{1}{3}+\frac{i}{3}\right)(-1)^{3/4}\, e^{-i R}\,\epsilon^2\,\text{Cos}[\theta]\,\left(-1+\Lambda^2+\text{Cos}[2\theta]\right)\text{Sin}[\theta]}{\sqrt{2}\,R\left(\Lambda^4+4\,\text{Sin}[\theta]^4-4\,\text{Sin}[\theta]^2\left(\Lambda^2+i\,\text{Cos}[\theta]\sqrt{-\Lambda^2+\text{Sin}[\theta]^2}\right)\right)}$$

```
(*____ ____ ____ ____ ____ ____ ____ ____ ____ ____ ____ ____ ____
  ____ ____ ____ ____ ____ ____ ____ ____ ____ ____ ____ ____ ____ ____ ____ ___   *)
(*                                J1β                                  *)
(*____ ____ ____ ____ ____ ____ ____ ____ ____ ____ ____ ____ ____
  ____ ____ ____ ____ ____ ____ ____ ____ ____ ____ ____ ____ ____ ____ ____ ___   *)
Clear[R, θ, Λ, z, z1, F, EE, a00, a10, a11, m, segundo, gH, τ, IgH, ddgH, gH2, gL, H00,
   H10, H11, L00, IH00, IH10, IH11, IL00, A00, temp1, A00ϵ4, A10, A11, B00, Ur1β];

 z = -m * Sin[θ] + I * τ^2 * Sin[θ] + τ * Cos[θ] * Sqrt[τ^2 + 2 * I * m];
 z1 = Simplify[D[z, τ]];
 F = (Λ^2 - 2 * z^2)^2 - 4 * z^2 * Sqrt[(z^2 - 1)] * Sqrt[(z^2 - Λ^2)];
 EE = 2 * Sqrt[z^2 - 1] * Sqrt[z^2 - Λ^2] * (Sin[ϵ * z] - ϵ * z * Cos[ϵ * z]) / (ϵ * z^3 * F);

 a00 = Exp[-I * Pi / 4] Gamma[1 / 2] / Sqrt[2 * Pi];
 a10 = Exp[-I * Pi / 4] * Gamma[3 / 2] / (2 * Sqrt[2 * Pi] );
 a11 = 4 * Exp[-3 * I * Pi / 4] * Gamma[1 / 2] / (2^5 * Sqrt[2 * Pi] );

 m = Λ;
 segundo = 0;
 gH = z^(3 / 2 - 0) * EE * z1;   (* for j=0 *)
 IgH = z^(3 / 2 - 1) * EE * z1;   (* for j=1 *)
 gH2 = Normal[Series[gH, {ϵ, 0, 2}]];
 ddgH  = D[D[gH2, τ], τ];

 gL = z^(3 / 2 - 1) * EE * z1;   (* for j=1 *)

 τ = 0;

 H00  =  (1 / Sin[θ]^(1 / 2)) * gH;
 H10  =  (1 / Sin[θ]^(1 / 2)) * ddgH;
 H11  =  (1 / Sin[θ]^(3 / 2)) * IgH;

 L00  =  (1 / Sin[θ]^(3 / 2)) * gL;

 IH00 = -I * Exp[-I * m * R] * a00 * H00 / R;
 IH10 = -I * Exp[-I * m * R] * a10 * H10 / ( R^2);
 IH11 = -I * Exp[-I * m * R] * a11 * H11 / ( R^2);

 IL00 = Exp[-I * m * R] * a00 * L00 / (2 * R^2);

 A00 = Simplify[Normal[Series[IH00, {ϵ, 0, 2}]], 0 ≤ θ && θ ≤ π / 2 && 0 ≤ Λ]

 temp1 = segundo * Coefficient[Normal[Series[IH00, {ϵ, 0, 4}]], ϵ^4];
 A00ϵ4 = segundo * Simplify[temp1 * ϵ^4, 0 ≤ θ && θ ≤ π / 2 && 0 ≤ Λ];

 A10 = segundo * IH10;
 A11 = segundo * Simplify[Normal[Series[IH11, {ϵ, 0, 2}]], 0 ≤ θ && θ ≤ π / 2 && 0 ≤ Λ];

 B00 = segundo * Simplify[Normal[Series[IL00, {ϵ, 0, 2}]], 0 ≤ θ && θ ≤ π / 2 && 0 ≤ Λ];

 Ur1β = A00 + segundo * (A00ϵ4 + A10 + A11 + B00)
```

$$-\frac{2\, i\, e^{-i R \Lambda}\, \epsilon^2\, \mathrm{Cos}[\theta]^2\, \mathrm{Sin}[\theta]\, \sqrt{-1+\Lambda^2\, \mathrm{Sin}[\theta]^2}}{3\, R \left(\Lambda + 4\, \Lambda\, \mathrm{Sin}[\theta]^4 - 4\, \mathrm{Sin}[\theta]^2 \left(\Lambda + i\, \mathrm{Cos}[\theta] \sqrt{-1+\Lambda^2\, \mathrm{Sin}[\theta]^2}\right)\right)}$$

$$-\frac{2\, i\, e^{-i R \Lambda}\, \epsilon^2\, \mathrm{Cos}[\theta]^2\, \mathrm{Sin}[\theta]\, \sqrt{-1+\Lambda^2\, \mathrm{Sin}[\theta]^2}}{3\, R \left(\Lambda + 4\, \Lambda\, \mathrm{Sin}[\theta]^4 - 4\, \mathrm{Sin}[\theta]^2 \left(\Lambda + i\, \mathrm{Cos}[\theta] \sqrt{-1+\Lambda^2\, \mathrm{Sin}[\theta]^2}\right)\right)}$$

```
(*___________________________________________________________
  _______________________________________________________________ *)
(*                         J0 α                                 *)
(*___________________________________________________________
  _______________________________________________________________ *)

Clear[R, θ, Λ, z, z1, F, EE, a00, a10, a11, m, segundo, g, τ, Ig, ddg,
   g2, G00, G10, G11, IG00, IG10, IG11, A00, temp1, A00ϵ4, A10, A11, Ur0α];

 z = -m*Sin[θ] + I*τ^2*Sin[θ] + τ*Cos[θ]*Sqrt[τ^2 + 2*I*m];
 z1 = Simplify[D[z, τ]];
 F = (Λ^2 - 2*z^2)^2 - 4*z^2*Sqrt[(z^2 - 1)]*Sqrt[(z^2 - Λ^2)];
 EE = (Λ^2 - 2*z^2) * (Sin[ϵ*z] - ϵ*z*Cos[ϵ*z]) / (ϵ*z*F);

 a00 = Exp[-I*Pi/4] Gamma[1/2] / Sqrt[2*Pi];
 a10 = Exp[-I*Pi/4] *Gamma[3/2] / (2*Sqrt[2*Pi] );
 a11 = 4*Exp[-3*I*Pi/4] *Gamma[1/2] / (2^5*Sqrt[2*Pi] );

 m = 1;
 segundo = 1;
 g = z^(3/2 - 1) *EE*z1;   (* for j=1 *)
 Ig = z^(3/2 - 2) *EE*z1;   (* for j=2 *)
 g2 = Normal[Series[g, {ϵ, 0, 2}]];
 ddg  = D[D[g2, τ], τ];

 τ = 0;

 G00  =  (1/Sin[θ]^(1/2)) *g;
 G10  =  (1/Sin[θ]^(1/2)) *ddg;
 G11  =  (1/Sin[θ]^(3/2)) *Ig;

 IG00 = Exp[-I*m*R] *a00*G00/R;
 IG10 = Exp[-I*m*R] *a10*G10/( R^2);
 IG11 = Exp[-I*m*R] *a11*G11/( R^2);

 A00 = Simplify[Normal[Series[IG00, {ϵ, 0, 2}]], 0 ≤ θ && θ ≤ π/2 && 0 ≤ Λ]

 temp1 = Coefficient[Normal[Series[IG00, {ϵ, 0, 4}]], ϵ^4];
 A00ϵ4 = segundo*Simplify[temp1*ϵ^4, 0 ≤ θ && θ ≤ π/2 && 0 ≤ Λ];

 A10 = segundo*IG10;
 A11 = segundo*Simplify[Normal[Series[IG11, {ϵ, 0, 2}]], 0 ≤ θ && θ ≤ π/2 && 0 ≤ Λ];

 Ur0α = A00 + segundo* (A00ϵ4 + A10 + A11);
```

$$\frac{\left(\frac{1}{3}-\frac{i}{3}\right) (-1)^{3/4}\, e^{-i R}\, \epsilon^2\, \mathrm{Cos}[\theta] \left(-1+\Lambda^2+\mathrm{Cos}[2\,\theta]\right) \mathrm{Sin}[\theta]^2}{\sqrt{2}\, R \left(\Lambda^4 + 4\, \mathrm{Sin}[\theta]^4 - 4\, \mathrm{Sin}[\theta]^2 \left(\Lambda^2 + i\, \mathrm{Cos}[\theta] \sqrt{-\Lambda^2+\mathrm{Sin}[\theta]^2}\right)\right)}$$

```
(*_____*)
(*                    J0β                    *)
(*_____*)

Clear[R, θ, Λ, z, z1, F, EE, a00, a10, a11, m, segundo, g, τ, Ig, ddg,
   g2, G00, G10, G11, IG00, IG10, IG11, A00, temp1, A00ϵ4, A10, A11, Ur0β];

z = -m * Sin[θ] + I * τ^2 * Sin[θ] + τ * Cos[θ] * Sqrt[τ^2 + 2 * I * m];
z1 = Simplify[D[z, τ]];
F = (Λ^2 - 2 * z^2)^2 - 4 * z^2 * Sqrt[(z^2 - 1)] * Sqrt[(z^2 - Λ^2)];
EE = 2 * Sqrt[z^2 - 1] * Sqrt[z^2 - Λ^2] * (Sin[ϵ * z] - ϵ * z * Cos[ϵ * z]) / (ϵ * z * F);

a00 = Exp[-I * Pi / 4] Gamma[1 / 2] / Sqrt[2 * Pi];
a10 = Exp[-I * Pi / 4] * Gamma[3 / 2] / (2 * Sqrt[2 * Pi] );
a11 = 4 * Exp[-3 * I * Pi / 4] * Gamma[1 / 2] / (2^5 * Sqrt[2 * Pi] );

m = Λ;
segundo = 1;
g = z^(3 / 2 - 1) * EE * z1;   (* for j=1 *)
Ig = z^(3 / 2 - 2) * EE * z1;   (* for j=2 *)
g2 = Normal[Series[g, {ϵ, 0, 2}]];
ddg = D[D[g2, τ], τ];

τ = 0;

G00 = (1 / Sin[θ]^(1 / 2)) * g;
G10 = (1 / Sin[θ]^(1 / 2)) * ddg;
G11 = (1 / Sin[θ]^(3 / 2)) * Ig;

IG00 = Exp[-I * m * R] * a00 * G00 / R;
IG10 = Exp[-I * m * R] * a10 * G10 / ( R^2);
IG11 = Exp[-I * m * R] * a11 * G11 / ( R^2);

A00 = Simplify[Normal[Series[IG00, {ϵ, 0, 2}]], 0 ≤ θ && θ ≤ π / 2 && 0 ≤ Λ]

temp1 = Coefficient[Normal[Series[IG00, {ϵ, 0, 4}]], ϵ^4];
A00ϵ4 = segundo * Simplify[temp1 * ϵ^4, 0 ≤ θ && θ ≤ π / 2 && 0 ≤ Λ];

A10 = segundo * IG10;
A11 = segundo * Simplify[Normal[Series[IG11, {ϵ, 0, 2}]], 0 ≤ θ && θ ≤ π / 2 && 0 ≤ Λ];

Ur0β = A00 + segundo * (A00ϵ4 + A10 + A11);
```

$$-\frac{2\, e^{-i R \Lambda}\, \epsilon^2\, \Lambda\, \text{Cos}[\theta]^2\, \text{Sin}[\theta]^2\, \sqrt{-1+\Lambda^2\, \text{Sin}[\theta]^2}}{3 R \left(\Lambda + 4 \Lambda\, \text{Sin}[\theta]^4 - 4\, \text{Sin}[\theta]^2 \left(\Lambda + i\, \text{Cos}[\theta]\, \sqrt{-1+\Lambda^2\, \text{Sin}[\theta]^2}\right)\right)}$$

```
(*_____________________________________________________________
  _____________________________________________________________ *)
(*                    Ur Summation of all sub-
 components                                                    *)
(*_____________________________________________________________
  _____________________________________________________________ *)
```

```
Clear[Ur, Urtotal]
```

```
Urtotal = -K * ro * Sin[ϕ] / μ * (  Ur0α + Ur0β - (Ur1α + Ur1β) / (R * Sin[Θ])  ) ;
```

```
co1 = Simplify[
  Coefficient[Urtotal, K * ro * ϵ^2 * Sin[ϕ] / μ * Exp[-I * R] / R, 0 ≤ Θ && Θ ≤ π / 2 && 0 ≤ Λ]
co2 = Simplify[Coefficient[Urtotal, K * ro * ϵ^4 * Sin[ϕ] / μ * Exp[-I * R] / R,
    0 ≤ Θ && Θ ≤ π / 2 && 0 ≤ Λ];
co3 = Simplify[Coefficient[Urtotal, K * ro * ϵ^2 * Sin[ϕ] / μ * Exp[-I * Λ * R] / R,
  0 ≤ Θ && Θ ≤ π / 2 && 0 ≤ Λ]
co4 = Simplify[Coefficient[Urtotal, K * ro * ϵ^4 * Sin[ϕ] / μ * Exp[-I * Λ * R] / R,
    0 ≤ Θ && Θ ≤ π / 2 && 0 ≤ Λ];
co5 = Coefficient[Urtotal, K * ro * ϵ^2 * Sin[ϕ] / μ * Exp[-I * Λ * R] / R^2];
co6 = Coefficient[Urtotal, K * ro * ϵ^2 * Sin[ϕ] / μ * Exp[-I * R] / R^2];
```

```
Ur = K * ro * ϵ^2 * Sin[ϕ] / μ * Exp[-I * R] / R * co1  + K * ro * ϵ^4 * Sin[ϕ] / μ * Exp[-I * R] / R * co2 +
    K * ro * ϵ^2 * Sin[ϕ] / μ * Exp[-I * Λ * R] / R * co3 +
    K * ro * ϵ^4 * Sin[ϕ] / μ * Exp[-I * Λ * R] / R * co4 + K * ro * ϵ^2 * Sin[ϕ] / μ *
     Exp[-I * Λ * R] / R^2 * co5 + K * ro * ϵ^2 * Sin[ϕ] / μ * Exp[-I * R] / R^2 * co6;
```

$$-\frac{\mathrm{i}\,\mathrm{Cos}[\Theta]\,\left(-1+\Lambda^2+\mathrm{Cos}[2\,\Theta]\right)\,\mathrm{Sin}[\Theta]^2}{3\left(\Lambda^4+4\,\mathrm{Sin}[\Theta]^4-4\,\mathrm{Sin}[\Theta]^2\left(\Lambda^2+\mathrm{i}\,\mathrm{Cos}[\Theta]\,\sqrt{-\Lambda^2+\mathrm{Sin}[\Theta]^2}\right)\right)}$$

$$\frac{2\,\Lambda\,\mathrm{Cos}[\Theta]^2\,\mathrm{Sin}[\Theta]^2\,\sqrt{-1+\Lambda^2\,\mathrm{Sin}[\Theta]^2}}{3\left(\Lambda+4\,\Lambda\,\mathrm{Sin}[\Theta]^4-4\,\mathrm{Sin}[\Theta]^2\left(\Lambda+\mathrm{i}\,\mathrm{Cos}[\Theta]\,\sqrt{-1+\Lambda^2\,\mathrm{Sin}[\Theta]^2}\right)\right)}$$

```
(* Calculation of Dispalcement
 in the little ϕ direction,
in cylindrical coordinates

  Uϕ= -K*r0*Cos[ϕ]/(r*μ) (Ur1α + Ur1β )

*)
```

```
Uϕtotal = -(Simplify[K * ro * Cos[ϕ] / μ * ( Ur1α / (R * Sin[θ])), 0 ≤ θ && θ ≤ π / 2 && 0 ≤ Λ] +
    Simplify[K * ro * Cos[ϕ] / μ * (Ur1β / (R * Sin[θ])), 0 ≤ θ && θ ≤ π / 2 && 0 ≤ Λ])
```

$$-\frac{\left(\frac{1}{3}+\frac{i}{3}\right)(-1)^{3/4}\, e^{-i R}\, K\, ro\, \epsilon^2\, \text{Cos}[\theta]\, (-1+\Lambda^2+\text{Cos}[2\theta])\, \text{Cos}[\phi]}{\sqrt{2}\, R^2\, \mu\left(\Lambda^4+4\,\text{Sin}[\theta]^4-4\,\text{Sin}[\theta]^2\left(\Lambda^2+i\,\text{Cos}[\theta]\sqrt{-\Lambda^2+\text{Sin}[\theta]^2}\right)\right)}+$$

$$\frac{2\,i\, e^{-i R \Lambda}\, K\, ro\, \epsilon^2\, \text{Cos}[\theta]^2\, \text{Cos}[\phi]\sqrt{-1+\Lambda^2\,\text{Sin}[\theta]^2}}{3\, R^2\, \mu\left(\Lambda+4\,\Lambda\,\text{Sin}[\theta]^4-4\,\text{Sin}[\theta]^2\left(\Lambda+i\,\text{Cos}[\theta]\sqrt{-1+\Lambda^2\,\text{Sin}[\theta]^2}\right)\right)}$$

```
(* Calculation of Dispalcement
 in the little z direction,
in cylindrical coordinates
  Uz= K*r0*Sin[ϕ]/μ (Uz1α + Uz1β)    *)

(*_____________________________________
  ____________________________________  *)
(*                J1α                  *)
(*_____________________________________
  ____________________________________  *)

Clear[R, θ, Λ, z, z1, F, EE, a00, a10, a11, m, segundo, gH, τ, IgH, ddgH, gH2, gL, H00,
  H10, H11, L00, IH00, IH10, IH11, IL00, A00, temp1, A00ϵ4, A10, A11, B00, Uz1α];

z = -m*Sin[θ] + I*τ^2*Sin[θ] + τ*Cos[θ]*Sqrt[τ^2 + 2*I*m];
z1 = Simplify[D[z, τ]];
F = (Λ^2 - 2*z^2)^2 - 4*z^2*Sqrt[(z^2 - 1)]*Sqrt[(z^2 - Λ^2)];
EE = (Λ^2 - 2*z^2)*Sqrt[z^2 - 1]*(Sin[ϵ*z] - ϵ*z*Cos[ϵ*z]) / (ϵ*z^3*F);

a00 = Exp[-I*Pi/4] Gamma[1/2] / Sqrt[2*Pi];
a10 = Exp[-I*Pi/4]*Gamma[3/2] / (2*Sqrt[2*Pi] );
a11 = 4*Exp[-3*I*Pi/4]*Gamma[1/2] / (2^5*Sqrt[2*Pi] );

m = 1;
segundo = 1;
gH = z^(3/2 - 0)*EE*z1;   (* for j=0 *)
IgH = z^(3/2 - 1)*EE*z1;   (* for j=1 *)
gH2 = Normal[Series[gH, {ϵ, 0, 2}]];
ddgH = D[D[gH2, τ], τ];

gL = z^(3/2 - 1)*EE*z1;   (* for j=1 *)

τ = 0;

H00 = (1/Sin[θ]^(1/2))*gH;
H10 = (1/Sin[θ]^(1/2))*ddgH;
H11 = (1/Sin[θ]^(3/2))*IgH;

L00 = (1/Sin[θ]^(3/2))*gL;

IH00 = -I*Exp[-I*m*R]*a00*H00/R;
IH10 = -I*Exp[-I*m*R]*a10*H10/(R^2);
IH11 = -I*Exp[-I*m*R]*a11*H11/(R^2);

IL00 = Exp[-I*m*R]*a00*L00/(2*R^2);

A00 = Simplify[Normal[Series[IH00, {ϵ, 0, 2}]], 0 ≤ θ && θ ≤ π/2 && 0 ≤ Λ]

temp1 = segundo*Coefficient[Normal[Series[IH00, {ϵ, 0, 4}]], ϵ^4];
A00ϵ4 = segundo*Simplify[temp1*ϵ^4, 0 ≤ θ && θ ≤ π/2 && 0 ≤ Λ];

A10 = segundo*IH10;
A11 = segundo*Simplify[Normal[Series[IH11, {ϵ, 0, 2}]], 0 ≤ θ && θ ≤ π/2 && 0 ≤ Λ];

B00 = segundo*Simplify[Normal[Series[IL00, {ϵ, 0, 2}]], 0 ≤ θ && θ ≤ π/2 && 0 ≤ Λ];

Uz1α = A00 + segundo*(A00ϵ4 + A10 + A11 + B00);
```

$$-\frac{\left(\frac{1}{3}-\frac{i}{3}\right)(-1)^{3/4}\,e^{-i\,R}\,\epsilon^2\,\text{Cos}[\theta]^2\,(-1+\Lambda^2+\text{Cos}[2\theta])\,\text{Sin}[\theta]}{\sqrt{2}\,R\left(\Lambda^4+4\,\text{Sin}[\theta]^4-4\,\text{Sin}[\theta]^2\left(\Lambda^2+i\,\text{Cos}[\theta]\sqrt{-\Lambda^2+\text{Sin}[\theta]^2}\right)\right)}$$

```
(*_____*)
(*          J1β          *)
(*_____*)

Clear[R, θ, Λ, z, z1, F, EE, a00, a10, a11, m, segundo, gH, τ, IgH, ddgH, gH2, gL, H00,
   H10, H11, L00, IH00, IH10, IH11, IL00, A00, temp1, A00ϵ4, A10, A11, B00, Uz1β];

z = -m * Sin[θ] + I * τ^2 * Sin[θ] + τ * Cos[θ] * Sqrt[τ^2 + 2 * I * m];
z1 = Simplify[D[z, τ]];
F = (Λ^2 - 2 * z^2)^2 - 4 * z^2 * Sqrt[(z^2 - 1)] * Sqrt[(z^2 - Λ^2)];
EE = 2 * Sqrt[z^2 - 1] * (Sin[ϵ * z] - ϵ * z * Cos[ϵ * z]) / (ϵ * z * F);

a00 = Exp[-I * Pi / 4] Gamma[1 / 2] / Sqrt[2 * Pi];
a10 = Exp[-I * Pi / 4] * Gamma[3 / 2] / (2 * Sqrt[2 * Pi] );
a11 = 4 * Exp[-3 * I * Pi / 4] * Gamma[1 / 2] / (2^5 * Sqrt[2 * Pi] );

m = Λ;
segundo = 1;
gH = z^(3 / 2 - 0) * EE * z1;   (* for j=0 *)
IgH = z^(3 / 2 - 1) * EE * z1;   (* for j=1 *)
gH2 = Normal[Series[gH, {ϵ, 0, 2}]];
ddgH = D[D[gH2, τ], τ];

gL = z^(3 / 2 - 1) * EE * z1;   (* for j=1 *)

τ = 0;

H00 = (1 / Sin[θ]^(1 / 2)) * gH;
H10 = (1 / Sin[θ]^(1 / 2)) * ddgH;
H11 = (1 / Sin[θ]^(3 / 2)) * IgH;

L00 = (1 / Sin[θ]^(3 / 2)) * gL;

IH00 = -I * Exp[-I * m * R] * a00 * H00 / R;
IH10 = -I * Exp[-I * m * R] * a10 * H10 / ( R^2);
IH11 = -I * Exp[-I * m * R] * a11 * H11 / ( R^2);

IL00 = Exp[-I * m * R] * a00 * L00 / (2 * R^2);

A00 = Simplify[Normal[Series[IH00, {ϵ, 0, 2}]], 0 ≤ θ && θ ≤ π / 2 && 0 ≤ Λ]

temp1 = segundo * Coefficient[Normal[Series[IH00, {ϵ, 0, 4}]], ϵ^4];
A00ϵ4 = segundo * Simplify[temp1 * ϵ^4, 0 ≤ θ && θ ≤ π / 2 && 0 ≤ Λ];

A10 = segundo * IH10;
A11 = segundo * Simplify[Normal[Series[IH11, {ϵ, 0, 2}]], 0 ≤ θ && θ ≤ π / 2 && 0 ≤ Λ];

B00 = segundo * Simplify[Normal[Series[IL00, {ϵ, 0, 2}]], 0 ≤ θ && θ ≤ π / 2 && 0 ≤ Λ];

Uz1β = A00 + segundo * (A00ϵ4 + A10 + A11 + B00);
```

$$-\frac{2\, e^{-i R \Lambda}\, \epsilon^2\, \Lambda \cos[\theta] \sin[\theta]^3 \sqrt{-1 + \Lambda^2 \sin[\theta]^2}}{3 R \left(\Lambda + 4 \Lambda \sin[\theta]^4 - 4 \sin[\theta]^2 \left(\Lambda + i \cos[\theta] \sqrt{-1 + \Lambda^2 \sin[\theta]^2}\right)\right)}$$

```
(*_____________________________________________________________
  _____________________________________________________________ *)
(*                    Uz Summation of all sub-components                    *)
(*_____________________________________________________________
  _____________________________________________________________ *)

Clear[co1, co2, co3, co4, co5, co6, Uz]

Uztotal = K * ro * Sin[ϕ] / μ * ( Uz1α + Uz1β );

co1 = Simplify[
  Coefficient[Uztotal, K * ro * ϵ^2 * Sin[ϕ] / μ * Exp[-I * R] / R], 0 ≤ θ && θ ≤ π / 2 && 0 ≤ Λ]
co2 = Simplify[Coefficient[Uztotal, K * ro * ϵ^4 * Sin[ϕ] / μ * Exp[-I * R] / R],
  0 ≤ θ && θ ≤ π / 2 && 0 ≤ Λ]
co3 = Simplify[Coefficient[Uztotal, K * ro * ϵ^2 * Sin[ϕ] / μ * Exp[-I * Λ * R] / R],
  0 ≤ θ && θ ≤ π / 2 && 0 ≤ Λ]
co4 = Simplify[Coefficient[Uztotal, K * ro * ϵ^4 * Sin[ϕ] / μ * Exp[-I * Λ * R] / R],
  0 ≤ θ && θ ≤ π / 2 && 0 ≤ Λ]
co5 = Coefficient[Uztotal, K * ro * ϵ^2 * Sin[ϕ] / μ * Exp[-I * Λ * R] / R^2];
co6 = Coefficient[Uztotal, K * ro * ϵ^2 * Sin[ϕ] / μ * Exp[-I * R] / R^2];

Uz = K * ro * ϵ^2 * Sin[ϕ] / μ * Exp[-I * R] / R * co1 + K * ro * ϵ^4 * Sin[ϕ] / μ * Exp[-I * R] / R * co2 +
   K * ro * ϵ^2 * Sin[ϕ] / μ * Exp[-I * Λ * R] / R * co3 +
   K * ro * ϵ^4 * Sin[ϕ] / μ * Exp[-I * Λ * R] / R * co4 + K * ro * ϵ^2 * Sin[ϕ] / μ *
    Exp[-I * Λ * R] / R^2 * co5 + K * ro * ϵ^2 * Sin[ϕ] / μ * Exp[-I * R] / R^2 * co6;
```

$$-\frac{i \cos[\theta]^2 \left(-1+\Lambda^2+\cos[2\theta]\right) \sin[\theta]}{3\left(\Lambda^4+4\sin[\theta]^4-4\sin[\theta]^2\left(\Lambda^2+i\cos[\theta]\sqrt{-\Lambda^2+\sin[\theta]^2}\right)\right)}$$

$$\frac{i \cos[\theta]^2 \left(-1+\Lambda^2+\cos[2\theta]\right) \sin[\theta]^3}{30\left(\Lambda^4+4\sin[\theta]^4-4\sin[\theta]^2\left(\Lambda^2+i\cos[\theta]\sqrt{-\Lambda^2+\sin[\theta]^2}\right)\right)}$$

$$-\frac{2\Lambda \cos[\theta] \sin[\theta]^3 \sqrt{-1+\Lambda^2\sin[\theta]^2}}{3\left(\Lambda+4\Lambda\sin[\theta]^4-4\sin[\theta]^2\left(\Lambda+i\cos[\theta]\sqrt{-1+\Lambda^2\sin[\theta]^2}\right)\right)}$$

$$\frac{\Lambda^3 \cos[\theta] \sin[\theta]^5 \sqrt{-1+\Lambda^2\sin[\theta]^2}}{15\left(\Lambda+4\Lambda\sin[\theta]^4-4\sin[\theta]^2\left(\Lambda+i\cos[\theta]\sqrt{-1+\Lambda^2\sin[\theta]^2}\right)\right)}$$

```
(*    TRANSFORMATION
 FROM CYLINDRICAL TO
 SPHERICAL COORDINATES    *)
```

```
Clear[UR, Uθ, co1, co2, co3, co4, co5, co6, URtotal, Uθtotal]

URtotal = Ur * Sin[θ] + Uz * Cos[θ];
co1 = Simplify[
  Coefficient[URtotal, K * ro * ϵ^2 * Sin[ϕ] / μ * Exp[-I * R] / R], 0 ≤ θ && θ ≤ π / 2 && 0 ≤ Λ]
co2 = Simplify[Coefficient[URtotal, K * ro * ϵ^4 * Sin[ϕ] / μ * Exp[-I * R] / R],
  0 ≤ θ && θ ≤ π / 2 && 0 ≤ Λ]
co3 = Simplify[Coefficient[URtotal, K * ro * ϵ^2 * Sin[ϕ] / μ * Exp[-I * Λ * R] / R],
  0 ≤ θ && θ ≤ π / 2 && 0 ≤ Λ]
co4 = Simplify[Coefficient[URtotal, K * ro * ϵ^4 * Sin[ϕ] / μ * Exp[-I * Λ * R] / R],
  0 ≤ θ && θ ≤ π / 2 && 0 ≤ Λ]
co5 = Coefficient[URtotal, K * ro * ϵ^2 * Sin[ϕ] / μ * Exp[-I * Λ * R] / R^2];
co6 = Coefficient[URtotal, K * ro * ϵ^2 * Sin[ϕ] / μ * Exp[-I * R] / R^2];

UR = K * ro * ϵ^2 * Sin[ϕ] / μ * Exp[-I * R] / R * co1 + K * ro * ϵ^4 * Sin[ϕ] / μ * Exp[-I * R] / R * co2 +
   K * ro * ϵ^2 * Sin[ϕ] / μ * Exp[-I * Λ * R] / R * co3 +
   K * ro * ϵ^4 * Sin[ϕ] / μ * Exp[-I * Λ * R] / R * co4 + K * ro * ϵ^2 * Sin[ϕ] / μ *
    Exp[-I * Λ * R] / R^2 * co5 + K * ro * ϵ^2 * Sin[ϕ] / μ * Exp[-I * R] / R^2 * co6;

Uθtotal = Ur * Cos[θ] - Uz * Sin[θ];
co1 = Simplify[
  Coefficient[Uθtotal, K * ro * ϵ^2 * Sin[ϕ] / μ * Exp[-I * R] / R], 0 ≤ θ && θ ≤ π / 2 && 0 ≤ Λ]
co2 = Simplify[Coefficient[Uθtotal, K * ro * ϵ^4 * Sin[ϕ] / μ * Exp[-I * R] / R],
  0 ≤ θ && θ ≤ π / 2 && 0 ≤ Λ]
co3 = Simplify[Coefficient[Uθtotal, K * ro * ϵ^2 * Sin[ϕ] / μ * Exp[-I * Λ * R] / R],
  0 ≤ θ && θ ≤ π / 2 && 0 ≤ Λ]
co4 = Simplify[Coefficient[Uθtotal, K * ro * ϵ^4 * Sin[ϕ] / μ * Exp[-I * Λ * R] / R],
  0 ≤ θ && θ ≤ π / 2 && 0 ≤ Λ]
co5 = Coefficient[Uθtotal, K * ro * ϵ^2 * Sin[ϕ] / μ * Exp[-I * Λ * R] / R^2];
co6 = Coefficient[Uθtotal, K * ro * ϵ^2 * Sin[ϕ] / μ * Exp[-I * R] / R^2];

Uθ = K * ro * ϵ^2 * Sin[ϕ] / μ * Exp[-I * R] / R * co1 + K * ro * ϵ^4 * Sin[ϕ] / μ * Exp[-I * R] / R * co2 +
   K * ro * ϵ^2 * Sin[ϕ] / μ * Exp[-I * Λ * R] / R * co3 +
   K * ro * ϵ^4 * Sin[ϕ] / μ * Exp[-I * Λ * R] / R * co4 + K * ro * ϵ^2 * Sin[ϕ] / μ *
    Exp[-I * Λ * R] / R^2 * co5 + K * ro * ϵ^2 * Sin[ϕ] / μ * Exp[-I * R] / R^2 * co6;
```

$$-\frac{i\,(-1+\Lambda^2+\cos[2\theta])\,\sin[2\theta]}{6\left(\Lambda^4+4\sin[\theta]^4-4\sin[\theta]^2\left(\Lambda^2+i\cos[\theta]\sqrt{-\Lambda^2+\sin[\theta]^2}\right)\right)}$$

$$\frac{i\cos[\theta]\,(-1+\Lambda^2+\cos[2\theta])\,\sin[\theta]^3}{30\left(\Lambda^4+4\sin[\theta]^4-4\sin[\theta]^2\left(\Lambda^2+i\cos[\theta]\sqrt{-\Lambda^2+\sin[\theta]^2}\right)\right)}$$

0

0

0

0

$$\frac{\sqrt{2}\ \Lambda\ \text{Cos}[\theta]\ \sqrt{-2+\Lambda^2-\Lambda^2\ \text{Cos}[2\,\theta]}\ \text{Sin}[\theta]^2}{3\ \left(\Lambda+4\,\Lambda\,\text{Sin}[\theta]^4-4\,\text{Sin}[\theta]^2\ \left(\Lambda+\text{i}\ \text{Cos}[\theta]\ \sqrt{-1+\Lambda^2\ \text{Sin}[\theta]^2}\right)\right)}$$

$$-\frac{\Lambda^3\ \text{Cos}[\theta]\ \text{Sin}[\theta]^4\ \sqrt{-1+\Lambda^2\ \text{Sin}[\theta]^2}}{15\ \left(\Lambda+4\,\Lambda\,\text{Sin}[\theta]^4-4\,\text{Sin}[\theta]^2\ \left(\Lambda+\text{i}\ \text{Cos}[\theta]\ \sqrt{-1+\Lambda^2\ \text{Sin}[\theta]^2}\right)\right)}$$

E.4 Integration of Total Displacement Field

The following code is simpler to understand than the previous ones, and as a result, I will not provide such detailed step-by step analysis. Instead a summary list is provided.

- The velocity fields for each of the four cases discussed in Sections 3.2 to 3.5, and are numbered 1 to 4 in order of presentation.

  For the Rayleigh waves, certain repeating variables are written first so as to simplify the presentation.

  The Rayleigh waves are also presented in spherical coordinates, however this description of them is not used as the integrals are small as mentioned in Section 3.7.

- After the velocity fields are completed, a section is presented where all the necessary constants and variables are defined. Then, each of the 11 integrals given in Equation 3.83 are solved.

  Each integral contains certain lines of code, the last of which corresponds to the numerical solution to the integral being solved.

  The lines given prior to the last line, correspond to the different terms and cross-terms that contribute to the integral from the appropriate P, S, and Rayleigh waves.

- This last step is repeated 3 more times, to complete the calculations for the two velocity models and the two shaking directions.

```
Clear[VR1, VR2, VR3α, VR4α, VR3β, VR4β, Vϕ1, Vϕ2, Vϕ3, Vϕ4, Vθ1, Vθ2, Vθ3α, Vθ4α,
 Vθ3β, Vθ4β, Vr3α, Vr4α, Vr3β, Vr4β, Vz3α, Vz4α, Vz3β, Vz4β, K, P, M, ro, ϵ, R,
 z, r, ϕ, Λ, μ, ΛRS, ΛRP, ω, Vp, Vs, VR, t, z, F, VR1, Vθ1, Vϕ1, V2, α, α1, β, β1]


(* Note:  Vr1 => V=Velocity,  r=Direction,  *)
(* 1=Order that corresponds to presentation in text of Chapter 3.  ie, *)
(* 1=Body Waves from a Shearing Motion *)


(* Velocity Field for Body Waves from a Shearing Motion *)

VR1 = (P * ω / (2 * π * μ)) * ( √(Λ^2 - Sin[θ]^2) * Sin[2 θ] / (Λ^4 + 4 Sin[θ]^4 - 4 Sin[θ]^2 (Λ^2 + i Cos[θ] √(-Λ^2 + Sin[θ]^2))) );

Vθ1 = (P * ω / (2 * π * μ)) * ( Λ (1 - 2 * Sin[θ]^2) * Cos[θ] / (Λ + 4 Λ Sin[θ]^4 - 4 Sin[θ]^2 (Λ + i Cos[θ] √(-1 + Λ^2 Sin[θ]^2))) );

Vϕ1 = (P * ω / (2 * π * μ));


(* Velocity Field for Body Waves from a Rocking Motion *)

VR2 = (M * ω / (2 * π * μ)) * ( i (-1 + Λ^2 + Cos[2 θ]) Sin[2 θ] / (2 (Λ^4 + 4 Sin[θ]^4 - 4 Sin[θ]^2 (Λ^2 + i Cos[θ] √(-Λ^2 + Sin[θ]^2)))) );

Vθ2 = (-M * ω / (2 * π * μ)) * ( √2 Λ Cos[θ] √(-2 + Λ^2 - Λ^2 Cos[2 θ]) Sin[θ]^2 / (Λ + 4 Λ Sin[θ]^4 - 4 Sin[θ]^2 (Λ + i Cos[θ] √(-1 + Λ^2 Sin[θ]^2))) );

Vϕ2 = 0;
```

```
(* Variables for Rayleigh Waves *)

F1 = 2 * (ΛRS^2 - 2 + Sqrt[1 - ΛRS^2] * Sqrt[1 - ΛRP^2]) + Sqrt[1 - ΛRP^2] / Sqrt[1 - ΛRS^2] +
   Sqrt[1 - ΛRS^2] / Sqrt[1 - ΛRP^2];          (* where, F1 = Derivative of F (k0) *)
A1 = ω^(7 / 2) / (Sqrt[2 * π] * VR^(7 / 2)) * (-2 * Sqrt[1 - ΛRS^2]);
B1 = ω^(7 / 2) / (Sqrt[2 * π] * VR^(7 / 2)) * (2 - ΛRS^2) * Sqrt[1 - ΛRS^2];
C1 = ω^(7 / 2) / (Sqrt[2 * π] * VR^(7 / 2)) * (-2 * Sqrt[1 - ΛRS^2] * Sqrt[1 - ΛRP^2]);
D1 = ω^(7 / 2) / (Sqrt[2 * π] * VR^(7 / 2)) * (2 - ΛRS^2);
A2 = -ω / VR * D1;
B2 = -ω / VR * C1;
C2 = ω^(9 / 2) / (Sqrt[2 * π] * VR^(9 / 2)) * (ΛRS^2 - 2) * Sqrt[1 - ΛRP^2];
D2 = ω^(9 / 2) / (Sqrt[2 * π] * VR^(9 / 2)) * 2 * Sqrt[1 - ΛRP^2];


(* Velocity Field for Surface Waves from a Shearing Motion *)
(* Note that the α and the β in the component subscript describes which *)
(* the term for each exponent being computed , i.e., e^(-αz) or e^(-βz)*)

Vr3α = (P * ω / (μ * F1)) * (A1);       (* Cylindrical Coordinates *)
Vr3β = (P * ω / (μ * F1)) * (B1);


Vϕ3 = 0;

Vz3α = (P * ω / (μ * F1)) * (C1);       (* Cylindrical Coordinates *)
Vz3β = (P * ω / (μ * F1)) * (D1);


VR3α = Simplify[(1 / Sqrt[Sin[θ]]) * (Vr3α * Sin[θ] + Vz3α * Cos[θ]),
   0 ≤ θ && θ ≤ π / 2 && 0 ≤ Λ];       (* Shperical Coordinates *)
Vθ3α = Simplify[(1 / Sqrt[Sin[θ]]) * (Vr3α * Cos[θ] - Vz3α * Sin[θ]), 0 ≤ θ && θ ≤ π / 2 && 0 ≤ Λ];
VR3β = Simplify[(1 / Sqrt[Sin[θ]]) * (Vr3β * Sin[θ] + Vz3β * Cos[θ]), 0 ≤ θ && θ ≤ π / 2 && 0 ≤ Λ];
Vθ3β = Simplify[(1 / Sqrt[Sin[θ]]) * (Vr3β * Cos[θ] - Vz3β * Sin[θ]), 0 ≤ θ && θ ≤ π / 2 && 0 ≤ Λ];


(* Velocity Field for Surface Waves from a Rocking Motion *)

Vr4α = (M * ω / (μ * F1)) * (A2);       (* Cylindrical Coordinates *)
Vr4β = (M * ω / (μ * F1)) * (B2);

Vϕ4 = 0;

Vz4α = (M * ω / (μ * F1)) * (C2);       (* Cylindrical Coordinates *)
Vz4β = (M * ω / (μ * F1)) * (D2);


VR4α = Simplify[(1 / Sqrt[Sin[θ]]) * (Vr4α * Sin[θ] + Vz4α * Cos[θ]),
   0 ≤ θ && θ ≤ π / 2 && 0 ≤ Λ];       (* Shperical Coordinates *)
Vθ4α = Simplify[(1 / Sqrt[Sin[θ]]) * (Vr4α * Cos[θ] - Vz4α * Sin[θ]), 0 ≤ θ && θ ≤ π / 2 && 0 ≤ Λ];
VR4β = Simplify[(1 / Sqrt[Sin[θ]]) * (Vr4β * Sin[θ] + Vz4β * Cos[θ]), 0 ≤ θ && θ ≤ π / 2 && 0 ≤ Λ];
Vθ4β = Simplify[(1 / Sqrt[Sin[θ]]) * (Vr4β * Cos[θ] - Vz4β * Sin[θ]), 0 ≤ θ && θ ≤ π / 2 && 0 ≤ Λ];
```

```
(* Estimate Radiated Energy for an EW shake *)
Clear [M, P]

M = 5370000;
P = 166000;
ρ = 1907;
f = 1.12;
ω = 2 * Pi * f;
VP = 710;
VS = 376;
VR = .9282 * VS;
Δ = VP / VS;
ΔRP = VR / VP;
ΔRS = VR / VS;
α = (I * ω / VP) * Sqrt[1 - Sin[θ]^2];
β = (I * ω / VS) * Sqrt[1 - Sin[θ]^2];
α1 = (ω / VR) * Sqrt[1 - ΔRP^2];
β1 = (ω / VR) * Sqrt[1 - ΔRS^2];
θP = ArcSin[VR / VP];
θS = ArcSin[VR / VS];
μ = ρ * VS^2;
T = 1 / f;
n = 50;


(* Solution to First Integral in Equation 3.83 *)
Clear[A1A, A1B, A1C, E1]

A1A = NIntegrate[Abs[VR1^2] * Sin[θ], {θ, 0, θP}]
A1B = NIntegrate[Abs[VR2^2] * Sin[θ], {θ, 0, θP}]
A1C = NIntegrate[Abs[VR1 * VR2] * Sin[θ], {θ, 0, θP}]
E1 = VP * (A1A + A1B + A1C)
```

6.42828×10^{-10}

5.19349×10^{-7}

1.82652×10^{-8}

0.000382163

```
(* Solution to Second Integral in Equation 3.83 *)
Clear[A2A, A2B, A2C, E2]

A2A = NIntegrate[Abs[VR1^2], {θ, θP, Pi / 2}]
A2B = NIntegrate[Abs[VR2^2], {θ, θP, Pi / 2}]
A2C = NIntegrate[Abs[VR1 * VR2], {θ, θP, Pi / 2}]
E2 = VR * (A2A + A2B + A2C)
```

1.61893×10^{-8}

7.21637×10^{-6}

3.3787×10^{-7}

0.00264211

```
(* Solution to Third Integral in Equation 3.83 *)
Clear[A3A, A3B, A3C, E3]

A3A = NIntegrate[Abs[VR1^2] * Sin[θ], {θ, θP, Pi / 2}]
A3B = NIntegrate[Abs[VR2^2] * Sin[θ], {θ, θP, Pi / 2}]
A3C = NIntegrate[Abs[VR1 * VR2] * Sin[θ], {θ, θP, Pi / 2}]
E3 = VP * (A3A + A3B + A3C)
```

1.31913×10^{-8}

5.58372×10^{-6}

2.68404×10^{-7}

0.00416437

```
(* Solution to Fourth Integral in Equation 3.83 *)
Clear[A4A, A4B, A4C, E4]

A4A = NIntegrate[Abs[VR1^2], {θ, θP, Pi / 2}]
A4B = NIntegrate[Abs[VR2^2], {θ, θP, Pi / 2}]
A4C = NIntegrate[Abs[VR1 * VR2], {θ, θP, Pi / 2}]
E4 = VR * (A4A + A4B + A4C)
```

1.61893×10^{-8}

7.21637×10^{-6}

3.3787×10^{-7}

0.00264211

```
(* Solution to Fifth Integral in Equation 3.83 *)
Clear[A5A, E5]

A5A = NIntegrate[(1 / (2 * α1)) * (Vr3α + Vr4α + Vz3α + Vz4α)^2 *
    Exp[-2 * α1 * Sqrt[(VP * n * T)^2 - r^2]], {r, 0, VR * n * T}]
E5 = A5A / (n * T)
```

```
NIntegrate::ploss :
 Numerical integration stopping due to loss of precision. Achieved neither the requested PrecisionGoal nor
   AccuracyGoal; suspect one of the following: highly oscillatory integrand or the true value of the
   integral is 0. If your integrand is oscillatory try using the option Method->Oscillatory in NIntegrate.
```

0.

0.

```
(* Solution to Sixth Integral in Equation 3.83 *)
Clear[A6A, A6B, A6C, E6]

A6A = NIntegrate[Abs[Vθ1^2] * Sin[θ], {θ, 0, θS}]
A6B = NIntegrate[Abs[Vθ2^2] * Sin[θ], {θ, 0, θS}]
A6C = NIntegrate[Abs[Vθ1 * Vθ2] * Sin[θ], {θ, 0, θS}]
E6 = VS * (A6A + A6B + A6C)
```

```
NIntegrate::ncvb : NIntegrate failed to converge to
   prescribed accuracy after 7 recursive bisections in θ near θ = 0.5622461762643494‘.
```

1.21875×10^{-7}

```
NIntegrate::ncvb : NIntegrate failed to converge to
   prescribed accuracy after 7 recursive bisections in θ near θ = 0.5622461762643494‘.
```

0.000199685

```
NIntegrate::ncvb : NIntegrate failed to converge to
   prescribed accuracy after 7 recursive bisections in θ near θ = 0.7852859817245872‘.
```

2.38292×10^{-6}

0.0760234

```
(* Solution to Seventh Integral in Equation 3.83 *)
Clear[A7A, A7B, A7C, E7]

A7A = NIntegrate[Abs[Vθ1^2], {θ, θS, Pi / 2}]
A7B = NIntegrate[Abs[Vθ2^2], {θ, θS, Pi / 2}]
A7C = NIntegrate[Abs[Vθ1 * Vθ2], {θ, θS, Pi / 2}]
E7 = VR * (A7A + A7B + A7C)
```

5.10287×10^{-9}

0.0000584723

5.46142×10^{-7}

0.0205994

```
(* Solution to Eight Integral in Equation 3.83 *)
Clear[A8A, A8B, A8C, E8]

A8A = NIntegrate[Abs[Vθ1^2] * Sin[θ], {θ, θS, Pi / 2}]
A8B = NIntegrate[Abs[Vθ2^2] * Sin[θ], {θ, θS, Pi / 2}]
A8C = NIntegrate[Abs[Vθ1 * Vθ2] * Sin[θ], {θ, θS, Pi / 2}]
E8 = VS * (A8A + A8B + A8C)
```

4.90508×10^{-9}

0.0000561636

5.24776×10^{-7}

0.0213167

```
(* Solution to Ninth Integral in Equation 3.83 *)
Clear[A9A, A9B, A9C, E9]

A9A = NIntegrate[Abs[Vθ1^2], {θ, θS, Pi / 2}]
A9B = NIntegrate[Abs[Vθ2^2], {θ, θS, Pi / 2}]
A9C = NIntegrate[Abs[Vθ1 * Vθ2], {θ, θS, Pi / 2}]
E9 = VR * (A9A + A9B + A9C)
```

5.10287×10^{-9}

0.0000584723

5.46142×10^{-7}

0.0205994

```
(* Solution to Tenth Integral in Equation 3.83 *)
Clear[A10A, E10]

A10A = NIntegrate[(1 / (2 * β1)) * (Vr3β + Vr4β + Vz3β + Vz4β) ^2 *
    Exp[-2 * β1 * Sqrt[(VS * n * T) ^2 - r^2]], {r, 0, VR * n * T}]
E10 = A10A / (n * T)
```

1.0924×10^{-54}

2.44697×10^{-56}

```
(* Solution to Eleventh Integral in Equation 3.83 *)
Clear[A11A, E11]

A11A = NIntegrate[Abs[Vϕ1^2] * Sin[θ], {θ, 0, π / 2}]
E11 = VS * A11A
```

4.75554×10^{-7}

0.000178808

```
(* Total Energy *)
Clear[Etot]

Etot = E1 + E2 + E3 - E4 + E5 + E6 + E7 + E8 - E9 + E10 + E11
```

0.102065

```
(* Estimate Radiated Energy for an NS shake *)

M = 12100000;
P = 384000;
ρ = 1907;
f = 1.64;
ω = 2 * Pi * f;
VP = 710;
VS = 376;
VR = .9282 * VS;
Δ = VP / VS;
ΔRP = VR / VP;
ΔRS = VR / VS;
α = (I * ω / VP) * Sqrt[1 - Sin[θ]^2];
β = (I * ω / VS) * Sqrt[1 - Sin[θ]^2];
α1 = (ω / VR) * Sqrt[1 - ΔRP^2];
β1 = (ω / VR) * Sqrt[1 - ΔRS^2];
θP = ArcSin[VR / VP];
θS = ArcSin[VR / VS];
μ = ρ * VS^2;
T = 1 / f;
n = 50;


(* Solution to First Integral in Equation 3.83 *)
Clear[A1A, A1B, A1C, E1]

A1A = NIntegrate[Abs[VR1^2] * Sin[θ], {θ, 0, θP}]
A1B = NIntegrate[Abs[VR2^2] * Sin[θ], {θ, 0, θP}]
A1C = NIntegrate[Abs[VR1 * VR2] * Sin[θ], {θ, 0, θP}]
E1 = VP * (A1A + A1B + A1C)
```

7.37552×10^{-9}

5.65371×10^{-6}

2.04131×10^{-7}

0.0041643

```
(* Solution to Second Integral in Equation 3.83 *)
Clear[A2A, A2B, A2C, E2]

A2A = NIntegrate[Abs[VR1^2], {θ, θP, Pi / 2}]
A2B = NIntegrate[Abs[VR2^2], {θ, θP, Pi / 2}]
A2C = NIntegrate[Abs[VR1 * VR2], {θ, θP, Pi / 2}]
E2 = VR * (A2A + A2B + A2C)
```

1.85749×10^{-7}

0.0000785584

3.77603×10^{-6}

0.0287998

```
(* Solution to Third Integral in Equation 3.83 *)
Clear[A3A, A3B, A3C, E3]

A3A = NIntegrate[Abs[VR1^2] * Sin[θ], {θ, θP, Pi / 2}]
A3B = NIntegrate[Abs[VR2^2] * Sin[θ], {θ, θP, Pi / 2}]
A3C = NIntegrate[Abs[VR1 * VR2] * Sin[θ], {θ, θP, Pi / 2}]
E3 = VP * (A3A + A3B + A3C)
```

1.51352×10^{-7}

0.0000607852

2.99968×10^{-6}

0.0453947

```
(* Solution to Fourth Integral in Equation 3.83 *)
Clear[A4A, A4B, A4C, E4]

A4A = NIntegrate[Abs[VR1^2], {θ, θP, Pi / 2}]
A4B = NIntegrate[Abs[VR2^2], {θ, θP, Pi / 2}]
A4C = NIntegrate[Abs[VR1 * VR2], {θ, θP, Pi / 2}]
E4 = VR * (A4A + A4B + A4C)
```

1.85749×10^{-7}

0.0000785584

3.77603×10^{-6}

0.0287998

```
(* Solution to Fifth Integral in Equation 3.83 *)
Clear[A5A, E5]

A5A = NIntegrate[(1 / (2 * α1)) * (Vr3α + Vr4α + Vz3α + Vz4α) ^ 2 *
    Exp[-2 * α1 * Sqrt[(VP * n * T) ^ 2 - r^2]], {r, 0, VR * n * T}]
E5 = A5A / (n * T)
```

```
NIntegrate::ploss :
 Numerical integration stopping due to loss of precision. Achieved neither the requested PrecisionGoal nor
   AccuracyGoal; suspect one of the following: highly oscillatory integrand or the true value of the
   integral is 0. If your integrand is oscillatory try using the option Method->Oscillatory in NIntegrate.
```

0.

0.

```
(* Solution to Sixth Integral in Equation 3.83 *)
Clear[A6A, A6B, A6C, E6]

A6A = NIntegrate[Abs[Vθ1^2] * Sin[θ], {θ, 0, θS}]
A6B = NIntegrate[Abs[Vθ2^2] * Sin[θ], {θ, 0, θS}]
A6C = NIntegrate[Abs[Vθ1 * Vθ2] * Sin[θ], {θ, 0, θS}]
E6 = VS * (A6A + A6B + A6C)
```

```
NIntegrate::ncvb : NIntegrate failed to converge to
   prescribed accuracy after 7 recursive bisections in θ near θ = 0.5622461762643494‘.
```

1.39834×10^{-6}

```
NIntegrate::ncvb : NIntegrate failed to converge to
   prescribed accuracy after 7 recursive bisections in θ near θ = 0.5622461762643494‘.
```

0.0021738

```
NIntegrate::ncvb : NIntegrate failed to converge to
   prescribed accuracy after 7 recursive bisections in θ near θ = 0.7852859817245872‘.
```

0.0000266314

0.827888

```
(* Solution to Seventh Integral in Equation 3.83 *)
Clear[A7A, A7B, A7C, E7]

A7A = NIntegrate[Abs[Vθ1^2], {θ, θS, Pi / 2}]
A7B = NIntegrate[Abs[Vθ2^2], {θ, θS, Pi / 2}]
A7C = NIntegrate[Abs[Vθ1 * Vθ2], {θ, θS, Pi / 2}]
E7 = VR * (A7A + A7B + A7C)
```

5.85481×10^{-8}

0.000636537

6.10368×10^{-6}

0.224304

```
(* Solution to Eight Integral in Equation 3.83 *)
Clear[A8A, A8B, A8C, E8]

A8A = NIntegrate[Abs[Vθ1^2] * Sin[θ], {θ, θS, Pi / 2}]
A8B = NIntegrate[Abs[Vθ2^2] * Sin[θ], {θ, θS, Pi / 2}]
A8C = NIntegrate[Abs[Vθ1 * Vθ2] * Sin[θ], {θ, θS, Pi / 2}]
E8 = VS * (A8A + A8B + A8C)
```

5.62787×10^{-8}

0.000611404

5.86489×10^{-6}

0.232114

```
(* Solution to Ninth Integral in Equation 3.83 *)
Clear[A9A, A9B, A9C, E9]

A9A = NIntegrate[Abs[Vθ1^2], {θ, θS, Pi / 2}]
A9B = NIntegrate[Abs[Vθ2^2], {θ, θS, Pi / 2}]
A9C = NIntegrate[Abs[Vθ1 * Vθ2], {θ, θS, Pi / 2}]
E9 = VR * (A9A + A9B + A9C)
```

5.85481×10^{-8}

0.000636537

6.10368×10^{-6}

0.224304

```
(* Solution to Tenth Integral in Equation 3.83 *)
Clear[A10A, E10]

A10A = NIntegrate[(1 / (2 * β1)) * (Vr3β + Vr4β + Vz3β + Vz4β) ^2 *
   Exp[-2 * β1 * Sqrt[(VS * n * T) ^2 - r^2]], {r, 0, VR * n * T}]
E10 = A10A / (n * T)
```

1.24131×10^{-52}

4.0715×10^{-54}

```
(* Solution to Eleventh Integral in Equation 3.83 *)
Clear[A11A, E11]

A11A = NIntegrate[Abs[Vϕ1^2] * Sin[θ], {θ, 0, π / 2}]
E11 = VS * A11A
```

5.45629×10^{-6}

0.00205156

```
(* Total Energy *)
Clear[Etot]

Etot = E1 + E2 + E3 - E4 + E5 + E6 + E7 + E8 - E9 + E10 + E11
```

1.11161

```
(* Estimate Radiated Energy for an EW shake *)
Clear [M, P]

M = 5370000;
P = 166000;
ρ = 1850;
f = 1.12;
ω = 2 * Pi * f;
VP = 597;
VS = 316;
VR = .9282 * VS;
Δ = VP / VS;
ΔRP = VR / VP;
ΔRS = VR / VS;
α = (I * ω / VP) * Sqrt[1 - Sin[θ]^2];
β = (I * ω / VS) * Sqrt[1 - Sin[θ]^2];
α1 = (ω / VR) * Sqrt[1 - ΔRP^2];
β1 = (ω / VR) * Sqrt[1 - ΔRS^2];
θP = ArcSin[VR / VP];
θS = ArcSin[VR / VS];
μ = ρ * VS^2;
T = 1 / f;
n = 50;


(* Solution to First Integral in Equation 3.83 *)
Clear[A1A, A1B, A1C, E1]

A1A = NIntegrate[Abs[VR1^2] * Sin[θ], {θ, 0, θP}]
A1B = NIntegrate[Abs[VR2^2] * Sin[θ], {θ, 0, θP}]
A1C = NIntegrate[Abs[VR1 * VR2] * Sin[θ], {θ, 0, θP}]
E1 = VP * (A1A + A1B + A1C)
```

1.36223×10^{-9}

1.10199×10^{-6}

3.87313×10^{-8}

0.000681827

```
(* Solution to Second Integral in Equation 3.83 *)
Clear[A2A, A2B, A2C, E2]

A2A = NIntegrate[Abs[VR1^2], {θ, θP, Pi / 2}]
A2B = NIntegrate[Abs[VR2^2], {θ, θP, Pi / 2}]
A2C = NIntegrate[Abs[VR1 * VR2], {θ, θP, Pi / 2}]
E2 = VR * (A2A + A2B + A2C)
```

3.43601×10^{-8}

0.0000153501

7.17919×10^{-7}

0.00472302

```
(* Solution to Third Integral in Equation 3.83 *)
Clear[A3A, A3B, A3C, E3]

A3A = NIntegrate[Abs[VR1^2] * Sin[θ], {θ, θP, Pi / 2}]
A3B = NIntegrate[Abs[VR2^2] * Sin[θ], {θ, θP, Pi / 2}]
A3C = NIntegrate[Abs[VR1 * VR2] * Sin[θ], {θ, θP, Pi / 2}]
E3 = VP * (A3A + A3B + A3C)
```

2.79929×10^{-8}

0.0000118762

5.70244×10^{-7}

0.00744721

```
(* Solution to Fourth Integral in Equation 3.83 *)
Clear[A4A, A4B, A4C, E4]

A4A = NIntegrate[Abs[VR1^2], {θ, θP, Pi / 2}]
A4B = NIntegrate[Abs[VR2^2], {θ, θP, Pi / 2}]
A4C = NIntegrate[Abs[VR1 * VR2], {θ, θP, Pi / 2}]
E4 = VR * (A4A + A4B + A4C)
```

3.43601×10^{-8}

0.0000153501

7.17919×10^{-7}

0.00472302

```
(* Solution to Fifth Integral in Equation 3.83 *)
Clear[A5A, E5]

A5A = NIntegrate[(1 / (2 * α1)) * (Vr3α + Vr4α + Vz3α + Vz4α) ^ 2 *
    Exp[-2 * α1 * Sqrt[(VP * n * T) ^ 2 - r^2]], {r, 0, VR * n * T}]
E5 = A5A / (n * T)
```

```
NIntegrate::ploss :
 Numerical integration stopping due to loss of precision. Achieved neither the requested PrecisionGoal nor
   AccuracyGoal; suspect one of the following: highly oscillatory integrand or the true value of the
   integral is 0. If your integrand is oscillatory try using the option Method->Oscillatory in NIntegrate.
```

0.

0.

```
(* Solution to Sixth Integral in Equation 3.83 *)
Clear[A6A, A6B, A6C, E6]

A6A = NIntegrate[Abs[Vθ1^2] * Sin[θ], {θ, 0, θS}]
A6B = NIntegrate[Abs[Vθ2^2] * Sin[θ], {θ, 0, θS}]
A6C = NIntegrate[Abs[Vθ1 * Vθ2] * Sin[θ], {θ, 0, θS}]
E6 = VS * (A6A + A6B + A6C)
```

```
NIntegrate::ncvb : NIntegrate failed to converge to
   prescribed accuracy after 7 recursive bisections in θ near θ = 0.5529528510368396‘.
```

2.59657×10^{-7}

0.000425793

```
NIntegrate::ncvb : NIntegrate failed to converge to
   prescribed accuracy after 7 recursive bisections in θ near θ = 0.5622461762643494‘.
```

5.07642×10^{-6}

0.136237

```
(* Solution to Seventh Integral in Equation 3.83 *)
Clear[A7A, A7B, A7C, E7]

A7A = NIntegrate[Abs[Vθ1^2], {θ, θS, Pi / 2}]
A7B = NIntegrate[Abs[Vθ2^2], {θ, θS, Pi / 2}]
A7C = NIntegrate[Abs[Vθ1 * Vθ2], {θ, θS, Pi / 2}]
E7 = VR * (A7A + A7B + A7C)
```

1.08661×10^{-8}

0.00012469

1.16379×10^{-6}

0.0369175

```
(* Solution to Eight Integral in Equation 3.83 *)
Clear[A8A, A8B, A8C, E8]

A8A = NIntegrate[Abs[Vθ1^2] * Sin[θ], {θ, θS, Pi / 2}]
A8B = NIntegrate[Abs[Vθ2^2] * Sin[θ], {θ, θS, Pi / 2}]
A8C = NIntegrate[Abs[Vθ1 * Vθ2] * Sin[θ], {θ, θS, Pi / 2}]
E8 = VS * (A8A + A8B + A8C)
```

1.0445×10^{-8}

0.000119767

1.11827×10^{-6}

0.038203

```
(* Solution to Ninth Integral in Equation 3.83 *)
Clear[A9A, A9B, A9C, E9]

A9A = NIntegrate[Abs[Vθ1^2], {θ, θS, Pi / 2}]
A9B = NIntegrate[Abs[Vθ2^2], {θ, θS, Pi / 2}]
A9C = NIntegrate[Abs[Vθ1 * Vθ2], {θ, θS, Pi / 2}]
E9 = VR * (A9A + A9B + A9C)
```

1.08661×10^{-8}

0.00012469

1.16379×10^{-6}

0.0369175

```
(* Solution to Tenth Integral in Equation 3.83 *)
Clear[A10A, E10]

A10A = NIntegrate[(1 / (2 * β1)) * (Vr3β + Vr4β + Vz3β + Vz4β) ^2 *
    Exp[-2 * β1 * Sqrt[(VS * n * T) ^2 - r^2]], {r, 0, VR * n * T}]
E10 = A10A / (n * T)
```

6.64827×10^{-54}

1.48921×10^{-55}

```
(* Solution to Eleventh Integral in Equation 3.83 *)
Clear[A11A, E11]

A11A = NIntegrate[Abs[Vϕ1^2] * Sin[θ], {θ, 0, π / 2}]
E11 = VS * A11A
```

1.01289×10^{-6}

0.000320072

```
(* Total Energy *)
Clear[Etot]

Etot = E1 + E2 + E3 - E4 + E5 + E6 + E7 + E8 - E9 + E10 + E11
```

0.182889

```
(* Estimate Radiated Energy for an NS shake *)

M = 12100000;
P = 384000;
ρ = 1850;
f = 1.64;
ω = 2 * Pi * f;
VP = 597;
VS = 316;
VR = .9282 * VS;
Δ = VP / VS;
ΔRP = VR / VP;
ΔRS = VR / VS;
α = (I * ω / VP) * Sqrt[1 - Sin[θ]^2];
β = (I * ω / VS) * Sqrt[1 - Sin[θ]^2];
α1 = (ω / VR) * Sqrt[1 - ΔRP^2];
β1 = (ω / VR) * Sqrt[1 - ΔRS^2];
θP = ArcSin[VR / VP];
θS = ArcSin[VR / VS];
μ = ρ * VS^2;
T = 1 / f;
n = 50;


(* Solution to First Integral in Equation 3.83 *)
Clear[A1A, A1B, A1C, E1]

A1A = NIntegrate[Abs[VR1^2] * Sin[θ], {θ, 0, θP}]
A1B = NIntegrate[Abs[VR2^2] * Sin[θ], {θ, 0, θP}]
A1C = NIntegrate[Abs[VR1 * VR2] * Sin[θ], {θ, 0, θP}]
E1 = VP * (A1A + A1B + A1C)
```

1.56296×10^{-8}

0.0000119965

4.3286×10^{-7}

0.00742964

```
(* Solution to Second Integral in Equation 3.83 *)
Clear[A2A, A2B, A2C, E2]

A2A = NIntegrate[Abs[VR1^2], {θ, θP, Pi / 2}]
A2B = NIntegrate[Abs[VR2^2], {θ, θP, Pi / 2}]
A2C = NIntegrate[Abs[VR1 * VR2], {θ, θP, Pi / 2}]
E2 = VR * (A2A + A2B + A2C)
```

3.94233×10^{-7}

0.000167104

8.02345×10^{-6}

0.0514824

```
(* Solution to Third Integral in Equation 3.83 *)
Clear[A3A, A3B, A3C, E3]

A3A = NIntegrate[Abs[VR1^2] * Sin[θ], {θ, θP, Pi / 2}]
A3B = NIntegrate[Abs[VR2^2] * Sin[θ], {θ, θP, Pi / 2}]
A3C = NIntegrate[Abs[VR1 * VR2] * Sin[θ], {θ, θP, Pi / 2}]
E3 = VP * (A3A + A3B + A3C)
```

3.21178×10^{-7}

0.000129285

6.37304×10^{-6}

0.0811798

```
(* Solution to Fourth Integral in Equation 3.83 *)
Clear[A4A, A4B, A4C, E4]

A4A = NIntegrate[Abs[VR1^2], {θ, θP, Pi / 2}]
A4B = NIntegrate[Abs[VR2^2], {θ, θP, Pi / 2}]
A4C = NIntegrate[Abs[VR1 * VR2], {θ, θP, Pi / 2}]
E4 = VR * (A4A + A4B + A4C)
```

3.94233×10^{-7}

0.000167104

8.02345×10^{-6}

0.0514824

```
(* Solution to Fifth Integral in Equation 3.83 *)
Clear[A5A, E5]

A5A = NIntegrate[(1 / (2 * α1)) * (Vr3α + Vr4α + Vz3α + Vz4α) ^ 2 *
    Exp[-2 * α1 * Sqrt[(VP * n * T) ^ 2 - r^2]], {r, 0, VR * n * T}]
E5 = A5A / (n * T)
```

```
NIntegrate::ploss :
 Numerical integration stopping due to loss of precision. Achieved neither the requested PrecisionGoal nor
   AccuracyGoal; suspect one of the following: highly oscillatory integrand or the true value of the
   integral is 0. If your integrand is oscillatory try using the option Method->Oscillatory in NIntegrate.
```

0.

0.

```
(* Solution to Sixth Integral in Equation 3.83 *)
Clear[A6A, A6B, A6C, E6]

A6A = NIntegrate[Abs[Vθ1^2] * Sin[θ], {θ, 0, θS}]
A6B = NIntegrate[Abs[Vθ2^2] * Sin[θ], {θ, 0, θS}]
A6C = NIntegrate[Abs[Vθ1 * Vθ2] * Sin[θ], {θ, 0, θS}]
E6 = VS * (A6A + A6B + A6C)
```

```
NIntegrate::ncvb : NIntegrate failed to converge to
   prescribed accuracy after 7 recursive bisections in θ near θ = 0.5529528510368396‘.
```

2.97919×10^{-6}

0.00463524

```
NIntegrate::ncvb : NIntegrate failed to converge to
   prescribed accuracy after 7 recursive bisections in θ near θ = 0.5622461762643494‘.
```

0.000056734

1.4836

```
(* Solution to Seventh Integral in Equation 3.83 *)
Clear[A7A, A7B, A7C, E7]

A7A = NIntegrate[Abs[Vθ1^2], {θ, θS, Pi / 2}]
A7B = NIntegrate[Abs[Vθ2^2], {θ, θS, Pi / 2}]
A7C = NIntegrate[Abs[Vθ1 * Vθ2], {θ, θS, Pi / 2}]
E7 = VR * (A7A + A7B + A7C)
```

1.24673×10^{-7}

0.00135739

0.0000130065

0.401989

```
(* Solution to Eight Integral in Equation 3.83 *)
Clear[A8A, A8B, A8C, E8]

A8A = NIntegrate[Abs[Vθ1^2] * Sin[θ], {θ, θS, Pi / 2}]
A8B = NIntegrate[Abs[Vθ2^2] * Sin[θ], {θ, θS, Pi / 2}]
A8C = NIntegrate[Abs[Vθ1 * Vθ2] * Sin[θ], {θ, θS, Pi / 2}]
E8 = VS * (A8A + A8B + A8C)
```

1.19841×10^{-7}

0.0013038

0.0000124977

0.415987

```
(* Solution to Ninth Integral in Equation 3.83 *)
Clear[A9A, A9B, A9C, E9]

A9A = NIntegrate[Abs[Vθ1^2], {θ, θS, Pi / 2}]
A9B = NIntegrate[Abs[Vθ2^2], {θ, θS, Pi / 2}]
A9C = NIntegrate[Abs[Vθ1 * Vθ2], {θ, θS, Pi / 2}]
E9 = VR * (A9A + A9B + A9C)
```

1.24673×10^{-7}

0.00135739

0.0000130065

0.401989

```
(* Solution to Tenth Integral in Equation 3.83 *)
Clear[A10A, E10]

A10A = NIntegrate[(1 / (2 * β1)) * (Vr3β + Vr4β + Vz3β + Vz4β) ^2 *
   Exp[-2 * β1 * Sqrt[(VS * n * T) ^2 - r^2]], {r, 0, VR * n * T}]
E10 = A10A / (n * T)
```

7.78677×10^{-52}

2.55406×10^{-53}

```
(* Solution to Eleventh Integral in Equation 3.83 *)
Clear[A11A, E11]

A11A = NIntegrate[Abs[Vϕ1^2] * Sin[θ], {θ, 0, π / 2}]
E11 = VS * A11A
```

0.0000116214

0.00367236

```
(* Total Energy *)
Clear[Etot]

Etot = E1 + E2 + E3 - E4 + E5 + E6 + E7 + E8 - E9 + E10 + E11
```

1.99187

Bibliography

Aagaard, B. T., Finite-element simulations of earthquakes, Ph.D. thesis, California Institute of Technology, 1999.

Achenbach, J. D., *Wave Propagation in Elastic Solids*, first ed., Elsevier Science Publishing B.V., 1993.

Beck, J. L. and E. Chan, Comparison of the response of Millikan Library to San Fernando and Whittier narrows earthquakes, 1995.

Beck, J. L., and J. F. Hall, Factors contributing th the catastrophe in México City during the earthquake of September 19. 1985, *Geophysical Research Letters*, *13*, 593–596, 1986.

Beck, J. L., B. S. May, and D. C. Polidori, Determination of modal parameters from ambient vibration data for structural health monitoring, In *First World Conference on Structural Control.*, Los Angeles, California, USA, 3-5 August, 1994.

Bender, C. M., and S. A. Orszag, *Advanced Mathematical Methods for Scientists and Engineers*, McGraw-Hill Book Co., 1978.

Blandford, R., V. R. McLamore, and J. Aunon, Analysis of Millikan Library from ambient vibrations, *Technical report, Earth Teledyne Co*, 1968.

Bradford, S. C., J. F. Clinton, J. Favela, and T. H. Heaton, Results of Millikan Library forced vibration testing, *Earthquake Engineering Research Laboratory*, *EERL*, 2004.

Bradford, S. C. and T. H. Heaton, Weather patterns and wandering frequencies in a structure, *in preparation*, 2004.

Brillouin, L., *Wave Propagation and Group Velocity*, Academic Press, 1960.

Brillouin, L., *Elements of Vibration Analysis*, McGraw-Hill, Inc., 1986.

Bycroft, G. N., Forced vibrations of a rigid circular plate on a semi-infinite elastic space and on an elastic stratum, *Philosophical Transactions of the Royal Society of London Series A - Mathematical and Physical Sciences*, *248*, 327–368, 1956.

Campillo, M., J. C. Gariel, K. Aki, and F. J. Sánchez-Sesma, Destructive strong ground motion in México City: Source, path, and site effects during the great 1985 Michoacán earthquake, *Bull. Seism. Soc. of Am.*, *79*, 1718–1735, 1989.

Cardenas, M., P.-Y. Bard, P. Gueguen, and F. J. Chavez-Garcia, Soil-structure interaction in México City. Wave field radiated away from Jalapa building: Data and modelling, *12th world conference on Earthquake Engineering, Auckland, New Zealand*, 2000.

Cherry, J. T. J., The azimuthal and polar radiation patterns obtained from a horizontal stress applied at the surface of an elastic half-space, *Bulletin of the Seismological Society America*, *52*, 27–36, 1962.

Chopra, A. K., *Dynamics of Structures - Theory and Applications to Earthquake Engineering*, Prentice Hall, 1995.

Clinton, J. F., Modern seismology - instrumentation, and small amplitude studies for the engineering world, Ph.D. thesis, California Institute of Technology, 2004.

Clinton, J. F., and T. H. Heaton, Potential advantages of a strong-motion velocity meter over a strong-motion accelerometer, *Seismological Research Letters*, *73*, 332–342, 2002.

Clinton, J. F., S. C. Bradford, T. H. Heaton, and J. Favela, The observed drifting of the natural frequencies in a structure, *To be Submitted to the Bulletin of the Seismological Society America*, 2004.

Clough, R. W., and J. Penzien, *Dynamics of Structures*, second ed., McGraw-Hill Book Co., 1993.

Crouse, C. B., B. Hushmand, J. E. Luco, and H. L. Wong, Foundation impedance functions: Theory versus experiment, *Journal of Geothechnical Engineering*, *116*, 432–449, 1990.

Duke, C. M., and D. J. Leeds, Site characteristics of southern California strong-motion earthquake stations, *Tech. Rep. 62-55*, Reprinted July 1972, by the Califorina Division of Mines and Geology, as: Special Publication 38, 1962.

Foutch, D. A., A study of the vibrational characteristics of two multistory buildings, Ph.D. thesis, California Institute of Technology, 1976.

Foutch, D. A., J. E. Luco, M. D. Trifunac, and F. E. Udwadia, Full-scale, three-dimensional tests of structural deformations during forced excitation of a nine-story reinforced concrete building, *Proceedings of the U.S. Natl. Conference on Earthquake Engineering, Ann Arbor Michigan*, 1975.

Gradshteyn, I. S., and J. M. Ryzhjk, *Table of Integrals, Series, and Products*, Elsevier Science and Technology Books, 1995.

Gueguen, P., P.-Y. Bard, and C. S. Oliveira, Experimental and numerical analysis of soil motions caused by free vibrations of a building model, *Bulletin of the Seismological Society America*, *90*, 1464–1479, 2000.

Hall, J. F., and J. L. Beck, Structural damage in México City, *Geophysical Research Letters*, *13*, 589–592, 1986.

Hauksson, E., P. Small, K. Hafner, R. Busby, R. Clayton, J. Goltz, T. H. Heaton, K. Hutton, H. Kanamori, and J. Polet, Southern California Seismic Network: Caltech/USGS element of TriNet 1997-2001, *Seismological Research Letters*, *72*, 690–704, 2001.

Hisada, Y., Efficient method for computing Green's-functions for a layered half-space with sources and receivers at close depths., *Bull. Seism. Soc. of Am.*, *84*, 1456–1472, 1994.

Hisada, Y., Efficient method for computing Green's-functions for a layered half-space with sources and receivers at close depths. 2., *Bull. Seism. Soc. of Am.*, *85*, 1080–1093, 1995.

Housner, G. W., and D. E. Hudson, *Applied Mechanics Dymamics*, Division of Engineering and Applied Science, California Institute of Technology, 1980.

Iemura, H. and P. C. Jennings, Hysteretic response of a nine-storey reinforced concrete building during the san fernando earthquake, *Earthquake Engineering Research Laboratory*, *EERL*, 1973.

Jennings, P., Distant motions from a building vibration test, *Bull. Seism. Soc. of Am.*, *60*, 2037–2043, 1970.

Jennings, P., and J. Kuroiwa, Vibration and soil-structure interaction tests of a nine-story reinforced concrete building, *Bull. Seism. Soc. of Am.*, *58*, 891–916, 1968.

Johnson, L. R., Green's function for Lamb's problem, *Geophys. J. R. Astr. Soc.*, *37*, 99–131, 1974.

Kanamori, H., P. C. Jennings, S. K. Singh, and L. Astiz, Estimation of strong ground motions in México City expected for large earthquakes in the Guerrero seismic gap, *Bull. Seism. Soc. of Am.*, *83*, 811–829, 1993.

Kinemetrics, *Operating Instructions for Vibration Generator System Model VG-1*, 1975.

Kuroiwa, J. H., Vibration test of a multistory building, Ph.D. thesis, California Institute of Technology, 1969.

Lay, T., and T. C. Wallace, *Modern Global Seismology*, Academic Press, 1995.

Lomnitz, C., J. Flores, O. Novaro, T. H. Seligman, and R. Esquivel, Seismic coupling of interface modes in sedimentary basins, *Bull. Seism. Soc. of Am.*, *89*, 14–21, 1999.

Luco, J. E., M. D. Trifunac, and F. E. Udwadia, An experimental study of ground deformations caused by soil-structure interaction, *Proceedings of the U.S. Natl. Conference on Earthquake Engineering, Ann Arbor Michigan*, 1975.

Luco, J. E., M. D. Trifunac, and H. L. Wong, On the apparent change in dynamic behavior of a 9-story reinforced-concrete building, *Bull. Seism. Soc. of Am.*, *77*, 1961–1983, 1987.

Luco, J. E., H. L. Wong, and M. D. Trifunac, Soil-structure interaction effects on forced vibration tests, *Tech. rep.*, Prepared for the University of Southern California, 1986.

McVerry, G. H., Frequency domain identification of structural models from earthquake records, Ph.D. thesis, California Institute of Technology, 1980.

Miller, G. F., and H. Pursey, The field and radiation impedance of mechanical radiators on the free surface of a semi-infinite isotropic solid, *Proceedings of the Royal Society*, *223*, 521–541, 1954.

Mita, A., and J. E. Luco, Dynamic response of a square foundation embedded in an elastic half-space, *Journal of Geothechnical Engineering*, *115*, 491–503, 1989.

Peddie, N. W., The magnetic field of the earth - 1990: Declination chart, *U S Geological Survey Geeophysical Investigations, Map GP-1004-D,*, 1993.

Sambridge, M., Geophysical inversion with a neighbourhood algorithm - I, Searching a parameter space, *Geophysical Journal International*, *2*, 479–494, 1999a.

Sambridge, M., Geophysical inversion with a neighbourhood algorithm - II, Appraising the ensemble, *Geophysical Journal International*, *2*, 727–746, 1999b.

Sanchez-Sesma, F., S. Chavez-Perez, M. Suarez, M. A. Bravo, and L. E. Perez-Rocha, The México earthquake of September 19, 1985 - on the seismic response of the valley of México, *Earthquake Spectra*, *4*, 569–589, 1988.

Shannon & Wilson, I., and A. Associates, Geotechnical and strong motion earthquake data from U.S. accelerograph stations, *Tech. Rep. NUREG-0029*, Prepared for U.S. Nuclear Regulatory Commission, 1966a.

Shannon & Wilson, I., and A. Associates, Geotechnical data from accelerograph stations investigated during the period 1975-1979, *Tech. Rep. NUREG/CR-1643*, Prepared for U.S. Nuclear Regulatory Commission, 1966b.

Shannon & Wilson, I., and A. Associates, Verification of subsurface conditions at selected 'rock' accelerograph stations in California, *Tech. Rep. NUREG/CR-0055*, Prepared for U.S. Nuclear Regulatory Commission, 1966c.

Singh, S. K., J. Lermo, T. Dominguez, M. Ordaz, J. M. Espinosa, E. Mena, and R. Quaas, The México earthquake of september 19, 1985 - a study of amplification of seismic waves in the valley of México with respect to a hill zone site, *Earthquake Spectra*, *4*, 653–674, 1988a.

Singh, S. K., E. Mena, and R. Castro, Some aspects of source characteristics of the 19 September 1985 Michoacán earthquake and ground motion amplification in and near México City from strong motion data, *Bull. Seism. Soc. of Am.*, *78*, 451–477, 1988b.

Teledyne-Geotech, Post-earthquake vibration measurements of Millikan Library, *Tech. rep.*, Prepared for the California Institute of Technology, Pasadena, California, 1971.

Trifunac, M. D., Comparisons between ambient and forced vibration experiments, *Earthquake Engineering and Structural Dynamics 1*, 133–150, 1972.

UBC, I. C. C. S., *Uniform Building Code*, International Code Council, 1997.

Udwadia, F. E. and P. Z. Marmarelis, The identification of building structural systems: I. the linear case, *Bull. Seism. Soc. of Am. 66*(1), 125–151, 1976.

Udwadia, F. E. and M. D. Trifunac, Ambient vibration tests of a full-scale structures, In *Preceedings, Fifth World Conference on Earthquake Engineering*, Rome, 1973.

Udwadia, F. E. and M. D. Trifunac, Time and amplitude dependent response of structures, *Int. J. Earthquake Engineering and Structural Dynamics 2*, 359–378, 1974.

Uhrhammer, R. A., S. J. Loper, and B. Romanowicz, Determination of local magnitude using bdsn broadband records, *Bulletin of the Seismological Society America*, *86*, 1314–1330, 1996.

Wong, H. L., and J. E. Luco, Table of impedance functions and input motions for rectangular foundations, *Tech. rep.*, Prepared for the University of Southern California, 1978.

Wong, H. L., M. D. Trifunac, and B. Westermo, Effects of surface and subsurface irregularities on amplitudes of monochromatic waves, *Bull. Seism. Soc. of Am.*, 1977.

Wong, H. L., M. D. Trifunac, and J. E. Luco, A comparison of soil-structure interaciton calculations with results of full-scale forced vibration test, *Soil Dynamics and Earthquake Engineering*, *7*, 22–31, 1988.